UNIVERSITY OF SOUTHAMPTON

FACULTY OF PHYSICAL SCIENCES AND ENGINEERING

Electronics and Computer Science

Advanced Microfluidic Impedance Cytometry for Point of Care Analysis

by

Daniel Spencer

Thesis for the degree of Doctor of Philosophy

September 2013

UNIVERSITY OF SOUTHAMPTON

ABSTRACT

FACULTY OF PHYSICAL SCIENCES AND ENGINEERING

Electronics and Computer Science

Doctor of Philosophy

ADVANCED MICROFLUIDIC IMPEDANCE CYTOMETRY FOR POINT OF CARE ANALYSIS

by Daniel Spencer

Microfluidic impedance cytometry is the dielectric characterisation of single particles flowing through a microfluidic channel. Microfluidic impedance cytometry offers a novel solution to counting and discrimination of different particles and cells. One application is discrimination of different blood cell types in a low cost Point of Care device. However, the accuracy of currently available systems is poor and inadequate for clinical use. A full numerical model, developed in this research, demonstrated that the main source of measurement inaccuracy relates to the position of the particle in the micro-channel. Particles travelling at the top or bottom of the channel close to the electrodes were found to have a higher impedance signal compared with particles travelling through the centre of the channel. Counter-intuitively, the model also showed that although the electrode geometry is symmetrical, the variation in signal is asymmetric about the vertical position of the particle within the channel. A new electrode geometry was developed to minimise particle positional dependence. When combined with new signal processing techniques which were also developed, this led to marked improvements in measurement accuracy. For example, the coefficient of variation of monodisperse beads were half the manufacturer's data.

Applications of the improved device were investigated by analysing a range of different cell types in blood. Measurements of the distribution width of red blood cells were successful and found to be within the known clinical range. It was also shown that combined with pre-enrichment techniques, the device successfully detected clinically relevant concentrations of individual tumour cells in a background of 10^6 times more white blood cells. In order to use microfluidic impedance cytometry for diagnostic blood counting applications, lysing of the more numerous red blood cells is required. Lysing methods suitable for implementing in a Point of Care device were evaluated and a stirred mixing system was developed. In summary, this thesis describes a new, high accuracy microfluidic impedance cytometer which has the potential to be integrated into a miniature blood counting device for Point of Care analysis.

Contents

List of Figures

List of Tables

Declaration of Authorship

I, Daniel Spencer , declare that the thesis entitled *Advanced Microfluidic Impedance Cytometry for Point of Care Analysis* and the work presented in the thesis are both my own, and have been generated by me as the result of my own original research. I confirm that:

- this work was done wholly or mainly while in candidature for a research degree at this University;
- where any part of this thesis has previously been submitted for a degree or any other qualification at this University or any other institution, this has been clearly stated;
- where I have consulted the published work of others, this is always clearly attributed;
- where I have quoted from the work of others, the source is always given. With the exception of such quotations, this thesis is entirely my own work;
- I have acknowledged all main sources of help;
- where the thesis is based on work done by myself jointly with others, I have made clear exactly what was done by others and what I have contributed myself;
- parts of this work have been published as:

    1. **Positional dependence of particles in microfluidic impedance cytometry**, Daniel Spencer and Hywel Morgan, 2011, *Lab Chip*, 11, 1234-1239.
    2. **Simultaneous high speed optical and impedance analysis of single particles with a microfluidic cytometer**, David Barat*, Daniel Spencer*, Giuseppe Benazzi, Matthew Charles Mowlem and Hywel Morgan, 2012, *Lab Chip*, 12, 118-126. *Joint first authors.
    3. **Comparison of venous and capillary differential leukocyte counts using a standard hematology analyzer and a novel microfluidic impedance cytometer**, Veronica Hollis, Judith Holloway, Scott Harris, Daniel Spencer, Cees van Berkel and Hywel Morgan, 2012, *PLoS One*, 9, 7, e43702.

4. **Apparatus for electrically measuring individual particles flowing in a liquid**, Daniel Spencer and Hywel Morgan, Patent application filed on 16th April 2013.
5. **A method of electrically measuring the size of individual particles flowing in a liquid**, Daniel Spencer and Hywel Morgan, filed on 16th April 2013.
6. **Identification of tumour cells using microfluidic impedance cytometry**, Daniel Spencer, Veronica Hollis and Hywel Morgan, 2012, *in Proc. NanoBioTech, Montreux, Switzerland.*
7. **Miniaturised point of care full blood count**, Daniel Spencer and Hywel Morgan, 2012, *in Proc. Bringing diagnostics prototypes to the point of care, Nairobi, Kenya.*

Signed:.....

Date:.....

Acknowledgements

I would like to thank Prof. Hywel Morgan for his support and guidance throughout this work. I am incredibly grateful for the fantastic opportunity to pursue this research. I would like to thank all my friends and colleagues in the centre for hybrid biodevices, both past and present. A special mention goes to Gregor Elliott, Veronica Hollis and Mark Friddin. Thanks also to Judith Holloway, Nicola Ingles, Pamela Dothie and the team at Philips, Cambridge for many fruitful discussions. I would also like to thank Katie Chamberlain for fabricating the MIC chips. Finally, I would like to express my gratitude to my family and Anne for their never ending support throughout this project.

List of Symbols

a	Particle diameter (m)
A	Area (m^2)
c_m	Speed of sound in medium (ms^{-1})
c_p	Speed of sound in particle material (ms^{-1})
C	Capacitance (F)
d	Distance (m)
$\mathbf{d}$	Displacement vector (Cm^{-2})
$\mathbf{E}$	Electric field (Vm^{-1})
$\tilde{f}_{CM}$	Clausius Mossotti factor $(-)$
$\mathbf{F}$	Force (N)
$\mathbf{F}_{ax}$	Primary axial radiation force (N)
$\langle F_{DEP} \rangle$	Time averaged dielectrophoretic force (N)
H	Channel height (m)
j	Imaginary number $(-)$
$\mathbf{J}$	Electric current density (Am^{-2})
k	Wavenumber (m^{-1})
k_b	Boltzmann constant $(1.38 \times 10^{-23} JK^{-1})$
K_s	Surface conductance (S)
l_0	Characteristic length (m)
p	Pressure (Pa)
$\mathbf{p}$	Dipole moment (Cm)
$\mathbf{P}$	Polarisation (Cm^{-2})
q	Elementary charge $(1.6 \times 10^{-19} C)$
Q	Volumetric flow rate $(m^3 s^{-1})$
r	Particle radius (m)
Re	Reynolds number $(-)$
T	Temperature (K)
u	Velocity (ms^{-1})
u_0	Mean fluid velocity (ms^{-1})
v	Particle volume (m^3)
W	Channel width (m)

Z	Impedance (Ω)
α	Polarisability (Fm^{-2})
Γ	Torque (Nm)
ε_0	Permittivity of free space ($8.85 \times 10^{-12} Fm^{-1}$)
ε_r	Relative permittivity ($-$)
$\tilde{\varepsilon}$	Complex permittivity ($-$)
$\tilde{\varepsilon}_p$	Complex permittivity of a particle ($-$)
$\tilde{\varepsilon}_m$	Complex permittivity of the suspending medium ($-$)
η	Kinematic viscosity (Pas)
κ^{-1}	Debye length (m)
ρ	Density (kgm^{-1})
ρ_m	Medium density (kgm^{-1})
ρ_p	Particle density (kgm^{-1})
σ	Conductivity (Sm^{-1})
σ_m	Medium conductivity (Sm^{-1})
σ_p	Particle conductivity (Sm^{-1})
τ	Relaxation time (S)
ψ	Volume fraction ($-$)
Φ	Acoustic contrast factor ($-$)
χ_e	Electric susceptibility ($-$)
ω	Angular frequency ($rads^{-1}$)

List of Abbreviations

CTC	Circulating Tumour Cell
CV	Coefficient of Variation
DEP	Dielectrophoresis
EDL	Electrical Double Layer
$EpCAM$	Epithelial Cell Adhesion Molecule
FBC	Full Blood Count
FEM	Finite Element Method
MCV	Mean Cell Volume
MIC	Microfluidic Impedance Cytometer
PBS	Phosphate Buffered Saline
$PMMA$	Poly (methyl methacrylate)
PoC	Point of Care
RBC	Red Blood Cell
RDW	Red Cell Distribution Width
WBC	White Blood Cell

Chapter 1

Introduction and Motivation

1.1 Introduction

Counting and analysing small particles such as cells, viruses and bacteria is an important and widely used measurement tool in medical science. For example, enumeration of different blood cells can be used to help diagnose a wide variety of medical conditions including anaemia, pneumonia, thrombocytopenia, or to indicate underlying health problems such as leukaemia (a type of cancer). This full blood count (FBC) currently uses large and expensive equipment which normally requires the patient's sample to be sent to a hospital for analysis. Several smaller Point of Care (PoC) analysers are commercially available but cannot perform all the analyses required for a FBC, and have limited applications.

A PoC FBC test would have many benefits, including home use by patients on chemotherapy, which would allow continuous adjustment of drugs and avoid infection risk from hospital visits by vulnerable patients. The immediate availability of the FBC results from a PoC device would also assist diagnosis in GP surgeries. A relatively cheap, robust and portable PoC device would also benefit developing countries where the costs of traditional tests are prohibitively high.

The primary aim of this research project was to develop a miniature system to count and analyse the different cells present in blood, which are typically between 2 and 15μm in diameter. However, the developed system can also measure many other small particles with diameters from 1 to 25μm. For example the research has included counting dust and pollen particles in ice core samples, which is important to date the cores as part of climate change research. It has also been used to detect and discriminate single cancer cells in blood which is an important marker to predict patient survival.

A microfluidic impedance cytometer (MIC), for counting and analysing small particles, had previously been developed and was the starting point for this project. The accuracy

of this first generation system was limited. For example, measurement of the distribution of monodisperse plastic beads was much greater than the actual size distribution reported by the manufacturer. To understand the cause of this problem, a full numerical model for the system was developed. The model demonstrated that the inaccuracies in the first generation system were due to particle position in the channel which was not accounted for. The model showed that particles travelling close to the electrodes have a higher measured signal compared with the same sized particle in the centre of the channel (away from the electrodes) and unexpectedly, despite the symmetric electrode geometry, the increase in signal is asymmetric about the vertical channel position. The numerical model was extended to include calculations of the flow profile to predict a velocity-impedance scatterplot of a population of particles. This enabled direct comparison of the simulation with experimental data and highlighted significant particle migration in the experimental data due to inertial focusing effects.

The numerical model was used to investigate new electrode geometries to reduce this particle positional dependence. An improved geometry was discovered and experimentally tested. New signal processing techniques were developed and, in conjunction with the new electrode geometry, the coefficient of variation (CV) of four different sized particles experimentally measured was approximately half of the manufacturer's data, demonstrating high accuracy particle measurement. Measurements of the distribution width of red blood cells (RBCs) are described and the results were found to be within the known clinical range. Also the continuous flow measurement capability is demonstrated for ice core samples, overcoming the calibration requirements for the standard equipment.

The system capability was further examined by exploring the impedance detection of tumour cells. The number of tumour cells in a blood sample is used as a clinically important prediction of the expected survival of cancer patients. However, these cells (called circulating tumour cells, CTCs) are challenging to count because they are rare (one in a background of billions of RBCs). Typically these cells are identified using their surface markers. However, this requires extensive sample preparation and there is the potential for CTCs without these markers to be missed. To this end, the use of MIC to characterise CTC-like tumour cell lines was investigated. The potential for CTC detection using MIC was investigated by measuring blood samples spiked with serially diluted samples of tumour cells using minimalistic sample preparation (chemical RBC lysis). Tumour cells in a background of 1000 times more white blood cells (WBCs) could be identified, however CTCs can be up to 1000 times rarer. Clinically relevant concentrations of tumour cells were measured using pre-enrichment to demonstrate the potential for CTC enumeration using MIC.

The first generation MIC system had been developed to measure the three most numerous subpopulations of WBC, which is an important part of the FBC. However, before measurement the blood needed to be manually mixed with different chemicals

for a precise time to remove the RBCs, thus limiting it to operation in a lab environment by a trained operator. The timing of this pre-processing was investigated and optimised to maximise the separation between each WBC subpopulation to enable accurate enumeration. Next, an automatic pre-processing cartridge using a microfluidic mixer was developed, however difficulties in achieving stable flow and reproducibility between experiments meant the system was not robust enough for a fully automatic system. Instead, a stirred mixing system was investigated and found to be a suitable pre-processing system which could be automated and integrated into a miniature MIC device. While developing the stirred lysis system, it was discovered that a high shear rate was required to lyse all the RBCs to successfully count the WBC subpopulations. This further discounts the use of a microfluidic mixer, which had a comparatively low shear rate.

1.2 Particle Counting and Analysis Techniques

The reference standard for cell counting is the haemocytometer, which is a widely used direct single cell counting technique. It consists of a transparent chamber and cover slip which is filled by capillary force with a small sample of the unknown cell suspension, Figure 1.1. The chamber is viewed using a microscope and the number of cells are counted within a grid machined into the bottom of the counting chamber. The grid size and chamber depth are predefined and thus the volume of the chamber is known and used to estimate the concentration of the cells. The main limitations with the haemocytometer are that counting is done manually and thus human error is introduced. Also, counting is slow (a few cells per second) and time constraints mean rare cell detection is difficult. Smaller particles such as bacteria or platelets are difficult to view using a conventional microscope making counting challenging. Basic cell analysis and identification can be performed using techniques such as staining with Trypan Blue to distinguish dead from living cells. Other stains can be used to discriminate different types of cells.

Flow cytometry is a generic technique used for measuring individual small particles, suspended in a liquid medium, which are passed individually through a detection region. The properties of the particles are measured, typically using electrical (resistance, impedance) or light (forward scatter, side scatter, occlusion or fluorescence) based techniques. The first flow cytometer was the Coulter counter (Coulter, 1956). The device, Figure 1.2, consists of two reservoirs separated by a small aperture. Particles are suspended in an electrolyte, placed in one reservoir and passed through the aperture to the second reservoir. A voltage is applied between the two measurement electrodes and the current flowing between the electrodes is monitored. Particles traverse the aperture one-by-one, reducing the current flow. The size of the current spike is proportional to the volume of the cell thus single particles can be counted and sized. Metering electrodes

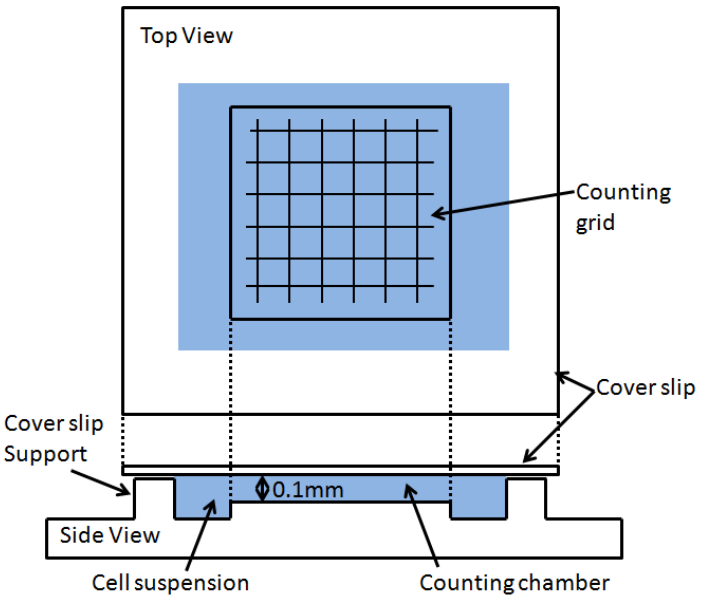

Figure 1.1: Overview of a haemocytometer used to count cells. The device consists of a base and cover slip which define a chamber of constant volume. The haemocytometer is viewed with a microscope and cells are counted within a grid and used to infer the concentration of cells.

are used to start and stop the particle counting when a fixed volume of liquid has been measured and this is used to calculate the particle concentration.

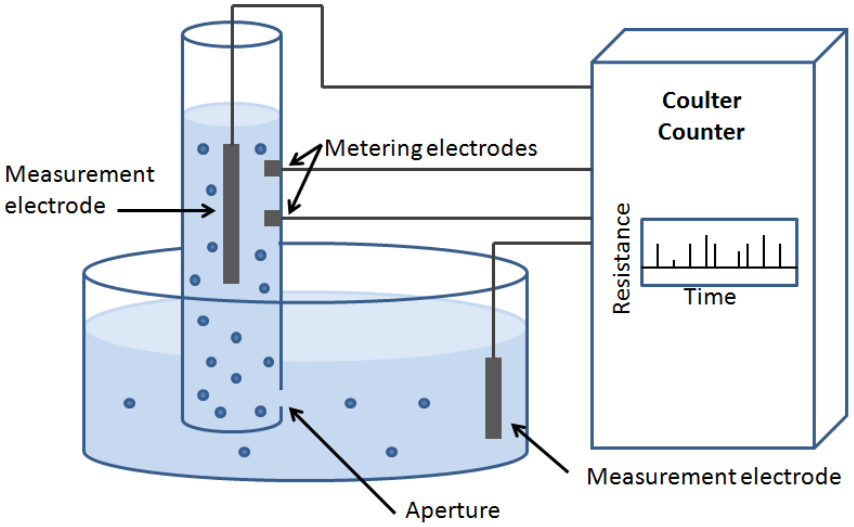

Figure 1.2: Overview of a Coulter counter. A small aperture separates two reservoirs with the sample loaded into one reservoir. Electrodes measure the current flow through the aperture which is reduced as a cell passes. Metering electrodes start and stop the measurement when a fixed volume of sample has been dispensed, so that the absolute cell particle concentration can be determined.

The first fluorescent based flow cytometer was developed in the late 1960's (Shapiro, 2003). The cells of interest are fluorescently labelled by incubating them with an

antibody conjugated to a fluorescent molecule. The suspension of cells is sheathed in a second liquid (usually saline) and then passed through a nozzle to reduce the stream width such that only one particle passes through the laser beam at any one time (Figure 1.3). The sheath flow is required because the intensity profile of a laser beam is Gaussian and thus particles must all pass through the same point within the beam to keep the interrogation power constant. Nowadays, commercial flow cytometers can measure up to 100,000 cells per seconds and simultaneously detect scattered light (cell size and granularity) and multiple fluorescent markers (Shapiro, 2003). Nonetheless, these cytometers are large and expensive due to the optical components such as lenses and filters required for the sheath flow system. Efforts are being made to miniaturise optical flow cytometers for portable operation: integrated fibre-optics, microlenses and waveguides have been demonstrated. However, the lasers, optical filters and detection systems (such as photomultiplier tubes) are bulky and have not yet been integrated.

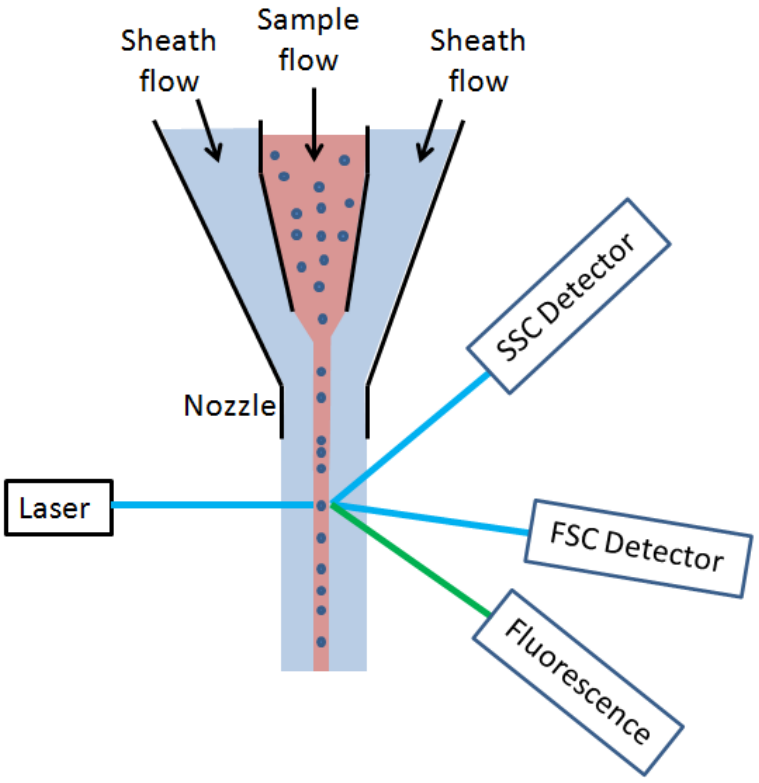

Figure 1.3: Illustration of an optical flow cytometer. A sheath flow is used to surround the sample (called hydrodynamic focusing) before it passes through a nozzle which generates a tight stream flowing through the centre of a laser beam. Scattered light (SSC: Side scattered and FSC: Forward scattered) and fluorescence is detected using photomultiplier tubes. The need for optics such as lenses and filters makes the system bulky.

A MIC is a type of Coulter counter which use miniature electrodes within a microfluidic channel (Figure 1.4). The dimensions of the fluidic channel and electrodes are of a similar magnitude to the diameters of the particles to be measured. For instance, to measure blood cells (2 to 15μm in diameter), the height and width of the channel should

be around 20 to 40μm. If the channel dimensions are too small, larger particles will block the channel. The limit of detection is proportional to the channel dimensions thus if the channel is too large, smaller particles cannot be measured. Compared with the large electrodes typically used in a Coulter counter, miniature electrodes mean that higher frequencies can be used which enables measurements of the membrane and cytoplasm properties of the cells. By using multiple simultaneous interrogation frequencies, label free measurement of both cell size and membrane capacitance is achieved. This enables the discrimination of different types of similarly sized cells. The electrical detection method of impedance cytometry is inherently smaller and simpler than conventional optical detection and offers a novel solution to low cost cell analysis and discrimination technology for PoC diagnostics.

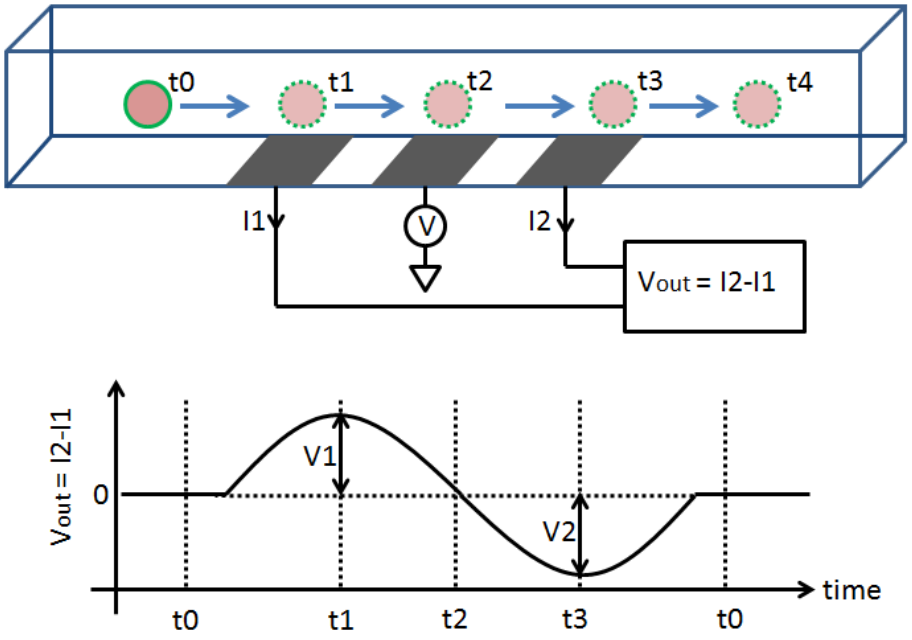

Figure 1.4: Diagram of a miniature impedance cytometer. Cells are suspended in an electrolyte and passed through a miniature channel (typical cross sectional dimensions of $40 \times 40\mu m$). The impedance is measured as cells pass over electrodes fabricated within the channel. The height of the impedance peak is equal to the depth of the trough ($V1 = V2$) and this signal is proportional to the volume of the measured particle.

In summary the haemocytometer is the most simple and widely using cell counting device, and can be used to discriminate sub-populations of cells. Due to the limits of optical microscopy, it is difficult to use haemocytometers to count small particles such as bacteria and accurate cell sizing is not possible. Optical flow cytometers can measure many thousands of particles per second, making rare cell identification feasible and can use multi-colour fluorescence to discriminate a mixture containing many different cells. However they are large and expensive and cannot accurately measure the particle size because light scatter is a non linear function of particle size. Standard Coulter counters accurately measure the size (electrical volume) of particles but cannot

distinguish between different cells of similar size. A MIC is a type of Coulter counter in which the electrodes are embedded within the orifice (microfluidic channel) as opposed to either side of the orifice as in a standard Coulter counter. This reduces the parasitic capacitances to enable high frequency measurements of cells (the membrane properties). In addition the miniature size of a MIC allows it to be used in portable applications along with integrated sample preparation.

1.3 Point of Care Testing

PoC testing is a generic term used to describe the medical testing of a patient using a device which is close to the patient. Typically, this means that the test is performed near to the patient's bed when the patient is in a hospital, at a GP's surgery when the patient has come in for a check-up or at the patient's home as part of ongoing monitoring. There are numerous PoC tests available on the market, examples include blood glucose level for diabetics, urine pregnancy tests and miniature blood cholesterol tests. However, there are still many tests which are not available in a portable PoC format. When PoC testing is not available, the patient's sample must be sent to a laboratory for testing, often meaning the patient must visit the hospital for the test. It can take hours or days for the delivery of the patient's sample to the laboratory and return of the results meaning a delay in treatment or the requirement of a second visit of the patient to receive the results. PoC testing would minimise this time by utilising small, portable testing machines which could be located in GP surgeries or at the patient's home. These devices have the potential to decrease running costs of hospitals and enable faster treatment of patients.

1.4 The Full Blood Count Measurement

A typical adult has approximately 6 litres of blood. Of this volume about 55% is plasma (consisting of about 90% water), the remaining 45% volume comprises of blood cells. The cells present, in order of abundance, are red blood cells whose role is to transport oxygen around the body, platelets which cause blood to clot and white blood cells which form the immune system. The full blood count (FBC) is a measurement of these cells and the test is widely used to diagnose many forms of disease. Tables 1.1 and 1.2 lists the parameters measured and typical ranges of the FBC test.

White Blood Cells	Normal Range	
	Count per nL	% of total
Total	4-11	100
Basophils	0-0.1	0-1
Eosinophils	0.04-0.4	1-6
Lymphocytes	1.5-4.5	20-45
Monocytes	0.2-0.8	2-10
Neutrophils	2-7.5	40-75

Platelets	Normal Range
Mean Volume	7.5-11.5 fL
Count per nL	150-400

Table 1.1: Normal WBC and platelet ranges for the complete blood count. Data from Longmore et al. (2010) and Kumar (2009).

Red Blood Cells	Normal Range	
	Male	Female
Count per pL	4.5-6	3.9-5
Packed cell volume in L/L	0.4-0.54	0.37-0.47
Volume in fL	80-96	80-96
Haemoglobin in g/dL	13.5-17.5	11.5-16.5
RBC size distribution (CV in %)	11-15	11-15
Mean cell Haemoglobin in pg	27-32	27-32
Mean cell Haemoglobin Concentration in g/dL	32-36	32-36

Table 1.2: Normal RBC ranges for the complete blood count. Data from Longmore et al. (2010) and Kumar (2009).

1.4.1 Clinical Diagnosis Using the Full Blood Count

1.4.1.1 Red Blood Cells and Haemoglobin

Red blood cells (RBCs) account for most of the cells present in blood. They are filled with haemoglobin which binds to oxygen and transports it around the body. The FBC measures the number of RBCs in blood and the amount of haemoglobin present. The red cell count is multiplied by the mean red cell volume to calculate the packed cell volume (haematocrit). A low haemoglobin count is usually associated with anaemia, however the mean volume of the RBCs (mean cell volume: MCV) is needed to diagnose the cause. For instance a low MCV indicates anaemia caused by an iron-deficiency, whereas a high MCV could indicate a B12 or foliate deficiency.

1.4.1.2 White Blood Cells

White blood cells (WBCs) form part of the immune system and defend the body from pathogens. There are five main types of WBC and these are described below in descending order of abundance.

Neutrophils can account for up to 75% of the total WBC count and are responsible for ingesting bacteria, fungi and damaged cells. An increased count is called neutrophilia

and can be an indication of a bacterial infection. Other causes of a high neutrophil count are stress (for instance trauma or burns) or inflammation (such as after a heart attack). A reduction in the neutrophil count means the body is less able to defend itself and is common in patients undergoing chemotherapy. It could also indicate a viral infection, severe bacterial infection (such as from typhoid) or bone marrow failure.

Lymphocytes are the second most numerous WBC population and are responsible for immunity and antibody protection. A high count is an indication of viral or chronic infection such as tuberculosis or hepatitis. The cells are further divided into three types: T-lymphocytes, B-lymphocytes and natural killer (NK) cells depending on the surface marker expression (T cells express either CD4 or CD8 whereas B-lymphocytes express CD19 and NK cells express CD16). A low T-lymphocyte (CD4) count is commonly associated with HIV infection.

Monocytes are a subpopulation of WBC which differentiate into macrophages to ingest pathogens and dead cells. An increased count can be seen post-chemotherapy, but can also be an indication of a chronic infection such as malaria or tuberculosis.

Eosinophils defend against infection from protozoa (parasites) and form part of the allergic response. A high count could be indicative of a parasitic infection or an allergic reaction such as hay fever.

Basophils are one of the rarest WBC subpopulations, usually accounting for less than 1% of the total WBCs. The physiological role is not known, but increased numbers are present in inflammatory disorders such as rheumatoid arthritis.

1.4.1.3 Platelets

Platelets make blood clot, for instance to stop bleeding from a wound. A low count, called thrombocytopenia, indicates that a patient could be susceptible to bleeding, which could for example be caused by an autoimmune disorder. A very low count (less than 20 per nanolitre) means the patient is at risk of spontaneous bleeding. High counts mean the blood is more likely to clot, however the activation level of platelets also determines how easily platelets form clots. The mean platelet volume increases when platelets are produced by the body at a higher rate and can be used to infer problems with platelet production.

1.4.2 Commercial Point of Care Devices

The FBC is widely used in hospitals, where the test is normally performed in centralised laboratories using haematology analysers such as the Sysmex XE-2100. This device can measure 150 samples per hour, however it costs around £100,000, requires 9 different

reagents and weighs more than $100kg$, and is thus not suitable for PoC applications. There are several portable blood counting devices currently on the market which are summarised below, however none of the devices can perform the full range of FBC measurements.

HemoCue make a portable, battery powered system to measure the five WBC subpopulations. The device was launched in 2012 and is based on a haemocytometer, but uses a camera to count the cells present. RBCs are chemically lysed and the WBCs stained to enable automatic counting of the total WBC. Discrimination between the WBC subpopulations is performed using image processing techniques to examine the shape of each cell. The HemoCue total WBC has been compared with a conventional Haematology analyser and found to be accurate to within 12% for all 200 clinical samples (Osei-Bimpong et al., 2012). However the device does not measure RBCs, platelets or haemoglobin and thus has limited diagnostic use. Also the device is not always accurate; high levels of normoblasts or reticulocytes (greater than 2%) interfere with the test results (Osei-Bimpong et al., 2012). These are immature red blood cells which are commonly seen in patients suffering from anaemia.

The Chempaq XBC is a small device that measures RBCs, haemoglobin and the three most numerous WBC subpopulations. The device performs a Coulter counter measurement using electrodes and an aperture built into each single-use cartridge to measure the cells. Haemoglobin is measured using a miniature photometric method. However, the device only performs one measurement at a time (either WBCs, RBCs or haemoglobin), each requiring a separate cartridge. The XBC produced similar results to a conventional haematology analyser when tested with a variety of clinical samples (Rao et al., 2011) except for monocytes which showed poor concordance. In addition the device does not measure platelets.

1.4.3 Summary

In summary, the FBC enumerates the cells present in blood and can be used to help diagnose many different diseases for instance aiding in differentiating between different causes of anaemia. However, the test is usually performed in centralised laboratories which require the patient to visit a hospital. There are currently two PoC tests commercially available for blood cell counting, however neither of these measure all the cells present in blood. A PoC FBC test would have many uses, but the greatest value of a cost-effective and simple to operate commercial system perhaps would be for home monitoring. Patients on chemotherapy suffer from destruction of neutrophils which makes them vulnerable to bacterial infections. A home monitoring FBC test would allow continual monitoring which would enable faster adjustment of the chemotherapy drugs. This would also avoid the infection risk from a hospital visit. The immediate availability of results from a simple PoC FBC test would also benefit diagnoses in GP surgeries;

currently the GP must send the patient's sample to hospital for this test. Miniaturised technologies typically require less blood (which can be taken from a fingerprick) and are suitable for infants. A miniature PoC device would also benefit developing countries where the costs of traditional tests are prohibitively high. This thesis therefore describes the development of MIC and automatic sample pre-processing towards a PoC FBC.

Chapter 2

Theory and Practice

2.1 Chapter Overview

This chapter explains the theory underlying impedance measurements described later in this thesis, followed by the experimental methodology pertinent to the experiments.

2.2 Underlying Theory

2.2.1 Introduction

The basic principles of electric charge and the electronic properties of conductors and insulators are described, followed by an introduction to dipoles and the forces that occur on dipoles when placed in an electric field. This chapter then describes polarisation which is a net movement of charge, the three forms of polarisation (electronic, atomic and orientation) that can occur in homogeneous materials and interfacial polarisation that can occur in combinations of materials with different dielectric properties. Permittivity, i.e. the amount a material polarises in the presence of an electric field is also described.

The theory behind dielectric relaxation, which relates to the time taken for dipoles to reach a random orientation from a fully polarised state after removal of the applied field is then presented. This includes the Debye dispersion formulas for for single Debye-type and modification to the formula for multiple closely spaced dispersions.

Maxwell-Wagner interfacial polarisation is a particular type of polarisation that occurs due to the discontinuity between the charge on either side of an interface between different dielectrics. This type of polarisation is particularly relevant to the work described in this thesis, and occurs for example in cells suspended in an electrolyte. Characterisation of relaxation using the Clausius Mossotti factor is also described.

Maxwell's mixture theory is then outlined. This allows multiple particles in a suspension to be modelled as one overall complex permittivity. Biological cells have a complex structure, comprising a thin insulating membrane surrounding a conducting cytoplasm; a nucleus may also be present. The theory of the simplification of this structure into a single shell model, which is an extension of Maxwell's mixture theory, is presented.

When an electrode or charged surface is placed into an electrolyte, ions in the electrolyte of opposite polarity to the surface charge move towards the surface to balance this surface charge to satisfy electro-neutrality. This is called the electrical double layer and has the effect of shielding the bulk charge of the solution from an electric field applied by the electrodes at low frequencies. The thickness of the layer is characterised by the Debye length and the measurement frequency required to overcome this polarisation is described. A description of each of the symbols and their SI units can be found in the list of symbols at the start of this thesis.

2.2.2 Electric Charge

Electric charge is a physical property of matter. A charged object is an object which has a different number of electrons compared to the number of protons. A difference of one proton or electron means the object has a charge of magnitude $1.6 \times 10^{-19} C$. Charged objects produce an electric field which exerts a force on other nearby charged objects.

The electronic properties of materials can be classified as either a conductor or an insulator according to their response to an electric field. A conductor has unbound charge (usually electrons), which can freely move when an electric field is applied across the material (Figure 2.1). The response of a conductor is described by Ohms law, Equation 2.1.

$$\mathbf{J} = \sigma \mathbf{E} \tag{2.1}$$

Where $\mathbf{J}$ is the electric current density, σ is the conductivity and $\mathbf{E}$ is the applied electric field.

Insulators are materials where all the charge is confined to individual atoms or molecules. This is called bound charge and means the material cannot conduct. However, the charge can move slightly in the presence of an electric field which is called polarisation.

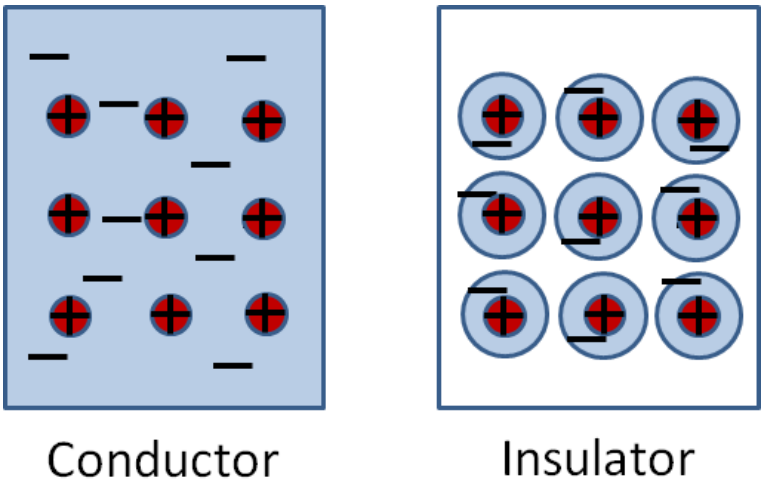

Figure 2.1: Illustration of the difference between a conductor and an insulator. In a conductor, charge (usually the electrons) can freely move. In an insulator, each atom has fixed charge which cannot move.

2.2.3 Dipoles

Dipoles consist of two sets of electrical charges of equal magnitude but opposite sign separated by a distance. When placed in an electric field the positive charge is attracted towards the negative electrode and the negative charge is attracted in the opposite direction. Since each force is equal, the dipole will not move closer to either electrode, however the dipole will experience a torque which will cause it to turn in the direction of the electric field.

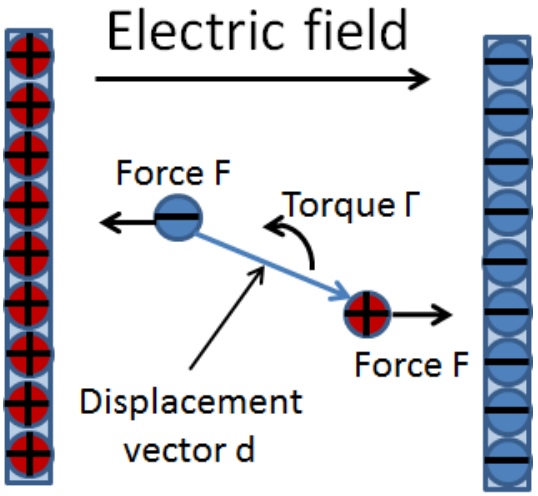

Figure 2.2: Diagram of a dipole between two charge electrodes. There is a force, **F**, acting on the negative charge of the dipole and an equal but opposite in direction force acting on the positive charge. The dipole experiences a torque which rotates the dipole to the horizontal position.

The force **F** acting on a dipole is proportional to the gradient of the electric field, Equation 2.2.

$$\mathbf{F} = \mathbf{p}\nabla\mathbf{E} \tag{2.2}$$

Where the dipole moment **p** is given by Equation 2.3.

$$\mathbf{p} = q\mathbf{d} \tag{2.3}$$

d is the displacement vector which points from the negative to the positive charge and q is the magnitude of each charge.

The torque Γ on the dipole due to the electric field **E** is the cross product ($\times$) between the dipole moment and the electric field (Equation 2.4).

$$\Gamma = \mathbf{p} \times \mathbf{E} \tag{2.4}$$

2.2.4 Polarisation

When an electric field is applied across any material, bound charges can move slightly. This is called polarisation and materials which exhibit polarisation are called dielectrics.

There are four types of polarisation: three of these (electronic, atomic and orientation) occur in homogeneous materials, while interfacial polarisation only occurs in heterogeneous materials which consist of two or more materials with different dielectric properties.

Electronic polarisation results from the application of an electric field to an atom. In an atom, a cloud of electrons (negative charge) surround a positively charged nucleus. The average positions of the positive and negative charge overlap and therefore there is no distance between the positive and negative charge and therefore no dipole as shown in Figure 2.3. When an electric field is applied across a material, the applied field causes a movement of the average position of the electron cloud in each atom. This movement of charge creates a distance between the average positive and negative charge and is called an induced dipole. This type of polarisation, called electronic polarisation, occurs in all materials.

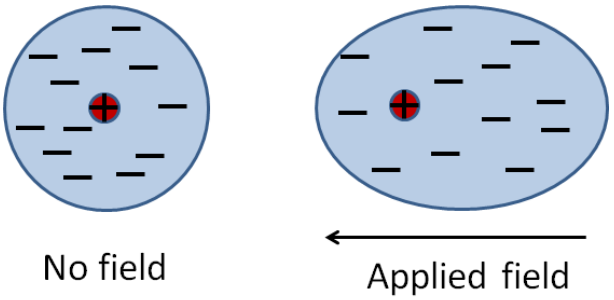

Figure 2.3: Diagram illustrating electronic polarisation. When an electric field is applied across an atom, the electrons orbiting the nucleus shift slightly, creating a distance between the net positive and negative charge.

Orientational polarisation results from molecules with a permanent dipole. In individual atoms the average position of all the positive and negative charges overlap and there is no net dipole. However in some molecules there is a distance between the average position of the positive and negative charges which forms a dipole. These molecules are termed polar and have permanent dipoles. Polar molecules arise due to differences in electronegativity between different atoms in a molecule. One example is water, which has a 104.5° angle between the two hydrogen atoms and the oxygen atom. Since oxygen is more electronegative than hydrogen, the electrons from the hydrogen atom spend more time close to the oxygen compared to the hydrogen resulting in the oxygen having a slight negative charge ($\delta-$) and the two hydrogen atoms having a slight positive charge ($\delta+$) as shown in Figure 2.4.

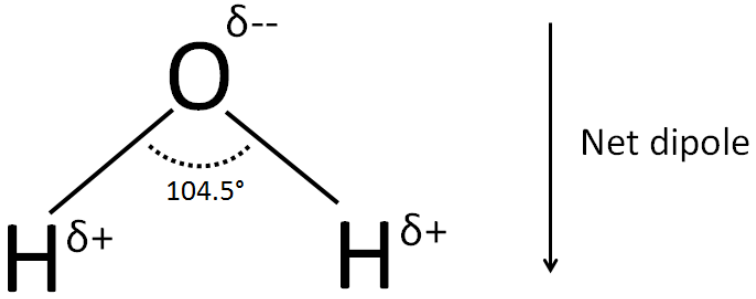

Figure 2.4: Diagram of a water molecule illustrating the bond angle and the net dipole due to the uneven sharing of the electrons.

If an electric field is applied across a polar molecule, the applied field creates a torque which causes the molecule to orientate such that the permanent dipole of the molecule is in the opposite direction as the applied field (Figure 2.5). This is called orientational polarisation and only occurs in molecules with a permanent dipole.

Ionic polarisation is caused by relative displacements between positive and negative ions in ionic crystals (for example, NaCl). If crystals or molecules comprise different atoms, the distribution of charges around individual atoms leans to positive or negative. As a result, when lattice vibrations or molecular vibrations induce relative displacements

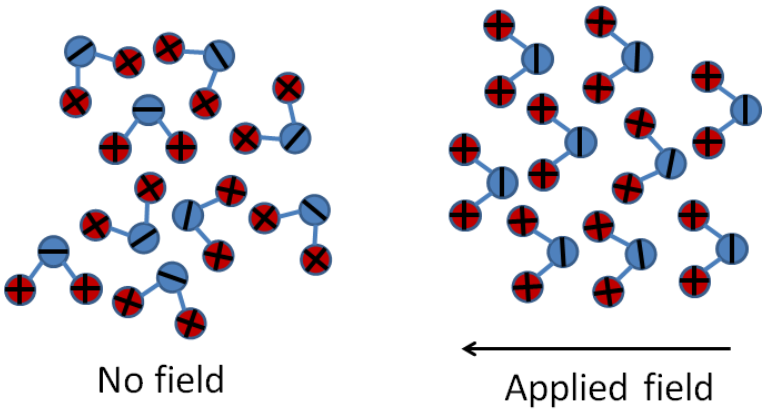

Figure 2.5: Illustration of orientational polarisation, showing the response of permanent dipoles to an electric field.

of the atoms, the centres of positive and negative charges might be in different locations. These centre positions are affected by the symmetry of the displacements. When the centres do not correspond, polarisation, termed ionic polarisation arise within molecules or crystals (Figure 2.6).

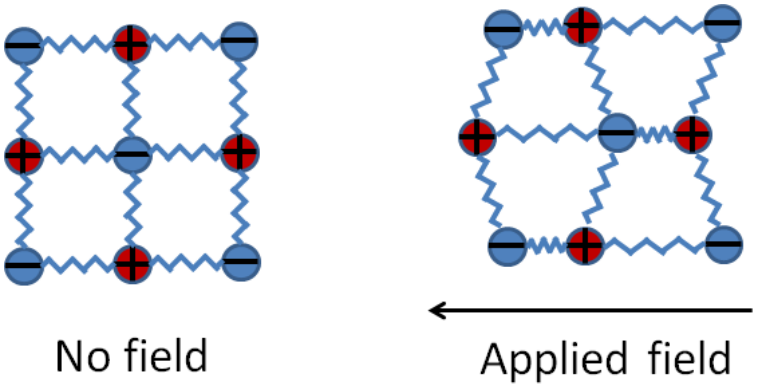

Figure 2.6: Illustration of ionic polarisation. Under the influence of an electric field, the average position of the positive and negative charge in a lattice structure can move slightly to create a dipole.

Interfacial polarisation only occurs in materials where there is an interface between two materials with different dielectric properties. This phenomenon is of particular relevance to this thesis and is described in Section 2.2.7.

The sum of the polarisabilities (α) makes the total dielectric response of the system, Equation 2.5.

$$\alpha_{total} = \alpha_{atomic} + \alpha_{orientational} + \alpha_{ionic} + \alpha_{interfacial} \tag{2.5}$$

When the frequency of the applied electric field is much greater than the characteristic relaxation frequency of a polarisation, no polarisation occurs. For instance, if the frequency of an applied field is greater than the characteristic relaxation frequency of the interfacial polarisation, then the polarisability is the sum of the three other polarisations (which relax at much higher frequencies).

The polarisation $\mathbf{P}$ is the average dipole moment per unit volume and is given by Equation 2.6 (Morgan and Green, 2003).

$$\mathbf{P} = n\alpha\mathbf{E} \tag{2.6}$$

where n is the number of dipoles per unit volume.

The electric susceptibility χ_e is a measure of how easily a dielectric material polarises in response to an electric field. It is related to the polarisation vector $\mathbf{P}$ and the electric displacement vector $\mathbf{D}$ by Equation 2.7

$$\begin{aligned} \mathbf{P} &= \varepsilon_0\chi_e\mathbf{E} \\ \mathbf{D} &= \varepsilon_0\varepsilon_r\mathbf{E} \\ \chi_e &= \varepsilon_r + 1 \end{aligned} \tag{2.7}$$

where ε_0 is the permittivity of free space and ε_r is the relative permittivity of the material. Permittivity, ε is the extent to which bound charge can be polarised by an external field (Pethig, 1979).

2.2.5 Complex Permittivity

Conductivity is proportional to the amount of unbound charge in a material. If a conductor is placed between two parallel plate electrodes, as shown in Figure 2.7a, the impedance Z can be calculated according to Equation 2.8.

$$Z = \frac{d}{A} \times \frac{1}{\sigma} \tag{2.8}$$

If a dielectric containing no unbound charge is placed between parallel facing electrodes, as shown in Figure 2.7b, the capacitance is given by Equation 2.9

$$C = \frac{\varepsilon_0 \varepsilon_r A}{d} \tag{2.9}$$

The impedance of this dielectric is frequency dependant and is given by Equation 2.10.

$$Z = \frac{1}{j\omega C} = \frac{d}{j\omega \varepsilon_0 \varepsilon_r A} \tag{2.10}$$

If a dielectric containing unbound charge is placed between parallel facing electrodes, as shown in Figure 2.7c, then the impedance is the parallel combination of the impedance due to the conductance and permittivity (Equation 2.11). This combination is called the complex impedance $\tilde{Z}$.

$$\tilde{Z} = \frac{d}{A(\sigma + j\omega \varepsilon_0 \varepsilon_r)} \tag{2.11}$$

Physically the conductivity component is the unbound charge and the permittivity is the ability of the dielectric to store energy as movement of the bound charge.

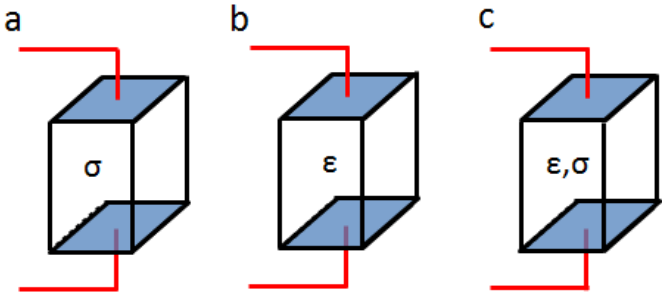

Figure 2.7: Illustration of two electrodes separated by a) a conductor b) a dielectric with no unbound charge and c) a dielectric with unbound charge.

2.2.6 Dielectric Relaxation

When an electric field is applied across a material, the material polarises. For instance in the case of water, the water molecules orientate in the direction of the applied field. The water molecules do not move instantly; it takes a fixed time to polarise the water. Likewise, when all the dipoles in a material are polarised and the electric field is removed, it takes some time for the dipoles to reach a random orientation and the polarisation to disappear. This time is called the relaxation time τ.

When the frequency of the applied electric field is far below the relaxation time, all the dipoles have time to orientate and amount of polarisation is maximum. As the frequency of the applied electric field is increased, the dipoles do not have time to move fully and the amount of polarisation is reduced.

When a material is polarised by an electric field, the dipoles will start in random orientations and align with the field. Some dipoles will therefore have to rotate further than others. Accordingly, on applying an electric field the polarisation will increase as a negative exponential function of Equation 2.12.

$$P(t) \quad = \quad P_1 + P_2(1 - exp(-\frac{t}{\tau})) \tag{2.12}$$

where P_1 is the polarisation due to much faster processes (for instance atomic polarisation), P_2 is the low frequency polarisation.

Converting to the frequency domain by taking the Fourier transform gives Equation 2.13

$$P(\omega) \quad = \quad P_1 + \frac{1}{1 + j\omega\tau} \tag{2.13}$$

Using $\mathbf{P} = \varepsilon_0\chi_e\mathbf{E}$ from Equation 2.7 gives Equation 2.14.

$$P(\omega) \quad = \quad \mathbf{E}\varepsilon_0(\chi_1 + \frac{\chi_2}{1 + j\omega\tau}) \tag{2.14}$$

This result gives a complex permittivity, $\tilde{\varepsilon}$, given by Equation 2.15 (Pethig, 1979).

$$\tilde{\varepsilon} \quad = \quad \varepsilon_0(\varepsilon_\infty + \frac{\varepsilon_s - \varepsilon_\infty}{1 + j\omega\tau}) \tag{2.15}$$

ε_∞ and ε_s are the permittivity of the material measured much above and below the relaxation frequency of the polarisation in question. For instance for the case of orientational polarisation of water the static permittivity, ε_s is 80. At frequencies above this polarisation, the permittivity drops to 4.5 (Pethig, 1979). This permittivity of 4.5 is due to other polarisations (such as atomic) which have much higher relaxation frequencies than the orientational polarisation. If the dielectric is conductive then an additional term of $\frac{-j\sigma}{\omega}$ is added to Equation 2.15 which is significant at low frequencies.

The complex permittivity can be separated into the real and imaginary parts ($\tilde{\varepsilon} = \varepsilon' - j\varepsilon''$), Equation 2.16.

$$\begin{aligned} \varepsilon' &= \varepsilon_0(\varepsilon_\infty + \frac{\varepsilon_s - \varepsilon_\infty}{1 + (\omega\tau)^2}) \\ \varepsilon'' &= \varepsilon_0(\frac{(\varepsilon_s - \varepsilon_\infty)\omega\tau}{1 + (\omega\tau)^2}) \end{aligned} \tag{2.16}$$

These equations are known as the Debye dispersion formula (Pethig, 1979). An example of the real and imaginary parts of a relaxation is plotted in Figure 2.8. The real part of the relaxation is proportional to the stored energy in the dielectric. It is maximum at low frequencies because the dipoles have time to move in the presence of the applied field. As the frequency is increased, the dipoles do not have time to move fully and the amount of stored energy is decreased. As the dipoles move (for instance water molecules orientate in response to an electric field) some of the energy is converted to heat as work is done moving the dipoles against the viscous medium (Morgan and Green, 2003).The imaginary part of the complex permittivity is proportional to this dissipation (loss) of energy within the dielectric. The imaginary part is maximum at the relaxation frequency because this is where the movement of the dipole occurs for the maximum time: the dipoles have just enough time to orientate before the field is reversed so they are kept moving continuously.

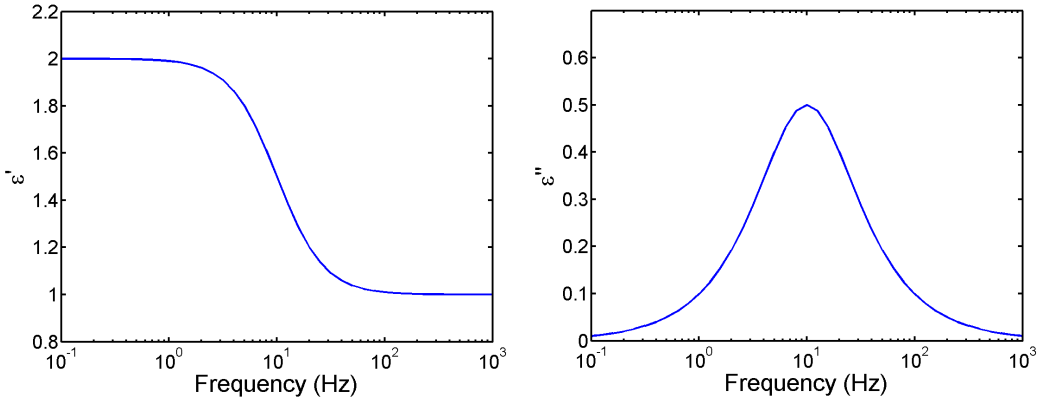

Figure 2.8: Plot of the real (ε') and the imaginary (ε'') parts of the Debye relaxation (Equation 2.16). In this example $\varepsilon_0 = 1$, $\varepsilon_S = 2$, $\varepsilon_\infty = 1$ and $\tau = 10$

The relaxation may be due to many components each with a slightly different relaxation frequency which will broaden the frequency response of the relaxation. To account for this the equation can be modified to Equation 2.17 (Pethig, 1979).

$$\tilde{\varepsilon} = \varepsilon_0(\varepsilon_\infty + \frac{\varepsilon_S - \varepsilon_\infty}{1 + (j\omega\tau)^\beta}) \tag{2.17}$$

where β is 1 for a single relaxation and 0 for an infinite number of relaxations.

Figure 2.9 shows the real and imaginary part of the complex permittivity for $\beta = 1$, 0.75 and 0.5. As more relaxations contribute to the response, the frequency range over which the relaxation occurs widens.

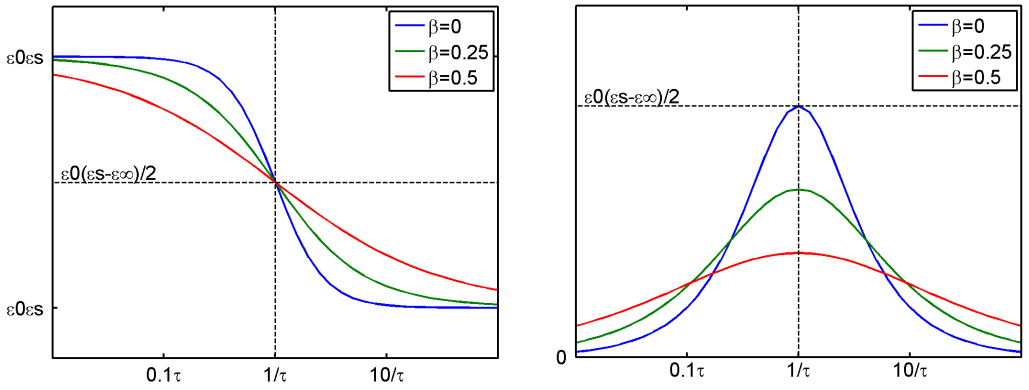

Figure 2.9: Plot of the real and imaginary parts of a Debye relaxation for a single ($\beta = 0$) and multiple overlapping relaxations ($\beta = 0.25$ and 0.5)

A plot of the real against the imaginary part of the complex permittivity (ε' against ε'') is known as the Cole-Cole plot. The data shown in Figure 2.9 is displayed in Figure 2.10 as a Cole-Cole plot. The advantage of using a Cole-Cole plot is that it is easier to estimate β from the experimental data. If the experimental data traces out a complete semicircle this indicates that the response is a single relaxation ($\beta = 1$), otherwise the response consists of multiple relaxations ($\beta < 1$).

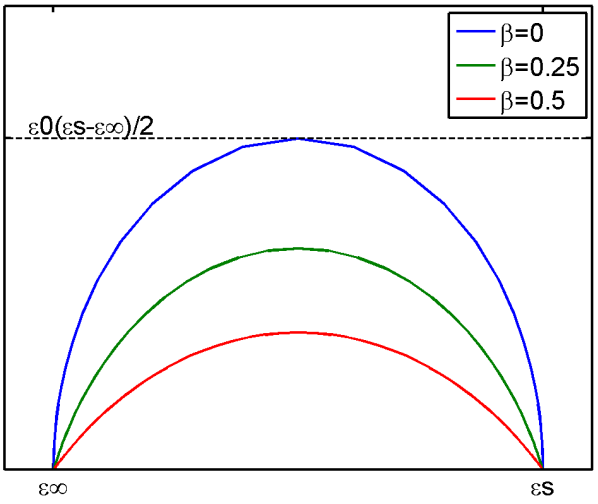

Figure 2.10: Plot of the real against imaginary part of a Debye relaxation, called a Cole-Cole plot, for the data presented in Figure 2.9

2.2.7 Maxwell-Wagner Interfacial Polarisation

At an interface between two different dielectrics, there is a discontinuity between the charge on either side of the boundary. If an electric field is applied across this interface, dipoles can be induced. The distance separating the charge in the induced dipole is usually much greater compared with the other polarisations (atomic, orientational and ionic) and is called Maxwell-Wagner interfacial polarisation. An example of this is a cell suspended in an electrolyte. When an electric field is applied across the electrolyte, charge at the surface of the cell moves in response to the field and a dipole is induced.

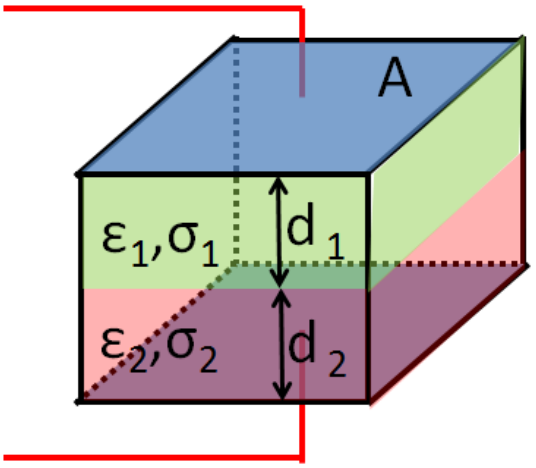

Figure 2.11: Diagram showing two different dielectrics between a pair of electrodes. When an electric field is applied across the two electrodes, charge will build up at the interface between the dielectrics creating an induced dipole.

Consider the case shown in Figure 2.11 of two dielectrics between a pair of electrodes: the impedance Z is the series combination of the impedance from the individual dielectrics, Equation 2.18.

$$\begin{aligned} Z_t &= Z_1 + Z_2 \\ \tilde{Z}_t &= \frac{d_1}{A(\sigma + j\omega_1\varepsilon_1)} + \frac{d_2}{A(\sigma + j\omega_2\varepsilon_2)} \end{aligned} \tag{2.18}$$

This can be written as a capacitance with a complex permittivity $\tilde{\varepsilon}$ given by Equation 2.19 (Morgan and Green, 2003).

$$\begin{aligned} \tilde{\varepsilon} &= \varepsilon' - j\varepsilon'' \\ &= \varepsilon_0(\varepsilon_{hf} + \frac{\varepsilon_{lf} - \varepsilon_{hf}}{1 + \omega^2\tau^2}) - j\varepsilon_0(\frac{\varepsilon_{lf} - \varepsilon_{hf}\omega\tau}{1 + \omega^2\tau^2} + \frac{\sigma}{\varepsilon_0\omega}) \end{aligned} \tag{2.19}$$

where

$$\begin{aligned} \varepsilon_{hf} &= \frac{(d_1+d_2)\varepsilon_1\varepsilon_2}{d_1\varepsilon_2+d_2\varepsilon_1} \\ \varepsilon_{lf} &= \frac{(d_1+d_2)(d_1\varepsilon_1\sigma_2^2+d_2\varepsilon_2\sigma_1^2}{(d_1\varepsilon_2+d_2\varepsilon_1)^2}) \\ \tau &= \varepsilon_0\frac{d_1\varepsilon_2+d_2\varepsilon_1}{d_1\sigma_2+d_2\sigma_1} \\ \sigma &= \frac{(d_1+d_2)\sigma_1^2\sigma_2^2}{d_1\sigma_2+d_2\sigma_1} \end{aligned} \tag{2.20}$$

This relaxation is due to the non-uniform distribution of charge at the interface between the two different dielectrics. The time period of the Maxwell-Wagner relaxation is much longer than the other polarisations (atomic, orientational and ionic) due to the longer distance separating the charge.

If a particle such as a polystyrene bead is placed in an electrolyte and an electric field is applied across the electrolyte then charge will build up at either side of the particle. The induced dipole moment is given by Equation 2.21 (Morgan and Green, 2003).

$$\mathbf{p} = 4\pi\tilde{\varepsilon_m}\frac{\tilde{\varepsilon_p}-\tilde{\varepsilon_m}}{\tilde{\varepsilon_p}+2\tilde{\varepsilon_m}}r^3\mathbf{E} \tag{2.21}$$

This can be written in terms of the volume of the particle volume, v, and the effective polarisability $\tilde{\alpha}$, Equation 2.22.

$$\begin{aligned} \mathbf{p} &= v\tilde{\alpha}\mathbf{E} \\ v &= \frac{4}{3}\pi r^3 \\ \tilde{\alpha} &= 3\varepsilon_m(\frac{\tilde{\varepsilon}_p-\tilde{\varepsilon}_m}{\tilde{\varepsilon}_p+2\tilde{\varepsilon}_m}) \end{aligned} \tag{2.22}$$

This is often written as Equation 2.23.

$$\tilde{\alpha} = 3\varepsilon_m\tilde{f}_{CM} \tag{2.23}$$

where $\tilde{f}_{CM}$ is the Clausius Mossotti factor which describes the complex effective permittivity of the particle in a medium, Equation 2.24.

$$\tilde{f}_{CM} = \frac{\tilde{\varepsilon}_p - \tilde{\varepsilon}_m}{\tilde{\varepsilon}_p + 2\tilde{\varepsilon}_m} \tag{2.24}$$

The relaxation time (τ) is given by Equation 2.25

$$\tau = \frac{\varepsilon_p - \varepsilon_m}{\sigma_p + 2\sigma_m} \tag{2.25}$$

The real and imaginary parts of the Clausius Mossotti factor ($\tilde{f}_{CM}$) are shown in Figure 2.12 for a particle in a medium where a) $\sigma_m >> \sigma_p$ and $\varepsilon_p >> \varepsilon_m$ and b) $\sigma_m << \sigma_p$ and $\varepsilon_p << \varepsilon_m$.

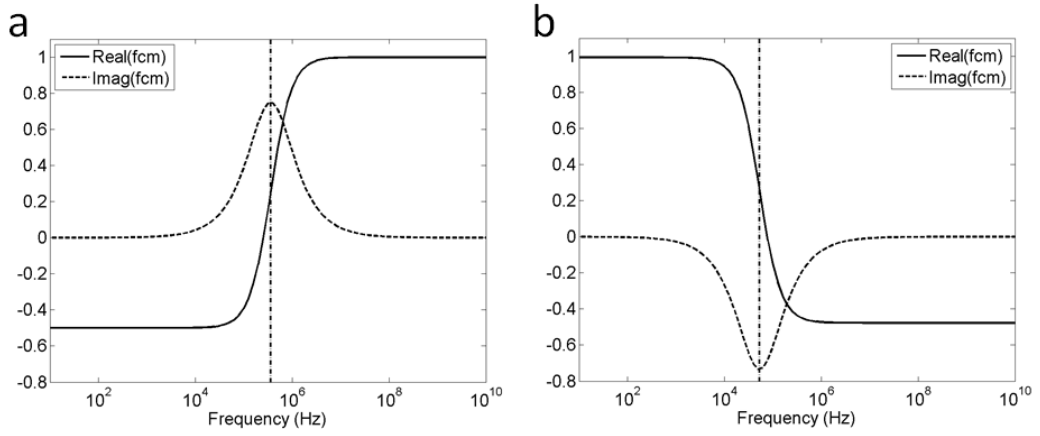

Figure 2.12: Graph showing the real and imaginary parts of the Clausius Mossotti factor for a sphere in an electrolyte where a) $\sigma_m >> \sigma_p$ and $\varepsilon_p >> \varepsilon_m$ and b) $\sigma_m << \sigma_p$ and $\varepsilon_p << \varepsilon_m$.

The example in Figure 2.12b is representative of a particle suspended in a low conductivity electrolyte.

The conductivity of a particle (σ_p) of radius r is given by Equation 2.26.

$$\sigma_p = \sigma_b + 2\frac{K_s}{r} \tag{2.26}$$

Where σ_b is the conductivity of the bulk medium and K_s is the surface charge. For micrometer sized latex beads, the surface charge dominates ($\sigma_b << 2\frac{K_s}{r}$). For example, for latex the surface charge is $1nS$ (Hughes and Morgan, 1999) and so the surface and bulk contributions for a $10\mu m$ polystyrene bead are shown in Equation 2.27.

$$\begin{aligned} \sigma_b &= 1 \times 10^{-18} Sm^{-1} \\ 2\frac{k_s}{r} &= 2\frac{1 \times 10^{-9}}{5 \times 10^{6}} = 4 \times 10^{-4} Sm^{-1} \end{aligned} \tag{2.27}$$

2.2.8 Maxwell's Mixture Theory

Multiple particles in suspension can be represented by a single dispersion using Maxwells mixture theory, Equation 2.28. This combines the dielectric properties of particles in suspension into one overall complex permittivity ($\tilde{\varepsilon}_{mix}$) as shown in Figure 2.13.

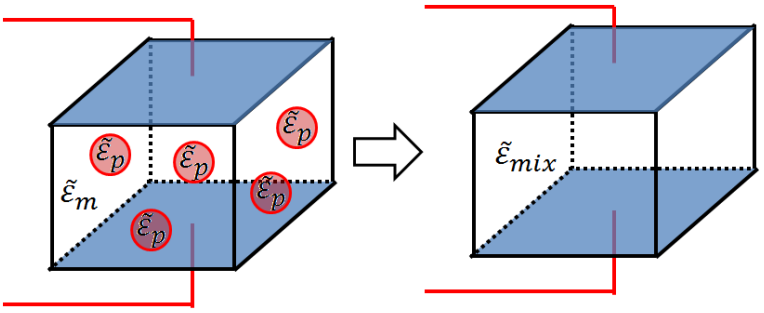

Figure 2.13: Illustration of Maxwell's mixture theory.

$$\begin{aligned} \tilde{\varepsilon}_{mix} &= \tilde{\varepsilon}_m \frac{1 + 2\psi\tilde{f}_{CM}}{1 - \psi\tilde{f}_{CM}} \\ &= \tilde{\varepsilon}_m \frac{1 + 2\psi\frac{\tilde{\varepsilon}_p - \tilde{\varepsilon}_m}{\tilde{\varepsilon}_p + 2\tilde{\varepsilon}_m}}{1 - \psi\frac{\tilde{\varepsilon}_p - \tilde{\varepsilon}_m}{\tilde{\varepsilon}_p + 2\tilde{\varepsilon}_m}} \end{aligned} \tag{2.28}$$

where ψ, is the volume fraction which is the total volume of the particles divided by the volume of the medium. For n particles of radius r in a box of size $x \times y \times z$ the volume fraction is given by Equation 2.29, which is valid when ψ is much less than 1.

$$\psi = \frac{\frac{4\pi n r^3}{3}}{xyz} \tag{2.29}$$

2.2.9 Single Shell Model

Biological cells can be modelled electrically as a thin insulating membrane surrounding a conductive cytoplasm. In the simplest case of a cell without a nucleus, the dielectric properties of a cell can be modelled as shown in Figure 2.14.

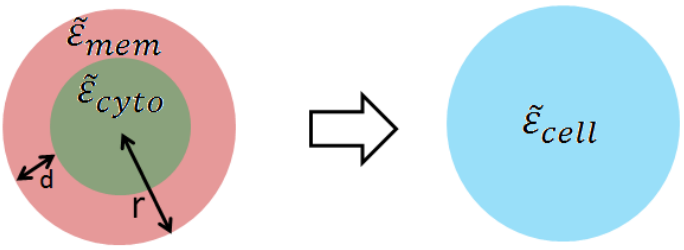

Figure 2.14: The simplest electrical representation of a biological cell is a conductive cytoplasm surrounded by an insulating membrane. Typically the radius of cells is $1-100\mu m$ and the thickness of the membrane is approximately $10nm$. Using Maxwell's mixture the cell can be represented as a sphere with an equivalent complex permittivity.

The complex permittivity of the cell is a combination of the permittivity and conductivity of the membrane and cytoplasm. This is called the shell model and is given by Equation 2.30.

$$\tilde{\varepsilon}_{cell} = \tilde{\varepsilon}_{mem}\frac{1+2\psi\frac{\tilde{\varepsilon}_{cyto}-\tilde{\varepsilon}_{mem}}{\tilde{\varepsilon}_{cyto}+2\tilde{\varepsilon}_{cyto}}}{1-\psi\frac{\tilde{\varepsilon}_{cyto}-\tilde{\varepsilon}_{mem}}{\tilde{\varepsilon}_{cyto}+2\tilde{\varepsilon}_{cyto}}} \tag{2.30}$$

In this case the volume fraction is given by Equation 2.31.

$$\psi = \frac{(r-d)^3}{r^3} \tag{2.31}$$

Where d is the thickness of the membrane.

The real and imaginary parts of the Clausius Mossotti factor for a $10\mu m$ diameter cell suspended in different conductivity electrolytes are shown in Figure 2.15. Phosphate buffered saline (PBS) is a typical isotonic suspension medium for cells and has a conductivity of $1.6Sm^{-1}$. Figure 2.15 shows that decreasing the medium conductivity decreases the Maxwell-Wagner relaxation frequency, but increases the change in the Clausius Mossotti factors. This is because, as the medium conductivity is decreased, there is a greater difference between the conductivity of the medium and of the cell cytoplasm.

The first dielectric measurements of a solution containing cells was performed over 100 years ago by Höber, who measured the properties of a suspension of red blood cells (RBCs) at around $150Hz$ and $5MHz$ (Pethig and Schmueser, 2012). Höber found that the conductivity of the cell suspension was significantly higher around $9MHz$ and suggested that biological cells consisted of a conductive centre (cytoplasm) surrounded

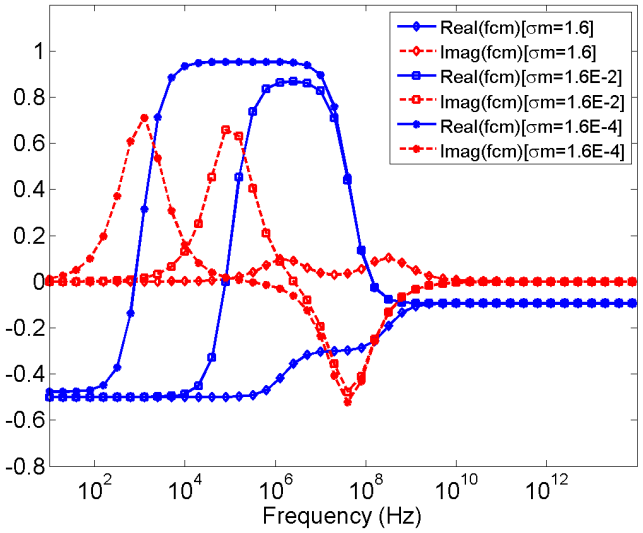

Figure 2.15: Graph showing the real and imaginary parts of the Clausius Mossotti factor for a cell suspended in different conductivity mediums. The cell was of radius $5\mu m$ and membrane thickness $10nm$. The relative permittivity of the medium, cell cytoplasm and cell membrane was 80, 60 and 10. The conductivity of the cell cytoplasm and cell membrane was 0.5 and 1×10^{-8} Sm^{-1} and the conductivity of the medium was either 1.6, 1.6×10^{-2} or 1.6×10^{-4} Sm^{-1}.

by an insulating membrane. This was confirmed by lysing the cells and demonstrating the suspension conductivity increased for the low frequency measurement and did not increase further at higher frequencies. Later, in 1925, Fricke performed similar measurements of the membranes of cells, estimating the capacitance to be $8.1mFm^{-2}$ and thickness to be $3.3nm$. This is close to today's accepted value of $5nm$; the difference between the values is that the head group in the lipid bilayer is conductive and thus not measured in the electrical measurements.

MIC operates on a similar principle, measuring the dielectric properties of a box containing the cells of interest suspended in an electrolyte. However, the box is miniaturised such that only one cell is inside the box at any time. This enables single cell measurements rather than bulk measurements to be performed as shown in Figure 2.16. The advantage of single cell measurements is that subpopulations of cells can be distinguished, whereas bulk measurement just gives the average population properties.

2.2.10 The Electrical Double Layer

To perform an impedance measurement of a solution, electrodes are immersed in the solution, a voltage is applied across the electrodes and the current flowing between the electrodes is measured. When an electrode is placed in an electrolyte, ions from

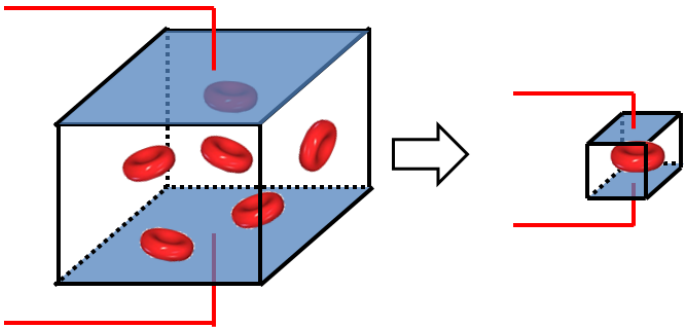

Figure 2.16: In traditional dielectric measurements, particles are suspended in an electrolyte and the impedance as a function of frequency is measured. In microfluidic impedance cytometry the measurement volume is miniaturised such that the dielectric measurement is for a single particle. This enables subpopulations to be detected which would be masked in traditional measurement.

the electrolyte build up at the interface between the electrolyte and the surface of the electrode. The electrode surface is usually charged (due to dissociation of chemical charges, or adsorption of molecules onto the surface), which attracts ions from the electrolyte of opposite charge (counter ions) as shown in Figure 2.17a. This is called the electrical double layer (EDL). The EDL screens the bulk of the electrolyte from the voltage applied at the electrode. If a fixed voltage is applied to the electrode, more counter ions are drawn to the surface. The potential decays across the diffuse layer exponentially. The Debye length is the distance at which the potential drops to a factor of $1/e$ compared to the potential at the surface. The Debye length can be calculated according to Equation 2.32

$$\kappa^{-1} = \sqrt{\frac{\varepsilon_0 \varepsilon_r k_b T}{2 N_A e^2 I}} \tag{2.32}$$

Where k_B is the Boltzmann constant, T is the temperature , N_A is the Avogadro constant and I is the ionic strength in moles per cubic metre (not the normal unit of moles per litre).

Close to the electrode surface there is a layer of tightly bound or associate counterions which make up the Stern layer. Within the Stern layer the potential falls linearly. A further refinement to the model was reported by Bockris in 1973 (Morgan and Green, 2003) who suggested that the Stern layer consisted of an inner layer of ions (both co and counter ions) adsorbed onto the surface and then a layer of bound solvated ions. The outer surface of the inner layer is called the inner Helmholtz plane (iHp on Figure 2.17) and the outer surface of the second layer is called the outer Helmholtz plane (oHp).

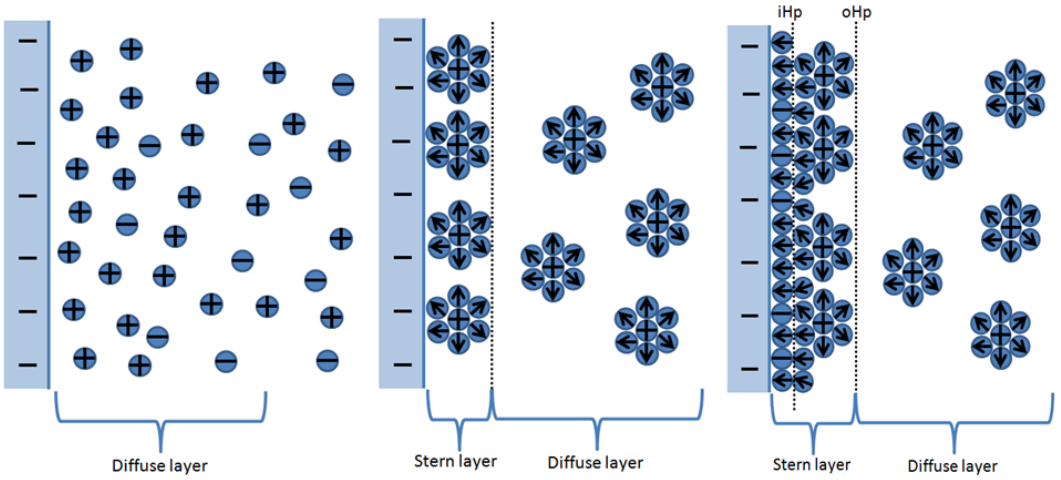

Figure 2.17: Diagram illustrating the electrical double layer. In the simplest cases, the charge at the surface of an electrode attracts counter-ions from the electrolyte resulting in the diffuse layer (a). However, there are usually counterions tightly bound to surface. This is called the Stern layer and is shown in (b). More recently, Bockris and Reddy suggested that the Stern layer consisted of an inner layer of ions (both co and counter ions) adsorbed onto the surface and then a layer of bound solvated ions. These inner and outer Helmholtz planes (iHp and oHp) are shown in (c).

In the majority of experiments presented in this thesis, the particles to be measured were suspended in PBS. The Debye length for PBS can thus be calculated, Equation 2.33.

$$\begin{aligned} \kappa^{-1} &= \sqrt{\frac{8.85 \times 10^{-12} \times 80 \times 1.38 \times 10^{-23} \times 300}{2 \times 6.022 \times 10^{23} \times (1.60 \times 10^{-19})^2 \times 0.137 \times 1000}} \\ \kappa^{-1} &= 0.8nm \end{aligned} \tag{2.33}$$

The capacitance of the double layer is the series combination of the Stern and diffuse layer capacitances.

The specific capacitance of the diffuse layer can be estimated from Equation 2.34.

$$\begin{aligned} C_d &= \varepsilon_0 \varepsilon_r \kappa \\ C_d &= 8.85 \times 10^{-12} \times 80 \times \frac{1}{0.8 \times 10^{-9}} = 0.885 Fm^{-2} \end{aligned} \tag{2.34}$$

The specific capacitance of the Stern layer is given by Equation 2.35.

$$C_S = \frac{\varepsilon_0 \varepsilon_r}{d_S} \tag{2.35}$$

Where d_S is the thickness of the Stern layer (typically $0.5nm$) and the relative permittivity of the layer will be between 6 and 20 (Morgan and Green, 2003).

$$\begin{aligned} C_S &= \frac{\varepsilon_0 \varepsilon_r}{d_S} = \frac{8.85 \times 10^{-12} \times 6}{0.5 \times 10^{-9}} = 0.106 Fm^{-2} \\ C_S &= \frac{\varepsilon_0 \varepsilon_r}{d_S} = \frac{8.85 \times 10^{-12} \times 20}{0.5 \times 10^{-9}} = 0.354 Fm^{-2} \end{aligned} \tag{2.36}$$

The total specific capacitance is the series combination of the diffuse and Stern layer capacitance, Equation 2.37

$$\frac{1}{C_T} = \frac{1}{C_d} + \frac{1}{C_S} \tag{2.37}$$

If the ionic concentration is low, the Debye length is long and the capacitance of the diffuse layer dominates the response. However, in the case of PBS the Stern layer dominates, Equation 2.38

$$\begin{aligned} \frac{1}{C_T} &= \frac{1}{0.885} + \frac{1}{0.106} = 0.0947 Fm^{-2} \\ \frac{1}{C_T} &= \frac{1}{0.885} + \frac{1}{0.354} = 0.253 Fm^{-2} \end{aligned} \tag{2.38}$$

The capacitance of the electrical double layer (C_{edl}) is the specific capacitance multiplied by the electrode area. The platinum electrodes used in this thesis were $30\mu m$ by $40\mu m$ so the capacitance can be calculated from Equation 2.39.

$$\begin{aligned} C_{edl} &= 0.0947 \times 30 \times 10^{-6} \times 40 \times 10^{-6} = 114 pF \\ C_{edl} &= 0.253 \times 30 \times 10^{-6} \times 40 \times 10^{-6} = 303 pF \end{aligned} \tag{2.39}$$

The double layer capacitance has the effect of screening the bulk conductivity of a solution at low frequencies. For example, Figure 2.18a shows a box filled with PBS of size $30 \times 30 \times 40\mu m$ with electrodes on the top and bottom of the box, to model the

detection region in the MIC chips described later in this chapter. The current flowing through the box is frequency dependent and can be calculated using the equivalent circuit model of Figure 2.18b.

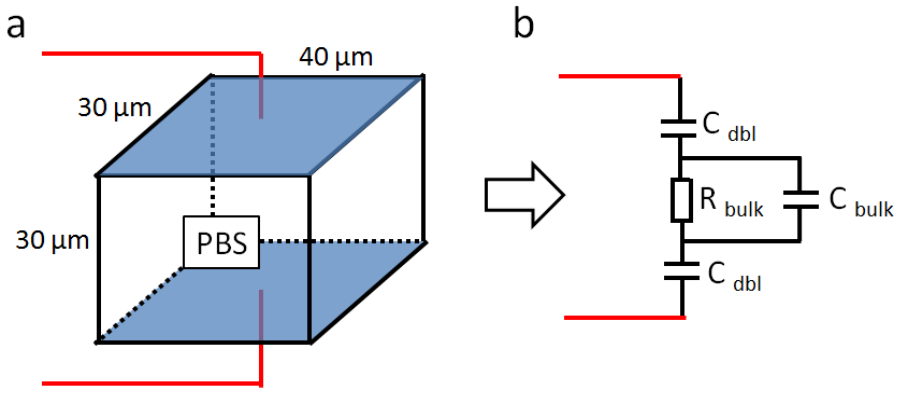

Figure 2.18: Diagram of a box of PBS with electrodes on the top and bottom of the box and the corresponding equivalent circuit. The current flowing between the electrodes is a function of frequency which depends on the bulk resistance and double layer capacitance.

The current flowing through the box is equal to the applied voltage divided by the impedance, Equation 2.40

$$I = \frac{V}{Z} \tag{2.40}$$

The impedance Z is given by the series combination of the double layer capacitance, (C_{dbl}) and the bulk resistance (R_{bulk}), Equation 2.41. The bulk capacitance is ignored because the response is insignificant at the measurement frequencies of interest ($< 10^7 MHz$).

$$Z = \frac{1}{j\omega C} + \frac{d}{A\sigma} + \frac{1}{j\omega C} \tag{2.41}$$

The current flowing between the two electrodes at $1V$ as a function of frequency is shown in Figure 2.19 for a double layer capacitance of $636pF$, calculated from Equation 2.39, along with a double layer capacitance 10 and 100 times smaller ($63.6pF$ and $6.36pF$). As the double layer capacitance is decreased (corresponding to a longer Debye length) the frequency required to overcome the double layer capacitance and measure the bulk conductivity increases.

In summary, the dielectric properties of a material are governed by the amount of charge in a material (both free and fixed). Fixed charge move in response to an electric field

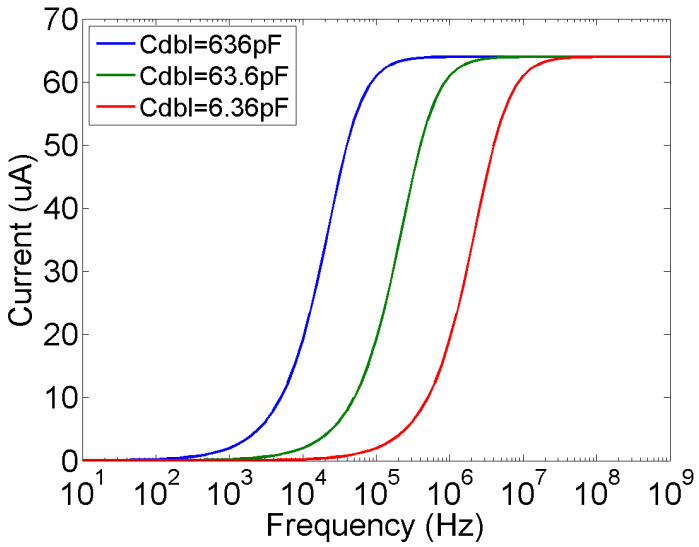

Figure 2.19: Graph of the current flowing between the electrodes shown in Figure 2.18 for different values of the double layer capacitance (Cdbl).

which is termed polarisation. The dielectric properties of a cell in suspension can be modelled as an equivalent complex permittivity using Maxwell's Mixture Theory and the Single Shell Model. In Chapter 6, this modelling is used to compare the frequency response of tumour cells with reported values from the literature.

2.3 Experimental Details

Figure 2.20 is a photograph of the MIC chip. Particles flow from the inlet to the outlet through the measurement region in the centre of the chip. This section describes the design and fabrication of these MIC chips. Details of the electrical and fluidic connections are also described, along with the signal processing algorithms which extract the particle impedance data from the raw signals obtained from the experiments.

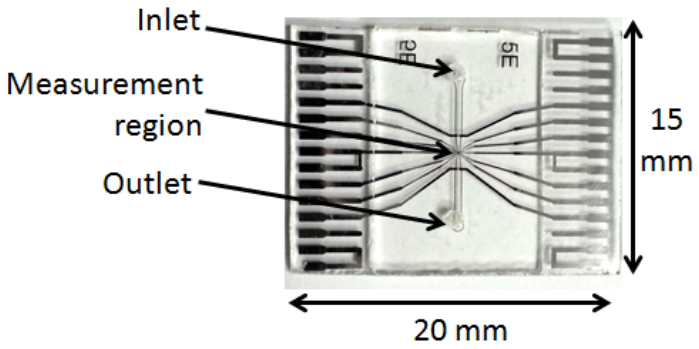

Figure 2.20: Photograph of an MIC chip. The chip is made of glass and the electrodes are platinum.

2.3.1 Chip Fabrication

The MIC chips used in this thesis were fabricated using standard photolithography techniques by Katie Chamberlain. The lithography masks for the first generation MIC were designed previously. I designed a new mask for a new electrode geometry for improved measurement accuracy which is described in Chapter 5.

An overview of the fabrication process is shown in Figure 2.21.

a) A $10nm$ thick layer of titanium and then a $200nm$ thick layer of platinum is sputtered onto a glass wafer. The titanium layer is an adhesion layer because platinum does not stick directly to glass.

b) Photoresist is spun onto the platinum, the photoresist is exposed to UV light through a mask, and the resist is developed. Ion-beam milling is used to etch the platinum and titanium layers which are not protected by photoresist. The photoresist is then removed to leave the patterned platinum electrodes.

c) Approximately $30\mu m$ thick SU-8 photoresist is deposited onto the surface.

d) Fluidic channels are defined in the SU-8 using standard photolithography.

e-f) A second wafer with pattered electrodes (from part b) is bonded to the wafer from part d) using a wafer bonder.

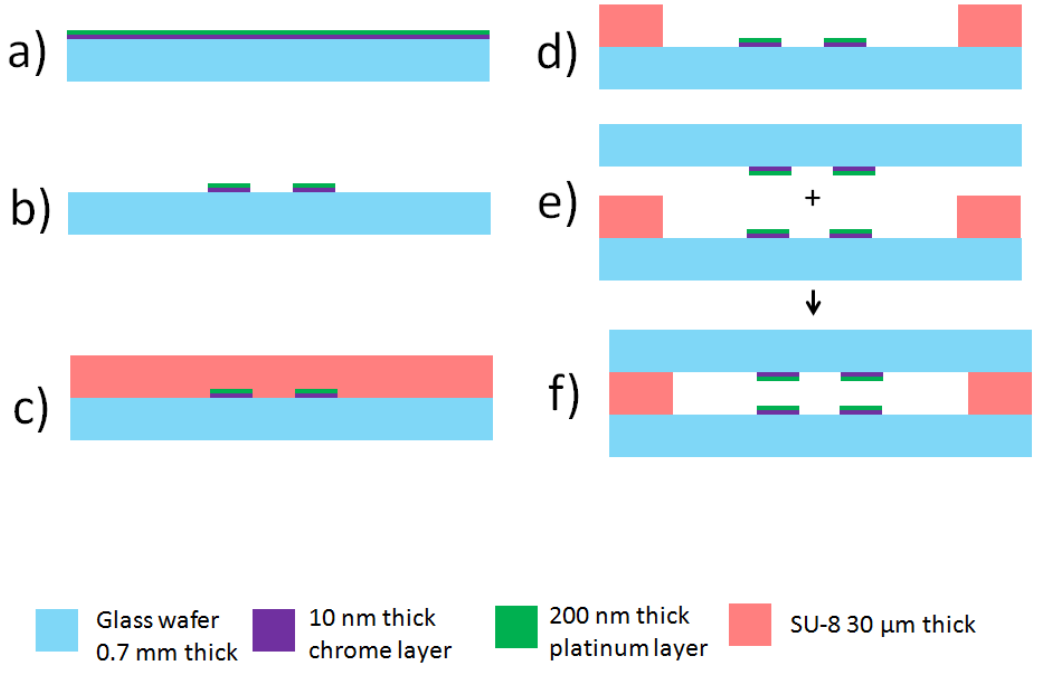

Figure 2.21: Illustration of the fabrication of the MIC chips. The diagram is not drawn to scale.

The wafer is then diced to form individual chips and fluidic inlet and outlet holes are drilled using a CO_2 laser, as shown in Figure 2.22.

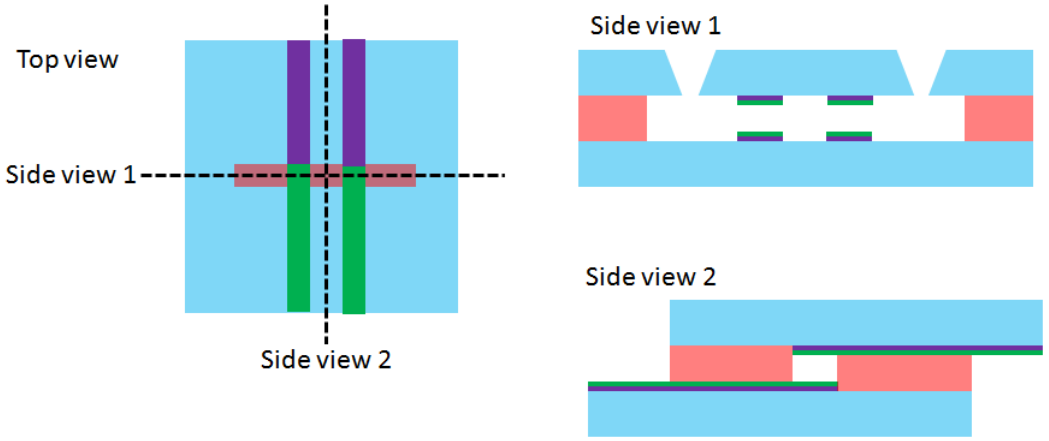

Figure 2.22: Illustration showing the dicing of individual MIC chips. Side view 2 shows the offset dicing which enables connection to the top and bottom electrodes. Side view 1 shows the inlet and outlet fluidic holes which are drilled though the top glass sheet.

2.3.2 Particle Measurement

To measure a sample of particles suspended in an electrolyte, the sample is loaded into a syringe and pushed through the microfluidic channel as shown in Figure 2.23. The sample is diluted sufficiently such that only one particle is in the detection region between the electrodes at any one time. An AC voltage is applied to the top two electrodes and the difference in current flowing into the bottom two electrodes is measured and recorded as the impedance signal. Figure 2.24 illustrates the change in the impedance signal as a particle travels through the electrodes. As the particle passes between the first pair of electrodes, a peak in the impedance signal is observed. The maximum of this peak is when the particle is half way between the first electrode pair (point t1). As the particle passes through the second electrode pair, a trough in the impedance signal is observed with the minimum of the trough equal in magnitude to the height of the peak. The time taken for the particle to pass between the electrodes from t1 to t3 is known as the transit time (dt).

2.3.3 Flow Profile

When a fluid flows through a channel, there are two forces which affect the movement of the fluid: inertial and viscous forces. Fluid motion is described by the Navier-Stokes equation, Equation 2.42 (Morgan and Green, 2003).

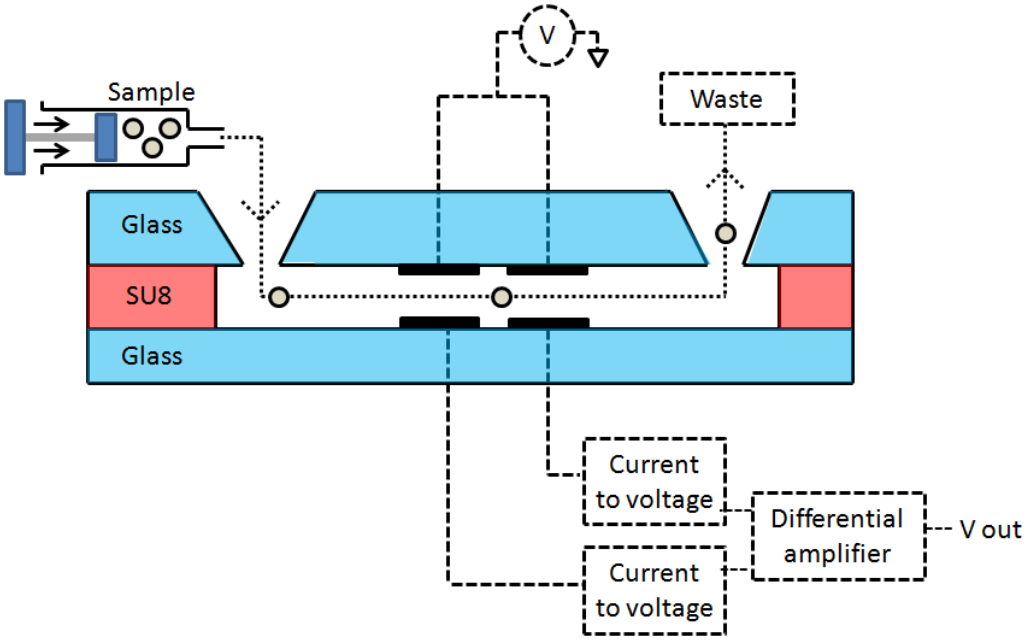

Figure 2.23: Illustration of the measurement of a sample of particles suspended in a liquid.

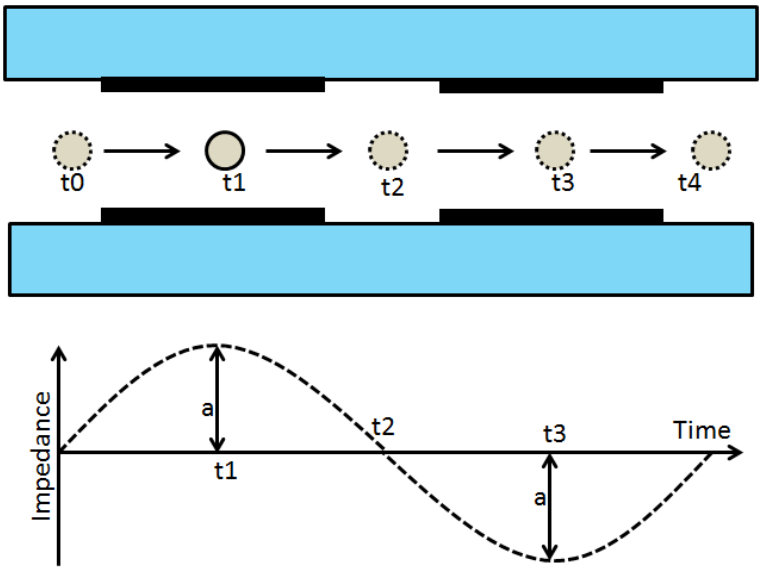

Figure 2.24: Illustration of the impedance signal as a particle moves through the fluidic channel past the measurement electrodes.

$$\rho_m \frac{d\mathbf{u}}{dt} + \rho_m(\mathbf{u}.\nabla)\mathbf{u} = -\nabla p + \eta\nabla^2\mathbf{u} + \mathbf{f} \tag{2.42}$$

Where ρ_m and η are the density and kinematic viscosity of the liquid, $\mathbf{u}$ is the velocity of the liquid p is pressure and $\mathbf{f}$ is an externally applied force.

The ratio of the inertial term $(\rho_m(\mathbf{u}.\nabla)\mathbf{u})$ to the viscous term $(\eta\nabla^2\mathbf{u})$ is known as the Reynolds number R_e, Equation 2.43.

$$R_e = \frac{\rho_m u_0 l_0}{\eta} \tag{2.43}$$

Where u_0 is the mean fluid velocity, l_0 is the characteristic length which, in the case of a spherical pipe, is the diameter, η is the dynamic viscosity which is $0.001Pas$ for water at $20°C$. R_e is a dimensionless number which describes whether the viscous forces dominate ($R_e << 10^3$) and the flow is laminar, or the inertial forces dominate ($R_e >> 10^3$) and the flow is non-laminar.

In the microfluidic impedance cytometer described in the later chapters, particles first flow along a channel $200\mu m$ wide by $30\mu m$ high, before entering the measurement region which is $40\mu m$ wide by $30\mu m$ high. Typically the volumetric flow rate is $40\mu l\ min^{-1}$. The average linear velocity is the volumetric flow rate (in $m^3\ s^{-1}$) divided by the channel cross-section (m^2). The average linear velocity for the wide and narrow channels are calculated in Equation 2.44 and Equation 2.45 respectively.

$$u_0 = \frac{40 \times 10^{-9} \times \frac{1}{60}}{200 \times 10^{-6} \times 30 \times 10^{-6}} = 0.111ms^{-1} \tag{2.44}$$

$$u_0 = \frac{40 \times 10^{-9} \times \frac{1}{60}}{40 \times 10^{-6} \times 30 \times 10^{-6}} = 0.555ms^{-1} \tag{2.45}$$

The corresponding Reynolds number for the wide and narrow section of channel are given by Equation 2.46 and Equation 2.47 respectively.

$$R_e = \frac{1000 \times 0.111 \times 30 \times 10^{-6}}{0.001} = 3.3 \tag{2.46}$$

$$R_e = \frac{1000 \times 0.555 \times 30 \times 10^{-6}}{0.001} = 16.7 \tag{2.47}$$

At these intermediate Reynolds numbers (of magnitude 10), the fluid flow through the device is laminar, not turbulent, but some inertial effects will be present such as inertial focusing of particles which is described later in this thesis.

The solution is pushed into the fluidic channel by applying pressure to the syringe. This pressure driven flow results in a parabolic flow profile. Figure 2.25 is a contour plot of the flow profile at a volumetric flow rate of $40\mu Lmin^{-1}$ in the wide and narrow sections of the channel. The flow profile was calculated using a numerical calculation from Thomas

et al. (2009). In the narrow section of the channel the contour lines are circular with the fastest flow ($1.05ms^{-1}$) occurring in the centre of the channel. The slowest particle velocity depends on the diameter of the particle. Larger particles physically cannot fit very close to the wall. For example, take a $10\mu m$ diameter particle touching the middle of the bottom of the channel as shown in Figure 2.25a. The streamline of the centre of the particle will be between 0.45 and $0.6ms^{-1}$. The average velocity of the flow will give the particle velocity. Take a $2\mu m$ diameter particle close to the middle of the top of the channel. The streamline in the middle of the particle is less than $0.15ms^{-1}$ and thus smaller particles can travel much slower than larger particles. The slowest particles will be travelling in the four corners.

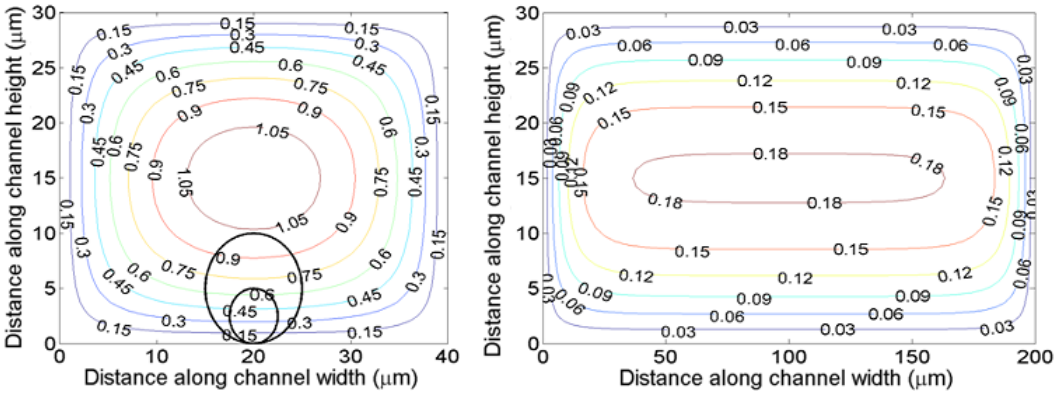

Figure 2.25: Contour plot of the parabolic flow profile when a liquid moves at a volumetric flow rate of $40\mu Lmin^{-1}$ through a channel a) $40\mu m$ wide by $30\mu m$ high and b) $200\mu m$ wide by $30\mu m$ high.

2.3.4 Signal Processing

This section describes the signal processing techniques used to extract particle impedance signals from the raw data. Figure 2.26 shows an example of experimental data of the impedance signal (differential current) as two particles pass through the channel. The measured impedance is the height of the peak, which is equal in magnitude to the trough. The least computational demanding approach to detect a particle is to set a trigger level and detect when the impedance signal rises above this level. The minimum and maximum of the impedance signal within a window is then found. This technique works when there is a large signal-to-noise ratio but is error prone when the impedance signal is noisy. In Chapter 5 of this thesis a new electrode geometry is described which improves the measurement accuracy. However the new geometry introduces smaller secondary peaks in the impedance signal which cause miss-triggers in the impedance signal.

A more robust technique is to convolute the impedance signal with a template signal (an anti-symmetric double Gaussian signal). Since the particles can have a range of transit

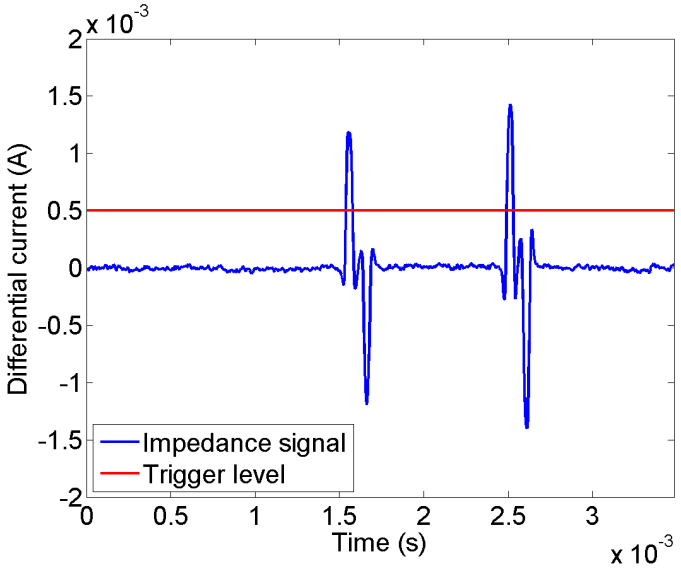

Figure 2.26: A section of experimental showing two particles passing through the detection region and a trigger level set to detect the two events.

times, a range of templates must be used. The minimum and maximum transit times can be calculated for known channel dimensions and define the range of templates. Figure 2.27 shows the convolution templates for the flow rate for the data shown in Figure 2.26.

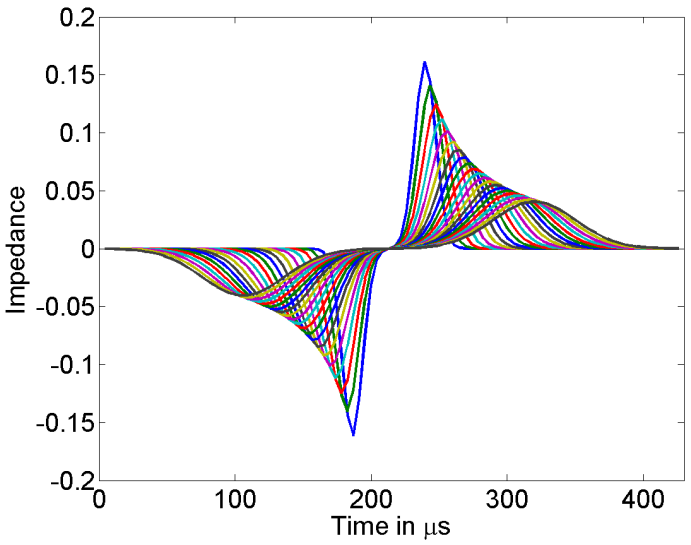

Figure 2.27: A set of 20 anti-symmetric double Gaussians, each with a slightly different transit time. The set is used as a convolution window to detect peaks in the experimental data.

Each template function, shown in Figure 2.27, is convoluted with the data, Figure 2.26 and the result of the convolution is shown as a heatmap in Figure 2.28. The bright spots (in red) are the positions in the data where the convolution template fits best. Since the

area under the template function is 1, the result of the convolution of the best matched template is equal to the height of the impedance signal peak.

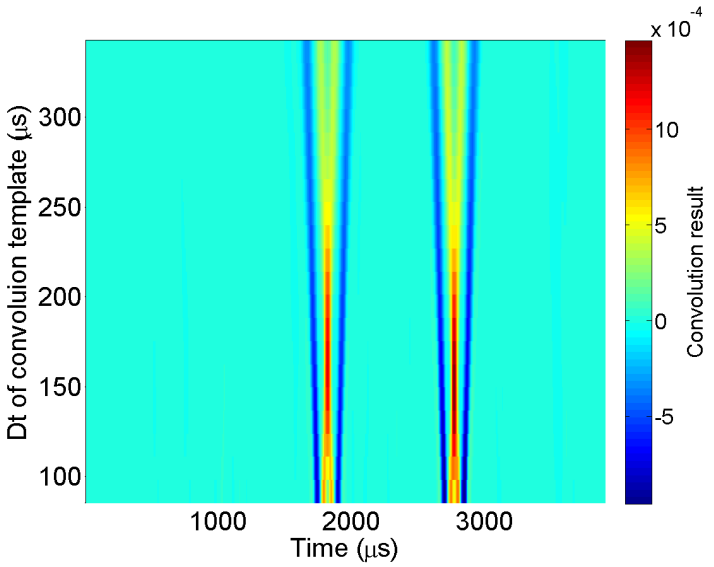

Figure 2.28: Heatmap showing the convolution of the experimental data (shown in Figure 2.26) and the convolution template (Figure 2.27).

The output of the convolution is then put through a running maximum filter and is shown in Figure 2.29 in red. The peaks of this give the impedance signal (height and centre position) shown in green. For each detected peak, an anti-symmetric double Gaussian could be fitted, using a non-linear least squares fit. However this is computationally demanding and so the maximum of the convolution output is taken as the impedance.

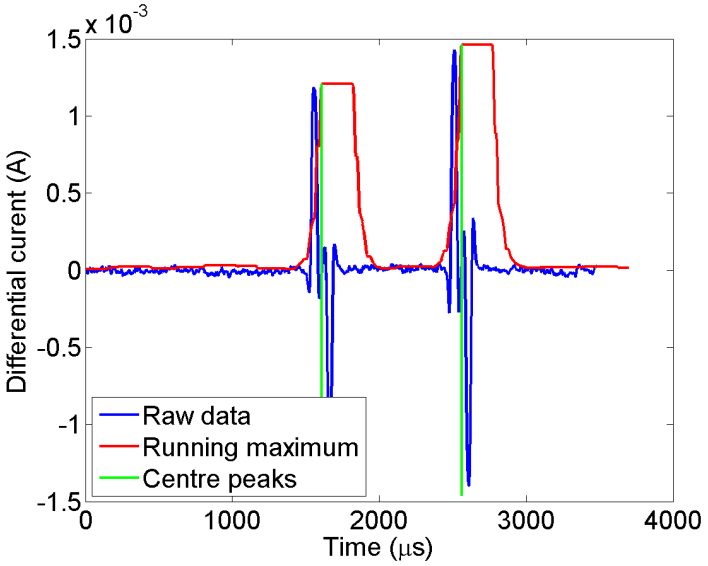

Figure 2.29: Graph showing the experimental impedance signal for two peaks, the result of a running maximum filter on the convoluted data (shown in Figure 2.28) and the detected centre of the peaks.

2.3.5 Limit of Detection

The limit of detection is defined by the signal to noise ratio. The impedance signal height depends on the size of the particle, the channel and electrode geometry, the applied voltage and any gain in the electronics. In most cases the noise from the electronic detection circuitry dominates. However, if there is a lot of debris in the liquid in which the particles are suspended, then the amount of debris can affect the noise level. In this thesis, polystyrene beads are used as test particles. These are suspended in filtered PBS and as there is little debris, the detection limit is governed by the noise in the detection circuits. However, as described in Chapter 7, when whole blood is chemically lysed to burst the RBCs, small fragments of membranes from the cells (debris) adds "fluidic" noise. This noise dominates the measurement compared to the electrical noise and limits the LoD. This is described in more detail in Chapter 7.

The volume fraction (ψ) is defined as the volume of the particle relative to the volume of the measurement region. Thus, a bigger particle compared to the measurement region will produce a bigger signal. However, the limit of detection depends on the level of the signal and the level of the noise. Consider a particle in a measurement region between two electrodes of variable height as shown in Figure 2.30. The current flowing between the electrodes (I1 and I2) is inversely proportional to the height of the channel. The simulated difference in current between an empty box and a box containing a $5\mu m$ diameter sphere (I2-I2) is shown in Figure 2.31. This differential current is inversely proportional to the square of the channel height. Thus, the differential current for a sphere in a $40\mu m$ high channel is a factor of four higher than the same sphere in a $80\mu m$ high channel. Considering a fixed gain transimpedance amplifier as used in this thesis, to achieve the same sensitivity, the applied voltage must be four times larger.

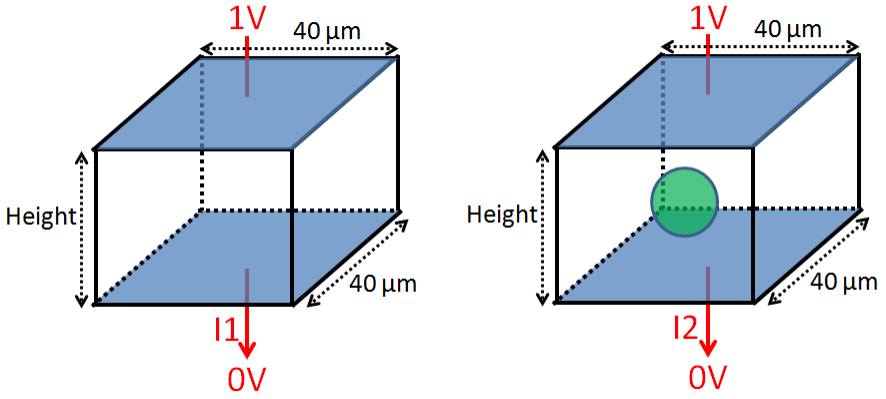

Figure 2.30: Diagram showing the simulation geometry to analyse the effect of channel height on the differential current (I1-I2).

Now consider the case of a fixed height and depth box of variable width as shown in Figure 2.32. For a fixed applied voltage, the current flowing into each electrode (I3, I4) is proportional to the electrode width. However the differential current (I3-I4) due

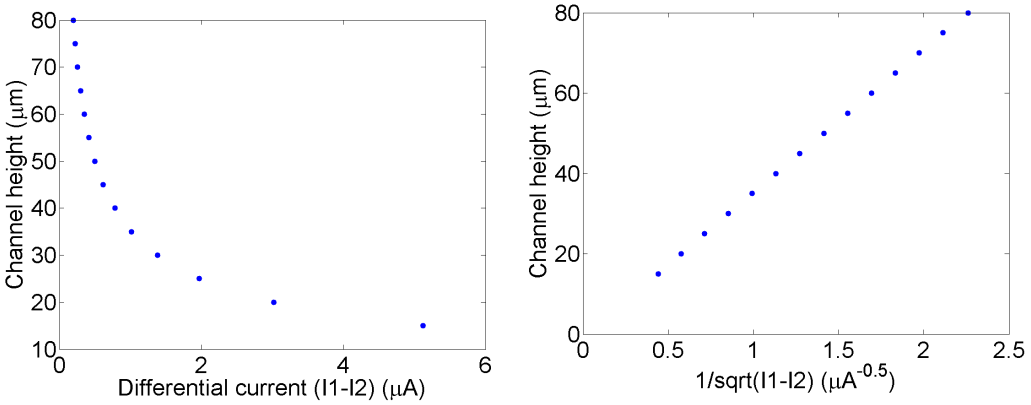

Figure 2.31: Simulated differential current $(I1 - I2)$ for the geometry shown in Figure 2.30 for a $5\mu m$ radius sphere.

to the sphere is constant. For a fixed voltage and transimpedance amplifier gain, the width of the measurement region does not affect the sensitivity, provided the currents I1 and I2 do not clip the transimpedance amplifier. This means that to increase device sensitivity, the channel should be made shallower.

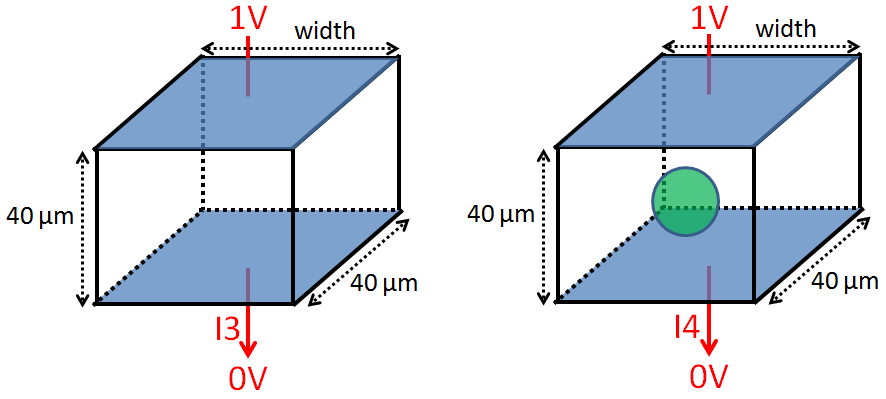

Figure 2.32: Diagram showing the simulation geometry to analyse the effect of channel width on the differential current (I1-I2).

2.3.6 Throughput

The maximum particle throughput depends on the channel geometry and the maximum sample rate of the electronic circuitry. The maximum concentration of particles must be limited such that there is only a single particle in the detection region at one time as shown in Figure 2.33. In the experimental devices described later in this thesis, the detection region is defined by the height and width of the channel ($30\mu m$ and $40\mu m$ respectively), the electrode width ($30\mu m$) and the distance between the electrodes ($40\mu m$). In this case the detection volume is $120pL$. The maximum particle concentration is therefore 8333 particles per microlitre.

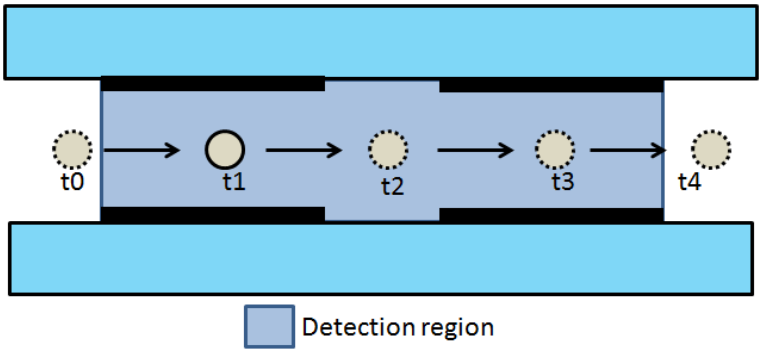

Figure 2.33: Diagram showing the detection region of the impedance cytometer. Typically the channel height and width is $30\mu m$, the electrodes are $30\mu m$ wide and separated by a $10\mu m$ gap.

The maximum volumetric flow rate depends on the sample rate and the maximum linear velocity of the particles. The maximum linear velocity is in the centre of the channel (due to the parabolic flow profile) and is shown in Figure 2.34 for a channel cross-section of $30\mu m$ by $40\mu m$.

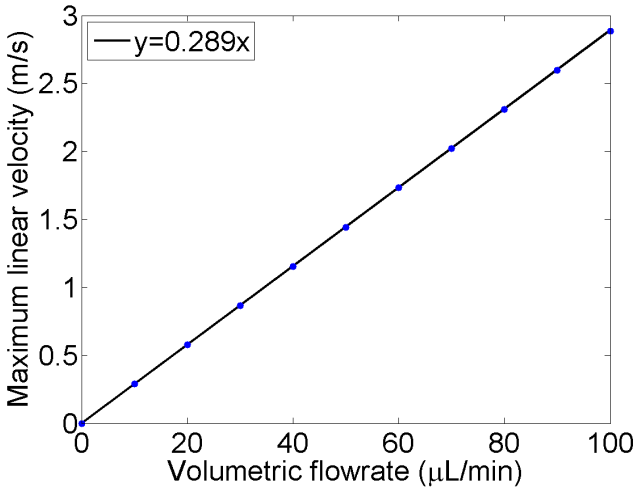

Figure 2.34: Graph of the theoretical maximum linear velocity plotted against volumetric flow rate for a channel cross-section of $30\mu m$ by $40\mu m$.

Figure 2.35 shows theoretical anti-symmetric double Gaussians at a sample rate of $230ksps$ for a linear velocity of 0.25, 0.5, 1, 2, 4 and $8ms^{-1}$ for electrodes $30\mu m$ wide and a spacing of $40\mu m$. At low linear velocities the peak and trough are reproduced with many data points and the maximum of the peak can be easily identified. At 1 and $2ms^{-1}$, the shape of the anti-symmetric Gaussian can be distinguished and the maximum of the peak can be identified by interpolation. At 4 and $8ms^{-1}$, the shape of the peak is lost and the maximum height of the peak would vary depending on the exact time the particle entered the detection region. This would introduce errors when detecting the particle volume which is proportional to the height of the peak.

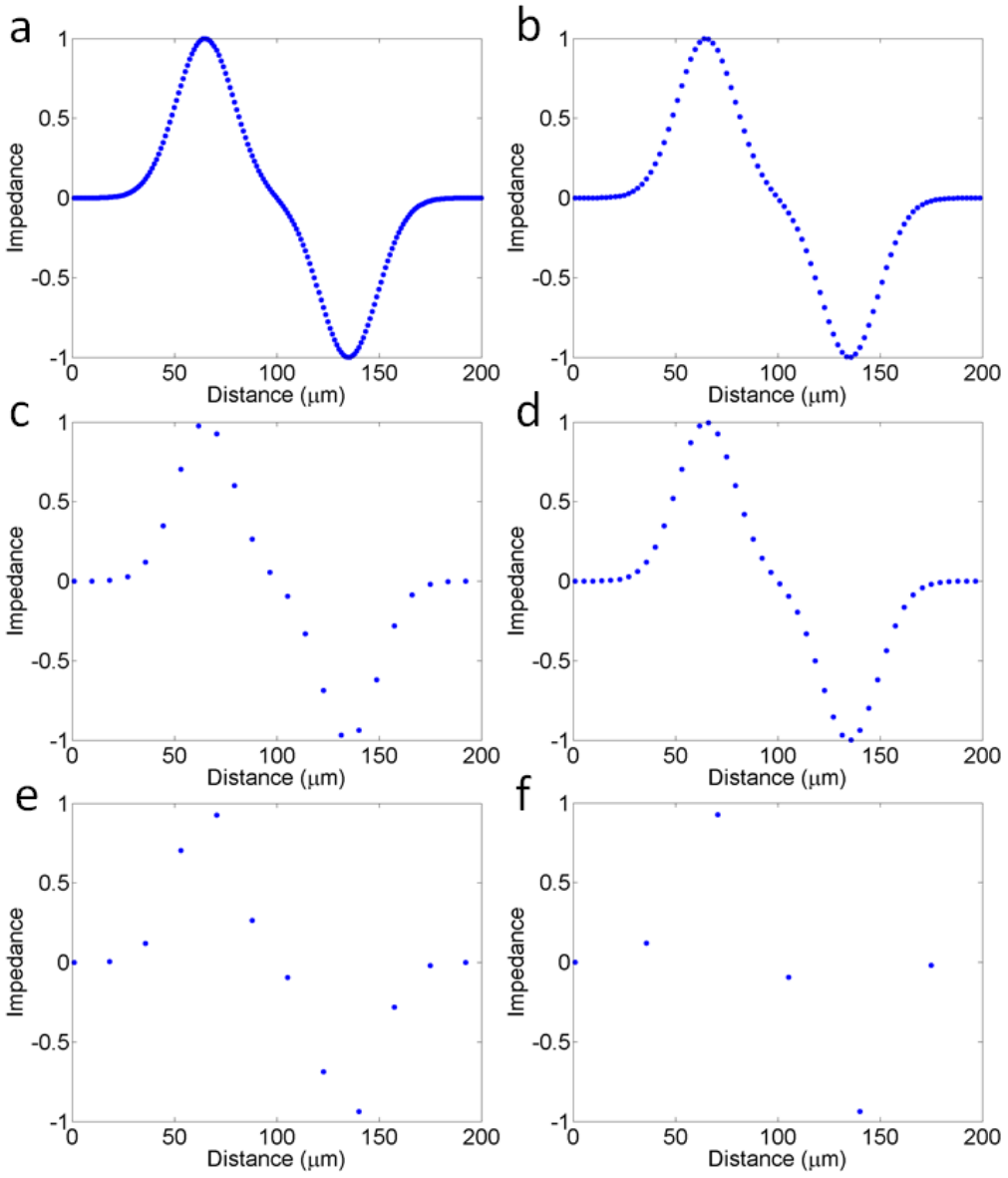

Figure 2.35: Graph illustrating the number of data points for an anti-symmetric double Gaussian for a particle travelling through the detection region of a MIC at a linear velocity of a) $0.25ms^{-1}$ b) $0.5ms^{-1}$ c) $1ms^{-1}$ d) $2ms^{-1}$ e) $4ms^{-1}$ f) $8ms^{-1}$.

Assuming a maximum linear velocity of $2ms^{-1}$ (for $230ksps$ to have enough data points to reconstruct the shape of the peak signal) the maximum volumetric flow rate is 69.2 $\mu Lmin^{-1}$. The absolute maximum throughput can be calculated as the maximum volumetric flow rate multiplied by the maximum particle concentration, Equation 2.48.

$$69.2 \times \frac{1}{60} \times 8333 \quad = \quad 9611 \text{ particles per second} \tag{2.48}$$

However, without particle focusing, if particles were pushed through the channel at high concentrations there would be a high level of coincidence where two particles would pass through the measurement region simultaneously. In this thesis, minimising coincidence (for accurate measurements) was more important than achieving the maximum throughput. Typically the particle concentration was between 100-1000 particles per microlitre and the volumetric flow rate was $40\mu Lmin^{-1}$ which corresponds to a throughput of between 67-667 particles per second.

2.3.7 Holder Design

A plastic holder as shown in Figure 2.36 was used to make electrical and fluidic connections to the MIC chip. The holder was designed using a commercial 3D drawing package (Solidworks) and built on a 3D printer. The holder consists of a printed plastic part which holds two PCBs. Each PCB has spring connectors which make electrical contact to the MIC chip. To make fluidic connection, the MIC chip is clamped onto an O-ring onto a metal ferrule which is fitted to PTFE tubing. A small insert (O-ring holder) is used to position the two O-rings in the centre of the MIC chip and metal ferrule. The advantage of this direct connection of the PTFE tubing to the MIC chip (through the O-ring) is the small dead-volume which could trap particles.

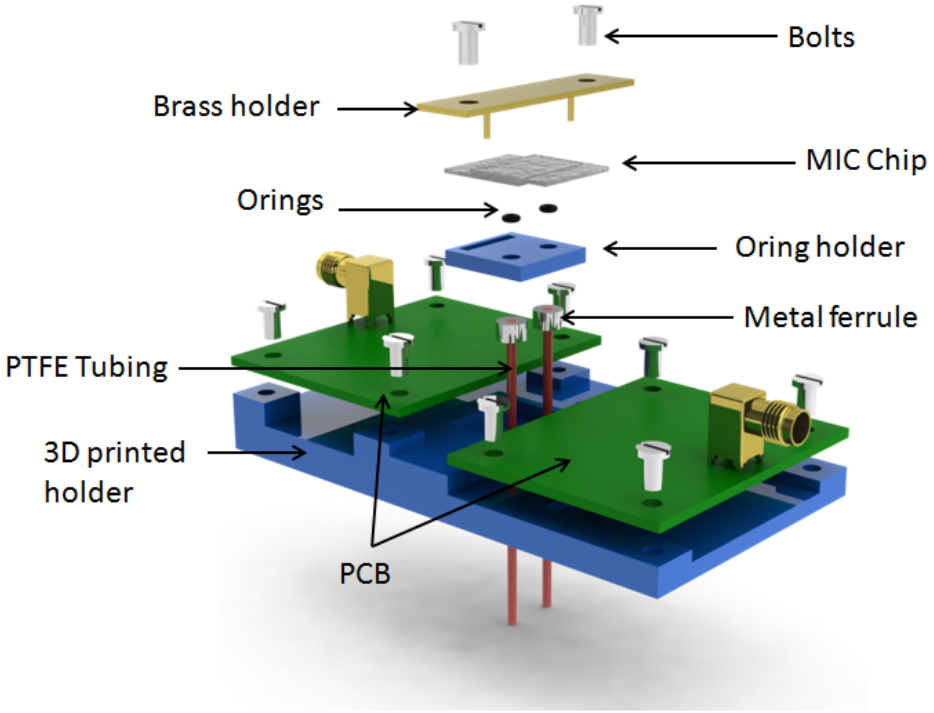

Figure 2.36: Overview of the electrical and fluidic connection to the MIC chips.

The design enables a MIC chip to be replaced, for instance if the channel becomes blocked. The MIC system is designed to be robust and reusable. In contrast, the

Chempaq and HemoCue (commercial) cartridges are single use. The cartridges are produced by injection molding and are pre-filled with reagents.

In summary, the MIC chips are fabricated in a batch process using standard photolithography and connected using a custom 3D printed holder. The signal processing is presented and used throughout this thesis to process the raw data and calculate particle impedance.

Chapter 3

Literature Review

3.1 Introduction

This chapter reviews the state of the art in micro flow cytometry. The majority of published research has focused on ensuring that all particles to be measured pass through the same position within the detection region in the channel. This is called particle focusing and is important for high accuracy measurements because of non-uniform excitation within the detection region. In optical cytometry the excitation profile of a laser is often Gaussian, thus particles passing through the centre of the beam will receive more light and produce a bigger output signal compared with particles passing through the edge of the beam. Similarly, in electrical measurements, the electric field is stronger close to electrode edges and thus impedance measurements will depend on particle position relative to the electrodes. To ensure high accuracy measurements, all particles must pass through the same position in the detection region to receive the same excitation and be measured equally. After reviewing particle focusing techniques, microfluidic impedance detection of single particles is discussed.

3.2 Particle Focusing

When measuring particles in a microfluidic cytometer, particles flow along a channel and through a detection region. Without particle focusing, the channel has one inlet and one outlet and particles can move along the channel in any position: through the centre, or close to any of the channel edges. In this thesis, the detection is impedance-based, using micro-electrodes fabricated on the top and bottom of the channel. The electric field within the channel is non uniform and the measured impedance signal of a particle will depend on its position within the channel. In addition, as the particles pass between the electrodes, the particles distort the electric field further, compounding the problem. This is called particle positional dependence and is described in detail in Chapter 4.

Particle focusing techniques can be grouped into two categories, sheath flow based and sheath less. In sheath flow focusing, a second flow surrounds the sample and guides the sample through the centre of the detection region. Sheath less focusing uses a force (either externally applied or induced from the channel topology) to move particles to specific positions within the channel. Each of these are reviewed below but, after consideration, neither are used in this thesis because sheath flow focusing adds complexity to device fabrication and in sheath less designs the focusing is limited to a narrow range of particle sizes. Instead, a new design of electrodes and signal processing algorithm have been developed which provide high accuracy measurements without any of the disadvantages of sheath less or sheath flow based particle focusing and is described in Chapter 5.

3.2.1 Sheath Flow Focusing

Particle focusing can be achieved using a second (sheath) flow to surround the sample flow, ensuring the sample flows through the centre of the detection region as shown in Figure 3.1a. This is also known as hydrodynamic focusing and is found in most commercial cytometers. The focusing is achieved in a flow cell (shown in Figure 3.1b), which is a precision manufactured 3D part.

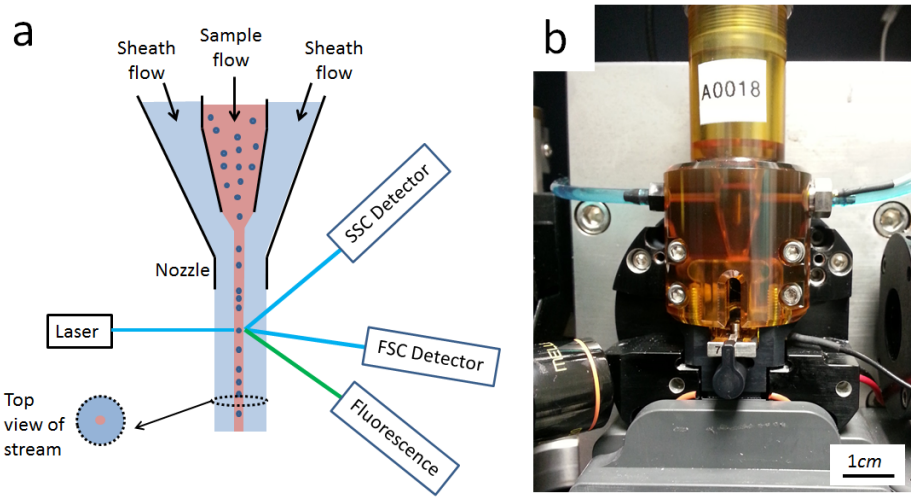

Figure 3.1: Illustration of sheath flow focusing. A sample stream containing the particles of interest is surrounded by a second (sheath) flow in a cylindrical geometry. This guides the particles through the centre of the detection region where the measurement is most linear with respect to particle position. b) Photograph of a flow cell in a commercial optical flow cytometer.

While this cylindrical geometry flow cell works well for large devices, it is difficult to miniaturise and integrate it into microfluidic channels. Generally, microfluidic devices use square or rectangular channels with the inlets and outlets perpendicular to the direction of flow. Instead, sheath flow focusing in microfluidic devices uses secondary inlets which join the sample flow stream at junctions.

Earlier work confined the sample stream horizontally (side-to-side) within a channel as shown in Figure 3.2a. This is actually 1D focusing, but is called 2D focusing in the literature and will be also be called 2D focusing in this thesis. 2D focusing could just confine the same stream vertically instead of horizontally, but this is more difficult to implement in a microchip. Later, 3D focusing was introduced which confines the sample both horizontally and vertically (Figure 3.2b), but at the expense of increased device complexity.

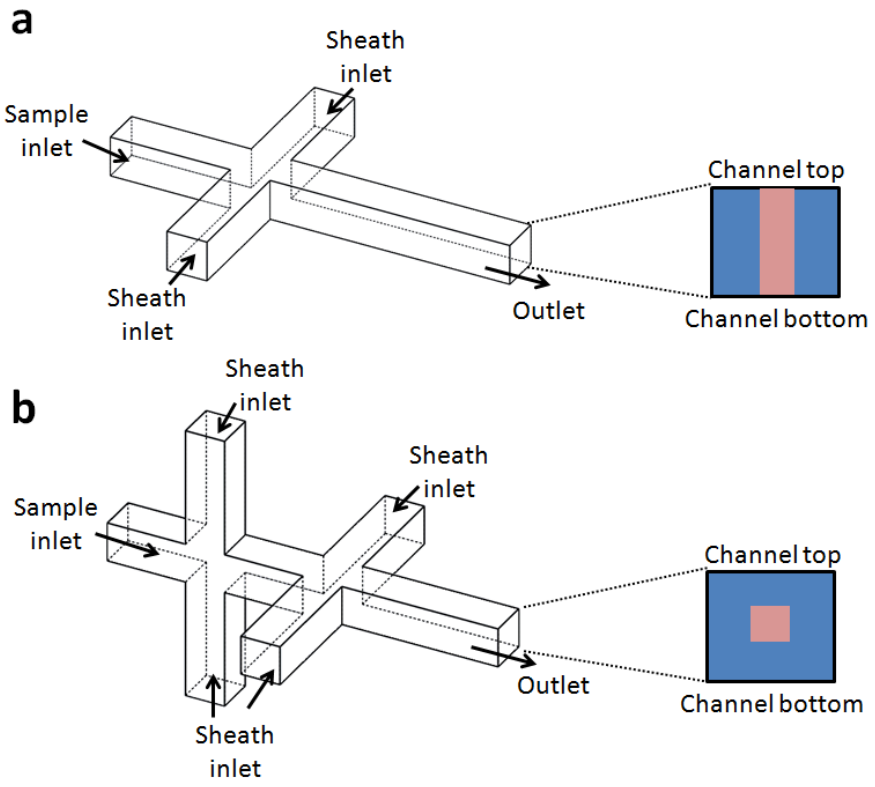

Figure 3.2: Illustration of sheath flow focusing in square microfluidic channels. a) In 1D focusing a sample stream containing the particles of interest is surrounded on two sides by a second (sheath) flow, guiding the horizontal particle position. b) In 2D focusing, a second pair of sheath inlets focus the vertical particle position.

The first sheath flow focusing system for a microfluidic device was reported by Jacobson and Ramsey (1997). The glass device focused the sample stream on two sides using a cross junction as shown in Figure 3.3. Unlike the other sheath flow devices reported, the fluids are moved by applying a voltage across the channel (electro-osmotic forces). By adjusting the voltage drop across the sample and sheath flows, the width of the sample stream could be adjusted. This vertical sheath flow is referred to as 2D focusing and can be achieved in a single layer device which is easy to fabricate. In the impedance cytometer described in this thesis, particles travelling close to the top or bottom of the channel would have a higher signal compared with the centre. Using 2D focusing would

mean that particles are confined horizontally but not vertically and so the variation in particle signal for the same sized particles would still be present.

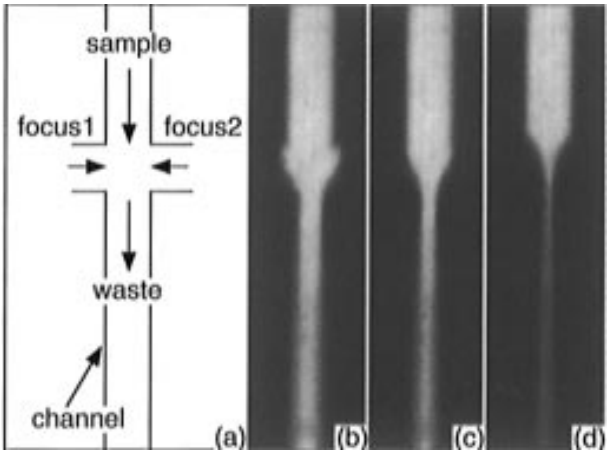

Figure 3.3: (a) Schematic of a 2D sheath flow focusing junction. (b-d) Microscope image of the sample stream showing adjustable stream widths by changing the voltage applied to the sample and sheath reservoirs. Image from Jacobson and Ramsey (1997)

Typically, the sample and sheath liquids are separately pumped through the device, in which case the sample width is defined by the ratio of the volumetric flow rates. Alternatively, a negative pressure can be applied to the outlet, pulling the sample and sheath flow through the channel. Lee et al. (2006) proposed two analytical models to calculate the sample width from the channel dimensions for symmetric and asymmetric 2D focusing schemes. The models account for the different channel aspect ratios which alter the flow profile within the channel. Lee et al. (2006) built the simulated device using an SU-8 master to cast PDMS and experimental sample widths matched the analytical models.

In 2D focusing schemes the sample of particles can still pass close to the top and bottom of the channel. Chapter 4 explains that this is still a problem for the impedance measurement system, causing variation in the detection and reducing the measurement accuracy. 3D focusing in microfluidic channels removes this problem by surrounding the sheath flow on all sides, just like the flow cell in Figure 3.1.

Sundararajan et al. (2004) simulated and then fabricated a 3D focusing device using PDMS as shown in Figure 3.4. The authors used confocal microscopy to show that a fluorescent sample stream (Rhodamine 6G) could be focused into the centre of the channel. The disadvantage of this design is the fabrication complexity; the device has five separate layers, and each layer must be aligned to the others. Subsequent research has aimed to reduce the number of fluidic layers required and simplify the fabrication process.

Simonnet and Groisman (2006) achieved 3D focusing in a two layer device. The sample stream is vertically focused using sheath flow inlets at the side of the main channel which

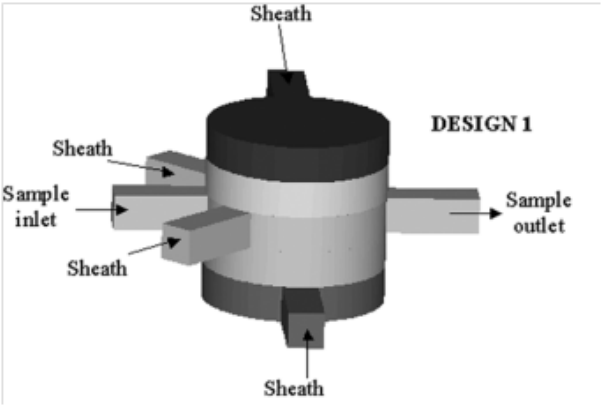

Figure 3.4: Microfluidic 3D sheath flow device produced by Sundararajan et al. (2004)

are shallower than the channel height, followed by horizontal focusing using two more sheath flows inputs at full channel height. Chang et al. (2007) noted that Simonnet and Groisman (2006) required two channels of different height and subsequently produced a modified design which uses two layers of equal height and was easier to fabricate (Figure 3.5).

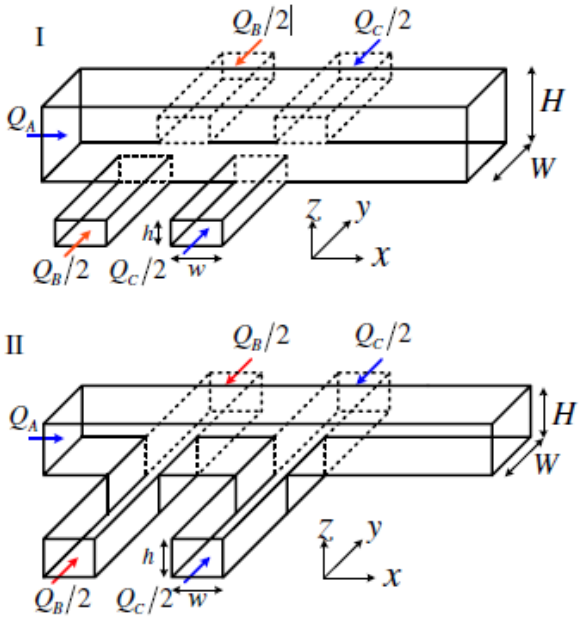

Figure 3.5: Schematic drawings of the 3D sheath flow designs proposed by Simonnet and Groisman (2006) and Chang et al. (2007). Both designs require two fluidic layers but the first design is more difficult to fabricate because two different depth fluidic layers are needed. Image from Chang et al. (2007)

Hairer et al. (2008) demonstrated 3D focusing in a single layer device, but focused the stream onto the bottom of the channel. The team reported a tight stream width, just $2.5\mu m$ in a $50\mu m \times 50\mu m$ channel. Although the sample stream was narrow, the sample stream extended vertically into the channel (Figure 3.6a-b). In addition, due to the

inherent parabolic flow profile, the sample core was wider where it made contact with the channel wall. Later, the authors added a further sheath flow input (Figure 3.6c) to lift the sample off the bottom of channel (Hairer and Vellekoop, 2009). By controlling each sheath flow input separately, they could move both the horizontal and vertical positions of the sample stream. Although the revised design overcomes the drawbacks of the first system, the device is complex to fabricate and the capability to adjust the sample stream position is not essential.

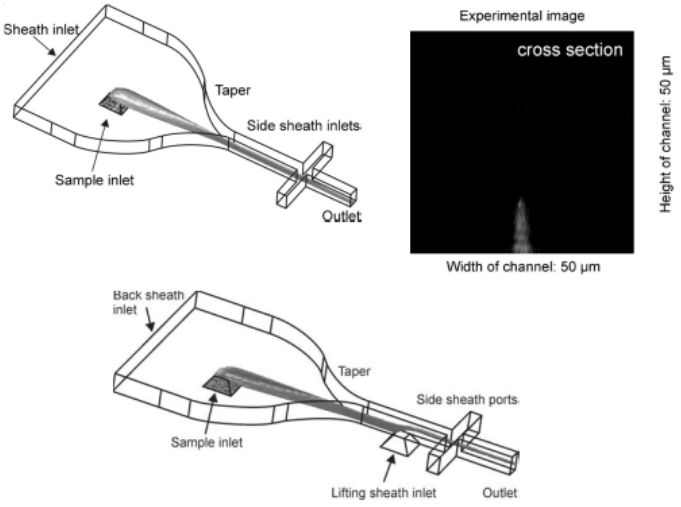

Figure 3.6: a) Design of the sheath flow system by Hairer et al. (2008). The sample is confined to the middle of the bottom of the channel as shown in b). The design was later improved using a further sheath flow input to lift the sample to the middle of the channel. Image from Hairer and Vellekoop (2009).

Watkins et al. (2009) used a similar focusing design to Hairer et al. (2008) in an impedance cytometer. Detection electrodes were located on the bottom of the channel (shown in Figure 3.7) which is easier to fabricate compared with electrodes on the top and bottom of the channel. An insulating sheath flow was used to increase the signal to noise ratio (SNR) by confining the electric field and CD4+ T-lymphocytes were detected. A problem with the design is that, because the electric field divergence is maximum at the electrode edges, the design is very sensitive to particle position. The sheath flow will not eliminate all positional dependence because there will still be some variation in the particle positions and subsequently particle positional dependence will be present.

Coincidence is a problem when two separate particles pass through the measurement region at the same time. Hou et al. (2009) proposed a sheath flow design with an added weir structure which is shown in Figure 3.8. The weir structure is positioned in the detection region to separate particles flowing in the vertical direction and to reduce coincidence. Using the weir, the group could distinguish between 5 and 10μm beads, for which the signals overlapped without the structure in place. However, no comparison of the level of coincidence for different particle concentrations was performed.

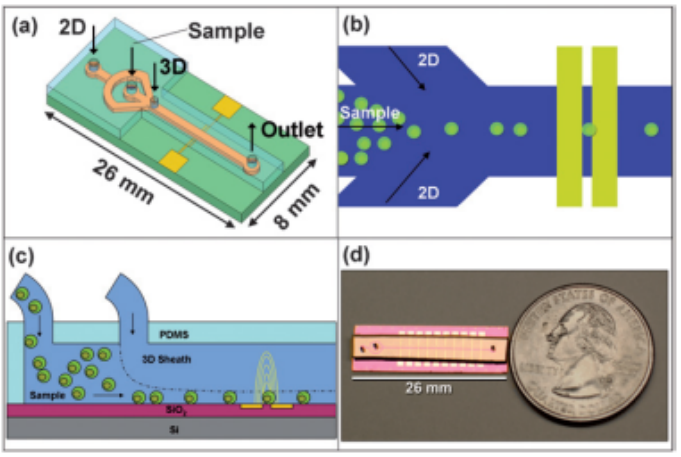

Figure 3.7: Watkins et al. (2009) used an insulating sheath flow to reduce the electrical measurement region in a microfluidic impedance cytometer.

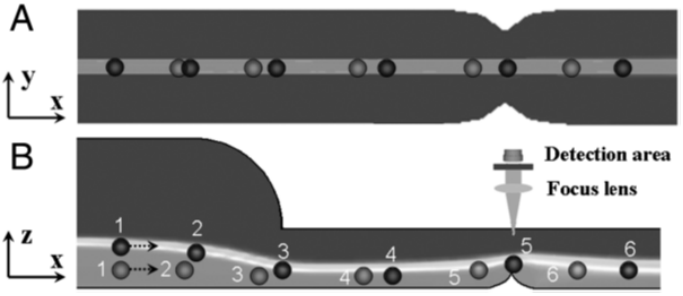

Figure 3.8: Schematic diagram showing the focusing design by Hou et al. (2009). The design uses a weir structure to separate particles in the vertical direction (and thus reduce coincidence).

Another 3D focusing device using two fluidic layers was reported by Kennedy et al. (2009). The sample flow in the top layer is vertically focused as it meets the sheath flow in the bottom fluidic layer as shown in Figure 3.9. Kennedy et al. (2009) varied the sheath flow rates to adjust the position of the sample stream which matched the positions expected from simulations.

Howell et al. (2008) published two 3D focusing designs using just one and two sheath flow inputs respectively. The designs (Figure 3.10) use just one fluidic layer but require grooves or chevrons to be fabricated into the top and bottom of the channel. Both designs were simulated (using fluidic modelling to solve the Navier-Stokes equation) and can be fabricated by milling, soft lithography or laser ablation. The simulations matched the experimental results across a broad range of sample to sheath ratios and the authors produced tight, narrow sample streams in the centre of the channel. The same group used the chevron based design to build a multi wavelength flow cytometer (Golden et al., 2009). The cytometer design was first modified to include a constriction at the sample inlet to reduce pulsation when using large sheath to sample ratios. Golden et al. (2009) measured E.coli bacteria using a fluorescent bead-based sandwich assay. The group also demonstrated multiplexed detection of bacteria and toxins captured on

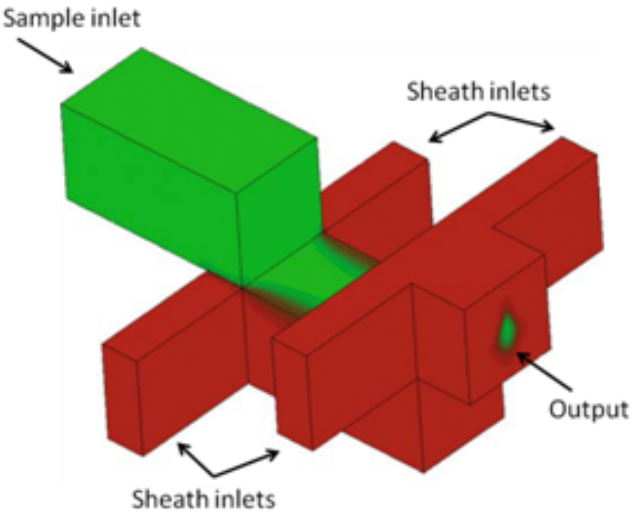

Figure 3.9: The 3D sheath flow device proposed by Kennedy et al. (2009). The design achieves 3D focusing using just two fluidic layers. Image modified from Kennedy et al. (2009).

beads at four different optical wavelengths (Kim et al., 2009). Results were compared with a commercial device and the LoD for both devices for two different toxins (cholera toxin and staphylococcal enterotoxin) were equal. The chevron focusing device has been shown to work across a wide range of sample to sheath ratios but device fabrication is challenging because the chevrons on the top and bottom of the channel must be aligned.

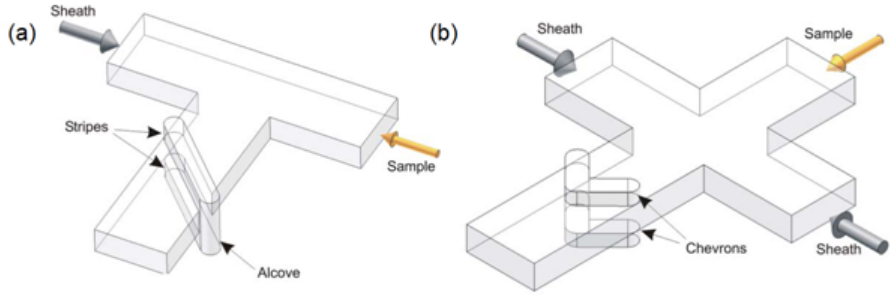

Figure 3.10: Diagrams showing the two 3D single layer focusing designs proposed by Howell et al. (2008). The designs use grooves or chevrons to twist sheath flow (from the side of the channel) underneath and over the top of the sample flow to achieve 3D focusing. Image from Howell et al. (2008)

Kummrow et al. (2009) fabricated a 3D focused micro cytometer by hot embossing Poly(methyl methacrylate) (PMMA) and polycarbonate into a micro machined mould. The cytometer, Figure 3.11, was able to measure platelets and RBCs by light scatter and labelled T-lymphocytes by light scatter and fluorescence. The group later compared their results with a commercial flow cytometer (Frankowski et al., 2011). Accurate detection of monocytes, lymphocytes and granulocytes was reported, however detection of the lower intensity fluorescent calibration beads was slightly worse in the micro-cytometer.

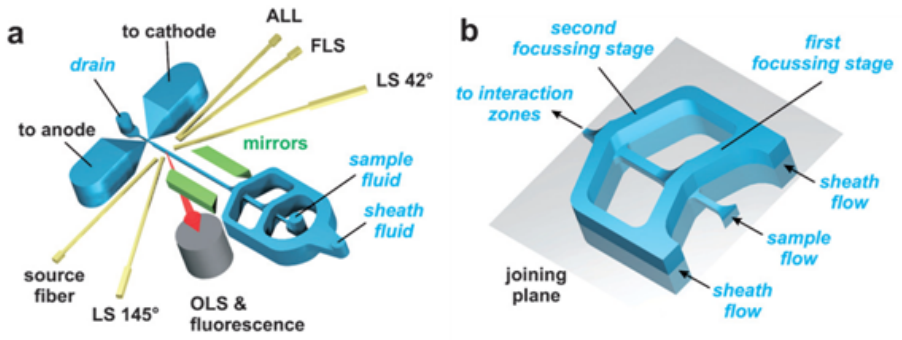

Figure 3.11: Cytometer design by Kummrow et al. (2009) with a 3D sheath flow, integrated electrodes for impedance measurement and fibres for scattered and fluorescent light. Image from Kummrow et al. (2009).

3.2.2 Dean Flow focusing

When a sample flows around a bend, Dean vortexes can be produced as shown in Figure 3.12. This effect has been used by Mao et al. (2007) to focus a sample stream both vertically and horizontally in a single layer device. The sample and sheath streams flow next to each other and around a 90° bend where the Dean vortexes vertically confine the sample. Two further sheath inlets horizontally confine the sample. The design was shown to focus $8\mu m$ beads and have a high throughput of 1700 beads per second.

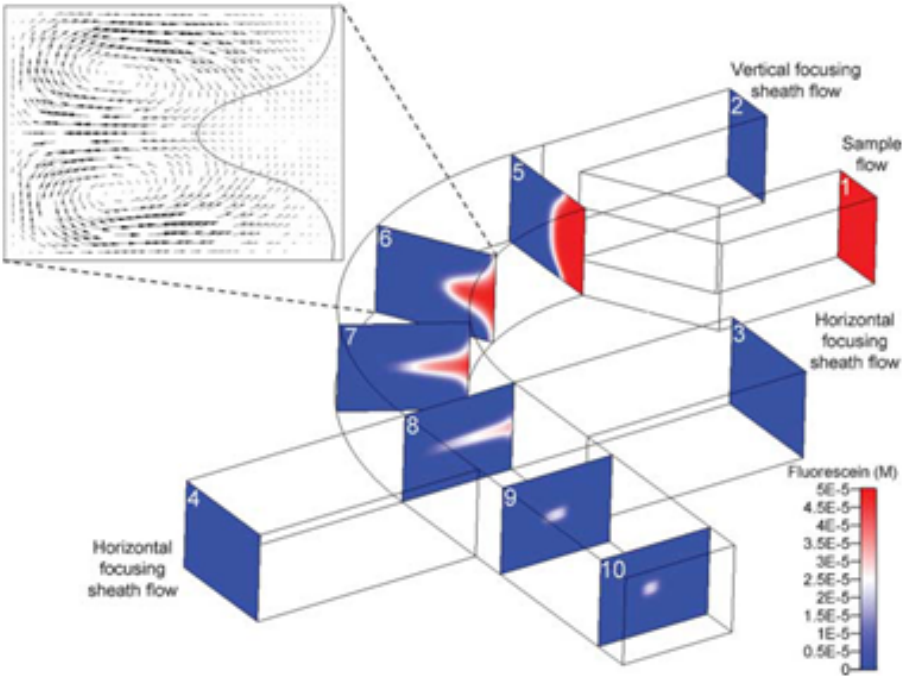

Figure 3.12: Schematic diagram of a single layer 3D focusing device. Sheath and sample flow side by side around a bend. Dean vortexes caused by the bend wrap the sheath flow around the sample achieving 3D focusing. Image from Mao et al. (2007).

The group later added optical fibres to the design to produce a miniature cytometer capable of detecting forward and side scattered light and fluorescence as shown in Figure 3.13 (Mao et al., 2012). Performance of the miniature device was found to be similar compared to a commercial device costing $100,000 for 7.3 and 15.5$\mu m$ beads, but no biological cells were measured.

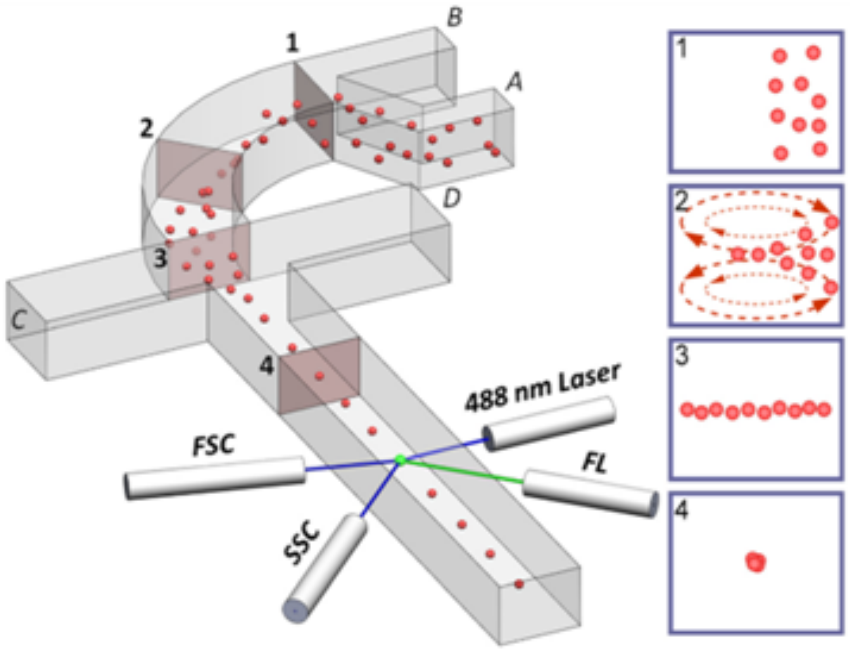

Figure 3.13: Mao et al. (2012) integrated fibre optics into their 3D sheath flow design to produce a miniature cytometer.

Lee et al. (2006) used Dean forces to 3D focus a sample in a single layer device with just one sheath input. The device (shown in Figure 3.14) consists of a series of contraction and expansion chambers which used Dean vortexes to surround the sample flow. Dean flow has the advantage that 3D focusing can be achieved in a single layer and therefore is a simple to fabricate device. However, notice in the corner of each expansion region (circled in Figure 3.14c) that some RBCs have accumulated. This is the region where there is the slowest flow and this could cause a problem if rare cell identification is required, since some cells may become trapped here.

In summary, sheath flow focusing has been achieved in microfluidic channels using a variety of different designs. The target has been to achieve horizontal and vertical confinement of the sample stream in the least complex and therefore robust and easy to manufacture device. However, all devices still require at least one additional input (for the sheath flow). In addition, to achieve a tight sample stream, the volumetric flow rate of the sheath must be much greater than the sample flow rate. This adds to reagent use which could be a problem for a miniaturised or hand held device and also dilutes the particles.

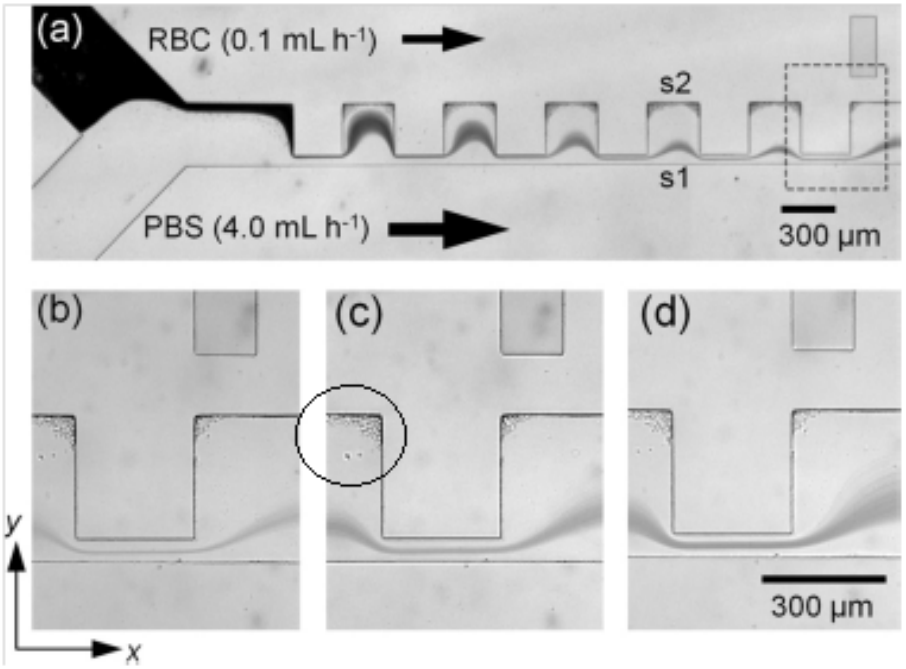

Figure 3.14: Design of the 3D sheath flow design by Lee et al. (2006). A stream of red blood cells (RBCs) was focused using a series of expansion and contractions in a single layer device.

Of particular note is the device produced by Mao et al. (2012). This is because it is a single layer device meaning fabrication is simple, yet the device achieved 3D focusing. Variation in the measurement of test particles was low; the CVs of measured particles were similar to an expensive commercial cytometer.

3.2.3 Sheathless Flow Focusing

In 1961, Segré (1961) observed under laminar flow conditions that millimetre sized particles focus to an annulus in a circular $1cm$ diameter pipe, with the annulus at 0.6 times the radius of the pipe as shown in Figure 3.15a. This effect is present at intermediate Reynolds numbers (around 1-100) and is called inertial focusing. The focusing is a result of two counter-acting forces; the wall lift force and the shear gradient force. In a fluidic channel under laminar flow conditions, the flow profile is parabolic. At intermediate Reynolds numbers, the shear gradient of the parabolic flow profile creates a lift force which causes particles to migrate away from the fastest flow in the centre of the channel and towards the slowest flow by the walls. However, particles flowing close to the edge of the wall experience a lift force directed away from the wall due to an asymmetric wake that is created, shown in Figure 3.15b.

Inertial focusing was first demonstrated in a square micro channel by Di Carlo et al. (2007), who noticed that at flow rates with Reynolds numbers of approximately 100,

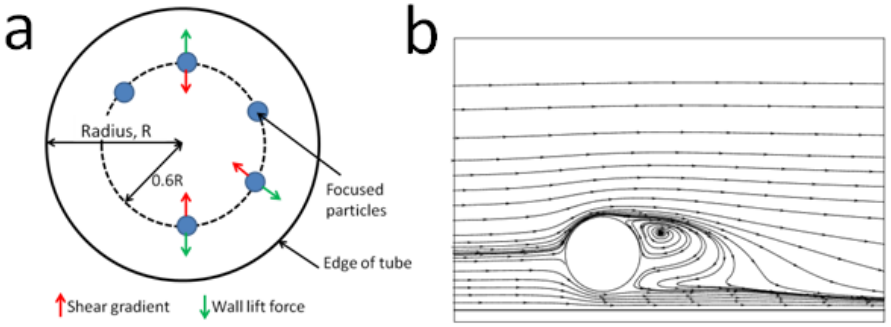

Figure 3.15: a) Illustration of inertial focusing in a circular channel. At intermediate particle Reynolds numbers (Rp), particles focus to an annulus 0.6 times the radius of the tube due to the balance of the wall lift force and shear gradient force. b) Simulation of the streamlines around a particle close to a wall at $Rp = 200$, performed by Zeng et al. (2005). The asymmetric streamlines create the wall lift force which move the particle away from the wall.

beads focused to four positions within the channel, as opposed to the annulus in a circular channel, as shown in Figure 3.16.

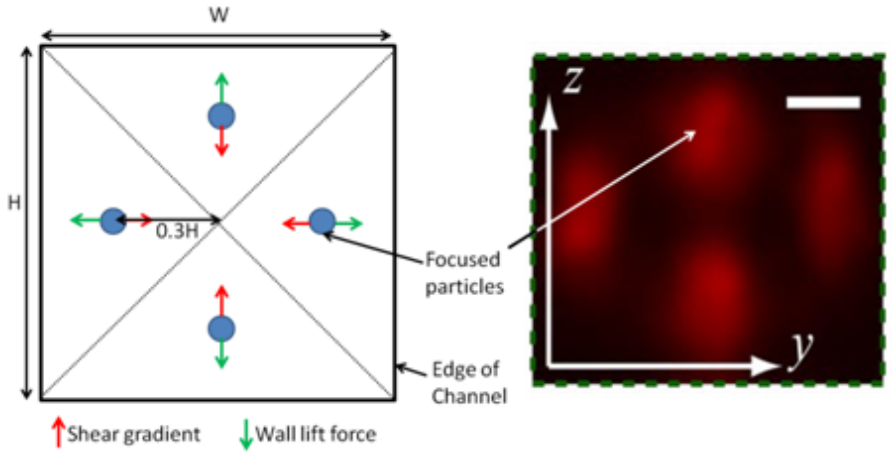

Figure 3.16: a) Diagram showing the preferential focusing points for inertialy focused particles in a square channel. b) Confocal image of a square channel showing fluorescent particles focusing to the four preferential positions. Image from Di Carlo et al. (2007).

Di Carlo et al. (2007) also noticed that in asymmetrically curving channels, the additional Dean force created by the curves reduced the four equilibrium positions to just one (Figure 3.17). The device was tested with particles more and less dense than the suspending liquid and the equilibrium positions were identical in both cases. In addition a longitudinal focusing effect (in the direction of the flow) was observed. This is advantageous in reducing coincidence.

Later, Di Carlo (2009) investigated inertial focusing in square channels for different particle sizes. It was found that the particle equilibrium position was mostly independent

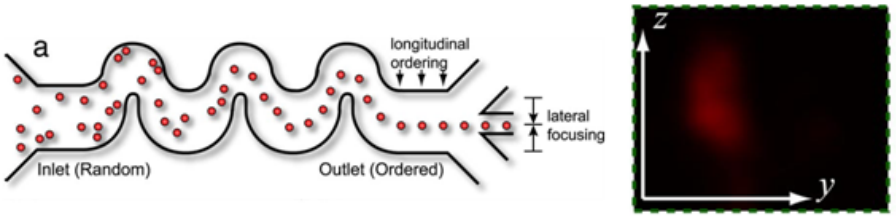

Figure 3.17: a) Diagram of an asymmetric curving channel to use Dean forces to inertialy focus particles. b) The four preferential positions in a square channel can be reduced to just one position using the curved channels. Images from Di Carlo et al. (2007).

of particle size; the position was only different for very large particles, for which the equilibrium position would be impossible since the particles would be touching the side wall (Figure 3.18).

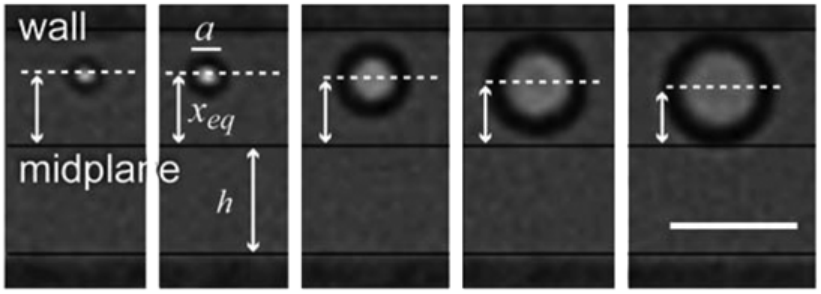

Figure 3.18: Microscope image of the preferential inertially focused position for different sized particles. The preferential position is independent of position except for very large particles where the particle touches the side wall. Image from Di Carlo (2009).

Asymmetrically curving channels were used by the same group (Oakey et al., 2010) to focus particles within an optical cytometer capable of detecting side scattered light and fluorescence. The channel structure focuses particles longitudinally in addition to vertically which ensures that no two particles pass though the detection region at the same time. Calibration beads with seven different fluorescence intensities were measured and showed a slightly tighter coefficient of variation (CV) compared with a commercial cytometer. However, the authors observed a decreasing focusing performance with lower particle concentration; to achieve the minimum CV of 6% in fluorescence the particle volume fraction needed to be 0.1% (approximately 2000 particles per microlitre which is too high for MIC). Low particle concentrations resulted in much higher variation (Figure 3.19), which would cause problems in applications with low particle counts such as environmental monitoring. The authors note the cause of this is likely to be an increase in the repulsive particle-particle interactions as the concentration increases, resulting in the particles reaching the equilibrium positions quicker.

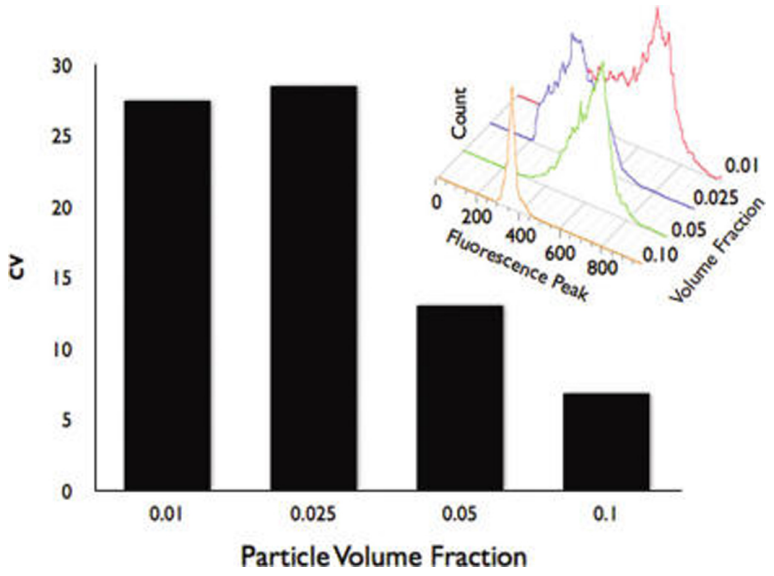

Figure 3.19: Coefficient of variance in fluorescence for inertialy focused particles at different particle volume fractions. Figure from Oakey et al. (2010).

Hur et al. (2011) used inertial focusing to focus beads and cells in 256 parallel rectangular channels. Using a high-speed camera, the authors could image 10 of the 256 channels simultaneously to count and distinguish different cells types. Hur et al. (2011) found that erythrocytes did not focus due to their discoid shape and had to be sphered before detection, adding complexity to the sample preparation. Acquisition optics with a larger field of view could be used to image more of the channels simultaneously, increasing device throughput and enabling the technology to be used for rare cell detection.

Inertial focusing in high aspect ratio channels was investigated by Bhagat et al. (2008) who found the four equilibrium positions in square channels reduced to two positions in rectangular channels with one position on each of the longer walls as shown in Figure 3.20a. This effect was used as a particle filter; a tall channel was used to inertially focus 1.9μm beads towards the two side walls. The stream close to each side wall containing the beads was discarded, leaving particle free solution (Figure 3.20b). Although this work shows inertial focusing could be used as a cheap particle filtering system, the focusing is size dependent; only the larger particles are removed.

The same group fabricated a spiral channel, Figure 3.21, and showed that the equilibrium position of focused particles was dependent on particle diameter. The device was shown to separate 10, 15 and 20μm diameter beads and in subsequent experiments was used to separate C6 neuroblastoma from smaller glioma cells (Kuntaegowdanahalli et al., 2009). Later, the group built a fluorescence cytometer, using a similar spiral geometry to focus beads and cells into a tight stream and detect fluorescent events with a laser counter (Bhagat et al., 2010). However, different sized particles will focus to different positions (and only particles in one position will be counted by the laser) meaning the device needs to be adapted for each particle size thus limiting the practical use of the technology.

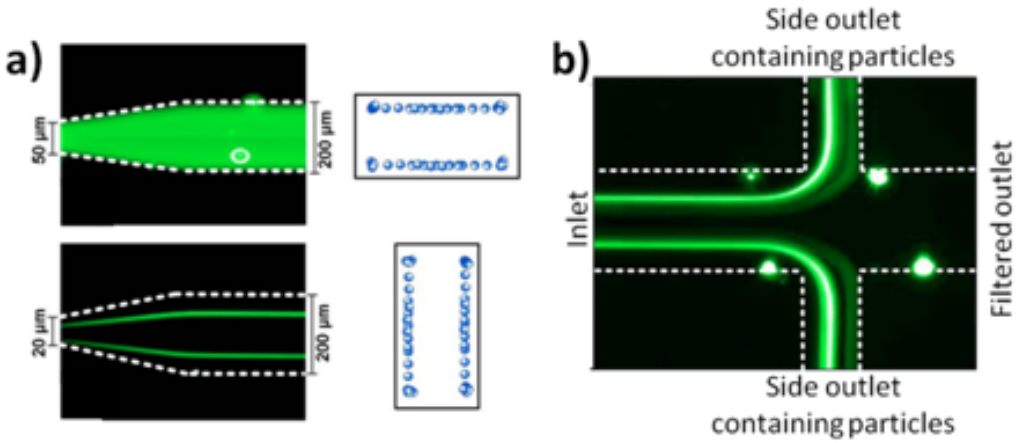

Figure 3.20: Diagram showing the equilibrium positions for particles in square and rectangular channels. In square channels particles focus along the four sides whereas in rectangular channels the particles only focus to the two longer sides. Image from Bhagat et al. (2008).

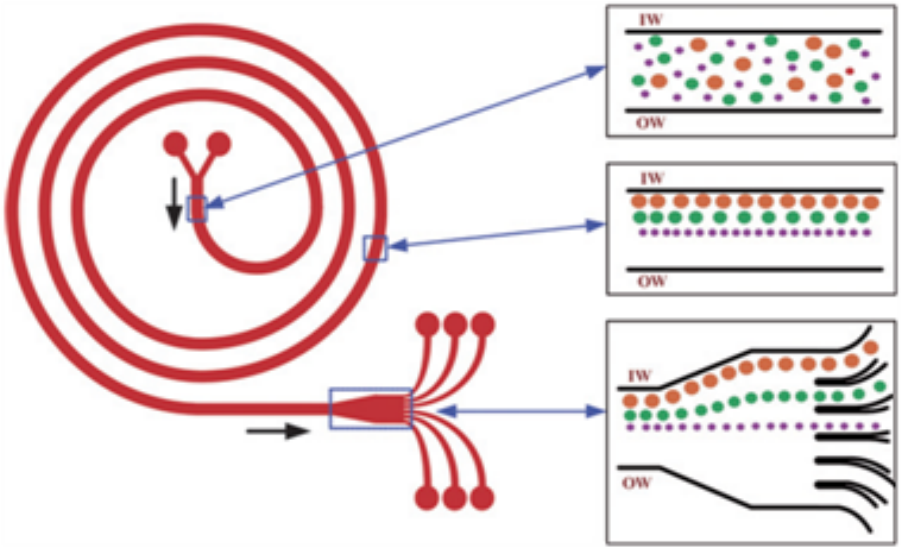

Figure 3.21: Curved microfluidic channel used by Kuntaegowdanahalli et al. (2009) to separate particles based on the particle size.

The advantage of inertial focusing over sheath flow focusing is that no additional inlets are required. All that is required is to optimise the dimensions of the channel to the flow rate and size of particle. However, the inertial focusing force which moves particles to their equilibrium positions is proportional to the square of the particle diameter. Figure 3.22 is a plot of the minimum channel length for inertially focusing particles in a channel $40\mu m \times 40\mu m$ at a flow rate of $40\mu L min^{-1}$ calculated using the equations from Di Carlo (2009). The figure shows that $20\mu m$ diameter particles will focus within $1mm$, and $7\mu m$ particles within $10mm$. However, to focus $2\mu m$ particles would require a $10cm$ channel. At this flow rate, the channel back pressure would be $8.4bar$ which is likely to burst open (de-laminate) the MIC chips.

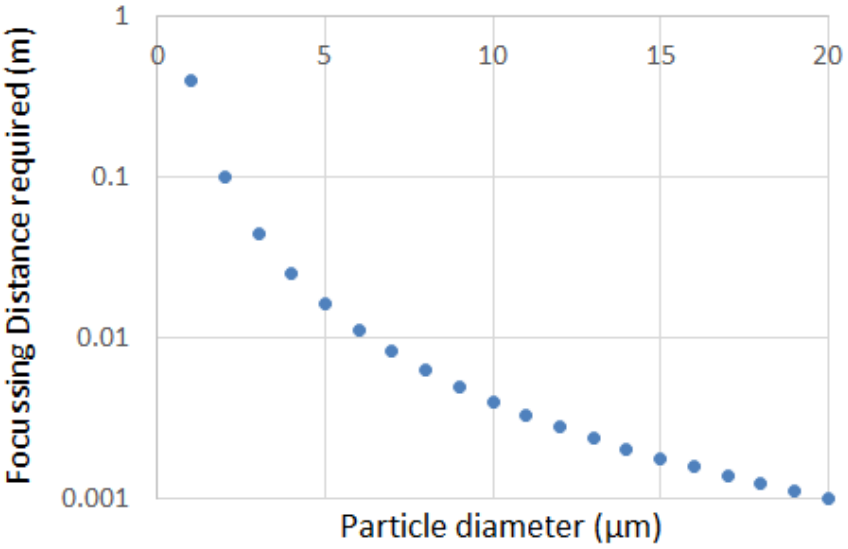

Figure 3.22: Graph of the minimum channel length required to focus particles in a $40\mu m \times 40\mu m$ channel at a flow rate of $40\mu L min^{-1}$.

3.2.4 Acoustic Focusing

In inertial focusing, the force required to move particles to equilibrium positions is induced by the channel shape. Alternatively this force can also be externally applied through an actuator. In acoustic focusing, an ultrasonic transducer is mounted close to the channel and driven to resonance, creating a standing pressure wave within the channel. This force moves particles within the channel to the minima of this standing wave. Mostly, acoustic focusing has been used to sort particles by making use of the fact that the acoustic force driving particles to the equilibrium position is proportional to the cube of the particle diameter. An example is shown in Figure 3.23. Particles enter the bottom of a channel through a small inlet. A standing wave moves the larger (yellow) particle to outlet A, whereas the force is not strong enough to move the smaller (red) particles, so these particles exit at the lower outlet B.

The acoustic force can also be used to focus particles into the centre of the channel as demonstrated by Shi et al. (2011). The device consisted of a PDMS channel bonded to a substrate between two sets of interdigitated transducers (IDT), Figure 3.24a. The transducers generate a standing acoustic wave (SAW) across the surface of the substrate which then leak into the microfluidic channel through interference (Figure 3.24b). The group were able to focus $1.9\mu m$ diameter beads into the centre of the channel, however the flow rate (and therefore throughput) was low ($7\mu L min^{-1}$ in the $100 \times 50\mu m$ channel). This is likely to have been constrained by the length of the channel and the time required to focus the particles to the equilibrium positions.

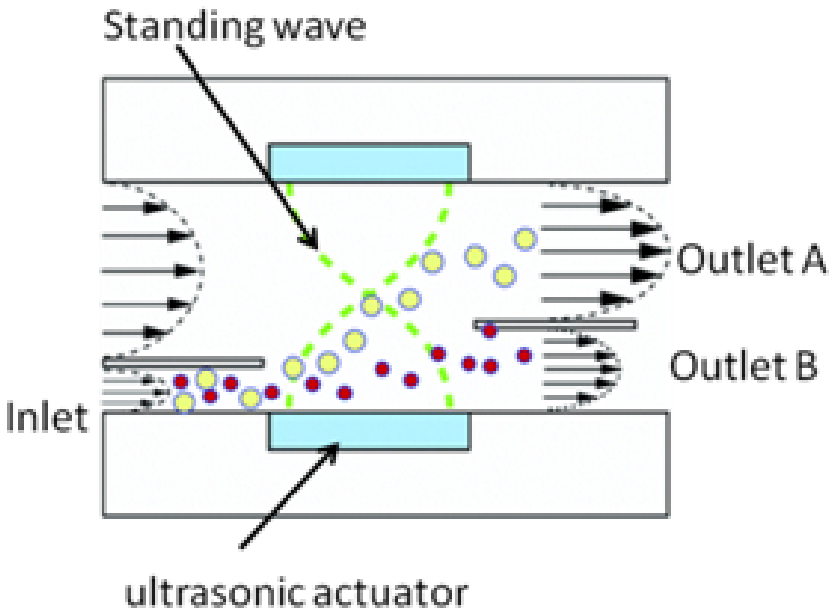

Figure 3.23: Diagram showing particle separation using acoustic focusing. An ultrasonic transducer creates a standing wave in the centre of the channel. This forces particles to the centre of the channel, however the force is greater for bigger particles which enables separation based on particle size. Image from Lenshof et al. (2012).

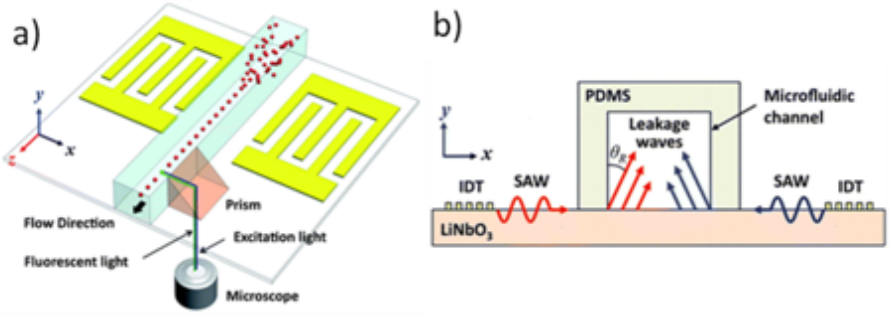

Figure 3.24: Acoustic focusing device by Shi et al. (2011). An interdigitated acoustic transducer on each side of a fluidic channel produces a standing acoustic wave (SAW). The SAW leaks into the fluidic channel through interference, creating an acoustic node in the centre of the channel which focuses particles.

Acoustic focusing has also been used in a commercial optical cytometer. In conventional cytometers the sample stream is confined to the centre of a channel using sheath flow (Figure 3.25a). To achieve the most accurate measurements, the core stream must be as small as possible. However, to increase the throughput the core stream is often widened. In the Attune cytometer, the sample stream is first acoustically focused before it is confined by a sheath flow (Figure 3.25b). This allows the sample flow rate (and throughput) to be increased without sacrificing measurement accuracy.

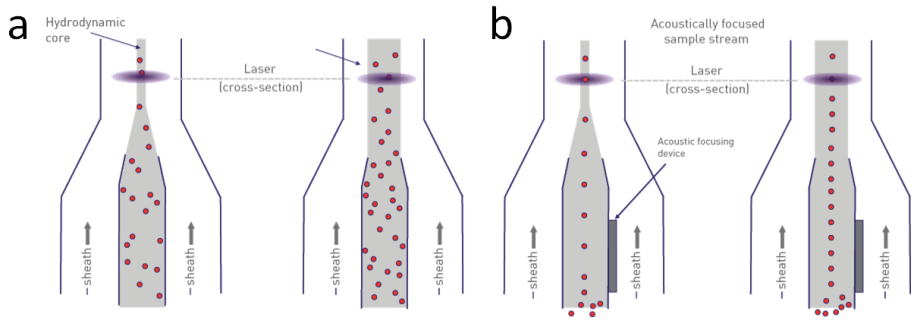

Figure 3.25: Diagram of a) sheath flow focusing in a traditional cytometer. For high accuracy measurements the sample stream width is small which sacrifices throughput, whereas a wide core gives high throughput at the expense of variation in the signals. b) A sheath flow system combined with acoustic focusing (Attune) for a high accuracy measurement mostly independent of throughput. Image from `http://www.invitrogen.com/etc/medialib/images/Cell-Analysis/`

In acoustic focusing, the force acting on the particle (F_{ax}) is given by Equation 3.1, Lenshof et al. (2012).

$$F_{ax} = 4\pi r^3 E_{ac} k sin(2kz)\phi \tag{3.1}$$

where r is the particle radius, E_{ac} is the acoustic energy density, k is the wavenumber ($\frac{2\pi f}{c_0}$), z is the distance from the pressure antinode and ϕ is the acoustic contrast factor given by Equation 3.2, Lenshof et al. (2012).

$$\phi = \frac{\rho_p + \frac{2}{3}(\rho_p - \rho_m)}{2\rho_p + \rho_m} - \frac{\rho_m c_m^2}{3\rho_p c_p^2} \tag{3.2}$$

where ρ_p and ρ_m is the density of the particle and medium and c_p and c_m are the speed of sound in the particle and medium.

Longer channels or lower flow rates are required to focus smaller particles. Although focusing has been demonstrated for polystyrene beads to show the concept, measurement of biological cells, which mostly consist of water, is more challenging as the acoustic contrast of a cell suspended in a buffer (salty water) will be much lower than that of polystyrene beads in the same medium.

3.2.5 Dielectrophoretic Focusing

Dielectrophoresis is the movement of a dielectric particle in the presence of a non-uniform electric field (as described in Chapter 2). This effect was used by Morgan and Green (2003) to focus nano-particles (40 to 400nm) in the centre of a channel for fluorescence detection. The system started to focus 40nm particles, but a tight distribution of particles was not observed (Figure 3.26).

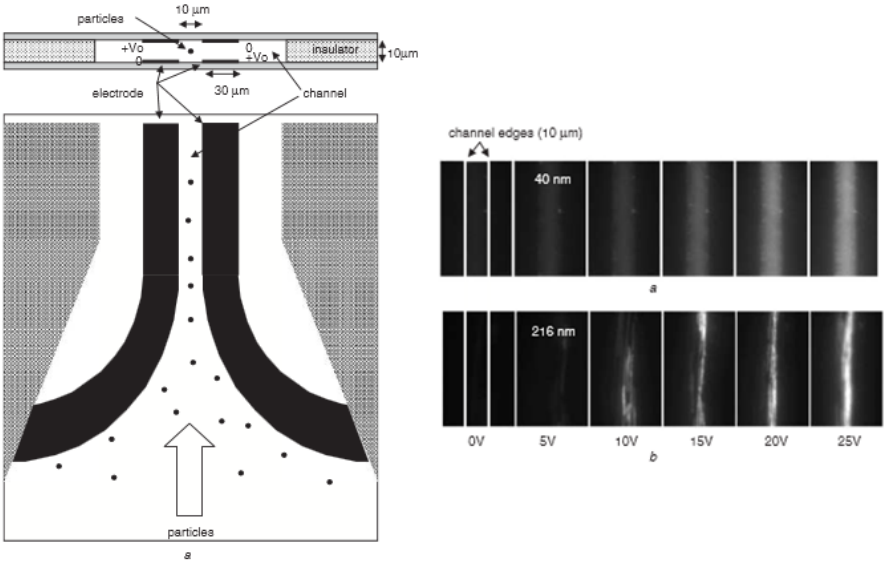

Figure 3.26: a) Dielectrophoresis focusing device built by Morgan and Green (2003) to focus nanometre sized particles into the centre of the channel. b). Image of a stream of fluorescent beads passing through the channel at different applied voltages to induce dielectrophoretic focusing. At 25V, the particles start to move towards the centre of the channel as seen by the increase in fluorescence, but a tight stream is not observed.

The system was developed further to include planar electrodes to detect the impedance of particles. The system could detect the impedance (electrical volume) and fluorescence of 4 and 5μm diameter particles. However, the system was slow (linear particle velocities of $5mms^{-1}$ compared to $1-2ms^{-1}$ for the particles in this thesis). The coefficient of variation for impedance or fluorescence was not stated and the signals with and without focusing were not compared.

More recently, Mernier et al. (2012) used dielectrophoresis to focus particles in the centre of a channel and additional electrodes to measure the impedance of particles. The advantage of this design was that all the electrodes were planar, all located on the bottom of the channel. To achieve a uniform electric field, the electrodes were placed in closed side channels, away from the main fluidic channel. The side channels confine the electric field, making it mostly linear by the time the electric field reaches the edge of the main channel. The group found the CV of 4 and 6μm diameter beads reduced from 27% to 5.6% with focusing, however the throughput was not stated.

As with acoustic focusing, the dielectrophoretic force required to focus particles is proportional to the cube of the particle diameter. The time averaged dielectrophoretic force acting on a spherical particle is given by Equation 3.3 (Morgan and Green, 2003).

$$\langle F_{DEP} \rangle = \pi \varepsilon_m r^3 Re(f_{CM}) \nabla \mid \mathbf{E} \mid^2 \tag{3.3}$$

Where ε_m is the medium permittivity, r is the particle radius, $Re(f_{CM})$ is the real part of the Clausius Mossotti factor, and $\nabla \mid \mathbf{E} \mid^2$ is the square of the gradient of the electric field. Thus, to focus smaller particles in the same device at the same voltage, the flow rate (and throughput) must be reduced.

3.2.6 Particle focusing Summary

Most applications of particle focusing have been for optical cytometers, which is important because the intensity profile of an optical signal across a channel is Gaussian; any off centre particles will scatter less light resulting in a measurement error. Nonetheless, the focusing techniques are all applicable to MIC where the impedance signal depends on particle position as described in the next chapter.

Sheathless flow focusing overcomes the disadvantage of sheath flow focusing (more complex designs) by using a force to move particles within the sample stream to the centre of the detection region. The force can be induced by channel shape as in the case of inertial focusing, or externally applied in the case of acoustic or dielectrophoretic focusing. However, the force is dependent on particle size which makes focusing smaller particles more challenging. In Chapter 5, a new electrode geometry and signal processing algorithm are used to provide high accuracy particle impedance measurement with the advantages of being sheath less and particle size independent.

For a more comprehensive review of particle focusing in microfluidic channel including acoustic and dielectrophoretic focusing see Xuan et al. (2010). Di Carlo (2009) reviewed inertial focusing in both straight and curving channel, and reported design rules for calculating channel dimensions to inertially focus channels. Ligler and Kim (2010) wrote a more general review of microfluidic flow cytometry concentrating on miniaturised optical detection but also covering particle focusing and electrical detection.

3.3 Impedance Detection

As described in the introduction, the first electrical measurements of cells were made using a Coulter counter (Coulter, 1956). Briefly, a voltage is applied between two

reservoirs which are separated by a small aperture. Cells placed in one reservoir pass through the aperture, blocking the current flow between the two reservoirs. Measurements are performed at low frequency to determine particle diameter. Higher frequency measurements (impedance) can be used to determine cell membrane and cytoplasm properties, however the parasitic capacitances of the large electrodes used in a Coulter counter restrict high frequency measurements.

To reduce the parasitic capacitances and achieve high frequency measurements, Morgan et al. (2006) fabricated measurement electrodes within a microfluidic channel. The device used negative dielectrophoresis (DEP) to focus particles into the centre of the channel prior to the detection region. Simultaneous florescence measurement was also performed. The device was tested using beads but the throughput was not stated. A similar device without DEP focusing was used by Benazzi et al. (2007) to analyse and discriminate phytoplankton.

Using Schwarz-Christoffel mapping, Sun et al. (2007b) analysed planar and parallel electrode geometries. For the same electrode width and separation, the parallel facing geometry was found to have a higher sensitivity due to the lower volume fraction. Although the increased sensitivity is at the expense of more complex device fabrication (because the electrodes top and bottom of the channel must be aligned to within a few μm) the parallel facing geometry has been used in recent publications.

Holmes et al. (2009) used impedance cytometry to demonstrate discrimination of the three main types of leukocyte using a single fingerprick of blood ($50\mu L$). Briefly, erythrocytes were lysed using a solution of saponin and formic acid, followed by addition of a quench solution which restores the solutions osmolarity. Lymphocytes were distinguished from granulocytes using a low frequency size measurement. A high frequency signal (not possible on a Coulter counter) measures the membrane capacitance of the cells and enables differentiation of monocytes from the similarly sized granulocytes. The technology has been integrated with microfluidic lysis for on-chip sample preparation, along with a serial diluter to count erythrocytes and platelets for PoC use (van Berkel et al., 2011).

A significant advantage of optical over electrical cytometry is that cell surface markers can be fluorescently labelled and detected. An equivalent "impedance label" was reported by Holmes and Morgan (2010), who used antibody coated beads to distinguish and detect T-lymphocytes. However, the impedance label system still has a drawback; only one impedance label can be used, (unlike fluorescent labelling where multiple different colours can be used).

In all the research presented above, the channel dimensions must be tailored to the size of particle being measured; if the channel is too narrow larger particles will block the channel, whereas a very large channel will limit the SNR. Bernabini et al. (2011) used overlapping electrodes in a wide channel to enable a wide range of particle size

measurements. An insulating sheath flow was used to adjust the sample stream width to maintain a high SNR. The device was used with a narrow stream to count E-coli bacteria. Simultaneous fluorescence detection was also implemented.

To measure particles at multiple simultaneous frequencies, a dedicated oscillator and lock in amplifier is required for each individual frequency. This is not practical for hundreds of different frequencies. Maximum Length Sequence, MLS, is a technique for measuring the impulse response of a time invariant system. MLS was used to measure the impedance of single cells at 512 frequencies simultaneously Gawad et al. (2007), Sun et al. (2007b) and Sun et al. (2007a). The disadvantage of MLS is that the systems to be measured must be time invariant. This is not the case in impedance cytometry since the particles flow through the detection region and as a result the maximum flow rate is limited.

Caselli et al. (2010) proposed a new electrode geometry, shown in Figure 3.27 and used FEM to simulate the response of different shaped particles. Although the new geometry could theoretically be used to detect the shape of particles (for instance the discoid shape of erythrocytes), it is virtually impossible to fabricate.

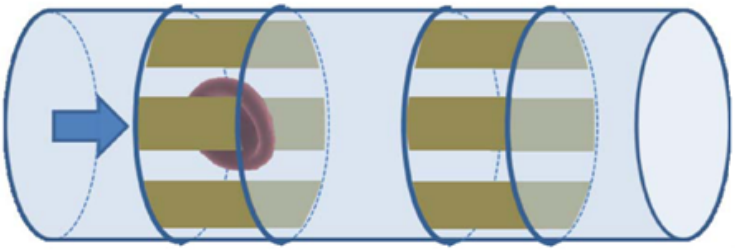

Figure 3.27: Geometry proposed by Caselli et al. (2010) to measure and distinguish different particles based on their shape. The new geometry is practically impossible to fabricate.

In summary, analytical models for both planar and parallel miniature electrodes in the channel have been reported. However, these models do not account for particle position in the channel. Instead, numerical modelling must be used which is described in the next chapter. Multi-frequency measurements of cells and beads have been reported along with simultaneous fluorescent measurement, but high accuracy (low CV) measurements have not been shown.

Chapter 4

Particle Positional Dependence

4.1 Overview

The maximum impedance signal of a particle (for instance a cell) passing through the centre of the MIC channel can be analytically calculated (Sun et al., 2007b). However, this method cannot determine how the impedance varies with the position of the particle in the channel. Instead, the impedance signal must be simulated using numerical techniques.

This chapter introduces the finite element method (FEM) which is a numerical technique used for modelling problems where an analytical model cannot be applied, for instance in a system which has a complicated geometry. FEM is used to create a full 3D model of the impedance signal for a particle in a MIC as a function of particle position in 3D space.

The model is first validated against analytical solutions, and then against experiment data of polystyrene beads which are used as test particles. The model shows that particles close to the electrodes have a higher measured signal compared to the same sized particle in the centre of the channel (away from the electrodes), and unexpectedly, despite the symmetric electrode geometry, this increase in signal is asymmetric about the vertical channel position. The FEM model described in this section has been used to develop an improved electrode geometry which is described in Chapter 5.

4.2 The Finite Element Method

This section describes the development and validation of the FEM model against analytical solutions. All modelling was performed using a commercial software package (Comsol V4.1).

The first step in developing a FEM model is to split the geometry of the system to be modelled into sections, which is called meshing. The geometry could be 1D, 2D or 3D depending on the problem to be addressed. For example, the large square in Figure 4.1 could represent a 2D geometry to model. When meshed, the square is split into smaller elements, in this case different sized triangles. The size of the mesh depends on the importance of each section of geometry. Unimportant areas, or areas where there is a small gradient in the simulation quantity (for instance electric field), can be meshed with large elements. Where there is a large gradient or when high numerical accuracy is needed, a finer mesh (smaller elements) is required. Typically the elements are triangular but higher order polygons can be used, although a comparison between element shapes is beyond the scope of this work.

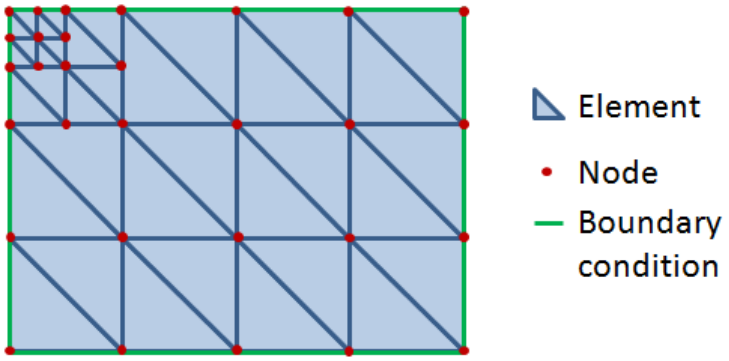

Figure 4.1: Illustration of meshing. The large rectangle is split into smaller triangles. The mesh density is increased where the field gradient is greatest (top left corner in this example) to reduce numerical errors.

Each point in the mesh is called a node (red dots in Figure 4.1). At each node the underlying equation for the model is solved. Under static conditions the electric field is the gradient in voltage, Equation 4.1.

$$\mathbf{E} = -\nabla V \tag{4.1}$$

Combining this with $\mathbf{D} = \varepsilon_0 \mathbf{E} + \mathbf{P}$ gives Equation 4.2

$$-\nabla(\varepsilon_0 \nabla V - \mathbf{P}) = \rho \tag{4.2}$$

The solution is approximated at each node and an iterative approach is used to calculate the electric field distribution within the modelled geometry.

Once the mesh is defined, boundary conditions must be applied. The conditions are applied to all boundaries on the edge of the geometry defined in the model (in green in

Figure 4.1). In this chapter, an electric field simulation is performed because the current flow between electrodes is of interest. The following boundary conditions are used.

- Potential: The node is at a specified potential ($\phi = V$) to model the surface of an electrode.
- Ground: The node is at zero potential ($\phi = 0$)
- Current source: The current flux through a node is at a specified value ($n.(J_1 - J_2) = Q_j$)
- Insulating boundary: No current flows through the node ($n.J = 0$).

where n is each node on the mesh, J is the current density and Q is the current source density.

4.3 Developing and Testing the Numerical Model

To check that the simulation agrees with analytical solutions, the impedance of a cube of electrolyte ($40\mu m^3$) was simulated with and without a $6\mu m$ insulating sphere in the centre as shown in Figure 4.2. Each side was set to an insulating boundary except the top ($\phi = 1V$) and bottom ($\phi = 0V$).

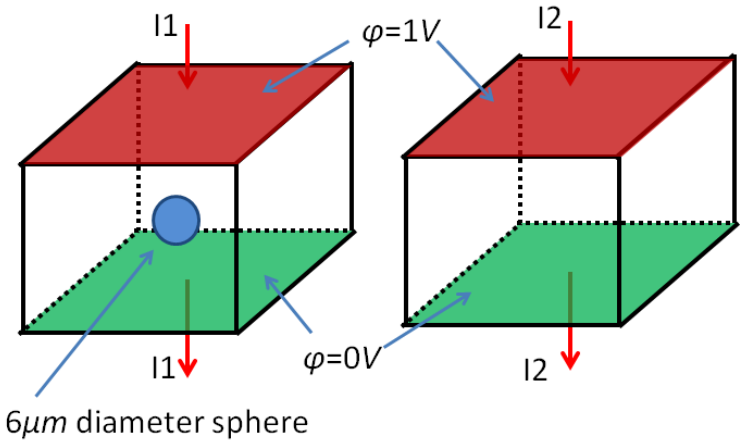

Figure 4.2: Two cubes with side dimensions $40\mu m$, with a $6\mu m$ bead in the first box. The currents I1 and I2 were simulated and compared with the analytical solutions.

The permittivity and conductivity of the electrolyte was set to model PBS ($\sigma = 1.6 Sm^{-1}$, $\varepsilon = 80\varepsilon_0$) which is used in experiments described later. To model a $6\mu m$ diameter polystyrene bead, a sphere of the same size was used, with a permittivity of polystyrene ($2.5\varepsilon_0$). The conductivity of an insulating sphere (σ_p) is dominated by its surface conductance (K_s) and is given by Equation 4.3.

$$\sigma_p = \sigma_b + 2\frac{K_s}{r} \tag{4.3}$$

For this test particle the conductivity is given by Equation 4.4.

$$\sigma_p = 1 \times 10^{-18} + 2 \times \frac{1 \times 10^{-9}}{3 \times 10^{-6}} = 6.67 \times 10^{-4} Sm^{-1} \tag{4.4}$$

Since the conductivity of the particle is much lower than the conductivity of the suspending medium ($1.6 sm^{-1}$), the measured impedance is proportional to the volume of the particle and will be unaffected by small changes in the surface conductance.

The currents I1 and I2 from the simulation were 63.8 and 64.0μA respectively. To validate the simulation, these values are compared with the analytical solutions as follows. The current I2 can be analytically calculated from Ohms law, Equation 4.5

$$I = abs(\frac{V}{Z}) \tag{4.5}$$

Where the impedance (Z) is given by Equation 4.6.

$$\begin{aligned} Z &= abs(\frac{d}{A\sigma} + \frac{d}{j\omega\varepsilon_0\varepsilon_R}) \\ &= abs(\frac{40 \times 10^{-6}}{40 \times 10^{-6} \times 40 \times 10^{-6} \times 1.6} + \frac{40 \times 10^{-6}}{j \times 2 \times \pi \times 80 \times 8.85 \times 10^{-12} \times 40 \times 10^{-6} \times 40 \times 10^{-6}}) \end{aligned} \tag{4.6}$$

Where A is the electrode area and d is the distance separating the electrodes.

This gives the analytical solution for I2 as 64.0μA, matching the simulated value.

For I1, Maxwells mixture theory, Equation 4.7 must be used to calculate the relative complex permittivity.

$$\tilde{\varepsilon}_{mix} = \tilde{\varepsilon}_m \frac{1 + 2\psi\frac{\tilde{\varepsilon}_p - \tilde{\varepsilon}_m}{\tilde{\varepsilon}_p + 2\tilde{\varepsilon}_m}}{1 - \psi\frac{\tilde{\varepsilon}_p - \tilde{\varepsilon}_m}{\tilde{\varepsilon}_p + 2\tilde{\varepsilon}_m}} \tag{4.7}$$

For this example the complex permittivity is given by Equation 4.8.

$$\begin{aligned} \tilde{\varepsilon}_p &= \varepsilon_0\varepsilon_p - \frac{j\sigma_p}{\omega} \\ &= 8.85 \times 10^{-12} \times 2.5 - \frac{j \times 6.67 \times 10^{-4}}{2 \times \pi \times 1 \times 10^6} \\ \tilde{\varepsilon}_m &= \varepsilon_0\varepsilon_p - \frac{j\sigma_m}{\omega} \\ &= 8.85 \times 10^{-12} \times 80 - \frac{j \times 1.6}{2 \times \pi \times 1 \times 10^6} \end{aligned} \tag{4.8}$$

This gives the analytical answer to the current I1 as $63.8\mu A$, also matching the simulation.

4.3.1 Simulation Geometry

The MIC chips have wide inlet and outlet channels connecting the narrow detection region in the centre of the device (where the electrodes are located). To minimise the simulation complexity, just the detection region, which contains the measurement electrodes, is considered. The simulation geometry consists of a rectangle $300\mu m$ wide, $40\mu m$ high and $40\mu m$ deep. The two sets of electrodes are each $30\mu m$ wide and $40\mu m$ deep, separated by a $40\mu m$ gap, to match the experimental device.

To simulate a particle moving through the channel, the particle motion is broken up into steps. A separate simulation is performed for a stationary particle at each step as shown in Figure 4.3. The distance between steps gives the time resolution of the differential current signal; in the results reported in the following section the step size is $3\mu m$ (a trade off between simulation speed and time resolution).

The electric field gradient is greatest at the electrode edges and so the mesh at these positions must be refined to minimise numerical errors. Figure 4.4 is a diagram showing the mesh used in the simulations, which was optimised by refining the mesh until a simulation of a PBS bead produced a negligible differential signal as described below. Meshing is a balance between simulation speed and accuracy: a coarse mesh consisting of a small number of large elements will be quick to simulate but will not be as accurate compared with a finer mesh due to numerical errors. The minimum feature sizes are the electrode edges ($1\mu m$) and the maximum feature size is $50\mu m$.

To ensure the mesh was detailed enough to prevent numerical errors, a PBS sphere is moved stepwise along the central axis through the simulation. A PBS sphere is a sphere with the same conductivity and permittivity as the electrolyte medium. Intuitively, this will not produce a difference in current flowing into the bottom two electrodes. However, any problems in meshing will show as a non-zero differential current. The dashed line in Figure 4.5 shows the differential current signal for a PBS bead for the

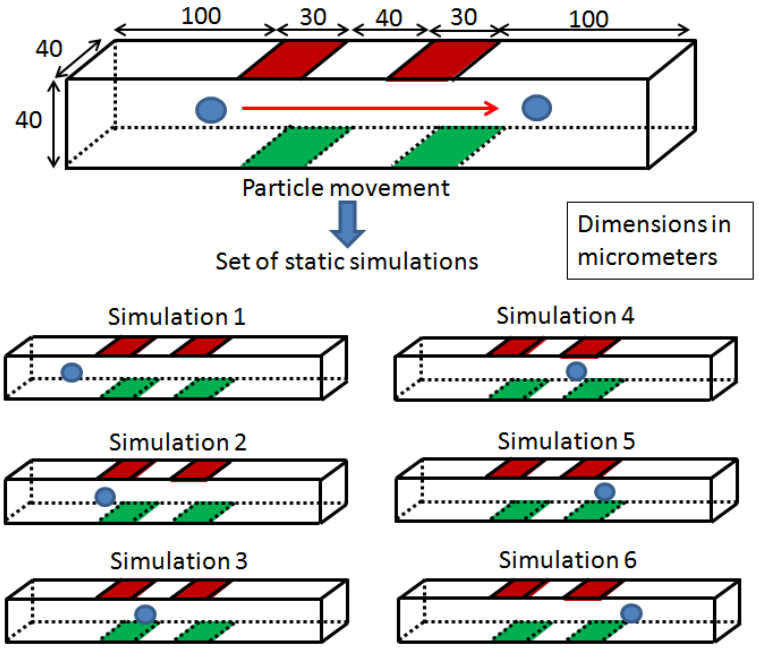

Figure 4.3: To simulate a particle moving through the channel, a set of static simulations is performed, with the particle moved slightly for each new simulation.

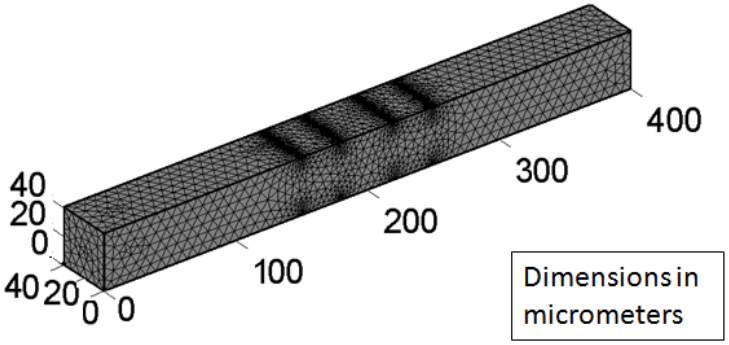

Figure 4.4: Diagram showing the meshing of the simulation geometry. The mesh density is greatest at the electrode edges where the divergence of the electric field is greatest. All distances are in micrometers.

mesh shown in Figure 4.4. Figure 4.5 shows the differential current is zero regardless of position, which is intuitively expected. Also shown is the differential current for a $6\mu m$ polystyrene (insulating) bead. In this case, the differential current produces the expected anti-symmetric double Gaussian signal.

A further validation that the simulation is realistic is to check that there is no net current, i.e. that the total current passing into the top electrodes is the same as the total current passing out of the bottom electrodes. This has been checked and verified to be the case in all the simulations reported in this thesis.

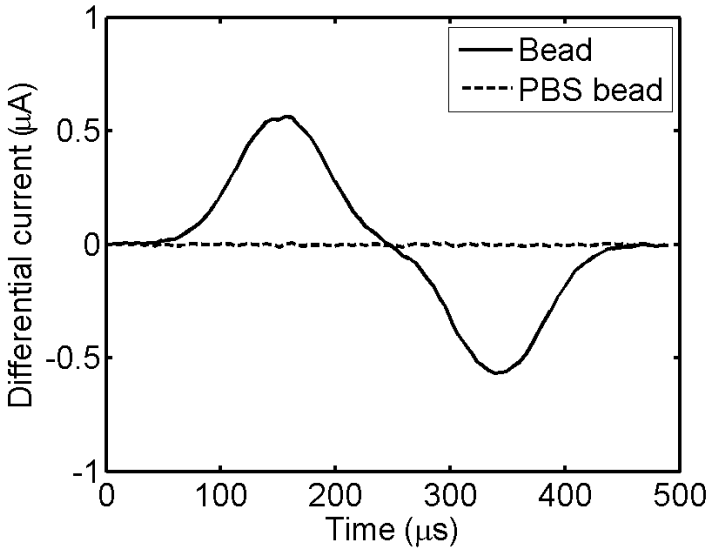

Figure 4.5: Simulation of a PBS bead (same permittivity and conductivity as the medium) passing through the centre of the MIC (dotted line). Also shown is the simulated impedance signal for an insulating bead (solid line) which is an anti-symmetric double Gaussian shape.

4.4 Particle Positional Dependence

In this section, the impedance signal for particles at different positions within the channel are simulated. Intuitively, the electric field strength is greatest at the electrode edges and thus the particle impedance signal should be higher at these positions, but this cannot be calculated using the analytical models previously developed (Sun et al., 2009).

A set of simulations was performed for different sphere (particle) trajectories through the MIC to examine the variation in impedance signal with particle position. The sphere was stepped through the channel in $3\mu m$ steps as depicted in Figure 4.3 to simulate a particle moving through the channel. The centre of the sphere was located either 5, 20 or $15\mu m$ from the bottom (or top) of the channel and 5, 20 or $15\mu m$ from one side of the channel: positions A-I in Figure 4.6. Only one position was simulated at a time. The impedance signals for a sphere in position A, B or C were identical and are shown in Figure 4.7a , likewise for positions D-F in Figure 4.7b and positions G-I in Figure 4.7c. The simulated impedance signal did not change with horizontal (y-axis) position and so the impedance signals for horizontal positions overlap.

The simulated impedance signal for particles moving through the channel equidistant from the top and bottom of electrodes (Figure 4.7b) is the familiar anti-symmetric double Gaussian. The simulations also show that the impedance signal is higher (for the same sized particle) passing close to the top or bottom electrodes. The signal is highest for the particle in positions G-H (for a particle close to the bottom electrodes) compared with close to the top electrodes, positions A-C.

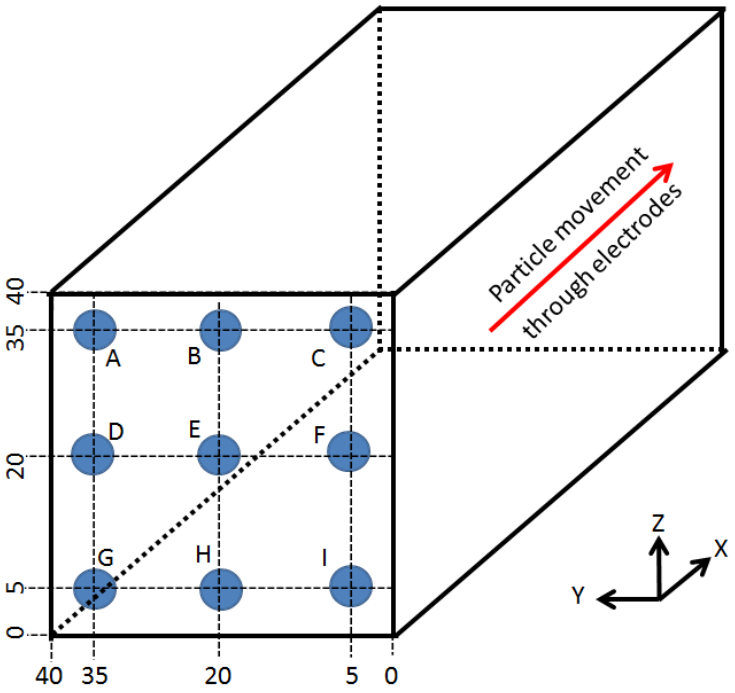

Figure 4.6: Diagram showing the simulated particle positions within the channel used to examine the dependence of the particle position on the impedance signal. Dimensions in micrometers.

This result is unexpected and counter-intuitive because the electrode geometry is symmetric. It can be explained by considering the current paths (a-d) shown in Figure 4.8. A voltage is applied to the top electrodes (1 and 3) and the difference in current flowing into the bottom electrodes (2 and 4) is measured.

The differential current I_{diff} is given by Equation 4.9

$$I_{diff} = d + c - (a + b) \tag{4.9}$$

When there is no particle between the electrodes, Figure 4.8(i), $a = d$ and $b = c$, and thus there is no differential current ($I_{diff} = 0$). If a bead is placed equidistant from electrodes 1 and 2 as shown in Figure 4.8(ii), the bead will block some of the current a and thus $d > a$. The bead will also block some of the currents b and c, but by the same amount in both cases. In this case the differential current is given by Equation 4.10.

$$\begin{aligned} b' &= c' \\ d' &> a' \\ I_{diff} &= d' - a' \end{aligned} \tag{4.10}$$

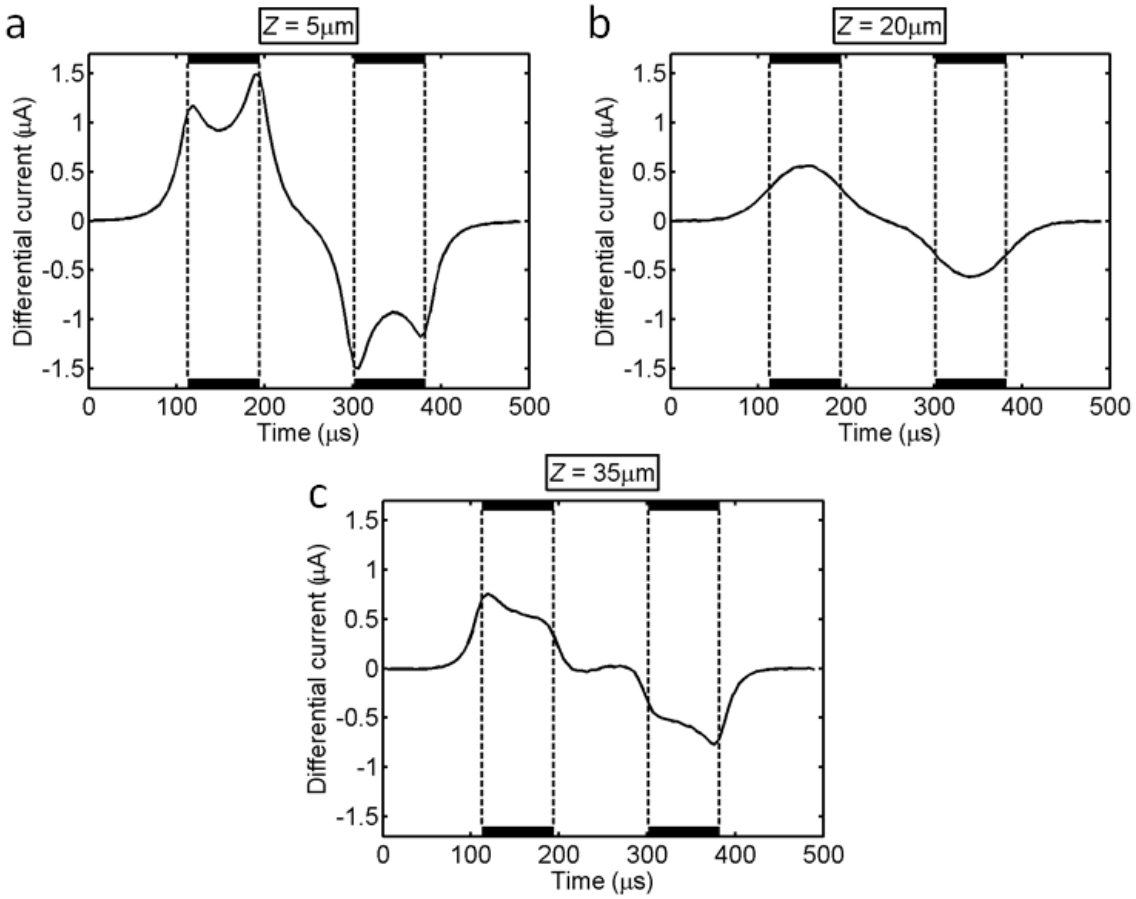

Figure 4.7: Simulated impedance signal for a particle passing (a) $5\mu m$ from the channel bottom, (b) through the channel centre and (c) $5\mu m$ from the top of the channel.

Now, consider a bead close to the bottom electrode as shown in Figure 4.8(iii). Similar to case (ii), the bead will block the current a and thus $d > a$. The bead will also block the cross current b, but not c. The difference in cross currents can be defined as δI, Equation 4.11.

$$\delta I \quad = \quad c - b \tag{4.11}$$

Then in case (iii) $c'' > b''$ and thus $\delta I'' > 0$. The differential current is given by Equation 4.12.

$$I_{diff} \quad = \quad d'' - a'' + \delta I'' \text{ with } (\delta I'' > 0) \tag{4.12}$$

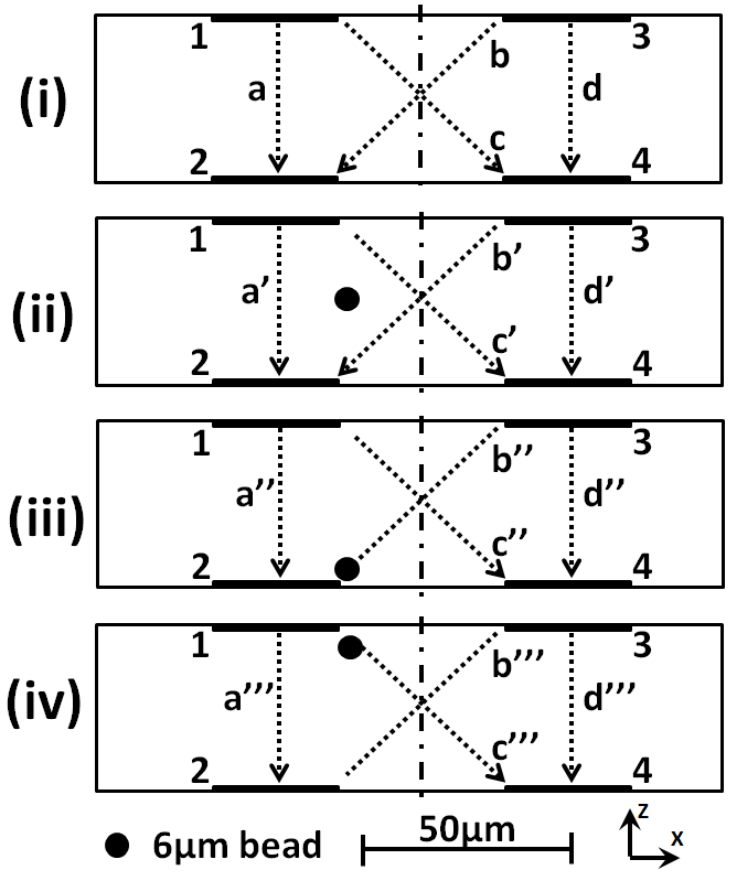

Figure 4.8: Diagram showing the current paths flowing between electrodes. A voltage is applied to the top electrodes and the bottom electrodes are connected to transimpedance amplifiers (virtual ground).

In the case of a bead near the top electrode (shown in Figure 4.8iv), $b > c$ and thus $\delta I''' < 0$. The differential current is given in Equation 4.13.

$$I_{diff} = d''' - a''' + \delta I''' \text{ with } (\delta I''' < 0) \tag{4.13}$$

This example is a simplified case, shown to illustrate the cause of the asymmetry in impedance signal with particle height in the channel. In the real device, the gradient in the electric field is greater close to the electrode edges, meaning a bead will block more current if it is close to the top or bottom electrodes ($a = a > a$). Also, the amount of cross current which is blocked will vary with particle position along the channel, which results in the double-peak signals shown in the simulations in Figure 4.7a and c. The sum of the currents flowing into all electrodes will always be zero and the differential signal will always be symmetric (in magnitude) about a centreline equidistant between the two pairs of electrodes.

4.5 Full Model

The FEM model is now extended to a large number of particles and combined with a calculated flow profile. The extended model is used to calculate the expected impedance-velocity plot for a random distribution of $6\mu m$ diameter particles passing through a channel to simulate a real experiment. This extended model was developed to allow direct comparison of the simulation results with the experimental data of Section 4.6.

To build a density plot from simulations, the impedance and particle signal must be calculated for every point in the channel where a particle can be located. A grid of particle positions (for the centre of each particle) was defined, illustrated in Figure 4.9. The particle position (centre of the particle) is limited by the size of the particle: the centre of a $6\mu m$ diameter particle cannot be closer than $3\mu m$ to the edge of the channel. For a $22 \times 52\mu m$ channel (as used in the experimental data of Section 4.6) the grid of possible particle locations was defined from 4 to $18\mu m$ vertically and 4 to $48\mu m$ horizontally, which leaves a $1\mu m$ gap from the channel wall to the edge of the particle. The $1\mu m$ gap was chosen because simulating a particle very close to the electrode edge will result in numerical errors due to meshing difficulty. In practice, in experiments the particles will be pushed away from the wall due to the wall lift force which is described later. The grid spacing is $0.1\mu m$ in each direction (not all grid points are shown in Figure 4.9). The spacing was considered sufficiently refined to enable comparisons between experimental and simulated data.

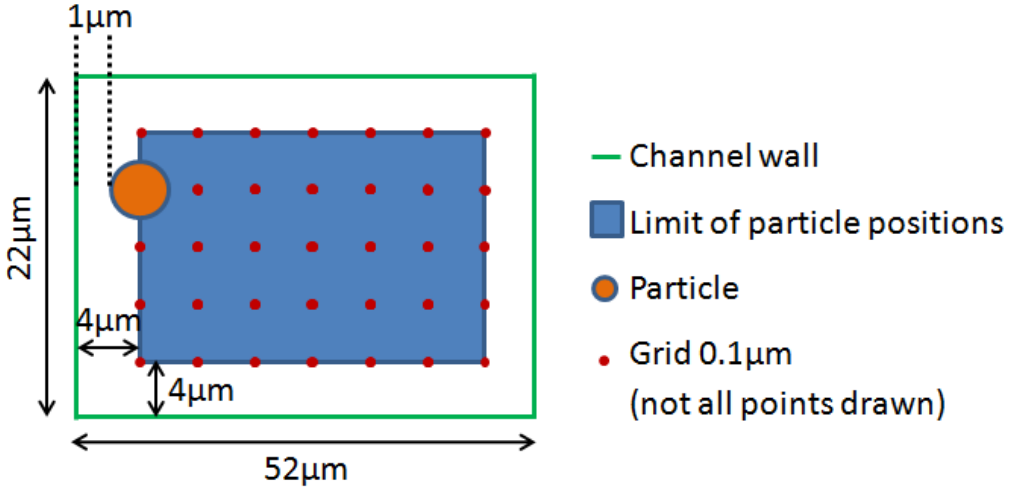

Figure 4.9: Illustration of the grid setup used to generate the simulated particle impedance-velocity plot. The distance of the particle centre to channel edge cannot be less than $4\mu m$. The particle impedance and velocity is calculated for each grid position. The grid spacing is small ($0.1\mu m$) and for clarity not all grid points are shown.

The particle impedance signal is dependent on the particle's vertical height in the channel, but not the horizontal position. This means that the particle impedance signal can be simulated for different particle heights in the channel, and the impedance for side-to-side variation can be inferred thus reducing computation time. A set of FEM simulations was performed for a $6\mu m$ sphere passing at different heights within the channel. The simulations were performed for the exact channel dimensions of the experimental chip ($52\mu m$ wide, $22\mu m$ high). Sphere height in the channel (sphere centre to channel bottom) was varied from $4\mu m$ ($1\mu m$ from sphere edge to bottom of the channel) to $15\mu m$ ($1\mu m$ from sphere edge to top of the channel) in $1\mu m$ steps. Figure 4.10 shows the maximum of the simulated impedance signal for each of the simulations (in blue). This data was interpolated using a spline fit to get the impedance signal for $0.1\mu m$ steps (shown in red in Figure 4.10). This interpolation was used to reduce the computation time from weeks for all points on a $0.1\mu m$ grid to days on a $1\mu m$ grid.

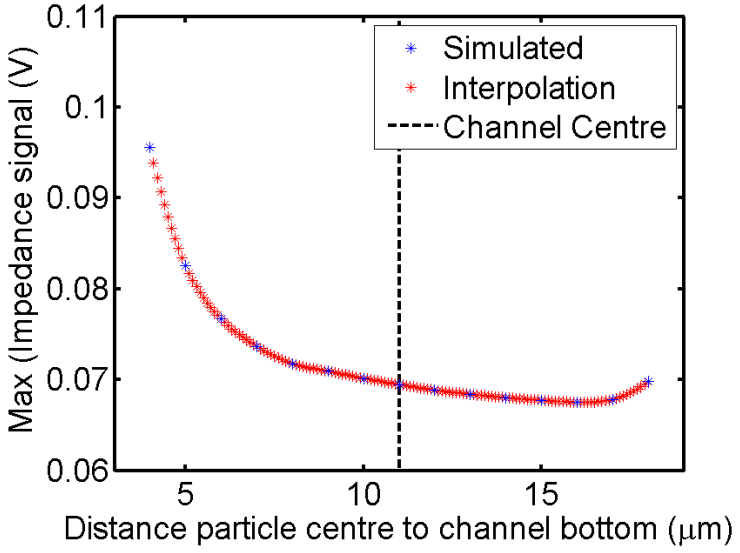

Figure 4.10: Graph of the maximum of the simulated particle impedance signal against particle height in the channel. The blue points are directly from the simulation, the red points are interpolated values to match the $0.1\mu m$ grid spacing.

The data in Figure 4.10 is then replicated for each point in the channel on the $0.1\mu m$ grid to create the density plot shown in Figure 4.11. The white border defines the boundary where a particle is excluded due to its size.

The fluid velocity was calculated using the Navier-Stokes equation (from a script by Thomas et al. (2009)) for each point on the grid for a volumetric flow rate of $10\mu L min^{-1}$, and is shown in Figure 4.12.

Since the fluid is flowing faster in the centre of the channel, it follows that there will be more particles flowing per second through the channel centre. Figure 4.13 is the calculated number of particles passing through the channel per unit time for a total of

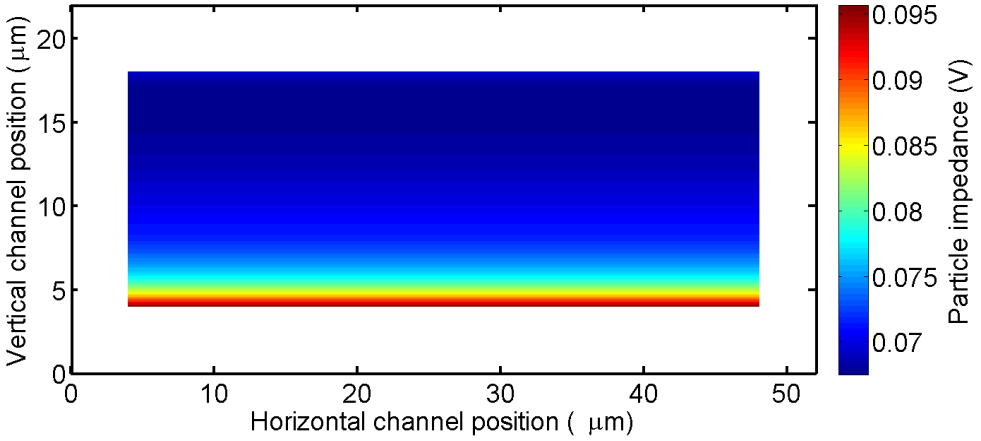

Figure 4.11: Simulated maximum of the particle impedance signal for all the particle positions in the channel.

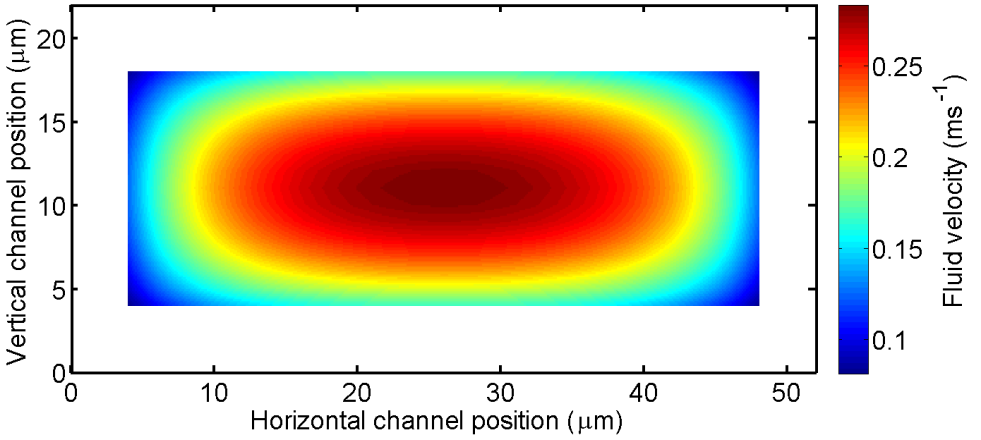

Figure 4.12: Calculated flow profile for the exact channel dimensions at a volumetric flow rate of $10\mu Lmin^{-1}$.

100,000 particles. The figure is similar to the velocity profile, but is quantised because there can only be an integer number of particles.

The simulated density plot of the particle impedance-velocity (Figure 4.14) is the combination of Figure 4.11, Figure 4.12 and Figure 4.13. The manufacturer's CV of the beads used in the experimental data was 3.2% (in volume). This was included in the calculation by generating a normal distribution (of the correct CV) for the simulated impedance signals.

The density plot of Figure 4.14 is a characteristic inverted V shape which can be directly compared with experimental data in the same format (in Section 4.6). Briefly, the plot shows that most of the simulated particles have the maximum velocity ($0.28ms^{-1}$, point a on the graph) and thus must pass through the centre of the channel. The slower particles move towards one of two positions (b and c). Particles at point c have a much higher impedance and correspond to particles travelling close to the bottom electrodes.

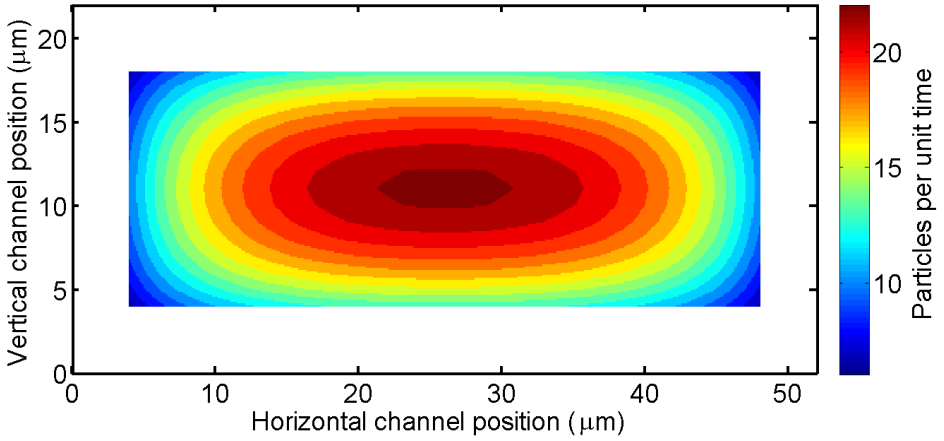

Figure 4.13: Density plot of the expected number of particles passing through each region (on a $0.1\mu m$ grid) for a total of 100,000 particles.

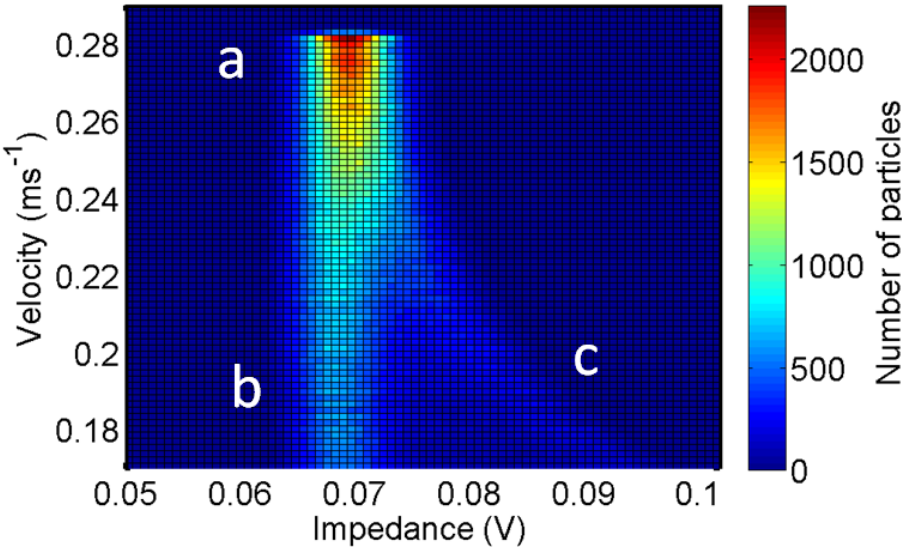

Figure 4.14: Simulated density plot of the impedance and velocity for 100,000 particles for the exact channel dimensions used in the experimental data at a flow rate of $10\mu L min^{-1}$, but excluding any inertial focusing effects.

Particles at point b have a similar impedance to those in the centre of the channel (point b) and correspond to particles travelling close to the top electrodes. In summary, a full numerical model of the MIC chip has been developed. In the next section, experimental data is reported and compared with this model.

4.6 Experimental Results

This section describes the procedure for collecting the experimental data. The nominal channel dimensions were $40\mu m \times 40\mu m$ in cross-section. However these dimensions varied

with manufacturing parameters, specifically the bonding parameters which usually squashed the channels, producing shallower but wider channels. The dimensions of individual chips were measured with a microscope and the chip selected for this set of experiments had a channel width of $52\mu m$ and a height of $22\mu m$. The electrode widths ($30\mu m$) and spacing ($40\mu m$ edge to edge) were defined by the lithography process and were thus accurate. Polystyrene beads with a $6\mu m$ diameter were diluted to a concentration of 1000 beads per microlitre in PBS containing 0.1% Tween 20 (v/v) and 7% sucrose (w/v). Tween 20 is a surfactant, used to prevent the beads sticking together. The addition of 7% sucrose increases the density of the medium to $1.05gmL^{-1}$ (the same as the polystyrene beads) to prevent the beads sedimenting. The bead suspension was loaded into a $1mL$ syringe and pushed through the MIC using a syringe pump at a flow rate of either 10 or $40\mu Lmin^{-1}$ (see later). The impedance of the beads was measured using a custom made front end amplifier (Philips) and a digital impedance amplifier (Zurich instruments). A signal of $4Vpp$ at $1MHz$ was applied to the top two electrodes and the differential current across the bottom two electrodes was sampled at $230kSas^{-1}$ as the impedance signal.

As each bead passes through the electrodes, the impedance is calculated as the magnitude of the maximum impedance signal (Equation 4.14) as shown in Figure 4.15. The velocity of the particle is determined from the particle transit time, which is the time between the maximum and minimum of the impedance signal, Equation 4.15. The distance between the centre of the first and second electrode pairs is $70\mu m$.

$$\text{Particle impedance} = (V2 - V1)/2. \tag{4.14}$$

$$\text{Particle velocity} = \frac{70\mu m}{(T2 - T1)} \tag{4.15}$$

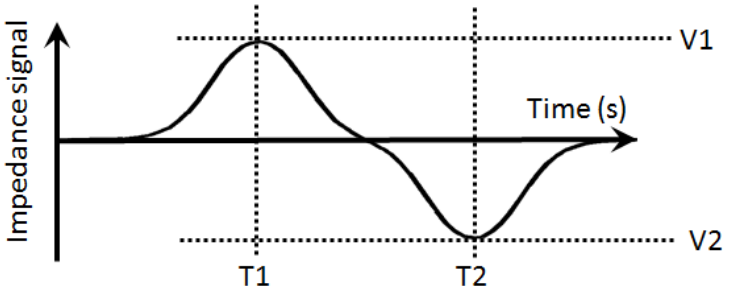

Figure 4.15: Illustration showing the signal processing. The particle impedance is taken to be the magnitude of the peak. The particle transit time is the time between the maximum and minimum impedance signal ($T2 - T1$).

Figure 4.16 is an impedance scatter plot for $6\mu m$ diameter beads passing through the device, for 20,000 events, measured at a flow rate of $10\mu Lmin^{-1}$ at $1MHz$, $4Vpp$. Particles travelling through the centre of the channel have the highest velocity (approximately $0.27ms^{-1}$) and are marked as a on Figure 4.16. In this position the particles have the smallest impedance signal ($0.65V$). Slower particles (travelling closer to the side walls) form two populations, one with an impedance signal similar to the fastest particles (point b), and one with a higher impedance signal (point c).

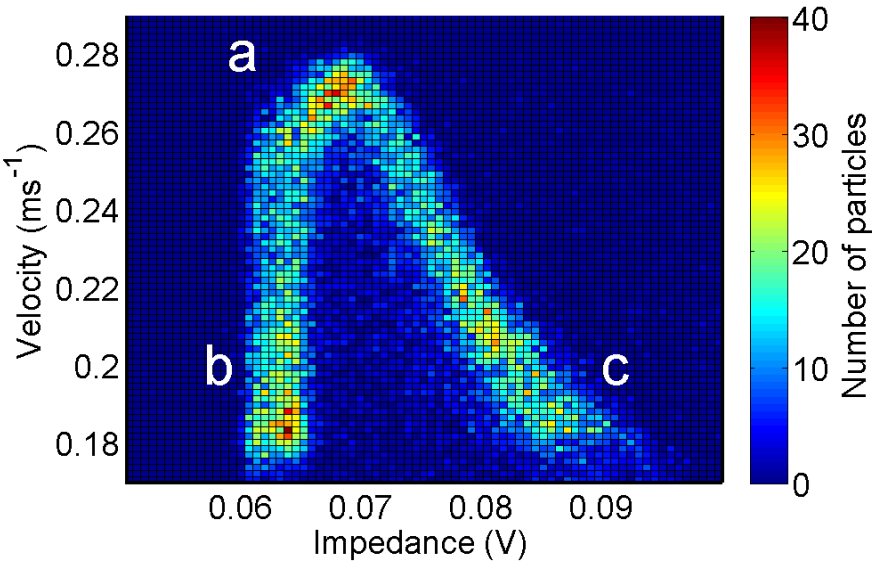

Figure 4.16: Density plot showing the impedance and velocity of 20,000 $6\mu m$ beads measured at a flow rate of $10\mu Lmin^{-1}$.

The simulations described in Section 4.4 (Figure 4.7) show that the highest impedance signal is from a particle passing close to the bottom of the channel and so the events in position c (Figure 4.16) correspond to beads passing close to the bottom of the channel. Position b is due to particles passing close to the top electrodes, which have a similar impedance to particles passing through the channel centre. The number of particles in arm b is similar to the number in arm c (49% to 51%) This is as expected since there should be an equal number of particles travelling in the upper and lower half of the channel because the particles are neutrally buoyant. When the volumetric flow rate is increased by a factor of four to $40\mu Lmin^{-1}$, the particles undergo inertial focusing and significant changes in the density plot (Figure 4.17) are observed. As described in Chapter 3, inertial focusing is the movement of particles across the streamlines to preferential positions within the channel, four for a square channel and two for a rectangular channel. Each preferential position is a distance 0.6 times the distance from the centre to the channel wall. In the device used in these experiments, the channel is rectangular and two preferential positions are expected.

In the density plot (Figure 4.17), two populations are observed (labelled d and e), each with a velocity around $0.8ms^{-1}$. These correspond to inertially focused beads

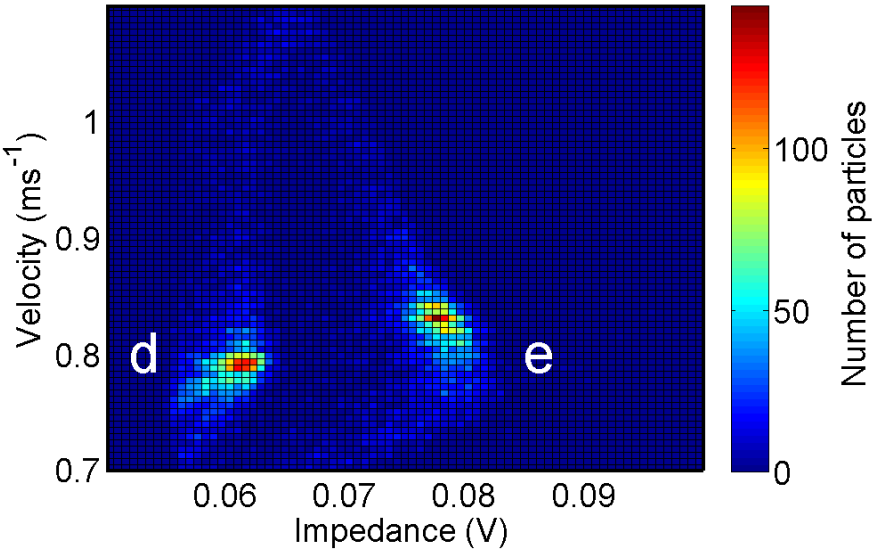

Figure 4.17: Density plot showing the impedance and velocity of 20,000 $6\mu m$ beads measured at a flow rate of $40\mu L min^{-1}$.

passing close to the top (d) and bottom (e) of the channel. The density plot shows an apparent small difference in the velocity of the two particles ($0.79ms^{-1}$ in position d and $0.83ms^{-1}$ in position e). The particles are travelling at the same velocity, and the discrepancy is because the impedance signal for off-centre particles is no longer Gaussian as shown in Figure 4.18. The transit time is calculated as the time between the maximum impedance (peak) and minimum (trough) signals. In the velocity calculation it is assumed that the impedance signal is Gaussian, and the centre of the peak and trough occurs when the particle is in the centre of the electrodes. This is not the case when the particle is off-centre and results in a slight error in the calculated particle velocity. In Figure 4.18a, the estimated transit time is overestimated because the peak and trough of the impedance signal occur towards the outer edges of the electrodes. In Figure 4.18b, the estimated transit time is underestimated because the peak and trough of the impedance signal occur towards the inner edges of the electrodes. This results in an error in the particle velocity because the calculation assumes the transit time occurs over a distance of $70\mu m$ (centre to centre of each electrode pair).

The velocity profile for the exact channel dimensions was calculated using the Navier-Stokes equation (Thomas et al., 2009) and is shown in Figure 4.19. The figure also shows two circles, $6\mu m$ in diameter, corresponding to a $6\mu m$ bead. The positions of the circles are the two preferential positions for inertially focused particles (particle centre at 0.6 times the distance from the channel centre to channel edge). The calculated velocity of the fluid at the centre of these two positions is approximately $0.8ms^{-1}$, matching the velocity of the $6\mu m$ beads in the experimental data.

The volumetric flow rate (Q) required to initiate inertial particle focusing depends on

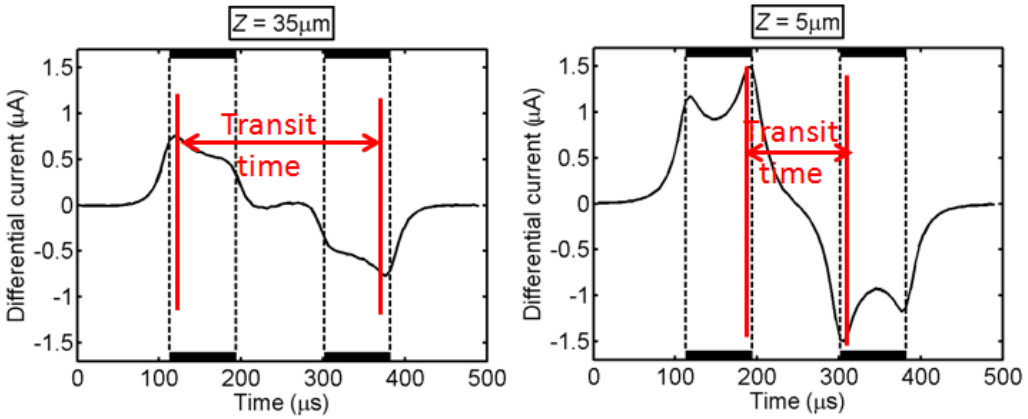

Figure 4.18: The velocity of the beads in the experimental data is estimated from the transit time, the time between the maximum and minimum of the impedance signal. When particles travel through the centre of the MIC, the impedance signal is an anti-symmetric Gaussian and the transit time is the time between the bead passing through the centre of the first and second electrode pairs. For off-centre particles secondary peaks occur which alter the transit time.

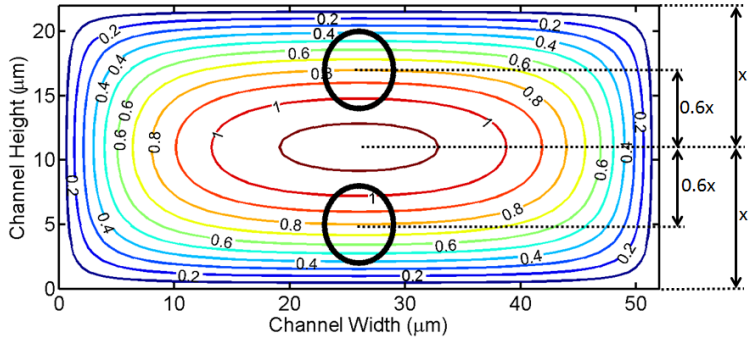

Figure 4.19: Velocity profile at a flow rate of $40\mu L min^{-1}$ for the exact channel dimensions calculated using the Navier-Stokes equation. The two circles are $6\mu m$ in diameter and correspond to the preferential positions for inertially focused particles in a rectangular channel.

a number of parameters including the particle size and channel length, Equation 4.16 (Di Carlo, 2009).

$$Q = \frac{2\pi\mu W H^3}{3\eta L a^2 f_L} \tag{4.16}$$

where μ and η are the density and viscosity of the suspending fluid (PBS), W, H and L are the channel width, height and length, a is the particle diameter and f_L is a factor that varies between 0.2 and 0.5 depending on the channel aspect ratio (from square to rectangular respectively).

In the MIC used in this experiment, focusing occurs in a wide channel ($300\mu m$ wide, $22\mu m$ high and $3.4mm$ long) before the fluid enters the narrower measurement region containing the electrodes. The volumetric flow rate required to achieve inertial focusing with this geometry is given by Equation 4.17.

$$\begin{aligned} Q &= \frac{2 \times \pi \times 0.0012 \times 300 \times 10^{-6} \times (22 \times 10^{-6})^3}{3 \times 1050 \times 3.4 \times 10^{-3} \times (6 \times 10^{-6})^2 \times 0.05} \\ &= 1.25 \times 10^{-9} m^3 s^{-1} \\ &= 75 \mu L min^{-1} \end{aligned} \tag{4.17}$$

Thus, for this experimental system, the predicted volumetric flow rate required to achieve complete focusing is nearly twice the flow rate of the data in Figure 4.17. This means partial focusing is observed at $40\mu Lmin^{-1}$. In the plot of Figure 4.17, there is a low density of particles with velocities greater than $0.8ms^{-1}$ indicating incomplete focusing. Due to the limited sample rate of the electronics ($230ksps$) higher flow rates could not be measured and complete focusing could not be demonstrated.

4.7 Comparing Simulated and Experimental Data

Comparing the scatterplots of the experimental data (Figure 4.16 and Figure 4.17), the simulated scatterplot of Figure 4.14 is similar in shape, but the number density of particles is different. The shape of both the simulated and experimental density plots follows the same inverted V shape. The shape and position of the two arms is similar between experimental and simulated data. This demonstrates the position dependent impedance is correctly calculated by the simulation.

The difference between the simulated and experimental density plots is the number of particles at each position in the V. This is because the simulation does not include inertial focusing effects which are present in the experimental data. Simulating inertial focusing requires computational fluid dynamics, requiring supercomputers and is beyond the scope of this work.

In the simulated impedance-velocity density plot of Figure 4.14 the majority of the particles pass through the centre of the channel each with a similar impedance of approximately $0.65V$ and a velocity of $0.28ms^{-1}$, marked as point a. Slower particles tend towards either point b or point c. Point b has a similar impedance to the fastest particles ($0.07V$), while the second population has a much higher impedance (reaching $0.09V$). Compared with the two arms in the experimental data, in two arms in the simulated data are not well-defined. This is due to inertial focusing that occurs in the

wider inlet channel ($300 \times 22\mu m$) leading up to the measurement channel that occurs in practice but is not modelled in the simulations.

Inertial focusing cannot be included in the simulation on a particle by particle basis. However, the overall effect can be included in the simulation. This is performed by excluding particles from the central region of the channel as shown in Figure 4.20. This region was chosen because inertial focusing is stronger in the vertical direction in shallow rectangular channels. After removing particles from the central region, the simulated density plot of Figure 4.14 changes to the plot in Figure 4.21. This new simulated density plot is similar to the two arms of the experimental data of Figure 4.16. The numbers of particles in each arm is approximately equal (ratio = 55% to 45%), which agrees more closely with the experimental data where the ratio is 49% to 51%.

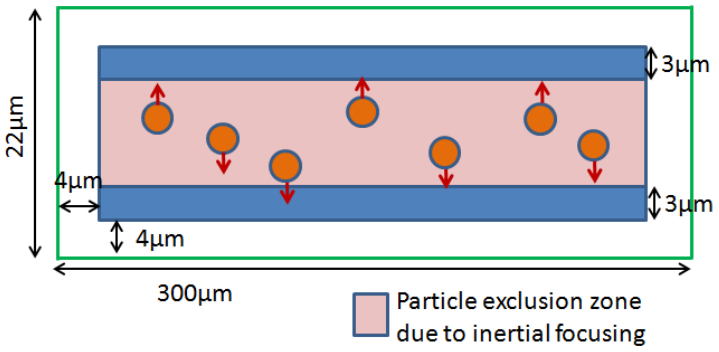

Figure 4.20: In the experimental MIC, the particles flow through a wide channel where particles migrate away from the centre of the channel (inertial focusing) before entering the measurement region. To simulate this effect, a particle exclusion zone in the centre of the channel is defined.

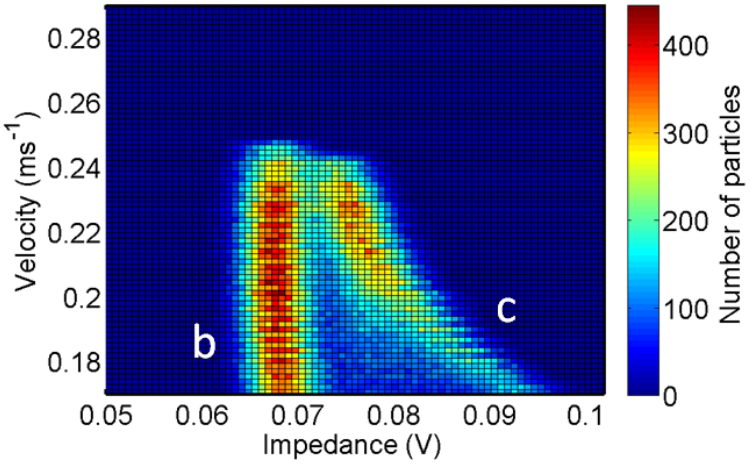

Figure 4.21: Simulated density plot of the impedance and velocity for the exact channel dimensions used in the experimental data at a flow rate of $10\mu Lmin^{-1}$, but excluding particles from the centre of the channel as shown in Figure 4.20. There is an approximately equal number of particles in each of the two arms labelled b and c (55% to 45%).

4.8 Summary

A complete 3D numerical model has been developed for the MIC chips. The model has been validated against analytical solutions and compared with experimental data (of polystyrene beads). Modelling the impedance signal along the trajectory of particles through the measurement cell has shown that the impedance signal of a particle passing closer to the bottom of the channel is higher when compared with a particle passing close to the top of the channel. Using circuit modelling, this was attributed to distortion of the electric field as the particle passes through the channel.

This asymmetric effect in the impedance signal was combined with simulated fluidic flow profiles of the channel to generate a complete model which could be directly compared with experimental data. The simulated density plots show similar trends to the experimental data in that the particles tend to group into three population groups within the measurement cell due to the flow profile within the channel. However, there were significant differences observed in the proportion of the particles in each group. This was attributed to inertial focusing in the wider channel upstream of the measurement cells, an effect which is not modelled in the FEM simulations.

The model developed in this chapter is used in the next chapter to develop new electrode geometries that reduce the particle positional dependence of the particle impedance signal.

Chapter 5

Electrode Geometry Optimisation

5.1 Introduction

The previous chapter demonstrated that the measured impedance of particles depends on the particle position within the detection region. A particle travelling close to the top or bottom electrodes has a higher measured impedance compared with the same sized particle travelling through the centre of the channel. This is a system error which limits the measurement accuracy of the system. The problem could be addressed by ensuring all particles travel through the centre of the measurement region, for example using sheath flow. However this would add complexity to the device hardware. A review of particle focusing methods including limitations of each technology can be found in Chapter 2. This chapter discusses new electrode geometry configurations and signal processing algorithms that have been developed to increase the measurement accuracy of the system without increasing the complexity of the device hardware.

5.2 Electrode Pair Spacing

The particle positional dependence is caused by current crossing between the two electrode pairs. The distance between the electrode pairs can be increased to reduce this current and this was investigated using FEM simulations, similar to those described in the previous chapter. Figure 5.1 is a diagram of the parametrised model used for the simulation. The fluidic channel is modelled by a $40 \times 40 \times 400\mu m$ box. Rectangular surfaces ($30 \times 40\mu m$) on the top and bottom of the box model the electrodes. A $10\mu m$ diameter sphere is defined within the box to model a polystyrene bead. Initially the separation between the two pairs of electrodes (ES) was set to $40\mu m$. The distance between the bottom of the channel to the sphere centre (SH, sphere height) was first set to $20\mu m$ (sphere equidistant from the top and bottom of the channel).

The sphere x-position (SX: from one end of the channel to the centre of the sphere) was varied from 80 μm to 320μm in 3μm steps. For each sphere position, an electric current simulation was performed and the differential current passing through the bottom two electrodes (3 and 4) was recorded. These simulations were repeated for different sphere heights within the channel (SH = 6, 13, 20, 27 and 34μm) to represent spheres passing closer to the bottom (SH=6, 13) or top (SH=27, 34) electrodes. The simulated differential current for the different sphere positions is shown in Figure 5.2a. Figure 5.2b and Figure 5.2c are plots of the simulated differential current for a wider spacing between the two electrode pairs (ES = 80 and 120μm). The maximum differential current for each sphere height (SH) from Figure 5.2a-c are plotted in Figure 5.2d.

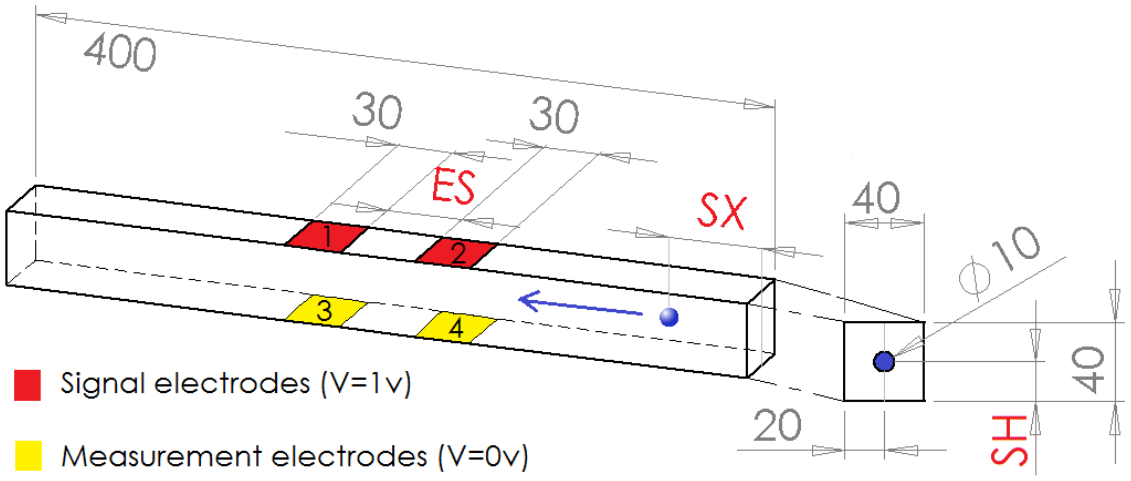

Figure 5.1: Diagram showing the dimensions of the simulation model used to investigate the effect of electrode separation width on particle positional dependence. All measurements are in μm. Electrodes on the top and bottom of the channel are set to $1V$ and $0V$ respectively. The electrode separation (ES) was set to either 40, 80 or 120μm. The sphere height (SH) in the channel (centre of sphere to bottom of channel) was set to either 6, 13, 20 27 or 34μm. The sphere distance along the channel (SX) was varied in 3μm steps from 80 to 320μm.

As expected, Figure 5.2a-c show that the magnitude of the differential current signal for each electrode spacing is symmetric about x=200μm which corresponds to the midpoint between the two pairs of electrode. Figure 5.2d demonstrates that, in the case of a sphere travelling close to the bottom of the channel (SH= 6μm), increasing the electrode separation distance (ES) decreases the maximum differential current and reduces the particle positional dependence.

With a 40μm electrode spacing, the simulated differential current of a 10μm diameter sphere travelling close to the bottom electrode (SH= 6μm) is 128% higher than that of the same sphere travelling through the centre of the device (SH=20μm). This implies that a 10.0μm diameter sphere travelling close the bottom of the channel would be measured as a 13.1μm sphere. The same calculation for a wider electrode spacing (ES

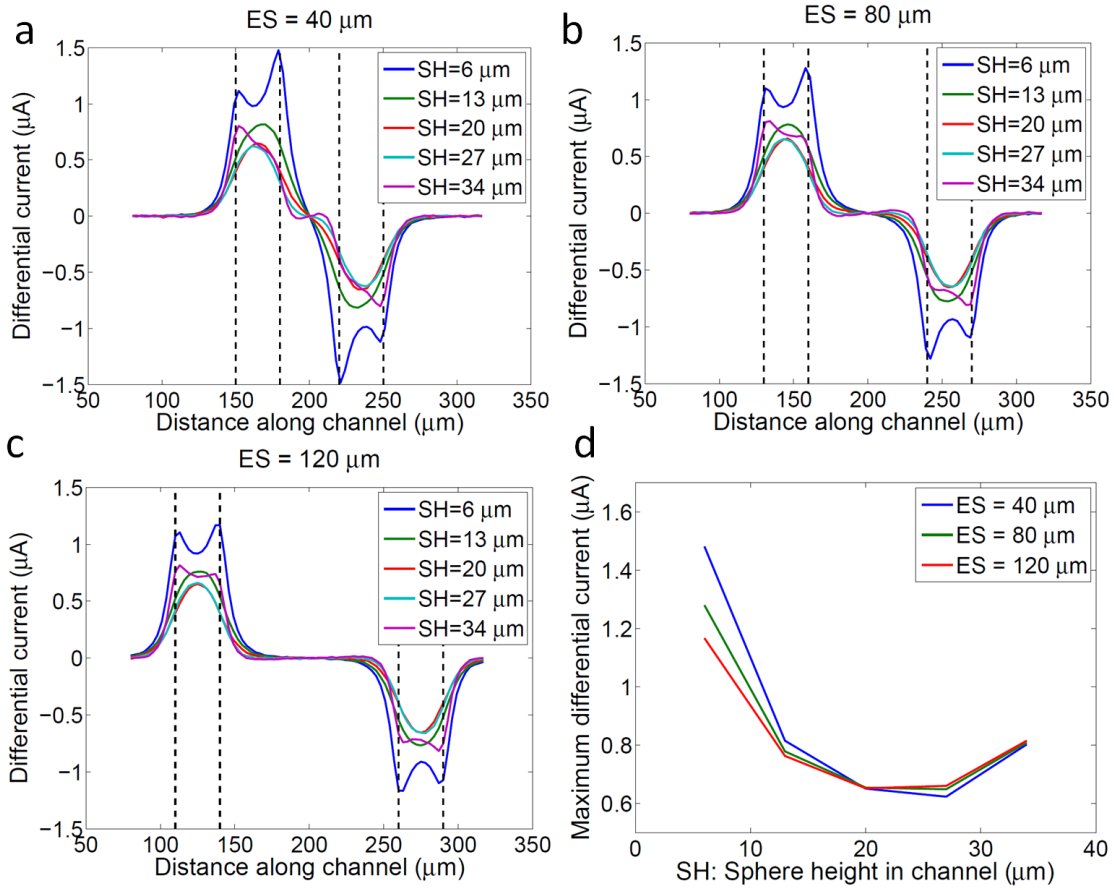

Figure 5.2: Electric current simulation for a $10\mu m$ sphere moving in a stepwise manner between two pairs of parallel facing electrodes (geometry in Figure 5.1) with spacing between the electrodes pairs (ES) of (a) $40\mu m$, (b) $80\mu m$ and (c) $120\mu m$. The dashed lines indicate the position of the electrodes. For each geometry the differential current was simulated for a sphere passing through the channel at varying heights (SH) within the channel. The maximum differential currents for each sphere height from (a)-(c) is plotted in (d).

= 80 and $120\mu m$) are 96% ($12.5\mu m$) and 79% ($12.1\mu m$) respectively. These numbers are close to the limit for the particle positional dependence: the bottom of the $10\mu m$ diameter sphere (in the position SH = $6\mu m$) is $1\mu m$ above the bottom of the channel. Most particles will not flow this close to the channel walls due to the parabolic flow profile within the channel.

Although increasing the electrode spacing decreases the particle positional dependence, the disadvantage is that the measurement throughput is reduced. Particles must be diluted sufficiently to ensure that only one particle occupies the measurement region. The measurement region for $30\mu m$ wide electrodes separated by a $40\mu m$ gap is $100\mu m$ wide. By increasing the electrode separation from 40 to $80\mu m$, the measurement region width is increased to $140\mu m$. However, to prevent coincidence, the suspension concentration of the particles (and therefore throughput) must be reduced by 40%.

5.3 Ground Electrode Geometry

An alternative electrode design which reduces the particle positional dependence is to place ground electrodes between the pairs of measurement electrodes, as illustrated in Figure 5.3. The geometry in Figure 5.3 was simulated using the same method described in the section 5.2, for varying sphere heights in the channel (SH = 6, 13, 20, 27 and 34μm). To enable direct comparison with the 4 electrode system (Figure 5.1), the simulation was repeated, but with the 6 ground electrodes removed. It should be noted that in this case the electrode pair spacing (ES) is 50μm, compared with 40μm in Figure 5.1.

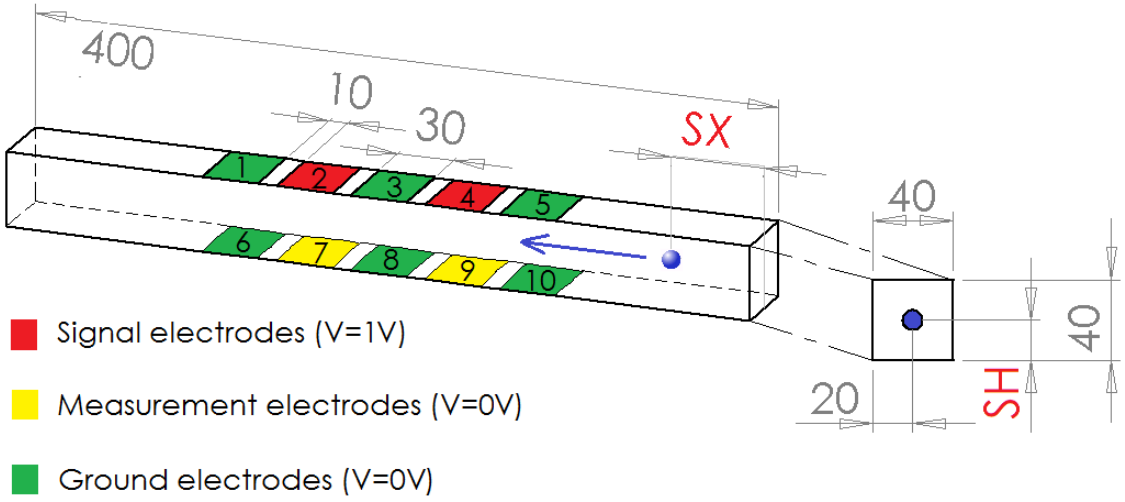

Figure 5.3: Diagram of the geometry of a 10 electrode impedance measurement system designed to reduce the particle positional dependence. All electrodes (numbered 1-10) are 30μm wide and separated by a 10μm gap. SH is the sphere height in the channel (centre of sphere to bottom of channel). SX is the sphere x-position (position along the channel).

The simulated differential current flowing into the measurement electrodes (7 and 9) is plotted in Figure 5.4a without ground electrodes and Figure 5.4b with ground electrodes. Figure 5.4c is the simulated maximum differential current for each of the sphere heights for Figure 5.4a and Figure 5.4b. The figure shows that there is a much smaller variation in the differential current with sphere position for the design with the ground electrodes, thus particle positional dependence is reduced. In Figure 5.4a the simulated differential current of a 10μm diameter sphere travelling at a sphere height of 6μm (close to the bottom electrode) is 116% higher compared with the differential current of the same sphere travelling through the centre of the device (SH=20μm). This means that a 10.0μm bead would be measured as a 12.9μm bead if it passed close to the bottom electrode. The same calculation for the design with ground electrodes is 21%. In this case a 10.0μm bead would measured as a 10.7μm bead if it passed close to the bottom electrode.

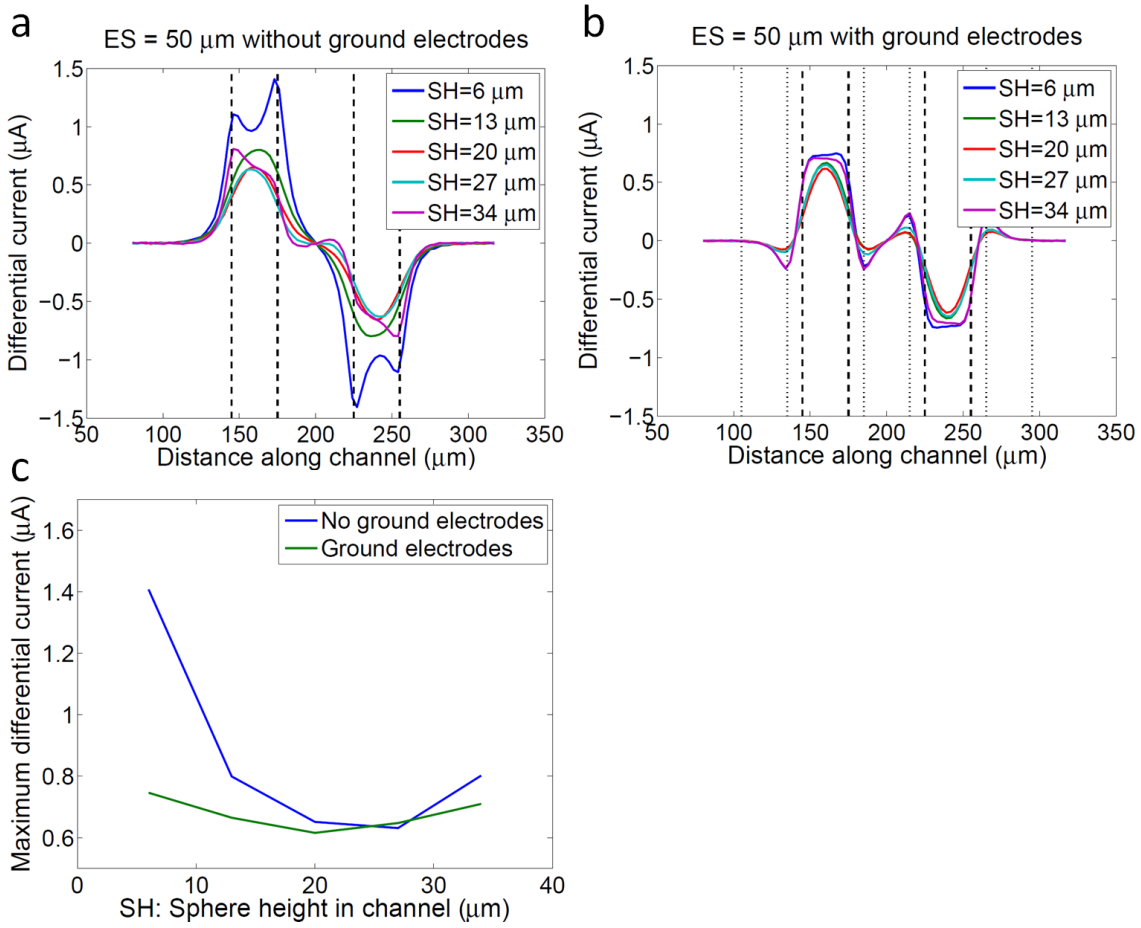

Figure 5.4: Electric current simulation results for a $10\mu m$ sphere moving in a stepwise manner between pairs of parallel facing electrodes for the geometry in Figure 5.3 a) without ground electrodes and b) with ground electrodes. The dashed and dotted lines indicate the position of the measurement and ground electrodes. The differential current is the difference in current flowing into the two measurement electrodes (7 and 9). For each geometry the differential current was simulated for a sphere passing at different heights (SH) through the channel. The maximum of the differential currents for each sphere height from (a)-(b) is plotted in (c).

5.4 Guard Electrode Geometry

The particle positional dependence of a traditional guard electrode system (Figure 5.5) was also investigated using FEM simulations. In a guard electrode system, additional electrodes are included to create a uniform electric field between the measurement electrodes. The simulated differential current flowing into electrodes 7 and 9 (Figure 5.5) for a $10\mu m$ sphere passing through the measurement region at different heights (SH = 6, 13, 20, 27 and $34\mu m$) is plotted in Figure 5.6a. The maximum differential current for each sphere height is shown in Figure 5.6b for the both the guard electrode configuration (Figure 5.3) and ground electrode configuration (Figure 5.5). Although the guard electrode configuration creates a uniform electric field within the channel, the particle

positional dependence for the guard electrode configuration is much higher compared to the ground electrode configuration.

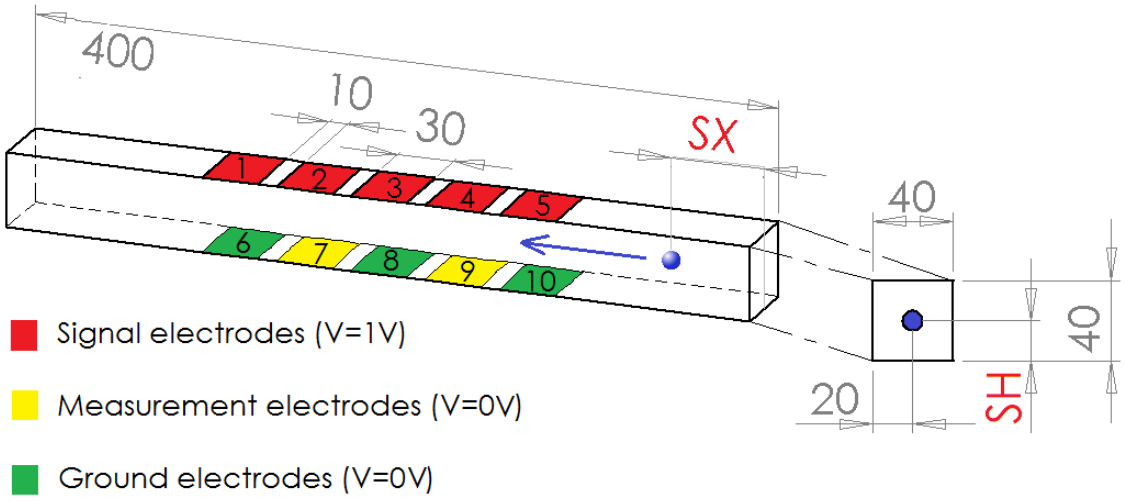

Figure 5.5: Diagram of the geometry of a 10 electrode system configured in a traditional guard electrode system. This configuration produces a uniform electric field between the measurement electrodes.

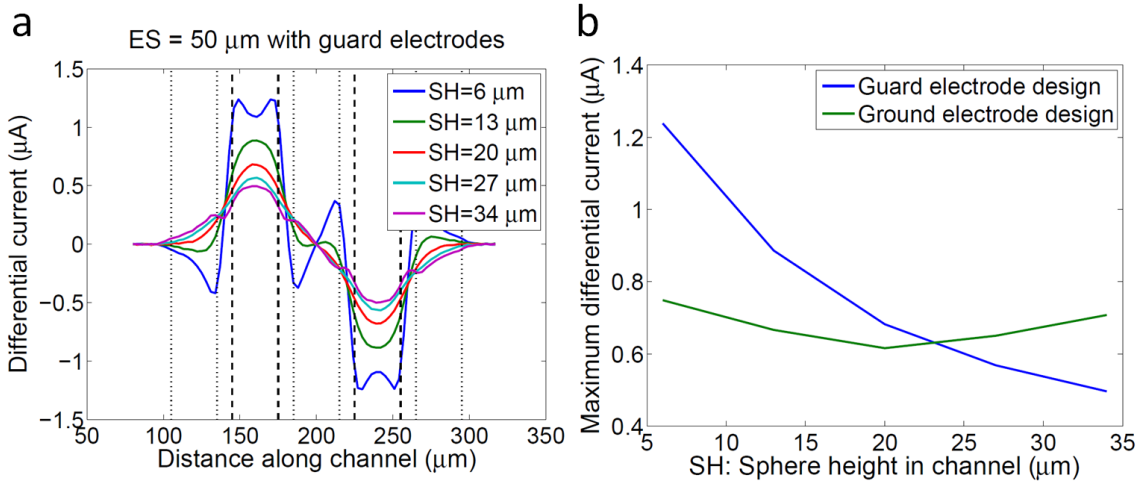

Figure 5.6: a) Electric current simulation results as a 10 μm sphere is moved in a stepwise manner between parallel facing electrodes configured in a traditional guard electrode configuration (Figure 5.5). The differential current was simulated for a sphere passing through the channel at varying heights (SH) within the channel. The maximum of the differential currents for each sphere height (SH) is plotted in b. Also shown in b is the maximum differential current for the ground electrode system (Figure 5.3).

In summary, a new electrode design which significantly reduces the particle positional dependence has been proposed. In the next section, the design is fabricated and experimentally tested.

5.5 Device Fabrication

The design of the 10 electrode impedance measurement system shown in Figure 5.3 was fabricated in a similar method to that described in Chapter 4. The mask was drawn using a commercial software package (Clewin) and is shown in Figure 5.7a; a zoomed section of the mask showing a single chip is in Figure 5.7b. The green layer is the metal mask design which is platinum in the final design. The metallised area around the edge of the channel of each chip is designed to increase the bond strength around the channel. The blue layer is the fluidic layer. Any areas which are not coloured purple in the mask design are SU8 in the manufactured device. The pillars defined in the fluidic layer let air escape during the bond process. After chip fabrication, a drop of epoxy glue (Epotek 302) was put on the edge of each chip. The glue filled the gaps between pillars by capillary force and provided reinforcement for the bond. One hole at each end of the channel was drilled through the top layer of glass using a CO_2 laser (Epilog) for the sample inlet and outlet. A finished chip measuring $15 \times 20mm$ is shown in Figure 5.7c and a microscope image of the centre of a chip is shown in Figure 5.7d.

5.6 Floating Electrodes

The 10 electrode impedance chip (Figure 5.7c) can be wired in a number of different configurations as shown in Figure 5.8. This facilitates direct comparison of different electrode geometries with identical channel dimensions including any imperfection arising from manufacture, for instance a difference in the channel dimensions relative to the mask design, or misalignment between the top and bottom electrodes.

To test a 10 electrode chip in a 4 electrode configuration, the unused electrodes are left floating (Figure 5.8). The voltage of these unused electrodes will equalise to the voltage of the surrounding liquid in the channel. To test that the floating electrodes do not significantly affect the particle impedance signal (i.e. Figure 5.8a produces similar results to Figure 5.1), the electrode geometries in Figure 5.8 were simulated. The simulations were performed using the same method as described in Section 5.2. The floating electrodes were defined to have zero current flowing through them. The electric potential within the channel for the three geometries (Figure 5.8) are shown in Figure 5.9. In Figure 5.9a and Figure 5.9c the voltage of the medium away from the electrodes is approximately $0.5V$. In Figure 5.9b the outer ground electrodes shield the applied voltage from the region distant from the electrodes, thus the medium is set to $0V$.

The simulated differential currents for the three geometries shown in Figure 5.8 are plotted in Figure 5.10. There are a few small differences between the configurations compared in Figure 5.10a (with floating electrodes) and Figure 5.4 (without floating

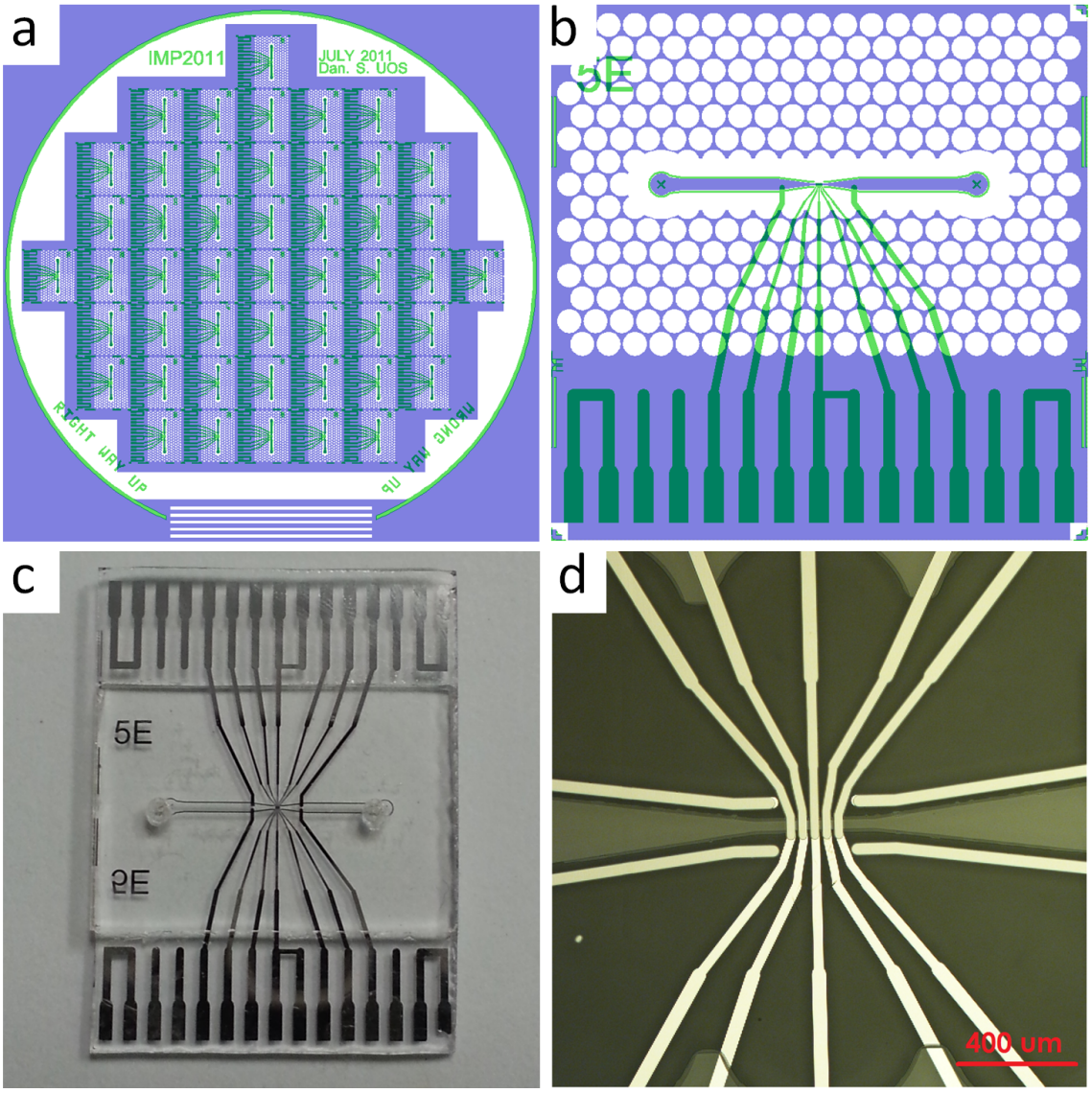

Figure 5.7: a) 6" wafer mask design for 10 electrode impedance chips. b) zoomed image of the mask design showing details of one individual chip. c) photograph of a fabricated chip which measures $15 \times 20mm$ (H×W). d) Microscope image of the measurement region of the chip photographed in c.

electrodes). The first point to notice is the shape of the differential current at x= $200\mu m$ (equidistant from each electrode pair). In Figure 5.10a the differential current is zero for approximately 10 μm either side of x=$200\mu m$, whereas in Figure 5.4a the differential current is zero at x=$200\mu m$ but deviates quickly. Secondly, the maximum positional dependence with the floating electrodes increases to 147 % compared to 116 % without floating electrodes shown in Figure 5.4. Reducing the electrode spacing from $50\mu m$ to $10\mu m$ (Figure 5.10c) further increases the positional dependence to 156 %. Although addition of the floating electrodes slightly increased the positional dependence, the simulations demonstrate that a 10 electrode chip can be configured in a 4 electrode configuration (leaving 6 electrodes floating) and used to directly compare

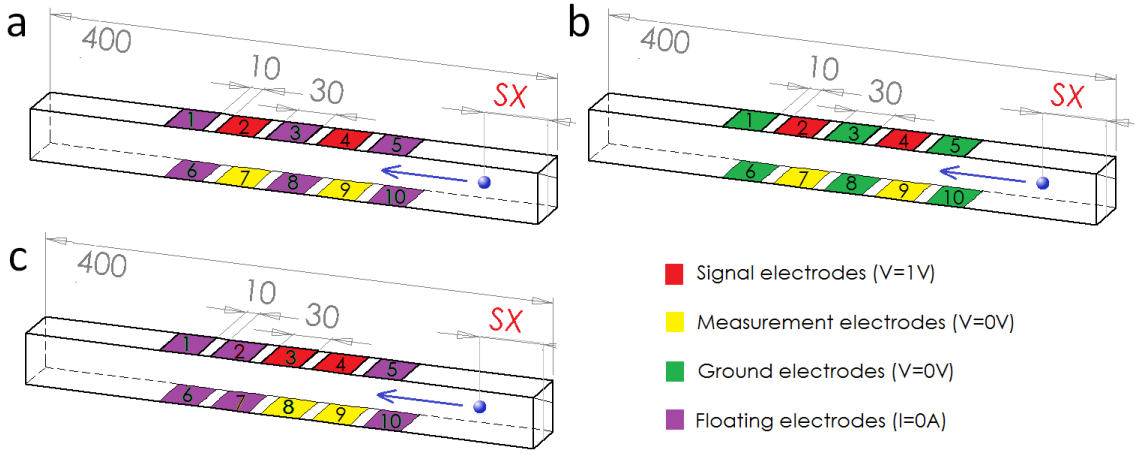

Figure 5.8: Diagram showing different wiring layouts used to compare the positional dependence of different electrode configurations using the impedance chip. All measurements in micrometers. (a) 4 electrode setup with electrode pair spacing (ES) of $50\mu m$ (b) 10 electrode setup with identical electrode pair spacing (c) 4 electrode setup with reduced electrode pair spacing (ES = $10\mu m$).

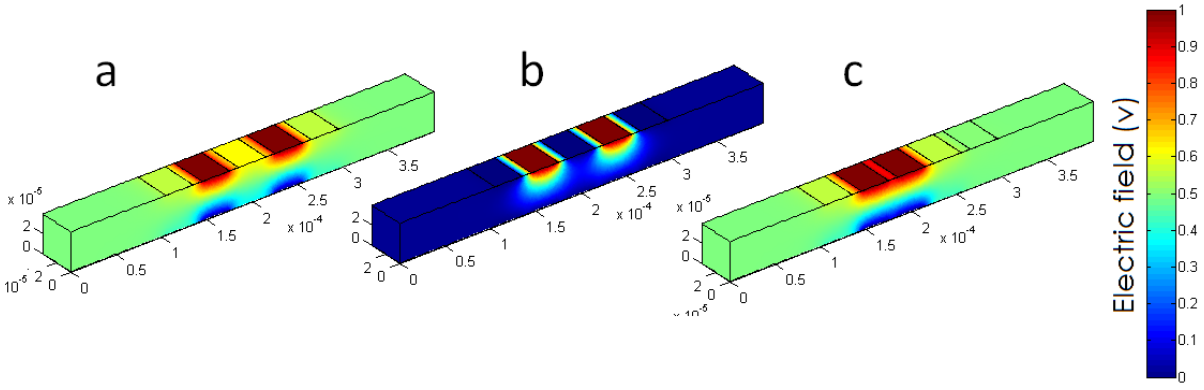

Figure 5.9: Simulated electric field within the channel for a 10 electrode device configured according to the three diagrams in Figure 5.8.

different electrode configurations.

5.7 Experimental Testing

A 10 electrode chip (Figure 5.7c) was tested with a mixture of 3, 4.5, 6 and $10\mu m$ polystyrene beads (Polysciences). The beads were diluted in approximately equal proportion (approximately 1000 beads per microlitre in total) in PBS. The beads were measured at a flow rate of $40\mu l$ min^{-1} for 75 seconds (50,000 total events). The same sample of beads was measured using the same chip for each of the three different electrode configurations shown in Figure 5.8. For each event (corresponding to a single bead passing through the measurement region) the particle impedance was recorded as the maximum of the impedance peak. As described in Chapter 4, the particle velocity

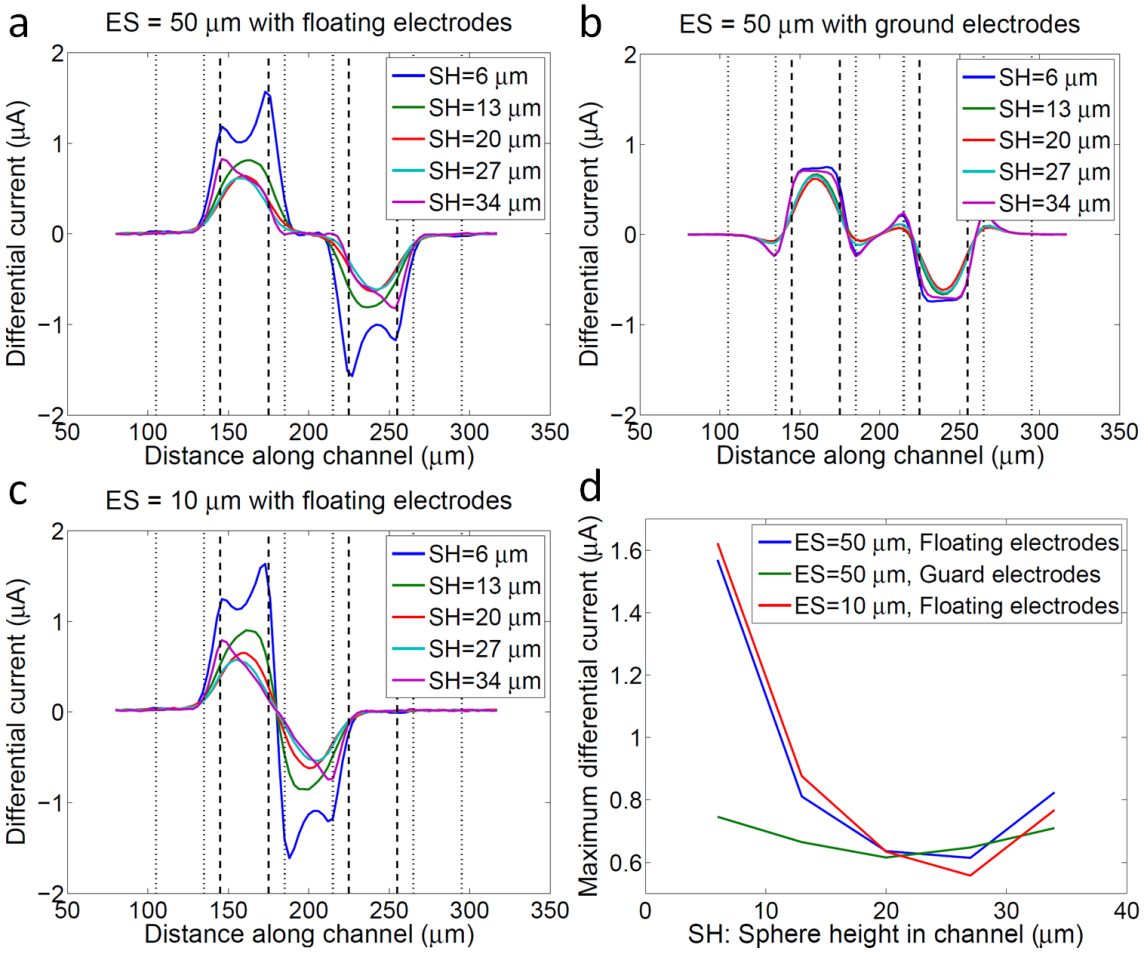

Figure 5.10: Simulated differential current for the electrode geometry shown in Figure 5.8. The dashed lines indicate position of the measurement electrodes and dotted lines are the positions of the ground or floating electrodes.

depends on the flow profile and position within the channel, and is determined from the time difference between the peak and trough in the differential current signal and the electrode spacing. The velocity-impedance profile for the sample measured in each of the electrode configurations is displayed as a density plot in Figure 5.11.

The shape of the velocity-impedance plots are similar to those presented in Chapter 4. Beads passing through the centre of the channel have the fastest velocity and the smallest impedance. Slower particles travel closer to the top or bottom electrodes where the electric field is higher and non-uniform. In Figure 5.11a and Figure 5.11c the impedance for particles travelling close to the bottom electrodes is higher than for particles travelling close to the top electrode, which causes the inverted V-shape. In Figure 5.11b there is a much smaller increase in impedance for slower particles compared with Figure 5.11a and Figure 5.11c which demonstrates that the ground electrode configuration reduces the particle positional dependence. The results show that the majority of the $10\mu m$ diameter beads have a lower velocity compared with the smaller diameter beads. This is due to the inertial focusing effect of the larger beads which tend to migrate away

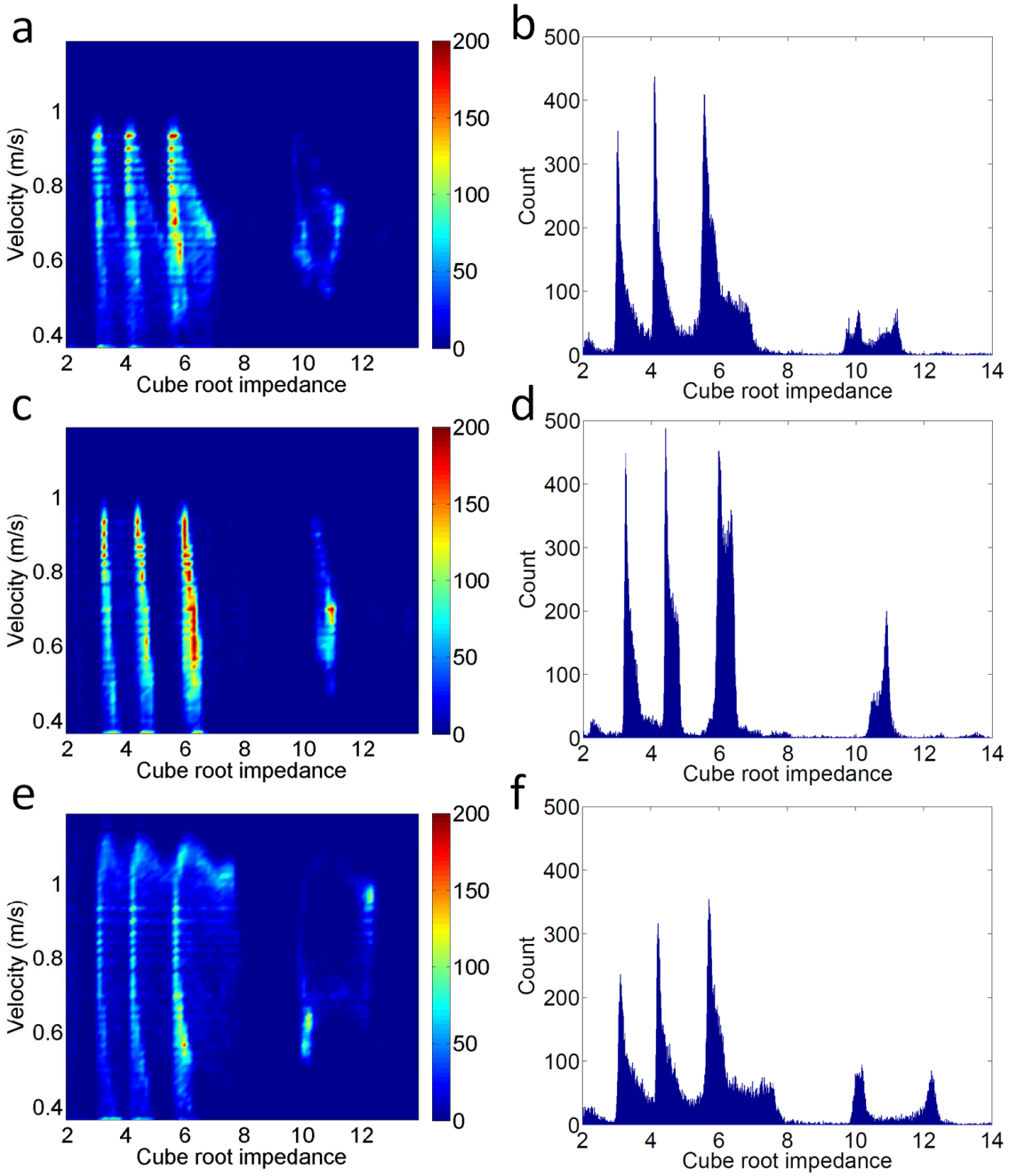

Figure 5.11: Velocity-impedance profile for a sample containing 3, 4.5, 6 and 10μm polystyrene beads. The beads were measured using the 3 different electrode configurations shown in Figure 5.8. Also shown are histograms of the impedance for the 3 data sets.

from the fastest flow in the centre of the channel. The 6μm beads start to migrate to 2 preferential positions. However, they do not form the tight distributions observed for the same 6μm beads described in Chapter 4, measured at the same flow rate. This is because inertial focusing is highly dependent on channel geometry. The channel in the 4 electrode measurement chip used in the previous chapter was shallower (22μm) compared with the new 10 electrode chip used in these experiments which were 30μm

high.

The spread in impedance is difficult to compare quantitatively for different electrode configurations. Ideally the coefficient of variation of each population of beads would be compared with the manufacturer's data. However, the populations do not follow Gaussian distributions and thus a fit cannot be applied. The width of each distribution cannot be compared because some of the populations overlap and the edges between each population cannot be defined. Qualitatively, the histograms in Figure 5.11 show the separation in measured impedance for the mixture of beads is greatest for the ground electrode configuration. This is in agreement with the simulation results (Figure 5.10) which shows that the ground electrode configuration has the lowest particle positional dependence (highest measurement accuracy).

5.8 Signal Processing to Correct for Positional Dependence

The previous section described a new electrode geometry that used ground electrodes to reduce the positional dependence of the measured particle impedance. Although by using ground electrodes the new geometry reduces the simulated maximum positional dependence by 82% (the simulated maximum dependence with and without ground electrodes is 21 % and 116 % respectively) there is still some dependence of the impedance on position. This can be seen in Figure 5.11(b). For each population of beads, the trend is for slower particles to have a slightly higher impedance.

This particle positional dependence can be reduced further by adding a compensation factor for particles travelling close to the top or bottom electrodes. To achieve this, an independent indicator of particle height from the bottom of the channel is required. Particle velocity not only depends on particle height within the channel, but also on particle position side-to-side within the channel and thus cannot be used. In the 10 electrode geometry (Figure 5.3) for particles passing along the channel past the edges of the ground electrodes, secondary peaks appear in the differential current signal, highlighted by the ovals in Figure 5.12. These secondary peaks are larger for particles passing close to the top or bottom electrodes (SH=6, 13, 27 or 34μm). This unique shape for the differential current signal can be used to determine the height of each bead in the channel.

Simulations of the differential current for a 6μm sphere were performed as described in Section 5.2, except the sphere height (SH in Figure 5.3) was varied from 4 to 26μm in 1μm steps. A sphere height of 4μm means the bottom of the 6μm bead is 1μm away from the bottom of the channel. The results of these simulations are plotted in Figure 5.13.

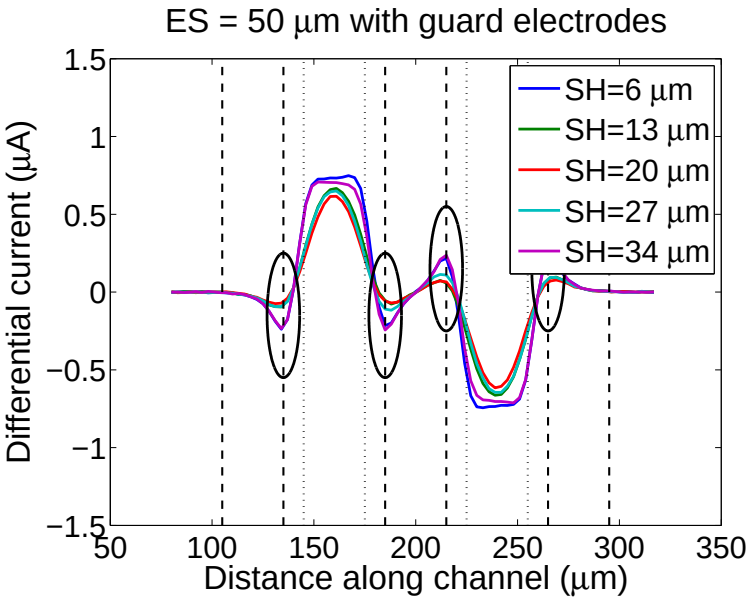

Figure 5.12: Simulated differential current for the electrode design in Figure 5.3. Position of the measurement and ground electrodes is indicated by the dotted and dashed lines. Secondary peaks indicated by the 4 ovals occur at the edges of the ground electrodes.

The experimental data for the populations of 3, 4.5, 6 and 10μm diameter beads presented in Figure 5.11b was re-analysed to estimate the height at which each bead passed through the measurement region, based on the shape of the differential current signal. The impedance signal for each measured event was compared with all of the 23 simulated signals of Figure 5.13. For each event (corresponding to a single bead) the code of the simulation which fitted the data best by least squares fit was recorded. The code of the best fit simulation is therefore an estimator of bead height within the channel. For instance, if the shape corresponding to simulation code 3 (SH=6μm) is the best fit for one event, the event is likely to have passed close to the bottom electrodes at a position SH=6. Examples of measured events and the best simulation fit are shown in Figure 5.14. These correspond to a 6μm bead passing close to the a) bottom, b) middle or c) top of the channel.

The impedance plotted against bead height, estimated by fitting the shape of the impedance signal to the simulations in Figure 5.13, for a mixture of 3, 4.5, 6 and 10μm diameter beads is displayed in Figure 5.15 as a density plot. Beads passing equidistant between the top and bottom of the channel are at SH = 15μm. The larger 10μm diameter beads are physically constrained to the centre of the channel (their centre cannot be closer than 5μm from the channel edge) which explains the reduced range of particle heights in the channel. Also, larger particles will migrate away from the channel walls due to inertial focusing (Chapter 3). A set of parabolas with the following equation is also plotted in Figure 5.15 where a1 is the 3, 4.5, 6 or 10. The equation of the parabolas was found by trial which best fitted the experimental data.

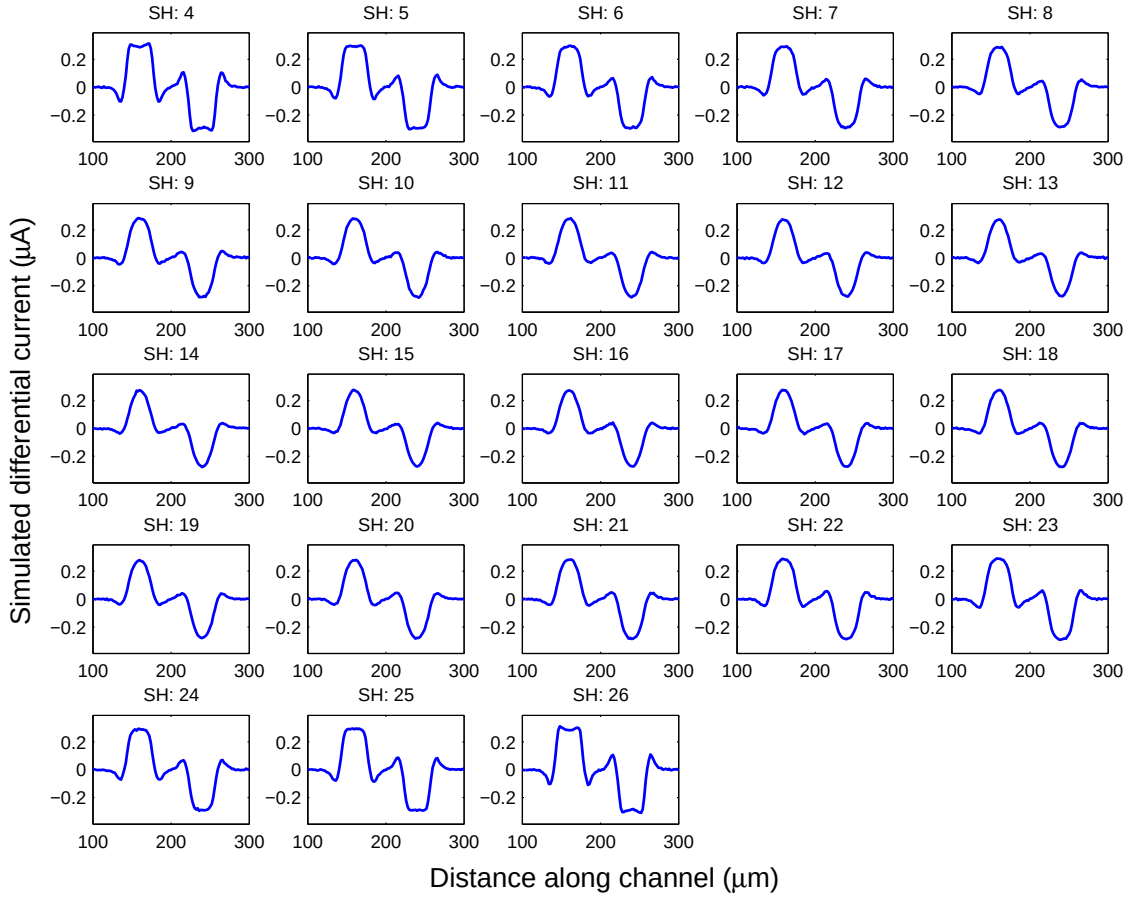

Figure 5.13: Simulated differential current of a $6\mu m$ sphere passing through measurement electrodes (geometry in Figure 5.3 at different sphere heights (SH).

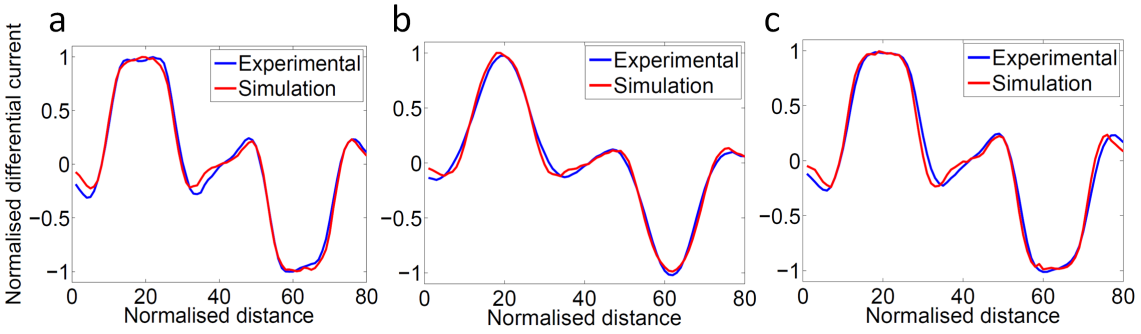

Figure 5.14: Example spectra of beads passing close to the a) top, b) middle and c) bottom of the channel and the best-fit simulation spectra from Figure 5.13.

$$x = a1 \times (1 + 0.001) \times (y - 15)^2 \tag{5.1}$$

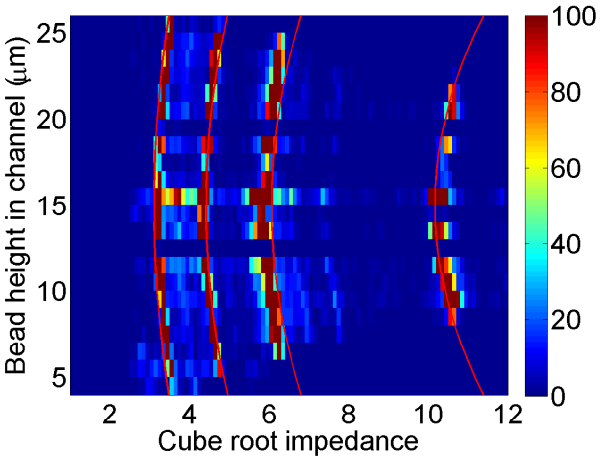

Figure 5.15: Density plot of the measured impedance of a sample containing 3, 4.5, 6 and 10μm beads. The bead height is determined by fitting the simulations displayed in Figure 5.13 to the impedance signal for each event.

To correct for the positional dependence, the measured impedance of each event is divided by the following compensation factor:

$$compensation\ factor \quad = \quad 1 + 0.001 \times (bead\ height\ (\mu m) - 15)^2 \tag{5.2}$$

For example, if an event has an impedance of 6.3 and is estimated from the shape of the differential current signal to be at a height within the channel of 6μm, then the compensation factor is:

$$compensation\ factor \quad = \quad 1 + 0.001 \times (6 - 15)^2 = 1.081 \tag{5.3}$$

and the corrected bead impedance is:

$$corrected\ bead\ impedance \quad = \quad 6.3/1.081 = 5.83 \tag{5.4}$$

The impedance for the population of 3, 4.5, 6 and 10μm beads after correction for positional dependence is displayed in Figure 5.16a. The plot shows that the impedance for each population of beads is the same for all particle velocities. This demonstrates that the particle positional dependence has been completely removed. A Gaussian was fitted to the histogram for the impedance for each population (Figure 5.16b). The coefficient of variation (CV) of each population was calculated using a best fit Gaussian and is compared with manufacturer's data in Table 5.1. The measured CV, after correction for position, is approximately half of the manufacturer's quoted CV, demonstrating the high measurement accuracy of the system.

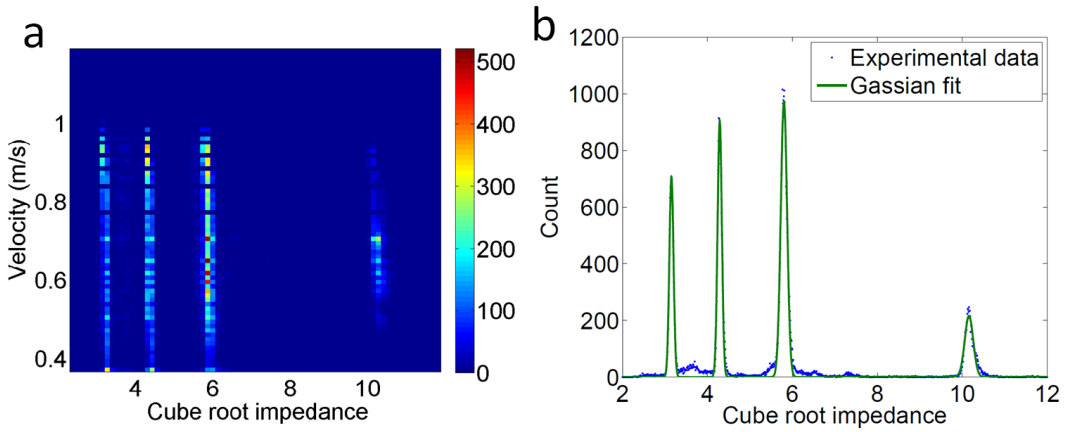

Figure 5.16: (a)Velocity vs impedance for a sample of 3, 4.5, 6 and 10μm beads after correction for particle position. (b)Histogram of the position-corrected impedance and the best fit Gaussian for each population which is used to calculate the CV for each population.

Nominal diameter (μm)	Manufacturers data			Experimental data		
	Diameter (μm)	S.dev	C.V.	Diameter (μm)	S.dev	CV
3	3.11	0.088	2.83	3.15	0.048	1.53
4.5	4.42	0.172	3.89	4.29	0.050	1.16
6	6.07	0.193	3.18	5.80	0.077	1.33
10	10.17	0.304	2.99	10.16	0.100	0.98

Table 5.1: Comparison of the CV of populations of different sized beads obtained experimentally and from the bead manufacturer

5.9 Red Blood Cell Analysis

Red blood cells (RBCs) are responsible for transporting oxygen around the body. Enumeration and measurement of the mean cell volume (MCV) and cell volume distribution width (RDW) is an important diagnostic tool. A combination of RDW and MCV is used to differentiate between different types of anaemia. For instance Vitamin B12 deficiency presents as a high MCV with a normal RDW. Iron deficiency anaemia shows normal MCV with an increased RDW.

The previous section has shown that impedance cytometry can accurately measure the volume of spherical objects. However, RBCs are non-spherical and this can affect the measurement. The impedance of a solid discoid-shaped object measured at various orientations was investigated using FEM simulations. A model of a discoid shaped object was created in Solidworks (Figure 5.17). The discoid has dimensions and a volume typical of a RBC. The RBC model was placed in the centre of a $40 \times 40 \times 40 \mu m$ box (Figure 5.18). A second identical box without the RBC was also created to use as a reference. All sides of both boxes were defined to be insulating, except both tops and bottoms which were defined to be $1V$ and $0V$ respectively. The RBC model was set to $\sigma = 2.4 \times 10^{-4} Sm^{-1}$ and $\varepsilon_r = 2.5$. The remaining volume within each box was set to

$\sigma = 1.6Sm^{-1}$ and $\varepsilon_r = 80$. The RBC model was rotated along one axis in the centre of the box from 0 to 90° in 5° increments. The difference in current flowing through the bottom of both boxes (I1-I2) was simulated for each angle of the RBC model and is plotted in Figure 5.19. The same simulation was also performed for a sphere of the same $90fL$ volume ($5.56\mu m$ diameter).

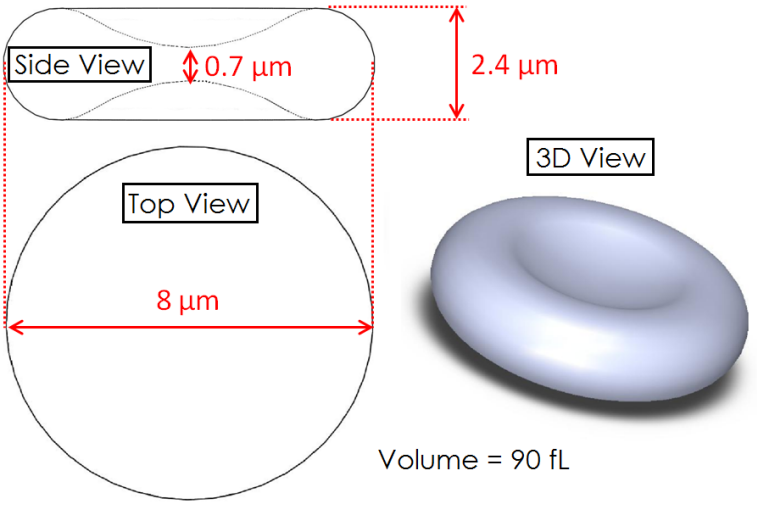

Figure 5.17: Dimensions of the discoid used to model a typical RBC in the FEM simulations.

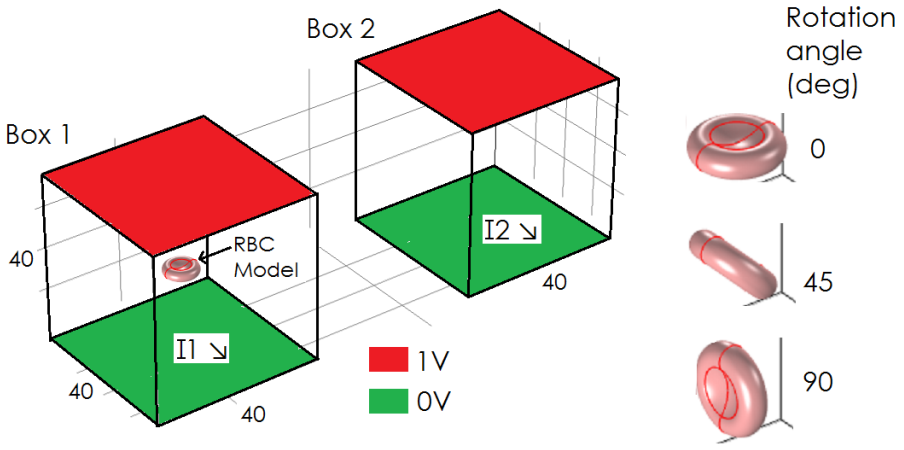

Figure 5.18: Diagram of the geometry used in the FEM simulation to investigate the impedance of RBCs measured at different orientations. Also shown is a diagram illustrating the rotation angle of the RBC model.

The simulation results (Figure 5.19) show that the measured impedance of a RBC will depend on the orientation of each individual cell passing through the detection region. The average simulated differential current of the discoid model measured across angles 0° to 90° is 45.7% higher compared with a sphere of the same volume.

RBCs are deformable and are known to tumble and roll while travelling along a microfluidic channel (Dupire et al., 2012). A measurement of RBCs was performed

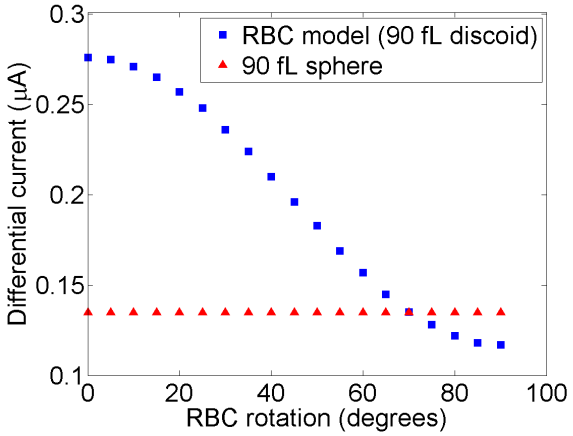

Figure 5.19: Simulated impedance of the RBC model measured at different orientations. Also shown is the impedance of a sphere of the same volume. The rotation angle is shown in Figure 5.18

to investigate if the cells preferentially focus while flowing along the inlet channel ($4mm \times 30\mu m \times 200\mu m$) prior to measurement. Whole blood ($1\mu L$) was diluted into $10mL$ PBS. The sample was pushed through the MIC at a flow rate of $40\mu L min^{-1}$. A high speed camera was used to capture images of RBCs entering the measurement region. No preferential orientation focusing was observed at this flow rate.

Therefore, to measure the RBC volume and distribution width accurately, the RBCs must be isovolumetrically sphered prior to measurement. RBCs were sphered and fixed using the recipe from Kim and Ornstein (1983). Whole blood ($1\mu L$) was added to $10mL$ PBS containing $3mg$ Sodium dodecyl sulfate and $100mg$ gluteraldehyde. The sample was viewed on a microscope and all cells appear spherical (Figure 5.20a). For comparison a microscope image of the unsphered sample is shown in Figure 5.20b. The sphered cells appear as circles with similar diameters, whereas the unsphered sample appear as larger circles or ovals depending on the orientation at which they are viewed.

The impedance of the sample of sphered and fixed RBCs was measured using the same method described in Section 5.5 using the ground electrode configuration. A histogram of the impedance of the cells is presented in Figure 5.21. For comparison the impedance of the unsphered sample using blood from the same donor is also shown.

Sphering the RBCs has a significant effect on the measured impedance. The CV in radius of the sphered and unsphered cells is 5.28% and 9.58% respectively. The mean impedance of the unsphered RBCs is 44.5% higher than the sphered sample. This is comparable to the simulation results which demonstrated that the mean differential current of the discoid was 45.7% higher compared with a sphere of the same volume.

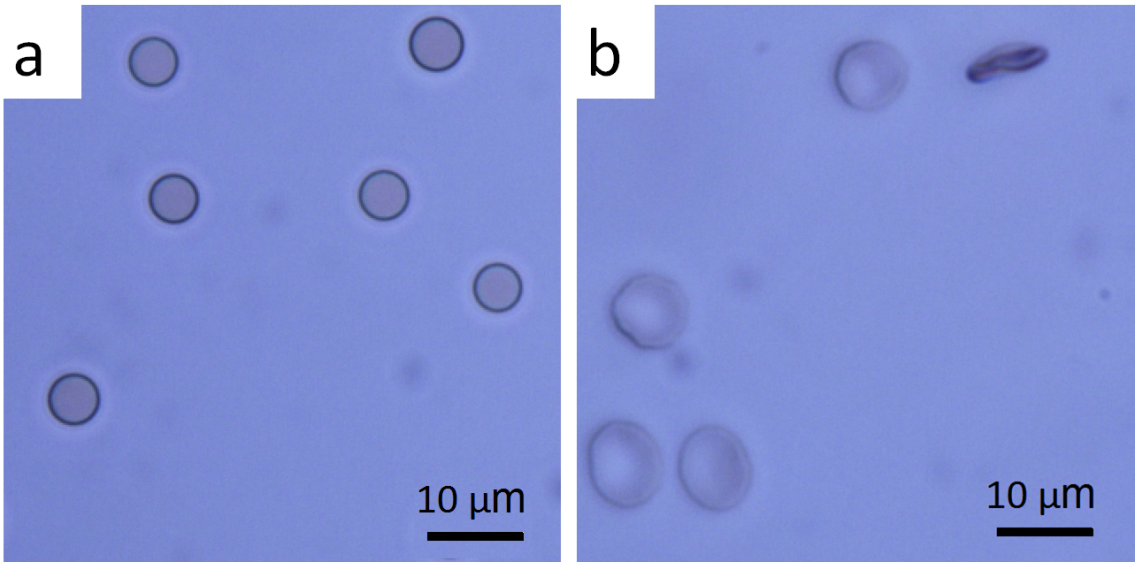

Figure 5.20: Microscope image of a) sphered and b) normal RBCs.

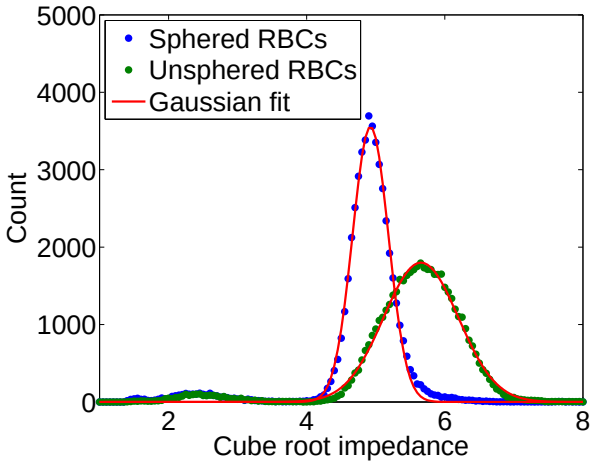

Figure 5.21: Histogram of the measured impedance of a population of normal and sphered RBCs. Also shown is the best fit Gaussian for each population.

5.9.1 Positional Correction

Some of the RBCs will move close to the top or bottom electrodes resulting in a higher measured signal (positional dependence), as described earlier with the measurements of polystyrene beads. The simulation templates (Figure 5.13) were fitted to the RBC measured data to estimate the height within the channel that each RBC was measured at. The impedance of the sphered sample of RBCs corrected for positional dependence is shown in Figure 5.22. The same correction factor as described in Equation 5.2 was used.

The CV in radius for the sphered sample is 4.68%. This is equivalent to a CV in volume (RDW) of 14.0%. Unfortunately no access to a commercial haematology analyser was available. However, this measurement does fall within the normal clinical range for RDW

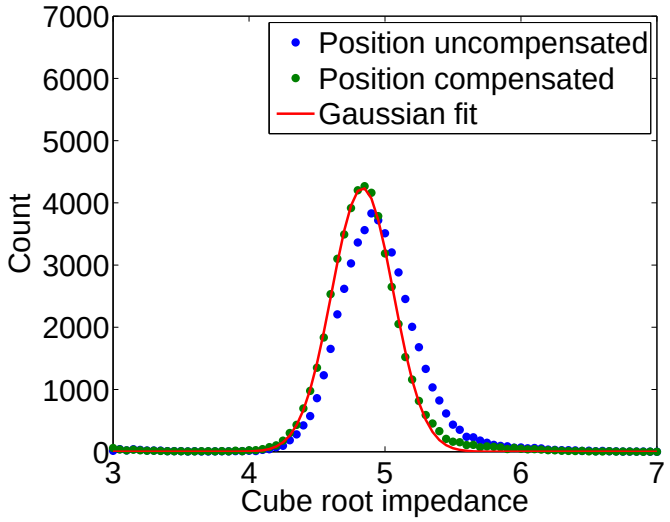

Figure 5.22: Histogram of the impedance of sphered RBCs before and after compensation for position.

which is 11-15%. The RDW of the sphered sample before correction for positional dependence is 15.8%. It is not known if commercial impedance based haematology analysers sphere RBCs before analysis. The Bayer ADVIA haematology analyser uses light scatter to measure RBCs which are chemically sphered before analysis (Advia, 2013). Also, the RDW measurement has not been standardised and varies between equipment. The median RDW for five haematology analysers varied from a minimum of 11.6% for the Abbott CD 4000 to a maximum of 14.4% for the ABX VEGA Retic (Buttarello and Plebani, 2008).

5.10 Continuous Flow Analysis

Enumeration of small particles in ice core samples, for instance dust and pollen, is a useful metric for determining the age of the ice, or correlating the depth of the sample with other ice cores from the same region. Within the ice core, there are layers which contain more particles which correlate with the seasons in a year: there is a spike in particle number each spring, as shown in Figure 5.23. Typically this is performed using a commercial Coulter counter. An ice core is melted, mixed with a salt solution to raise the conductivity and then measured. However, this only gives the average properties of the particles in that sample.

Continuous flow analysis is a process where the ice core is continuously melted from one end and measured as shown in Figure 5.24. This enables high resolution measurements to be made. This is important for older ice core samples because the ice has been compressed which makes the seasonal layers close together and difficult to measure with discrete sampling.

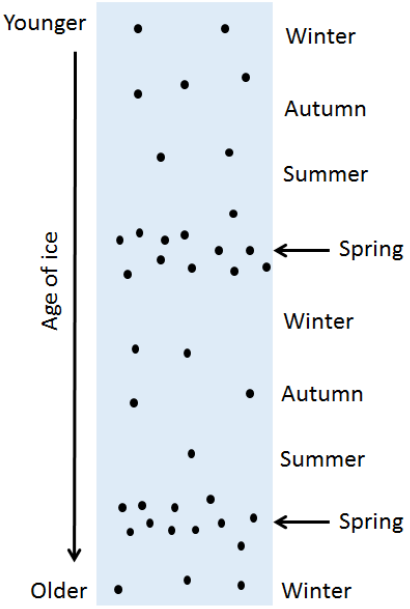

Figure 5.23: Illustration of the distribution of small particles (1 to 10μm) in ice core samples. A increase in the number of particles is present at each spring.

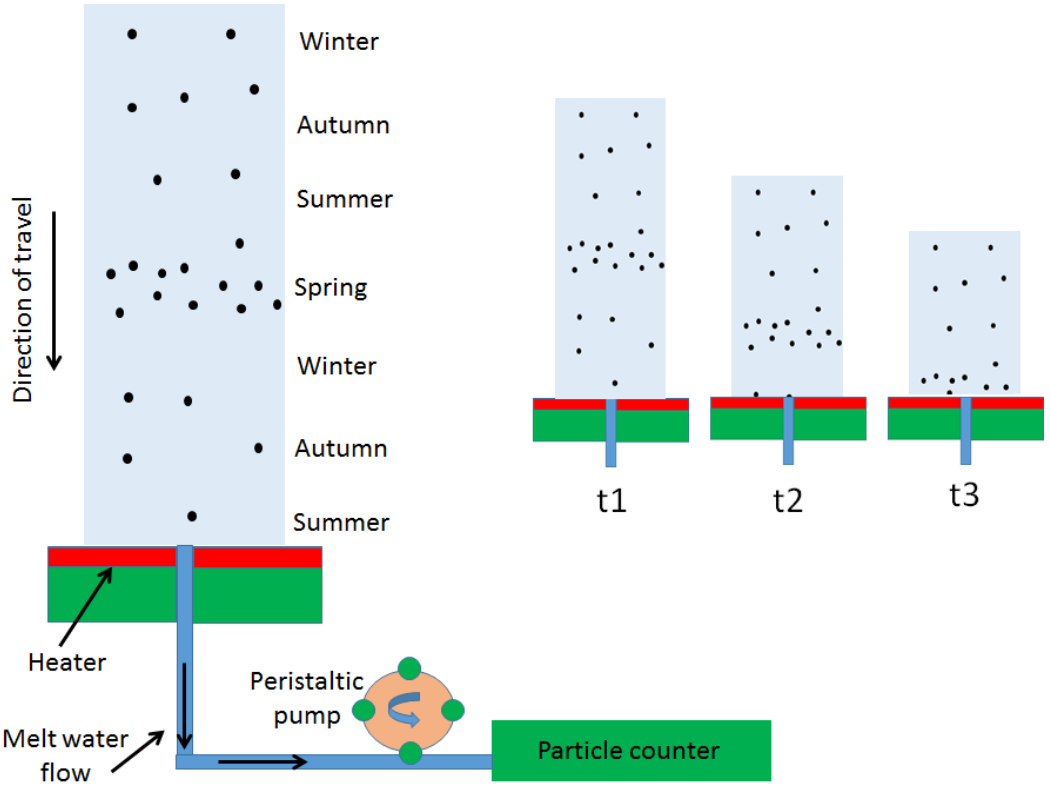

Figure 5.24: Illustration of continuous flow analysis. An ice core is gradually melted from one end. The melt water is continuously sampled and measured using a particle counter.

A problem with continuous flow analysis is that Coulter counters cannot be used because they measure a fixed finite volume (necessary for absolute quantification) and the sample

must be mixed with a salty solution to raise the conductivity of the melt water. Instead, laser particle counters are used but these must be calibrated against a Coulter counter. Also, light scatter is not accurate for particle sizing because light scatter is not a linear function of particle size (Ligler and Kim, 2010). This section describes a MIC setup in a continuous flow configuration to count and size particles present in an ice core. The advantage of using MIC is that it can provide high accuracy particle sizing (like the Coulter counter) in a continuous flow mode (like the laser particle counter).

The conductivity of the melt water is of the order of mSm^{-1} which is too low for MIC, which requires the sample to have a conductivity of around $1Sm^{-1}$. To raise the conductivity, the melt water was mixed with 10x concentrated PBS in a ratio of 1 to 9 respectively. The mixing was performed in a microfluidic channel shown in Figure 5.25. Melt water and PBS (10x) enter at the top inlets and meet at a T-junction. They flow along the serpentine channel which has chevron shaped ridges on the bottom of the channel to aid mixing. The channels were $1mm$ wide by $200\mu m$ high and were fabricated using standard replica moulding (soft lithography) which is described in Chapter 7. The two inlet lengths were designed in a 1 to 9 ratio (5.5 and $49.5mm$) so a single pump at the outlet could be used and the mixing ratio would be constant (decided by the input resistances). The mixing worked at the correct ratio (1 to 9) when the inlets were connected to reservoirs. However, when the inlet was directly connected to the melt water, other resistances in the fluidic systems dominated which changed the ratio to approximately 1 to 1. Instead, the two inlets were driven from a single peristaltic pump with separate pump tubing for the two inputs. The inner cross-sectional area of the two different tubing was in a 1 to 9 ratio. Separate peristaltic pumps could have been used, but it was considered beneficial to using a single pump to minimise errors in the mixing due to the pulsate nature of peristaltic pumps.

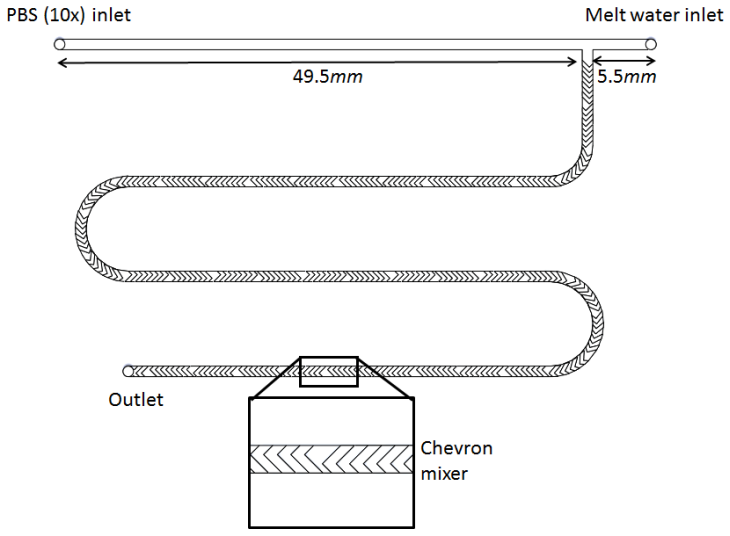

Figure 5.25: Diagram of the microfluidic mixer used to mix the melt water with PBS (10x).

	CV (%)	
Bead diameter (μm)	Continuous flow mixing	Offline mixing
1.2	7.5	6.4
2.2	5.1	3.2
5.2	6.0	4.8

Table 5.2: Comparison of the CV of monodisperse beads measure in continuous flow and offline mixing.

If the conductivity of the solution varies then the measured electrical volume of a particle measured by MIC will vary by the same amount. It is therefore important to test that the conductivity of the mixed solution did not change. This was checked by measuring solutions of monodisperse beads in water which were mixed in a 1 to 9 ratio with PBS (10x) offline using pipettes, and online using the continuous flow system. Three sizes of beads (1.2, 2.2 and 5.16μm in diameter) were tested which were chosen to cover the expected size range. The CVs of the populations are shown in Table 5.2. Although the CVs are slightly higher in continuous flow mode, the CVs are low when compared to other reported impedance measurement systems (which are discussed later) and shows successful operation in continuous flow mode. The data also demonstrates that the MIC analysis software handles pulsed flow which is an inherent problem of peristaltic pumps.

Continuous flow analysis of an ice core from Greenland was performed using the MIC system. The melt water flow was split to measure in parallel with a laser particle counter (Abacus) which is traditionally used. Figure 5.26a is a photograph of the ice core half way through melting. When the ice cores are drilled, they are split into 55cm high sections for transportation. Figure 5.26b is a graph of the particle count over time for the impedance and laser counter systems. The flow rate through the abacus was $1.9mLmin^{-1}$ which is 24 times greater than through the impedance chip which was $80\mu Lmin^{-1}$. Figure 5.26b shows that the graphs overlap, and the MIC can detect the rise in particle numbers corresponding to the two spring seasons.

The LoD of the MIC was 1.5μm for these experiments. This is slightly higher than the measurements of monodisperse beads, which is because of the higher flow rate ($80\mu Lmin^{-1}$ compared to $40\mu Lmin^{-1}$). This reduces the number of data points for the convolution fit in the signal processing, increasing the LoD. The mode of the particle size is an important measurement, but the LoD of the MIC is above the particle size mode which is typically around 1μm. This section has demonstrated that MIC is useful for continuous flow analysis, however the throughput and sensitivity must be improved. To increase the sensitivity the channel dimensions could be reduced, for instance to 15μm square (approximately half the size) because the largest particles are no more than 10μm. However, this would reduce the volumetric throughput because the measurement limit is the linear particle speed which is higher at the same flow rate in a smaller channel. Increasing the throughput without duplicating the measurement equipment is

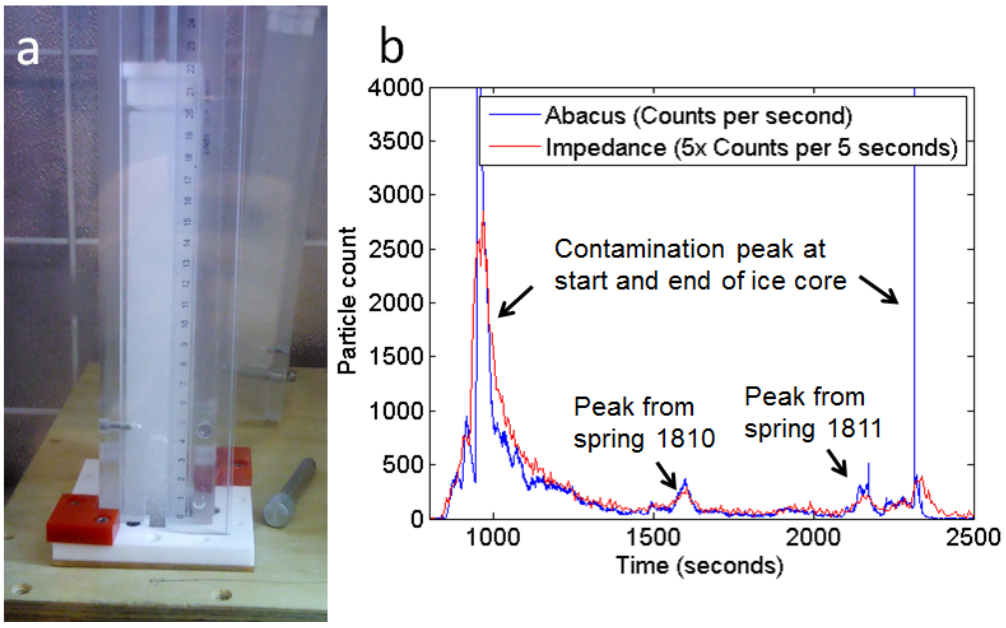

Figure 5.26: a) Photograph of a second of ice core which is mounted into the continuous flow analysis system. b) Comparison between the particle count in an ice core sample measured using MIC and an Abacus laser particle counter.

challenging, but dedicated multiplexed circuits could be built to run multiple channels in parallel.

5.11 Discussion

This chapter has presented a new electrode geometry designed to reduce the particle positional dependence of the impedance signal. A correction algorithm to eliminate the particle positional dependence is also presented. In the standard parallel plate geometry a $10\mu m$ diameter particle would be measured as a $12.9\mu m$ diameter particle if it passed close to the bottom electrodes. For the same sized particle in the new electrode geometry the maximum measured diameter would be $10.7\mu m$. In addition, the shape of the impedance signal for the new electrode geometry provides information on the height at which each particle passes through the measurement electrodes. This extra information was used to correct for the particle positional dependence of the impedance signal, eliminating the effect. The measured CV's of 3, 4.5, 6 and $10\mu m$ beads were approximately half of the manufacturer's quoted CV, demonstrating the high measurement accuracy of the system.

The electrode geometry and correction algorithm described in this chapter have also been used to measure the mean cell volume and cell volume distribution width of RBCs, which are important diagnostic parameters for various forms of anaemia. The impedance of a RBC was found to vary substantially, depending on the orientation of the cell

when travelling through the measurement region. Consequently, it was found to be necessary to isovolumetrically sphere the RBCs prior to measurement. Measurement of the distribution width using the new electrode geometry and particle positional dependence algorithm demonstrated that on a sample of normal healthy blood cells, the distribution width, after correction for positional dependence, was within the normal clinical range. These results demonstrate that the device could be developed to provide a miniature diagnostic tool for red blood cell anomalies.

5.11.1 Comparison with Particle Focusing

Positional dependency is mitigated in commercial optical flow cytometers by using sheath flow to ensure that the particles all pass through the same position within the channel, normally through the centre of the measurement region. However, sheathing a sample stream with a second flow requires complicated hardware. Also, any particles or bubbles which become trapped on channel side walls will interrupt the interface between the sample and sheath flow and move the position of the sample stream within the channel. A further disadvantage of using sheath flow focusing is that the sample becomes mixed and diluted with the sheath flow. In the system presented in this chapter the sample can be recovered unchanged after measurement.

Particles could also be forced through the same position within the channel using sheath less flow focusing. In this technique an externally applied force (for instance dielectrophoretic) causes particles to migrate to a specified position within the channel. To focus particles, the applied force must be great enough to move the particle across the flow before it reaches the measurement region. However, there is a limit to the amount of external energy which can be applied. The migration force is inversely proportional to the cube of the particle radius. Consequently, to focus small particles, prohibitively low flow rates (and therefore throughput) would be required. For example Holmes et al. (2006), used dielectrophoresis to focus beads within the centre of a channel and was limited to a maximum velocity of $1mm$ per second for $6\mu m$ diameter beads. This is approximately 1000 times slower than the measurement presented in this chapter ($1ms^{-1}$).

In contrast to particle focusing techniques, the new electrode geometry and correction algorithm accurately measures particles without any of the disadvantages associated with particle focusing, such as the increased hardware complexity associated with sheath flow, or size limitations associated with sheath less focusing. The only disadvantage is that the correction algorithm will not work for particle sizes close to the limit of detection. To correct for position, the secondary impedance peaks must be detected. These peaks are approximately 20% of the main peak height, thus the SNR must be 5 times higher compared with detection of the main peaks. For the system presented above, the limit of detection of the system without correction is approximately $0.9fL$,

which corresponds to a $1.2\mu m$ diameter sphere (data not shown). The LOD therefore becomes $4.5fL$ ($5 \times 0.9fL$), which corresponds to a $2\mu m$ diameter bead. Despite this limit, the current system can accurately measure a wide range of cell sizes spanning over 3 orders of magnitude in volume, from platelets (normal range is $7.5-11.5fL$) to WBCs ($268-905fL$, 8-12μm diameter) and MCF7 cancer cells ($1767-8181fL$, 15-25μm).

5.11.2 Positional Dependence in Coulter Counters

Positional dependence in a traditional Coulter counters has only been studied by a few people. Smythe (1972) calculated theoretical values for the apparent increase in tube length for offset particles. The tabulated increase in length depends on particle diameter and varied from 0.02% to 58% for spheres of radius 0.1 and 0.6 in a tube of radius 1. More recently, Berge et al. (1990) experimentally determined the increase in resistance for offset particles travelling through a long orifice. A maximum increase in resistance of 10% was found for a $20\mu m$ diameter sphere in a $30\mu m$ diameter pore of length $315\mu m$. Smaller particles relative to the pore diameter produced smaller positional dependence. In contrast, the positional dependence of particles in the standard parallel plate geometry is present for all particle sizes. The miniature system used two pairs of electrodes to increase sensitivity by performing a differential measurement. Consequently, off-centre particles interrupt the current flow between electrode pairs causing a positional dependence.

Saleh and Sohn (2002) corrected for the positional dependence in a Coulter counter based on the transit time of particles. Both transit time and the resistance increase in their cylindrical orifice are solely dependent on the axial offset position. Thus by measuring transit time, a simple correction to the resistance pulse can be applied. The correction reduced the CV of a population of $560nm$ colloids from 7.1 to 3.5%. The problem with the correction for position demonstrated by Saleh and Sohn (2002) is that the particle transit time must be known. However, due to entry effects, the resistance pulse starts before the particle enters the orifice. To accurately calculate the transit time a long orifice must be used, but the measurement sensitivity is inversely proportional to the orifice length.

5.11.3 Comparison of Measurement Accuracy with Alternative Miniature Electrode Systems

To increase the sensitivity of a micro Coulter counter without reducing channel dimensions (which could cause clogging), Watkins et al. (2009) used a non-conductive sheath flow to guide a sample stream close to a set of coplanar electrodes where the electric field is strongest. The problem with this design is that the electric field is non uniform close to the electrodes which leads to variation in measurements: the CV

for monodisperse beads was 25% in volume which is 8.5% in radius. Bernabini et al. (2011) used oil as a sheath flow to confine a sample stream horizontally in the middle of a wide channel. In this case parallel facing electrodes were used which provided a more uniform electric field. The CVs for 1 and 2μm particles of 5-8%, were substantially higher than the reported manufacturers CV measurements of 1-5%. Mernier et al. (2012) used DEP focusing to focus particles horizontally between pairs of "liquid electrodes". Focusing 6μm beads horizontally reduced the CV from 27% to 5.6% (manufacturer's CV was 3.6%). Segerink et al. (2011) reported a floating electrode structure, similar to the standard 4 electrode parallel facing geometry but simpler to manufacture. The system was tested with a mixture of 3 and 6μm polystyrene beads. The CV of the measured data was not reported, however a histogram of experimental data showed the two populations overlapping which indicates poor experimental measurement accuracy. In contrast to Segerink et al. (2011), the results presented in this chapter show a clear space between the populations of 3, 4.5 and 6μm beads.

5.11.4 Summary

This chapter has described a new electrode geometry together with a signal processing algorithm which enables high accuracy measurements of particles. The system does not use particle focusing which has resulted in a robust fluidic design consisting of a single inlet and outlet for the sample. The device has a higher measurement accuracy compared with rival miniatured systems which focus particles either using more complicated fluidic designs (which are more complex to fabricate and less robust), or sheathless particle focusing which is not practical for small particles. Additionally, measurements of isovolumetrically sphered red blood cells were within the normal clinical range. This demonstrates the potential for development into a miniature diagnostic tool for detecting red blood cell anomalies.

Chapter 6

Impedance Analysis of Tumour Cell Lines

6.1 Introduction

The spread of cancer from a primary tumour to distant sites around the body is called metastasis, and is responsible for more than 90% of cancer-related deaths (Wirtz et al., 2011). In a process called intravasation, single cells detach from a primary tumour and migrate into the blood stream. These cells, called Circulating Tumour Cells (CTCs), move around the body in the blood stream and can adhere to the blood vessel wall or become trapped in narrow blood vessels. Once trapped, CTCs can migrate through the blood vessels into other tissues (called extravasation) and form secondary tumours which are distant from the primary tumour.

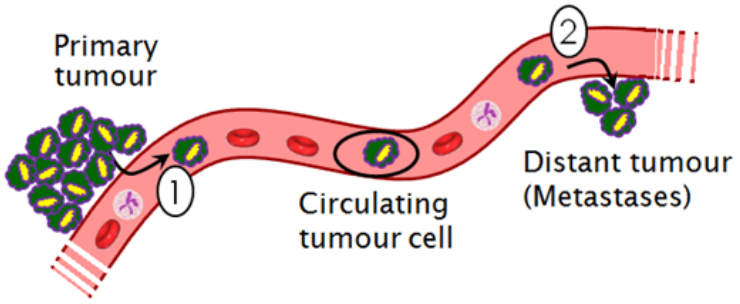

Figure 6.1: Illustration of the spread of cancer in a process called metastasis. (1) In a process called intravasation, single cancer cells from the primary tumour enter the blood stream. These single cells, called CTCs, circulate the body in the blood stream until they become trapped in small blood vessels. (2) CTCs then exit the blood stream into distant organs in a process called extravasation and can multiply to form secondary tumours.

CTCs were first discovered by Ashworth (1869) while investigating a patient with tumours in the thorax, abdomen and also on the left thigh (metastatic cancer). At

the time it was unknown how cancer spread, so Ashworth examined a sample of blood taken from the right leg which was free from tumours. He identified cells which were identical to the tumour cells and speculated that if the cells were from an existing cancer then they must have passed through the circulatory system.

More recently, it has been demonstrated that enumeration of CTCs is important to monitor cancer progression and predict re-occurrence, for instance in patients with breast cancer (Cristofanilli et al., 2004). CTCs are rare (a few cells per millilitre of blood which also contains $5-6\times10^9$ RBCs), and are typically distinguished from other blood cells using a specific surface marker called EpCAM (epithelial cell adhesion molecule). However, not all cancer cells express this marker (Spizzo et al., 2011). This chapter focuses on the use of MIC to characterise CTC-like tumour cells. Firstly, recent progress in CTC detection from the literature is reviewed. Most research has concentrated on separating CTCs from blood, whereas this chapter concentrates on analysis of tumour cells. Identification of tumour cells spiked into whole blood using MIC and optical cytometry was compared and a greater difference is observed in the MIC. Frequency sweep measurements were performed to determine the optimum measurement frequency to distinguish the tumour cells from blood cells. These frequency sweeps were used to characterise the dielectric properties and the data was compared with literature values. Since CTCs are rare in whole blood, serial dilution experiments were performed to determine if clinically relevant levels could be measured on the MIC. Small numbers (around 100) of tumour cells could be identified when spiked into $50\mu L$ whole blood, however this is higher than human CTC levels. Magnetic pre-enrichment was performed which enabled the detection limit to reach clinically relevant levels.

6.2 Recent Progress in CTC Enumeration

6.2.1 Veridex CellSearch

CellSearch by Veridex is the only Food and Drug Administration (FDA) approved system for CTC enumeration (Veridex LLC). The CellSearch performs magnetic separation using the epithelial surface marker EpCAM to enrich CTCs from $7.5mL$ of whole blood, as shown in Figure 6.2. The cells are stained and classified as a CTC if they are CD45 negative (a WBC marker), cytokeratin positive (specific for the intracellular protein which is characteristic of epithelial cells) and DAPI positive (a cell nucleus stain which binds to A-T regions in DNA). Each cell identified by the system as a CTC is then presented to a trained operator who checks that the morphology of the suspect cell is consistent with other CTCs.

Cristofanilli et al. (2004) was the first to demonstrate the prognostic value of CTC enumeration. Patients with metastatic breast cancer were tested using the CellSearch

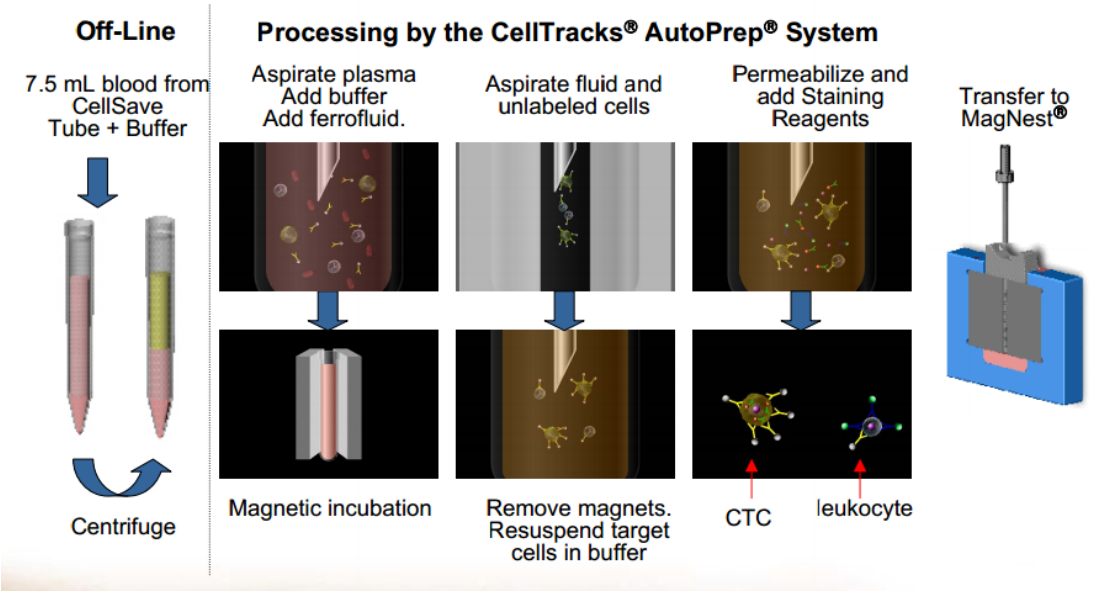

Figure 6.2: Overview of the Veridex system to enumerate CTCs. Whole blood is drawn into a "Cellsafe" tube containing a specially designed anticoagulant to protect the CTCs. The CTCs are magnetically separated and then each cell is imaged and presented to a trained user for verification. Image from Veridex (2013).

system before starting treatment. Those with 5 or more CTCs per $7.5mL$ blood had a median progression-free survival of 2.7 months compared with 7.0 months for those who had less than 5 CTCs. After starting therapy, the trend continued: overall survival was 10.1 months for those who had 5 or more CTCs compared with longer than 18 months for those with fewer than 5 CTCs. Similar studies have demonstrated the prognostic value of CTC counting for patients with colorectal or prostate cancers (Miller et al., 2010). Absolute counting using the CellSearch system is subjective because the final decision of whether a suspect cell is a CTC is determined by a trained operator. Identical images of suspect CTCs identified by the CellSearch were classified differently in a study with 6 trained operators in different centres (Miller et al., 2010).

Spiking known numbers of cultured tumour cells into whole blood, Allard et al. (2004) demonstrated the CellSearch system was only linear when counting above 5 CTCs per $7.5mL$ blood. When 4 tumour cells were spiked into $7.5mL$ whole blood, on average the system over counted by 10%. Also, when more than 1000 tumour cells were spiked into the sample the system under counted by 15%. Allard et al. (2004) also demonstrated that none of the 145 healthy patients and just one of the 199 patients with non-malignant disease (such as diabetes or asthma) had greater than 2 CTCs per $7.5mL$ blood. Whereas 36% of the patients with metastatic cancer patients had greater than 2 CTCs per $7.5mL$ blood. The problem with the CellSearch system is that it is expensive and the system requires a trained operator to interpret the results. Also, not all cancer cells express EpCAM.

6.2.2 Microfluidic Devices for CTC Capture

Nagrath et al. (2007) captured CTCs from patients with metastatic lung, prostate, pancreatic, breast or colon cancer using a "CTC-chip" in which whole blood was passed between 78000 EpCAM antibody coated micro posts, shown in Figure 6.3. To identify CTCs from other blood cells captured in the device, the captured cells were stained with DAPI, Cytokeratin and CD45. Capture purity was 50% which means that for each measurement the total captured cells could not simply be counted. Each sample must be labelled, thus a fluorescent microscope and trained operator is needed to enumerate captured CTCs. More than 4 CTCs per $1mL$ blood were detected in 115 of 116 blood samples from cancer patients and none of the 20 healthy control patients had more than 4 CTCs per millilitre of blood. However, the capture yield for spiked cancer cells from a cell line was only 65% thus low levels of CTCs could be missed.

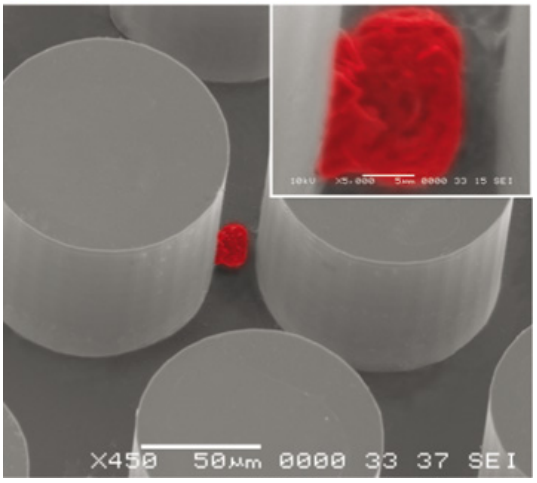

Figure 6.3: SEM image of the micro pillars used by Nagrath et al. (2007) to isolate CTCs from whole blood, showing a captured lung cancer cell coloured in red. Image from Nagrath et al. (2007).

The same group later replaced the pillars with herringbone grooves in the channel to induce micro vortexes to bring cells into contact with the EpCAM coated surfaces (Stott et al., 2010). The new device, Figure 6.4, increased capture efficiency to 92%. Greater than 10 CTCs per millilitre of whole blood were detected in 15 out of 16 patients with metastatic prostate cancer. Automated imaging algorithms were used to detect CTCs however fluorescent staining was still required which is time consuming.

Gleghorn et al. (2010) captured CTCs from prostate cancer patient using a microfluidic device called GEDI (geometrically enhanced differential immunocapture). The device, shown in Figure 6.5, is a pillar array similar to the design reported by Nagrath et al. (2007). However, GEDI uses rows of pillar which are staggered (offset from the previous row by $7\mu m$. This increases the collisions of the larger CTCs to enhance the capture rate, while decrease the number of collisions of the smaller WBCs to reduce the non-specific capture. The pillars were coated with an antibody for prostate-specific antigen and

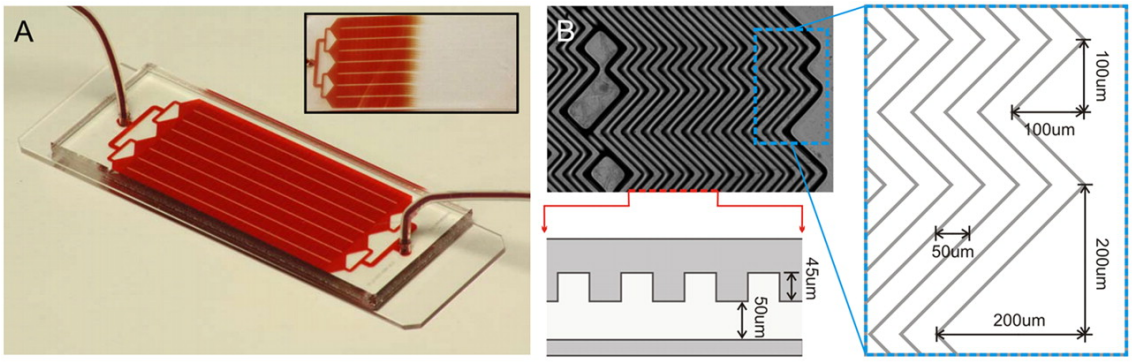

Figure 6.4: Photograph and schematic of the herringbone design used by Stott et al. (2010) to isolate cancer cells from whole blood. Image from Stott et al. (2010).

tested with cultured cancer cells spiked into whole blood. The device captured most of the cells (85%) and capture purity was 68% which is much greater than the 50% reported by Nagrath et al. (2007). Whole blood ($1mL$) from prostate cancer patients was also tested. The blood sample was pumped through the device at $1mL$ per hour followed by a wash at the same flow rate for 10 minutes using PBS. Reproducibility was good (27 ± 4 captured cells) from 4 repeats of the same blood sample and cells were captured in 90% of samples from cancer patient. However, like Nagrath et al. (2007) and Stott et al. (2010), the captured cells must be fluorescently labelled to identify the CTCs from blood cells. Later, the group compared the CTC capture efficiency with the CellSearch system (Kirby et al., 2012). The capture rate of the GEDI was 2-400% higher, but the definition of CTC was not consist (PSMA+ for the GEDI and EpCAM+ for the CellSearch). Kirby et al. (2012) identified that some PSMA positive and CD45 negative cells are EpCAM negative, however so far the prognostic value has only been shown for EpCAM positive CTCs.

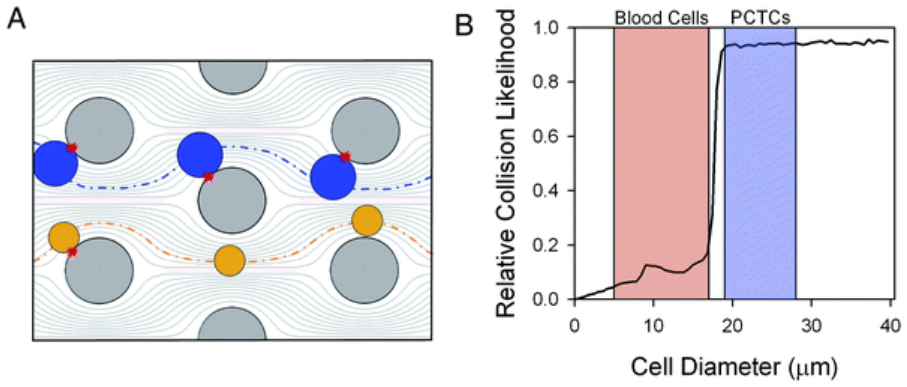

Figure 6.5: Illustration of the GEDI device reported by Gleghorn et al. (2010). As cells flow through the pillar device, they collide with the antibody coated pillars. The pillar array is offset to maximise the number of collisions of larger cells (such as CTCs), while minimising the number of collisions of smaller cells (such as WBCs) which could be non-specifically attached. Image modified from Gleghorn et al. (2010).

6.2.3 Size Filtration

Although the level of EpCAM expression is high in most metastases, some tumours are EpCAM negative, for instance urothelial (bladder) cancer or breast cancer with lobular histology (Spizzo et al., 2011). Vona et al. (2000) was the first to investigate capture of CTCs using a size filter. A single cell from one of three cancer cell lines which model CTCs (HepG2, LNCap or MCF7) was spiked into $1mL$ whole blood. The single spiked cell was captured using an $8\mu m$ pore size in 12 of 15 experiments which demonstrates a near single cell sensitivity. Between 0 and 5 CTCs per millilitre of blood were detected in patients with liver cancer, but no comparison was made with other CTC detection techniques (such as the CellSearch) and capture sensitivity was not reported. De Giorgi et al. (2010) investigated detection of CTCs from malignant melanoma (skin cancer) patients using size filtration. No CTCs were detected in healthy volunteers and non-melanoma skin tumour patients (no false negatives) however CTCs were only detected in 29% and 63% of primary invasive melanoma and metastatic melanoma patients respectively.

Lin et al. (2010) compared size filtration using a lithography defined parylene membrane ($8\mu m$ pore size) with the Veridex CellSearch system. They first spiked 10 cancer cells from cell lines into $10mL$ whole blood. On average they captured 4.6 cells from $7.5mL$ of this sample using the size filtration, but detected only 1.2 cells on average for the CellSearch system. Lin et al. (2010) next compared CTC enumeration from patients with metastatic prostate, breast, colorectal or bladder cancer. Using the filter device, CTCs were detected in 51 out of 57 patients whereas CTCs were only detected in 26 patients using the CellSearch. However the definition of a CTC was not consistent: the size filter included both EpCAM positive and negative cells whereas the CellSearch only includes EpCAM positive cells. Although some cancers do not, or only weakly express EpCAM, the prognostic value of CTC enumeration has so far only been statistically proven for EpCAM positive cells. Another problem with the size filtration technique reported by Lin et al. (2010) is that the cells must be partially fixed prior to filtration, which means they cannot be cultured for further investigation. The group later modified the device from a single to a double layer filter to reduce the membrane stress on trapped cell and eliminate the requirement for fixing cells (Zheng et al., 2011). Capture efficiency of approximately 300 cultured tumour cells in $1mL$ whole blood was on average 87%.

6.2.4 Dielectrophoretic Separation

Becker et al. (1995) used electrorotation to compare the dielectric properties of blood and cultured cancer cells. They found the cancer cells had a significantly higher membrane capacitance compared to blood cells, and used this to separate a mixture of cancer and blood cells (in a ratio 1:3) with greater than 95% purity using an interdigitated

electrode array. The team later showed enrichment of 1 cancer cell in 3×10^5 blood cells but did not mention how many blood cells were also captured (Gascoyne et al., 1997). One problem with the device is that it operates in batch mode and has a total cell limit of approximately 10^6 cells. At higher load levels, cell to cell dipole interactions disturb the DEP separation force and reduce separation efficiency. Later, the device was modified to a larger separation chamber to increase loading capacity (Gascoyne et al., 2009). Out of 100 spiked cancer cells, 92 were recovered in a background of 10^5 cells which corresponded to a low loading level. At intermediate total cells present (10^6), approximately 50% of spiked cancer cells were recovered, whereas at high levels (2.25×10^7) capture efficiency was just 10%.

To eliminate the total cell limit, a commercial DEP-based cell separation device called ApoStream was reported which operates in a continuous flow mode (Gupta et al., 2012). The cell sample is injected into the bottom of the device, Figure 6.6. Cells flow along the bottom of a fluidic channel covered in interdigitated electrodes. An AC frequency is applied which levitates blood cells (by negative DEP) and attract cancer cells as shown in Figure 6.6. The device was tested with between 4 and 23 cultured cancer cells spiked into approximately 12×10^6 WBCs which were harvested from $7.5mL$ whole blood using standard density gradient separation. The cancer cells were fluorescently stained to enable tracking through the device. The average capture efficiency was 68.3% and the average percentage reduction in PBMCs was 99.33%. This capture efficiency compares favourably to other studies, however the enriched sample of tumour cells is in a background of approximately 80000 WBCs.

DEP separation requires a fundamental dielectric difference between cancer cells and blood cells. Gascoyne et al. (2013) studied the dielectric properties of over 50 cancer cell lines using field flow fractionation. The data was compared with optical images which showed that tumour cells were bigger than blood cells and had a rougher membrane, which corroborated the lower dielectric crossover frequency and increased membrane capacitance of tumour cells observed in the experimental data.

6.2.5 Summary of Recent CTC Literature

CTC capture using EpCAM coated surfaces has a high level of CTC capture from clinical patients. CTC identification requires intervention to label cells, but automated image analysis software is a step towards full automation. The system is however very slow, taking many hours to process a single $7.5mL$ blood sample and will not capture EpCAM negative CTCs. Size filtration is a fast capture method; a $7.5mL$ blood sample can be filtered in 3 to 5 minutes. When compared to the CellSearch system, size filtration detects more CTCs, but counts both EpCAM positive and negative cells as CTCs. Dielectric separation captures CTCs into a solution (as opposed to on a surface or in a pore) which preserves the cells and enables further manipulation. However, the system

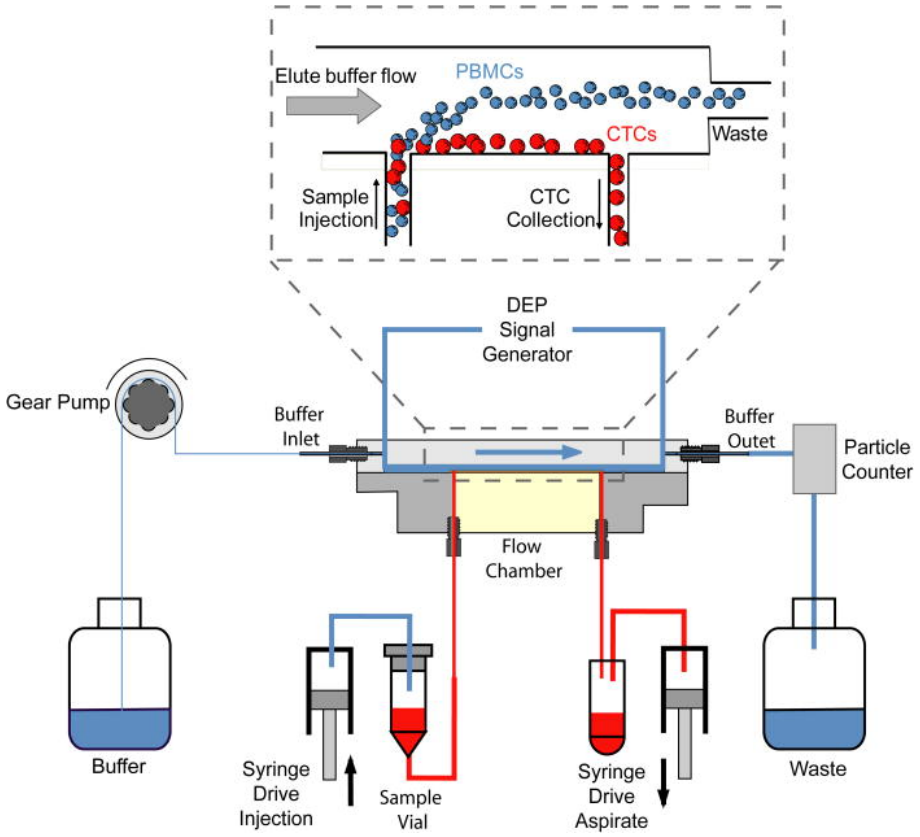

Figure 6.6: Schematic diagram of the commercial ApoStream DEP separation device reported by Gupta et al. (2012).

is the only setup which requires the RBCs to be removed prior to separation. RBCs could be removed by chemical lysis or density fractionation, however this additional step could also remove some of the CTCs. Dielectric separation has not been tested with clinical samples and is slower than size filtration, taking one hour to process a single sample. Although the CellSearch system is expensive and is limited to EpCAM positive CTCs, it can predict patient survival in a range of different cancers, and this prognostic value has only been demonstrated for enumeration of EpCAM positive CTCs.

In this chapter, MIC is used as a label-free technique to characterise tumour cells in whole blood, with the ultimate target to distinguish human CTCs from other blood cells without using surface markers. The MCF7 cells used in this chapter are cultured cancer cells originally sourced from a breast tumour, and are commonly spiked into healthy whole blood as a model for CTCs. The experimental work in Sections 6.3-6.9 was performed with Veronica Hollis.

6.3 Cell Culture and Blood Handling

MCF7 cells are EpCAM positive immortalised cancer cells originating from a breast cancer patient. MCF7 cells were grown in $75cm^2$ flasks in $10mL$ DMEM (Dulbecco's

Modified Eagle Medium) supplemented with 10% (v/v) heat-inactivated FBS (fetal bovine serum), $2mM$ L-glutamine, $1mM$ sodium pyruvate, 1% NEAA (non-essential amino acids) and penicillin-streptomycin, at $37°C$ in 5% CO_2. Cells were detached with trypsin/EDTA, washed and re-suspended in growth medium prior to experiments.

Whole blood samples were obtained from healthy donors with informed consent. Finger prick and venous blood (0.5 and $6mL$ respectively) was collected into Vacutainer tubes (K_2EDTA 15% Becton Dickinson). Following collection the blood tubes were placed on a roller and continually mixed at room temperature; all subsequent processing and experimental work was carried out within 8 hours.

In all experiments, RBC lysis was performed to enrich the number of rare cells compared to the total number of cells present. This was achieved by addition of lysis solution (0.12% formic acid, 0.05% saponin) to whole blood, $12\mu L$ lysis solution per $1\mu L$ blood. The reaction was quenched after 6 seconds by the addition of 0.6% w/v sodium carbonate and 3% sodium chloride, $4.4\mu L$ per $1\mu L$ whole blood. Typically $50\mu L$ whole blood is lysed with $600\mu L$ lysis solution and then $265\mu L$ quench solution is added. This is the protocol reported by Holmes et al. (2009) to remove RBCs from whole blood to measure the WBCs. The effect of RBC lysis on the MCF7s was investigated and is discussed in Section 6.5.

6.4 Identification of Tumour Cells in Blood

Identification and discrimination of MCF7s from other blood cells was investigated using MIC and results compared with optical detection using a BD FACSAria. $10\mu L$ of a stock solution of MCF7s containing approximately 5×10^6 cells per mL was spiked into $50\mu L$ whole blood. Next MCF7s were labelled by addition of $50\mu L$ anti-EpCAM-FITC and incubated at 5°C for 10 minutes as specified by the manufacturers' instructions. RBCs were lysed as described in Section 6.3. The sample was divided in two, and half was measured on the MIC at $500kHz$ and $2MHz$ ($2.5Vpp$) at a flow rate of $40\mu Lmin^{-1}$. The MIC chip was suspended over a custom optical setup to simultaneously measure fluorescence to verify the MCF7 cells. The optical setup can detect 3 colour fluorescence (515, 675 and $>715nm$), has 2 excitation lasers (488 and $633nm$) and was built previously by Holmes et al. (2009). The second half of the solution was measured on a BD FACSAria at a relative flow rate of 4 which corresponds to approximately $40\mu Lmin^{-1}$, the same as used on the MIC.

Figure 6.7 and Figure 6.8 show a scatterplots of the optical and electrical properties of the cells, colour coded for fluorescence (EpCAM). MCF7s are approximately twice the diameter of WBCs and this difference is seen in the low frequency impedance which measures the volume of cells. The MIC is compared with literature values in Table 6.1. The table shows the mean diameter of the WBC subpopulations and MCF7s is similar

to previous studies performed using electrorotation or field flow fractionation. For some cell types a range of values is listed because of multiple literature values. Forward scattered light (FSC) also measures cell size but does not scale linearly and thus the overlap between MCF7s and WBCs is greater.

	MIC		Literature (Gascoyne et al., 2013)	
Cell type	Mean diameter	SDev diameter	Mean diameter	SDev diameter
MCF7	18.0	2.1	18.2	7.4
Lymphocyte	6.7	0.37	6.0-7.0	0.1-2.6
Monocyte	8.4	0.32	8.4-9.2	0.1-0.7
Neutrophils	8.2	0.36	8.1	0.12

Table 6.1: Comparison of the diameter of MCF7s and blood cells measured on the MIC with values from the literature.

Side scattered light (SSC) measures the granularity of cells and the results show the MCF7 population is close to the monocyte subpopulation. The ratio of high to low frequency impedance is a measure of cell membrane capacitance relative to cell volume. It is known that tumour cells tend to have a higher membrane capacitance than blood cells which is due to ruffles, folds and microvilli which increase the surface area of the membrane relative to volume of the cell (Shim et al., 2013). This difference is observed as a difference in impedance ($2MHz$ / $500kHz$) between the MCF7s and WBCs, thus if the MCF7s were smaller, identification could still be achieved based on opacity. The impedance of MCF7s at different frequencies is described in Section 6.6. Overall there is a much greater separation between the MCF7s and WBCs when measured on the MIC compared to the FACSAria. This large difference in electrical properties demonstrates the potential for identifying low numbers of tumour cells from a large number of blood cells using the MIC.

6.5 Viable and Non-viable Discrimination

This section demonstrates discrimination of viable (healthy) and non-viable tumour cells. A cell is defined as viable if its membrane is intact, which is tested by adding a dye to the cell suspension. If the dye penetrates the membrane, the cell is non-viable. For viable cell counting using flow cytometry, Propidium Iodide (PI) is commonly used, which penetrates the membrane of non-viable cells, binds to DNA and fluoresces red on excitation with a blue or green light source. MIC should be able to determine the viability of cells without the need for a cell stain because if the cell membrane is leaky the electrical properties of a cell will be different. To investigate this, MCF7s were harvested as described in Section 6.3, except the cells were resuspended in PBS instead of cell media. PBS is the correct pH and osmolarity for cells, except that it is missing the nutrients required for growth. The cells were left for two hours at room temperature and then stained with FITC-EpCAM and PI. MCF7s express EpCAM and

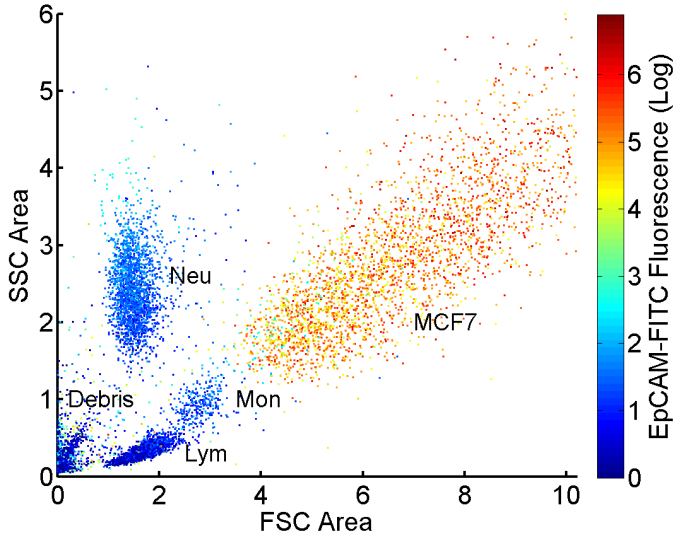

Figure 6.7: FACS measurement of a sample containing WBCs and MCF7 cells (30,000 total events). MCF7s are EpCAM positive and all WBCs are EpCAM negative. The three most numerous WBC subpopulations can be distinguished: Neutrophils (Neu), Monocytes (Mon) and Lymphocytes (Lym). The debris is cell fragments and ghosts which are left over from the RBC lysis.

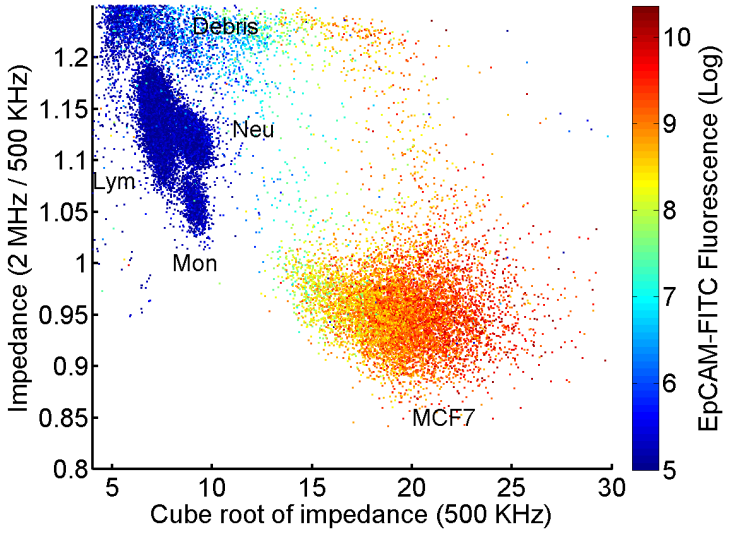

Figure 6.8: MIC measurement of a sample containing WBCs and MCF7 cells (30,000 total events). Simultaneous fluorescence was also measured to identify the EpCAM positive MCF7s from the EpCAM negative WBCs. The three main WBC subpopulations and lysis debris are also labelled.

are fluorescent in the FITC channel. Beads ($6\mu m$ diameter) were added to the cell suspension and the mixture was measured at a flow rate of $40\mu L min^{-1}$ at $500kHz$ and $2MHz$. Simultaneously two colour fluorescence ($515nm$ for FITC and $675nm$ for PI) was measured.

Figure 6.9a shows the impedance data of the MCF7 cells and beads coloured according to EpCAM fluorescence. The figure shows there is wide distribution of MCF7s from approximately 15-25μm (x-axis) and 0.75-1.1 (y-axis). Figure 6.9b is the same impedance data, but coloured according to the second fluorescence channel (PI). The beads are fluorescent in the PI channel and appear as a tight distribution around the coordinates (*6, 1.15*). MCF7s above 1 (y-axis) stain positive for PI indicating they are non-viable. This explains the wide distribution in impedance of cells at $2MHz$ / $500kHz$ when compared to Figure 6.8.

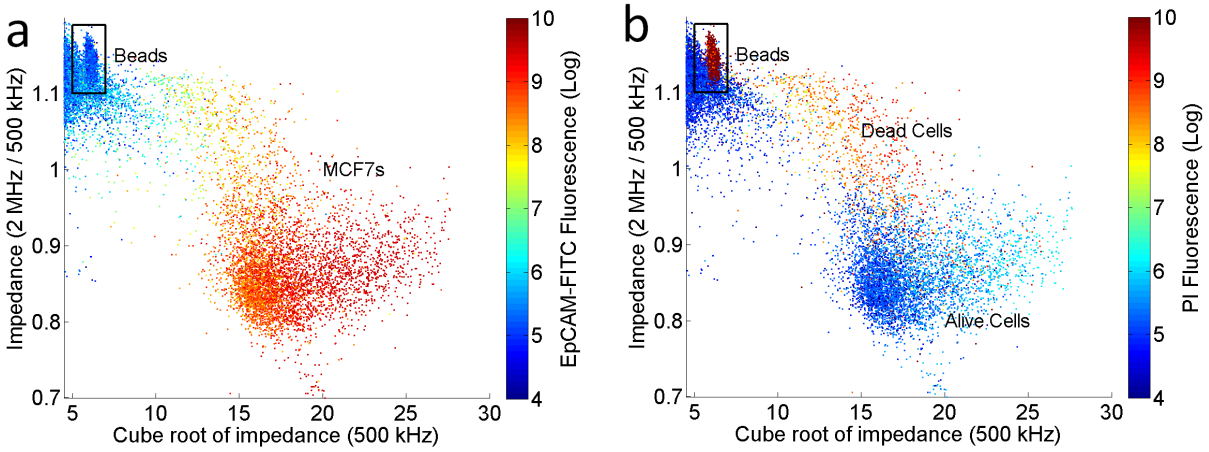

Figure 6.9: Scatterplot of the impedance of a mixture containing MCF7s and beads (30,000 events), colour coded for a) EpCAM fluorescence which MCF7s express and b) PI which labels non viable cells.

6.6 Effect of RBC Lysis on the MCF7 Count

Human CTCs are very rare and can be as low as one cell per millilitre of blood, which contains approximately 5×10^9 RBCs. The maximum throughput of MIC is around 1000 cells per second, thus to measure every cell in $1mL$ of whole blood would take 58 days. The RBCs can be selectively lysed which leaves the CTCs and WBCs (7×10^6) which would reduce the measurement time by around 700. To check that the lysis protocol (described in Section 6.3) did not damage or remove the MCF7 cells, MCF7s were spiked into whole blood before lysis and compared with MCF7s spiked into a sample of blood after lysis as illustrated in Figure 6.10.

$10\mu L$ MCF7 stock solution (containing 5×10^6 MCF7s per mL) was spiked into $50\mu L$ whole blood either before or after RBC lysis and measured at 0.5 and $2MHz$ using the MIC. Each experiment (corresponding to a before/after pair) was performed in triplicate for 3 different blood donors and MCF7s harvested on 3 different days. Figure 6.11 and Figure 6.12 are example scatterplots of the measured impedance when MCF7s were added to whole blood before and after lysis respectively.

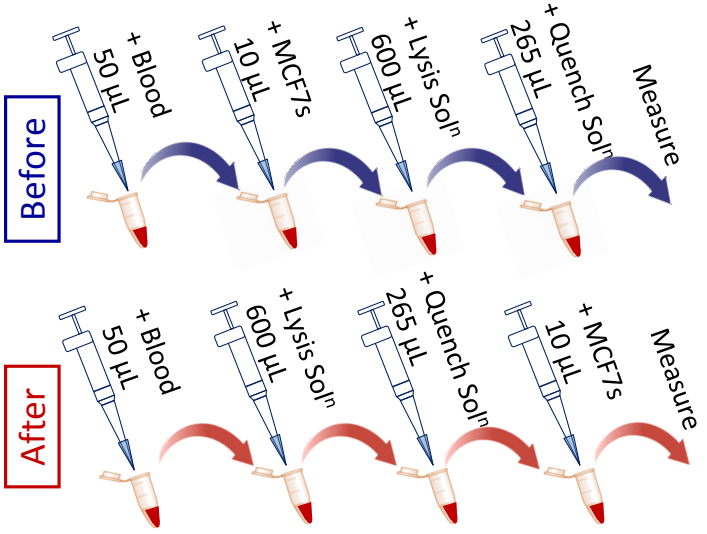

Figure 6.10: Illustration of the protocol used to test if MCF7s are damaged or removed by the RBC lysis protocol. MCF7s are spiked into blood before or after lysis and the count is compared.

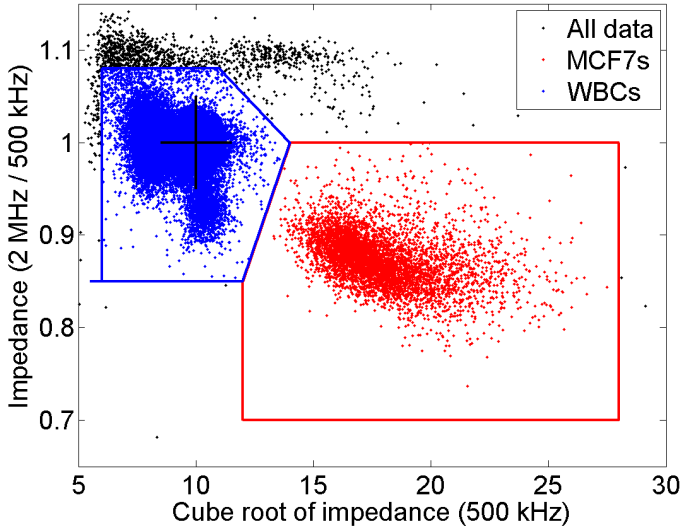

Figure 6.11: Scatterplot of the impedance of MCF7s and WBCs. The MCF7s were spiked into whole blood before RBC lysis.

To determine the ratio of MCF7s and WBCs, each graph was normalised and gates were used to maintain consistency between experiments. Each scatterplot was first normalised such that the centre of the neutrophil populations (the most numerous WBCs, marked with the + sign in each figure) appeared at (*11,1*). This was performed so that the same gates could be used to automatically count the WBCs and MCF7s for each experiment. This normalisation was achieved using a single multiplication scaling factor for each of the x and y coordinates. The scaling factors only varied slightly between experiments; the CV of the scaling factors from the 9 experiments were 6% and 2% for the x-axis and

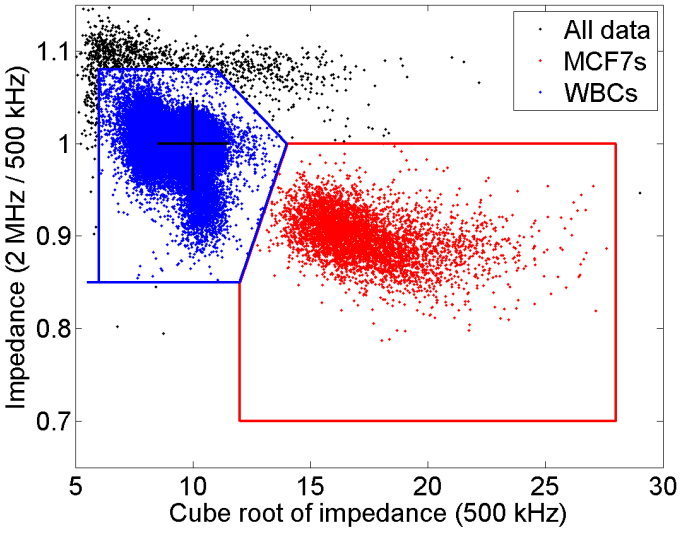

Figure 6.12: Scatterplot of the impedance of MCF7s and WBCs. The MCF7s were spiked into whole blood after RBC lysis.

y-axis respectively. The number of WBCs and MCF7s within each gate shown in the figures were counted using a Matlab script.

The ratio of the WBCs to MCF7s count is shown in Figure 6.13. There is no significant difference in the WBC/MCF7 count between spiking MCF7s into the blood before or after lysis (two tailed t-test, P=0.997). Donor 3 had a particularly low WBC count hence the WBC/MCF7 count for the sample was smaller, but similar, for lysis before or after MCF7 addition. This demonstrates the lysis protocol can be used to remove the RBCs without damaging or removing the MCF7s, and thus enrich the MCF7s.

6.7 Optimum Measurement Frequency

To detect low numbers of human CTCs in a background of many thousands of WBCs, there must be a significant separation in the two populations. The low frequency impedance signal measures the electrical volume of each cell and reducing this frequency will not change the discrimination. In these experiments the lowest measurement frequency is $500kHz$ with the present electrodes. At lower frequencies, the double layer capacitance (discussed in the Chapter 2) shields the bulk electrolyte from the applied voltage and prevents cell measurement. Although the MCF7 cells used in this study are representative of human CTCs, it is expected that some CTCs are smaller than MCF7s and will overlap the WBC populations in size. To aid separation, there will be an optimum high frequency measurement signal which will emphasise the difference in membrane capacitance between the cancer and blood cells. This was investigated by simultaneous multi-frequency measurement of a mixture of MCF7s and WBCs.

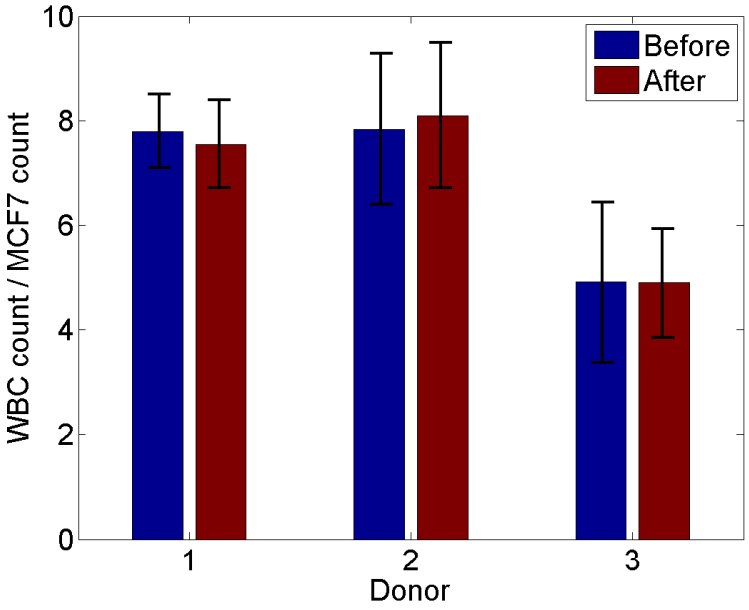

Figure 6.13: Bar chart shows the ratio of WBCs to MCF7s when MCF7s were added before or after RBC lysis.

$10\mu L$ of MCF7 stock solution (5×10^6 cells per mL) was spiked into $50\mu L$ whole blood. Next RBCs were lysed as described in Section 6.3. Polystyrene beads ($6\mu m$ diameter) were added to the sample and used to normalise the frequency response. Solid insulating objects have a constant impedance across the frequency range used in these experiments, and can be used to remove any non-linear response due to the double layer capacitance or parasitic capacitances in the electronic detection circuit.

The sample containing WBCs, MCF7s and beads was measured simultaneously at five frequencies (0.5, 1, 2, 4, $8MHz$) at $1Vpp$ per frequency at a flow rate of $40\mu Lmin^{-1}$. This was performed in triplicate for three different blood donors and MCF7s harvested on different days.

Figure 6.14 is a scatter plot of the impedance at $500kHz$ and $8MHz$ for one of the experiments. At $8MHz$ the separation between the beads and WBCs is greatest and each population can be easily gated. The bead population was used to normalise the scatter plot such that the centre of the bead population was set to the coordinates (*6,1*). The scaling was performed using a multiplication factor for the x and y values for each experiment, which enables the same gates to be used across all experiments.

The frequency response of the WBCs and MCF7s is plotted in Figure 6.15 and was calculated as follows.

1. Calculate the mean impedance of the bead population at each of the 5 frequencies.
2. Individually normalise each event by dividing the impedance of each MCF7 and WBC event by the mean impedance of the bead population at each frequency.

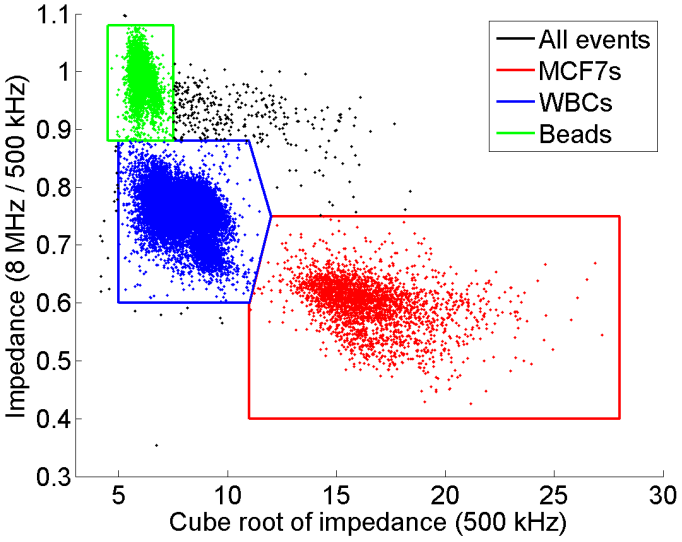

Figure 6.14: Scatter plot of the impedance of a mixture of MCF7s, WBCs and 6 μm diameter beads measured at $500kHz$ and $8MHz$. The data has been normalised by a scaling factor for the x and y values such that the beads are at the coordinates *(6,1)*. Also shown are the gates used to identify each population.

3. Divide the impedance of each MCF7 and WBC event at 1, 2, 4 and $8MHz$ by the impedance at $500kHz$.

4. Calculate the mean and standard deviation of the the MCF7 and WBC populations and plot.

Out of the 4 upper frequencies (1, 2, 4 and $8MHz$), the separation between WBCs and MCF7s is greatest at $4MHz$. There is similar separation at $8MHz$, but at this frequency the magnitude of the signal is reduced due to parasitic capacitances in the electrical connection. This figure is compared to simulations based on values from the literature in the next section.

6.8 MCF7 and WBC Simulation

Maxwell's mixture theory was used to simulate the frequency dependent dielectric properties of model MCF7s and WBCs, and compared to the experimental data shown in Figure 6.15. The permittivity and conductivity of the medium were set to model PBS ($1.6Sm^{-1}$ and $80\varepsilon_0$). The dielectric properties of the cell were varied in the range shown in Table 6.2, based on expected values from the literature. At each of the four opacity frequencies (1,2,4 and $8MHz$) the model was compared with the mean of the experimental results to find the dielectric parameters which produced the least squared error between the model and the four experimental data points. The resulting parameters are shown in Figure 6.16 along with the fit using values from the literature.

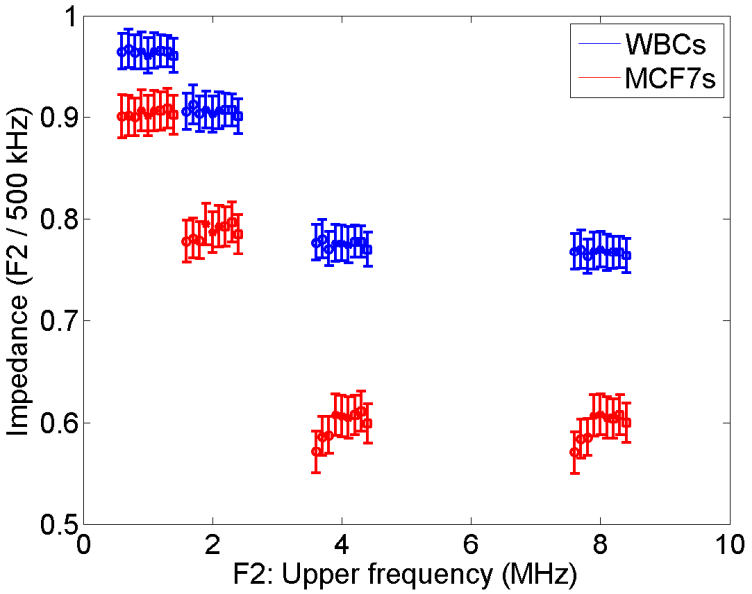

Figure 6.15: Simultaneous frequency sweep of a mixture of MCF7s and WBCs normalised against $6\mu m$ diameter beads. The x-axis values are plotted offset for visual clarity, and the same frequencies were used in each experiment. The reduction in impedance of the cells at higher frequencies is due to the membrane relaxation.

	Model range	Model best fit	Literature
WBCs			
Membrane capacitance (mFm^{-2})	5 to 30 (steps of 1)	18	9-15
Cytoplasm conductivity (Sm^{-1})	0.1 to 2 (steps of 0.02)	0.34	0.56-0.73
Cytoplasm permittivity (Relative)	40 to 200 (steps of 5)	85	104-151
Radius (μm)	3 to 10 (steps of 0.1)	7.7	3.3-4.7
MCF7s			
Membrane capacitance (mFm^{-2})	10 to 30 (steps of 1)	29	22.2
Cytoplasm conductivity (Sm^{-1})	0.1 to 2 (steps of 0.02)	0.62	0.14-0.40
Cytoplasm permittivity (Relative)	40 to 200 (steps of 5)	40	NA
Radius (μm)	3 to 10 (steps of 0.1)	10.5	9.1+/-3.7

Table 6.2: Table of dielectric parameters. Literature values from Gascoyne et al. (2013).

There is a significant difference in the parameters from the best fit model, and values from the literature. The problem in fitting dielectric parameters to this experimental data is because at the low frequency measurement ($500KHz$) there is some dielectric relaxation. Ideally, more lower frequency measurements (below the relaxation frequency) should be used so that the entire relaxation can be observed.

Figure 6.17 show the simulated impedance of a WBC and MCF7 with varying membrane capacitance and cytoplasm conductivity (parameters in figure caption) over a wider frequency range. (a) shows that at 4 and $8MHz$, the MCF7 impedance is entirely determined by the cytoplasm conductivity. Below this frequency both membrane

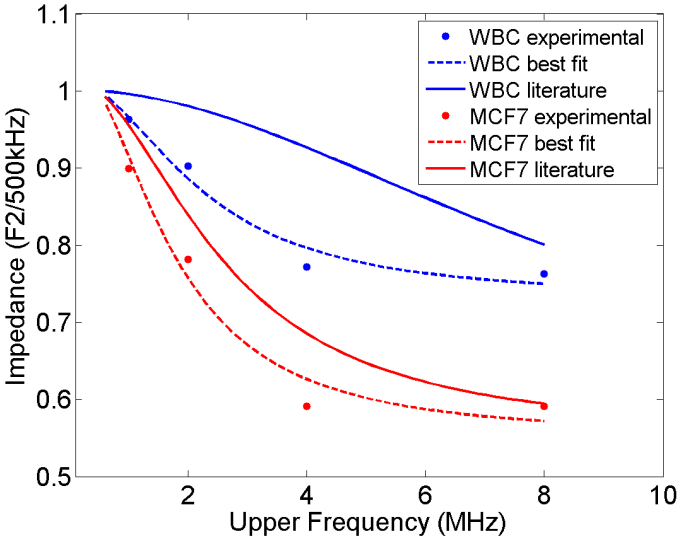

Figure 6.16: Average values of the experimental data of Figure 6.15 along with the best fit dielectric model (MMT). Also shown is the expect response based on values from the literature.

capacitance and cytoplasm conductivity change the response. For the WBCs (b), the response at $8MHz$ is determined by the cytoplasm conductivity, whereas at $4MHz$, both the membrane capacitance and cytoplasm conductivity determine the response. The magnitude of the impedance at each frequency is higher for the MCF7 model due to the bigger size of the MCF7 (double in radius = 8× in electrical volume).

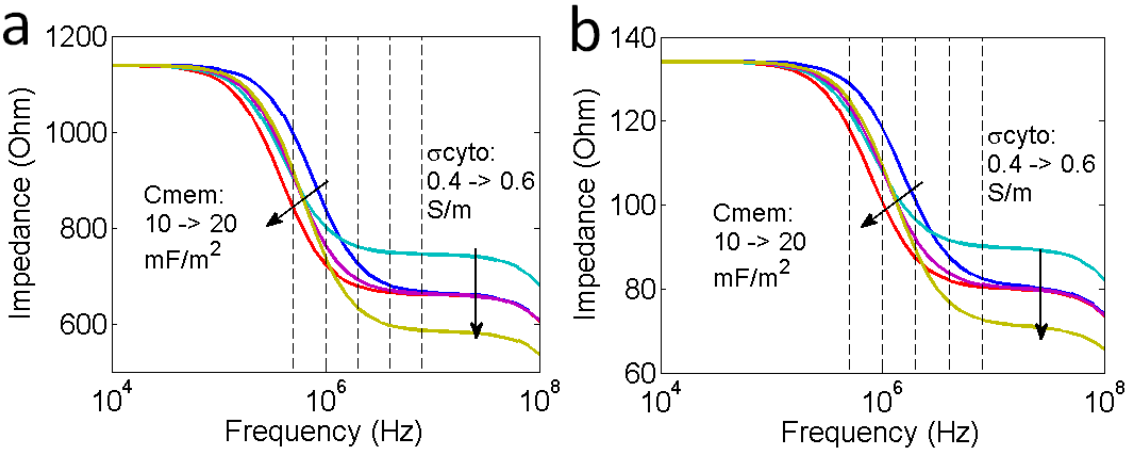

Figure 6.17: Simulated impedance of a) a model MCF7 of radius 10 μm and b) a model WBC of radius 5 μm. In both cases the membrane conductance was 10^{-8} and the membrane thickness was $5nm$. The membrane capacitance, Cmem, was varied (10, 15 and $20mFm^{-}2$) for a fixed cytoplasm conductivity, σcyto of $0.5Sm^{-1}$. Separately σcyto was varied (0.4, 0.5 and $0.6Sm^{-1}$) for a fixed Cmem ($15mFm^{-2}$). The impedance was calculated as the difference between a box containing PBS $(40\ \mu m)^3$, $\varepsilon = 80\varepsilon_0$, $\sigma = 1.6Sm^{-1}$) and the same box with the cell model in the centre.

The dielectric properties of MCF7s and WBCs from the literature suggest that membrane capacitance is approximately $20mFm^{-2}$ and $10mFm^{-2}$ respectively. This suggests that the difference in impedance at high frequency (Figure 6.15) is a combination of differences in both cytoplasm conductivity and membrane capacitance of the MCF7s and WBCs. Maxwells mixture theory was used to find the dielectric parameters which best fitted the experimental data. The best fit parameters indicated that the MCF7s have a higher specific membrane capacitance than the WBCs which is expected from the literature, however the value was higher than expected in both cases.

6.9 Enumeration Limit

Since human CTCs are rare (typically 1-100 per millilitre of whole blood), the limit of detection of the MIC system was tested by spiking in MCF7s from serial diluted stock solutions. A solution of MCF7s in media (3×10^6 per mL) was prepared as described in Section 6.3. Samples of this solution were diluted 1:10 and 1:100 with media. $10\mu L$ of the three MCF7 stock solutions containing approximately 30000, 3000 and 300 MCF7s was spiked into $50\mu L$ whole blood. Assuming a typical WBC count of 6×10^6 per mL, the MCF7 to WBC ratio is 1:10, 1:100 and 1:1000. RBCs were lysed and $6\mu m$ beads were added as a reference. Each sample was measured using the MIC at $40\mu Lmin^{-1}$ at 0.5 and $4MHz$ which was determined to be the optimal measurement frequency in Section 6.7. Not all the sample was measured; the measurement time was 2, 5 and 13 minutes for the 1:10, 1:100 and 1:1000 samples to ensure at least 100 MCF7s were measured in each case. For each set of dilutions a control was performed where $10\mu L$ media (without MCF7s) was spiked into $50\mu L$ whole blood, RBCs were lysed and the sample was measured for 13 minutes. Each experiment was performed in triplicate for three different blood donors and MCF7 stock solutions. Figure 6.18 shows scatter plots of the impedance for 1 set of experiments (1:10, 1:100, 1:1000 dilution and control). The $6\mu m$ beads were used to normalise the scatter plots such that the mean of the bead population appeared at *(6,1)* and the same gates could be used in all experiments.

The ratio of the MCF7s to WBCs for the different dilutions is displayed in Figure 6.19 as a bar chart. Each blood donor naturally has a different total WBC count (normal clinical range is 4–11 per fL) and is seen in the figure as the slight variation in bar heights. In the 9 control experiments, the following numbers of events were found within the MCF7 gate (despite no MCF7s being added): 0, 2, 1, 0, 1, 0, 0, 1, 0 (average = 0.56 events). These unknown events are cells, not solid objects because their y-position indicates they exhibit membrane relaxation. Solid particles (such as beads) appear much higher (around 1) on the y-axis. However, it is not clear what these cells are.

The results show a linear trend indicating the MIC is capable of measuring low concentrations of MCF7s in whole blood, however human CTCs are still approximately

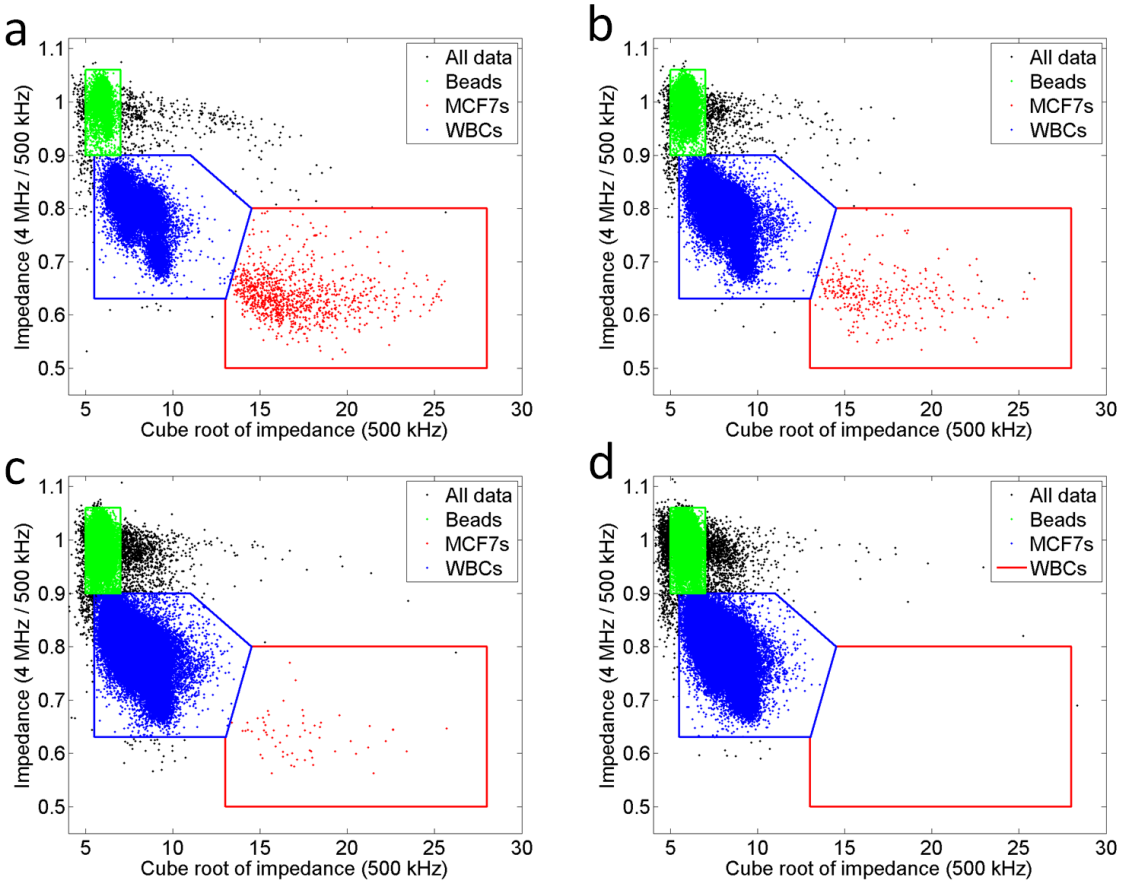

Figure 6.18: Scatterplot of the impedance of a mixture of MCF7s, WBCs and 6 μm beads. The ratio of MCF7s to WBCs is approximately (a)1:10, (b)1:100 and (c)1:1000. Results of the control experiment where no MCF7s were added is shown in (d).

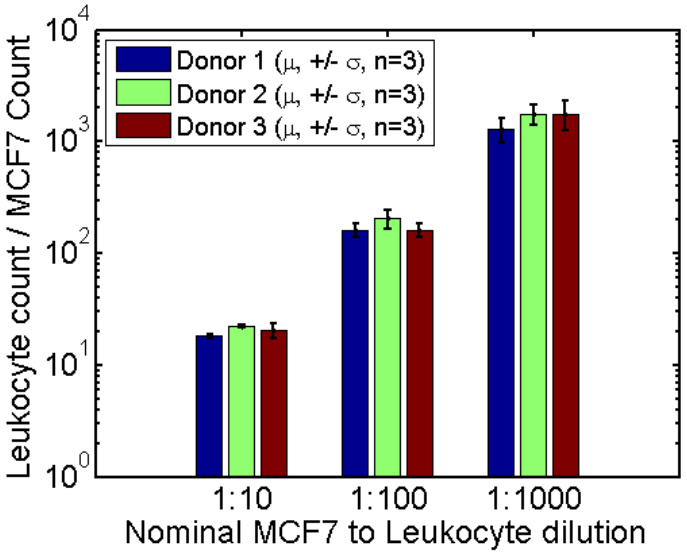

Figure 6.19: Bar chart showing the measured WBC count divided by MCF7 count for serial diluted samples.

1000 times less concentrated. The detectable level of MCF7s using MIC is limited by the measurement time. To measure $1mL$ of lysed blood would take 7.6 hours at the flow rate used in these experiments ($40\mu Lmin^{-1}$). To detect lower numbers of tumour cells in blood, the throughput must be increased or the sample must be pre-enriched. The throughput could be increased by flowing faster but the flow rate is limited by the sampling rate of the electronics. Parallel devices could be used however each device would require separate measurement electronics.

6.10 Rare Cell Enrichment

This section demonstrates detection of low levels of MCF7s close to the clinically relevant level of CTCs using magnetically activated cell sorting (MACS) to pre-enrich the MCF7s. Although MACS enriches MCF7 using the EpCAM surface maker and is therefore not label-free, it is used in these experiments for proof-of-principle and could be replaced with DEP pre-enrichment such as the ApoStream system (Gupta et al., 2012) described in Section 6.2.4.

In MACS, magnetic nanoparticles ($50nm$) are coated with a cell-specific antibody and added to a mixture containing the cells of interest. The magnetic particles bind to the target cells and a magnet is used to separate the target cells from the mixture.

MACS sorting of MCF7s was performed as shown in Figure 6.20 and as follows: Approximately 100 MCF7s ($10\mu L$ of MCF7 stock containing 10^4 cells per mL) were spiked into $1mL$ whole blood. The spiked blood was incubated with $200\mu L$ anti-EpCAM magnetic nanobeads and $100\mu L$ FcR blocking reagent (Miltenyi Biotec) for 30 minutes on a roller at room temperature. FcR blocking reagent was used to prevent non-specific binding of the magnetic beads to EpCAM negative cells. Next RBCs were lysed as described in Section 6.3. The magnet was placed on the column (MS, Miltenyi Biotec) and $3mL$ running buffer (PBS + $2mM$ EDTA + 0.5% bovine serum albumin) was passed through the column under gravity to prime it. Next the lysate was passed under gravity through the column. The solution was collected at the bottom of the column. Any cells not magnetically labelled pass through the column and are collected in this fraction which is called the negative fraction. Next the magnet was removed from the column. Magnetically labelled cells were removed from the column by pushing $1mL$ filtered elution buffer (Miltenyi Biotec) through the column using a supplied plunger. The plunger also pushed some air through the column which also removed any trapped liquid in the column and consequently the positive fraction volume was higher than the $1mL$ elution buffer used. In each case this volume was measured and was typically $1.35mL$. For each experiment a control was performed using an identical procedure except the MCF7s were not included. This protocol was repeated 5 times, each with blood from a different donor and MCF7s harvested on a different day.

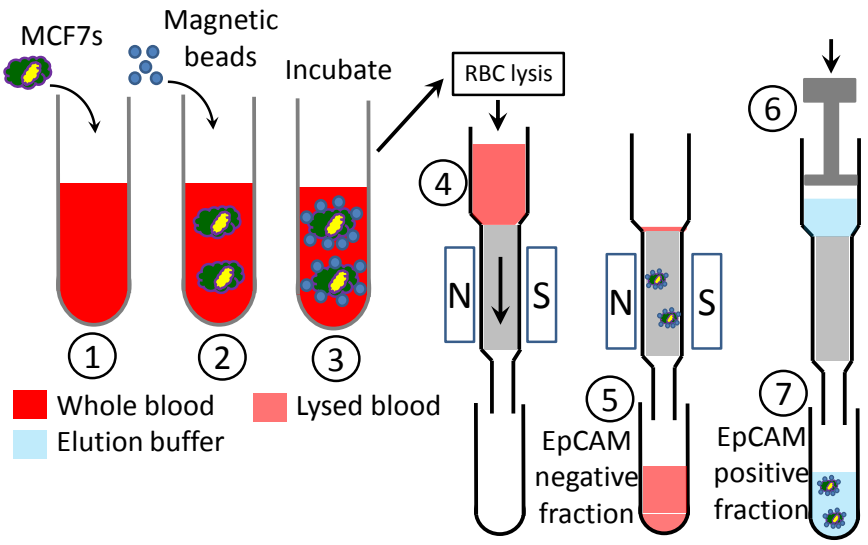

Figure 6.20: Overview of the MACS protocol used to enrich MCF7s from whole blood. (1) MCF7s were spiked into whole blood. (2) Magnetic nanoparticles were added and the sample was (3) incubated for 30 minutes. Red blood cells were lysed and the sample was passed through the column under gravity (4) and the output collected (5). The magnetic was removed and elution buffer was forced through the column (6) and the output collected (7).

The MCF7 stock solution and the positive and negative fractions were measured with MIC at $500kHz$ and $4MHz$ at $40\mu Lmin^{-1}$. In each case $6\mu m$ diameter beads were added and used to normalise the data so that the same gates could be used for all experiments. Figure 6.21 shows the scatterplots for the positive and negative fractions when MCF7s were added (a and c), and the control where no MCF7s were added (b and d). The stock solution measurement is shown in Figure 6.21e. The gates used in the positive and negative fraction measurement are identical to the gates used in the serial dilution experiments (in Section 6.9). The gate for the MCF7 stock measurement (Figure 6.21a) was adjusted due to different conductivity of the suspending liquid (cell culture media).

Measurement of the MCF7 stock solution was used to determine the exact concentration and therefore the number of MCF7s spiked into the sample. The MCF7 stock solution was measured for approximately 2 minutes corresponding to around $80\mu L$. The negative fraction was also measured for 2 minutes which is a small percentage of the total volume of around $18mL$. Measuring the whole negative fraction would take too long (7.5 hours). Approximately half of the positive fraction was measured which took around 15 minutes. The entire positive fraction could not be measured because some solution was lost while loading the device.

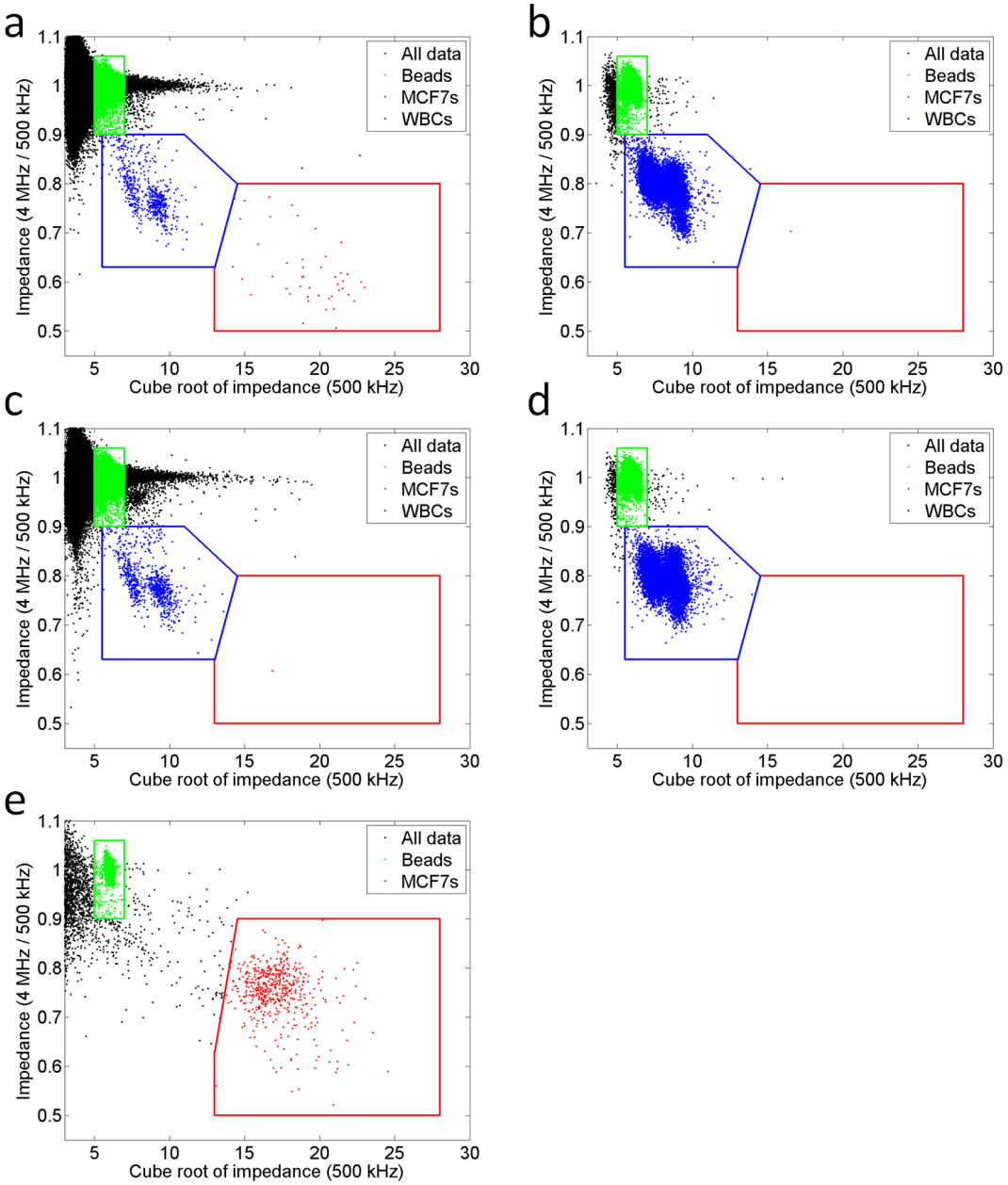

Figure 6.21: Scatterplots showing EpCAM positive (a) and negative (b) selection of approximately 100 MCF7s spiked into $1mL$ whole blood. (c) and (d) show a repeat of procedure without adding MCF7s (control). (e) shows the measurement of the MCF7 stock solution which was used to calculate the number of cells added.

The results of the experiments are shown in Table 6.3. The number of MCF7s added is the measured MCF7 stock solution concentration (cells per mL) divided by 100 since $10\mu L$ stock solution was spiked into the $1mL$ whole blood. The volume of the positive fraction measured (%) is the measurement time (seconds) multiplied by the volumetric flow rate (40/60 μLs^{-1}), divided by the total eluted volume of the positive fraction (typically $1.35mL$, but this varied slightly between experiments and was measured in

each case). The expected MCF7 count is the number of MCF7s added (column 2), multiplied by the fraction of the total volume measured (% measured /100).

Donor	MCF7s added	Positive fraction (MCF7s)			Positive fraction (Control)		
		Volume measured	MCF7 events		Volume measured	MCF7 events	
			Expected	Measured		Expected	measured
1	71	43%	30	11	42%	0	0
2	74	43%	32	33	50%	0	3
3	68	50%	34	45	49%	0	1
4	65	50%	33	32	48%	0	1
5	48	50%	24	22	46%	0	0

Table 6.3: Table showing the number of measured MCF7 events compared with the expected number.

The results demonstrate that using MACS pre-enrichment, tumour cells can be detected in whole blood close to the diagnostic level of human CTCs. Average recovery of the MCF7s was 102%, however recovery was only 36% in experiment 1 which indicates many MCF7s were lost or damaged during the process. This loss is likely to be during the MACS separation, but it is unclear why only this experiment was affected. Recovery in experiment 3 was 131% which indicates some other cells were present in the MCF7 gate. These are most likely to be WBCs, but it is unclear why these are present only in this one experiment. Recovery in the other 3 experiments was 104%, 98% and 92%, all close to ideal recovery.

This section has demonstrated impedance analysis of tumour cell lines spiked into whole blood, and shown than MIC has the potential to measure CTCs. In this study, tumour cells were spiked into whole blood by adding a small volume of a dilute cell suspension (around 100 cells). Human CTCs can be rarer, and so the limit of detection and experimental repeatability needs to be tested. This would be performed by manually pipetting a precise number of single cells one-by-one using a microscope. The cells could be marked with a fluorescent dye to confirm detection and to quantify the number of non tumour cells detected in the positive gate. In these experiments, the gate used to decide if a detected cell was a tumour cells was kept consistent across experiments, however the position of the gate was manually determined by eye. If there was more experimental data, a 2D Gaussian could be fitted to find the optimum position of a gate and provide the probability of non tumour cells within the gate.

Magnetic enrichment of MCF7s was used as a proof of principle procedure to demonstrate that MIC can measure low numbers of MCF7s spiked into whole blood. It would be beneficial to use a label-free separation technique such as DEP to enrich all tumour cells (not just EpCAM positive cells). If this were to be developed, the system would need to be tested with clinical samples: the number of detected CTCs would be corroborated with the clinical outcome of patents to determine if the measured level of CTCs was of diagnostic or prognostic value.

6.11 Conclusions

Using MIC label-free detection and identification of tumour cells (MCF7s) spiked into whole blood was demonstrated with simultaneous fluorescence measurement used to confirm the tumour cell population. RBCs were sucessfully removed without reducing the MCF7 count using a lysis solution of saponin and formic acid. This decreased the background cell count and enabled the detection limit of tumour cells to be 3 orders of magnitude lower.

The frequency response of WBCs and MCF7s was investigated using simultaneous multi-frequency measurements. Experimental data showed that the separation in populations (for distinguishing between cell type) was greatest at $4MHz$. This dielectric difference between the cell populations was investigated by theoretical modelling. Maxwell's mixture theory was fitted to the experimental data to determine the best fit dielectric parameters of the MCF7s and WBCs. The best fit showed that the the MCF7s have a higher specific membrane capacitance than WBCs which is in agreement with the literature. In the future, platinum black electrodes could be used to extend the measurement frequency range.

At this optimal measurement frequency which was found using the frequency sweep, MIC could detect rare tumour cells: small numbers of MCF7s (10's) in a background of 1000 times more WBCs. The only limit to measurement of clinically relevant levels (1000 times rarer) just using MIC is measurement time. This could be achieved by increasing the flow rate or running multiple devices in parallel. Instead, pre-enrichment of tumour cell was investigated. Magnetic separation was used to pre-enrich EpCAM positive cells before measurement using the MIC. Approximately 100 MCF7s were spiked into $1mL$ whole blood which is close to the clinical level of human CTCs. Recovery was close to ideal with an average recovery of 102%. Control experiments where no MCF7s were added showed almost no events (false positives) in the same MCF7 gate, on average just 1 event compared to around 30 events in the positive case. This demonstrates the high level of specificity of the MIC to detect tumour cells.

In summary, this chapter has demonstrated the potential to use MIC for label-free detection of tumour cells in whole blood, identifying breast cancer cells from WBCs based on dielectric differences between the cells. The device has the potential to offer a broader detection compared to the specific antibody markers which are typically used. The next step would be to test blood from cancer patients and compare the results with the FDA approved Veridex CellSearch.

Chapter 7

Erythrocyte Lysis

7.1 Introduction and Overview

The full blood count (FBC) is a widely used measurement of the most numerous cells present in blood. It can be used to diagnose a number of different diseases as described in Chapter 1. A single microlitre of blood contains approximately 5-6 million RBCs and 0.15-0.4 million platelets. To measure these cells, whole blood is diluted in a physiological buffer such as PBS and a size-based measurement is used to distinguish the smaller platelets ($10fL$) from the larger RBCs ($90fL$). Whole blood also contains five different subpopulations of white blood cells (WBCs), however the concentration of these is three orders of magnitude lower than the RBCs. To enable measurement of the WBCs in a practical time scale, the RBCs must first be lysed (removed) so that they are not counted. If the RBCs were removed from $3\mu L$ whole blood, a measurement of the remaining WBCs (21,000 cells) would take one minute at a throughput of 350 cells per second. This volume of blood contains enough WBCs to discriminate and count the three major subpopulations. If the RBCs remained, the measurement would take around twelve hours at the same throughput. This chapter describes the research that has been carried out to develop an automatic system to chemically lyse the RBCs to allow measurement of the three most numerous WBC subpopulations. This research builds on previous work which is summarised in the next section.

7.2 Background

Holmes et al. (2009) demonstrated measurement of the three main subpopulations of WBCs from whole blood (called a 3-part differential measurement) using an MIC. Chemical lysis of RBCs was performed by adding a lysis reagent (0.05% saponin + 0.12% formic acid) to whole blood, mixing with a pipette and then 6 seconds later adding

a quench solution (0.6% sodium carbonate, 3% sodium chloride) to halt the reaction (Figure 7.1). The mixture containing the WBCs was measured on the MIC with two simultaneous frequencies of $500KHz$ and $2MHz$. Lymphocytes ($7-8\mu m$ diameter) were distinguished from the larger granulocytes and monocytes ($10-12\mu m$) using the low frequency (electrical volume) measurement (Figure 7.2a). The impedance ratio ($2MHz$ / $500kHz$) is called the opacity and is a measurement of membrane properties of cells and can distinguish the similarly sized monocytes from neutrophils. Confirmation of each cell type was performed by labelling each cell type and using a custom fluorescence detection system. There was a good correlation (95% overall) between the MIC results and a commercial haematology analyser for the relative ratios of the WBC subpopulations for seven different samples (Figure 7.2b).

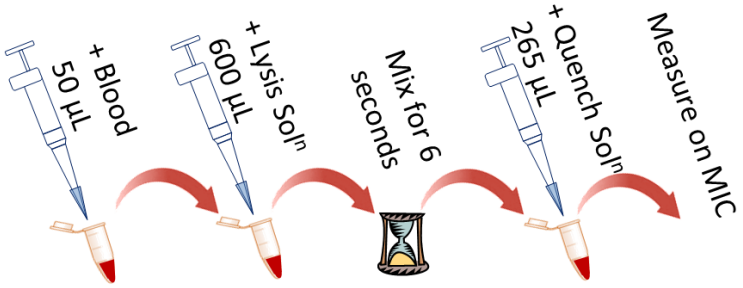

Figure 7.1: Standard RBC lysis protocol. Blood is mixed with a lysis solution for 6 seconds before a quench solution is added. This is referred to as "bulk lysis".

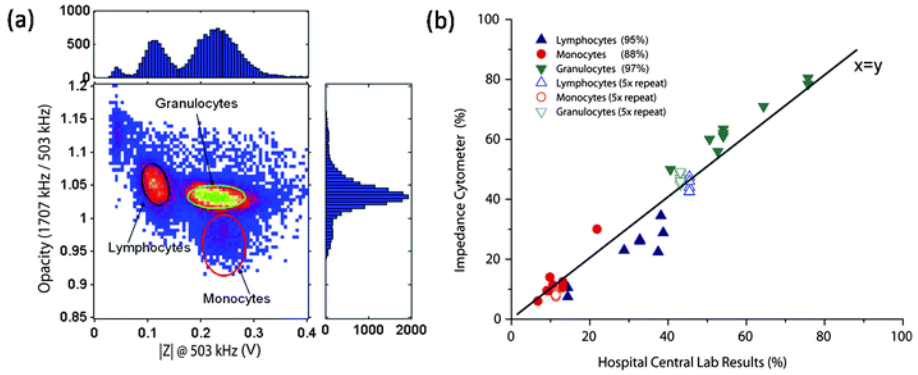

Figure 7.2: a) Density plot of the 3 main WBC subpopulations measured from whole blood (after RBC lysis). b) Comparison of the relative ratios of the 3 main WBC subpopulations measured on the MIC and on a commercial haematology analyser. Image from Holmes et al. (2009).

In this system, the measuring and mixing was performed by hand using pipettes, which is clearly not suitable for a consumer product. This is referred to as "bulk lysis". Later, the system was modified to use a continuous flow microfluidic lysis system (Han et al., 2012). The blood and lysis reagents flow through microfluidic channels where they mix

by diffusion for a specified time which is determined by the flow velocity and the channel lengths. Figure 7.3 shows an overview of the system.

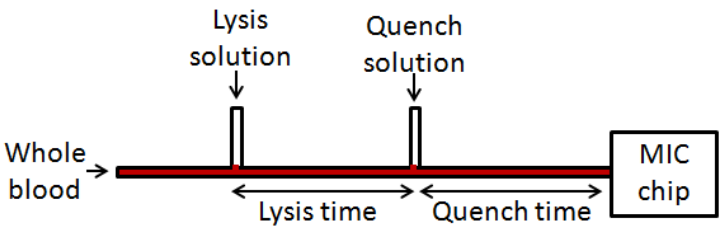

Figure 7.3: Illustration of a microfluidic lysis system. Whole blood flows along a channel where it meets a second channel containing lysis solution. Both liquids flow co-linearly and mix by diffusion. After the liquids have mixed for a predefined time (determined by the flow velocity and channel length), the mixture meets a channel containing quench solution. Mixing is performed by diffusion until the mixture flows through the MIC measurement chip and the individual cells are measured.

The lysis efficiency was measured at a range of different flow rates, which resulted in a range of different lysis times due to the fixed channel dimensions. The flow rate was varied between 80% and 130%, which equates to lysis times of between 4.6 and 7.5 seconds. The optimal flow rates were found to be 100 and 110% equating to a lysis time of 6.0 or 5.5 seconds respectively. However, subpopulation separation was poor (Figure 7.4) and sophisticated fitting algorithms were needed to distinguish each subpopulation.

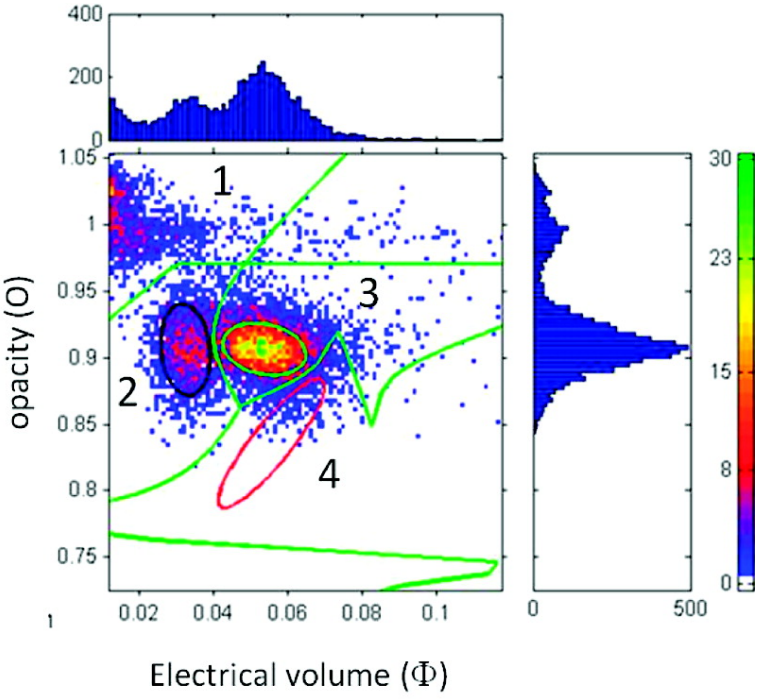

Figure 7.4: Density plot of the 3 main WBC subpopulations measured from whole blood after microfluidic RBC lysis. Image from Han et al. (2012).

The target of the research presented in this chapter was to maximise the separation in impedance signal between the three WBC subpopulations and to develop a system which can automatically perform RBC lysis. Firstly, the timing of the RBC lysis protocol was investigated over a much wider range compared with Han et al. (2012) to determine optimum lysis conditions. Secondly, a new microfluidic lysis with a micro mixer was developed. However, difficulties in repeatability and device manufacture of the microfluidic system led to the development of a stirred lysis system which produced clear separation between WBC subpopulations with the potential to be automated.

7.3 Bulk Lysis

The RBC lysis protocol used by Holmes et al. (2009) was sourced from a patent by Ledis et al. (1984). The lysis time was chosen to be 6 seconds and the time between quenching the reaction and measuring the cells (quench time) was not disclosed in the patent. In this section the effect of the lysis and quench time on the WBC differential measurement for bulk lysis (manual pipette mixing) was investigated, with the aim of optimising the protocol to obtain maximum separation between WBC subpopulations.

7.3.1 Lysis Timing

Whole blood ($50\mu L$ with EDTA anticoagulant) was added to an eppendorf and then mixed for 3 seconds with $600\mu L$ of lysis solution using a pipette (P1000). Mixing was performed by drawing and releasing the mixture, typically three times in the 3 seconds. The solution was left for 0, 3, 6, 9 or 12 seconds before adding the quench solution, giving a total lysis time of 3, 6, 9, 12 or 15 seconds (Figure 7.5). The mixing was performed identically for the first 3 seconds of the total lysis time to keep the mixing method constant across each experiment. The time between adding the quench and measuring the sample was kept constant at 5 minutes. This quench time was chosen to allow enough time to transfer the sample to a syringe, load into a syringe pump and ensure a stable flow through the MIC. The same blood sample was used for each experiment. Each sample was measured on the MIC at two frequencies of $500kHz$ and $2MHz$ at $40\mu Lmin^{-1}$ for 60 seconds.

The results of the five lysis times are shown in the scatter plots of the impedance signal in Figure 7.6a-e. The figure shows the three most numerous WBCs: lymphocytes (LYM), monocytes (MON) and neutrophils (NEU). The two other WBC subpopulations (eosinophils and basophils) overlap the three main populations, but account for less than 1% of total WBC count and can be ignored. The debris is likely to be a few remaining RBCs and reformed cell membranes (ghosts).

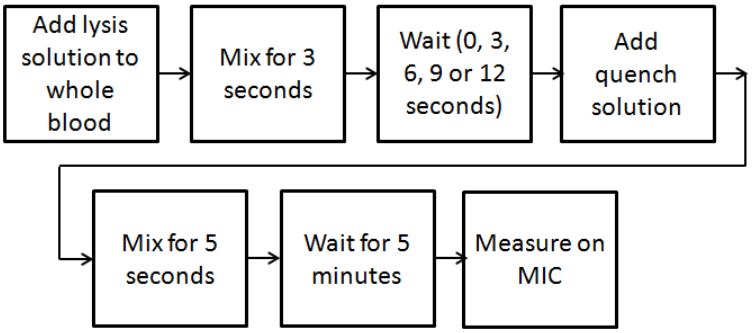

Figure 7.5: Protocol used to investigate the effect of lysis time on WBC subpopulation discrimination.

Qualitatively each figure looks similar, including the distribution of each subpopulation and the separation between subpopulations. The total number of WBCs in each figure was counted within a square gate (Figure 7.6f), using the same square gate for each graph. The counts (Table 7.1) are similar in all cases, with all values lying within 5% of the mean count. There is no trend in the count between the figures; the count does not appear to vary significantly with lysis time. The difference between counts can be attributed to pipetting errors due to the viscous nature of blood. If the counts reduced with increasing lysis times, it would indicate some WBCs were being lysed, however this is not the case.

Lysis time (seconds)	3	6	9	12	15
Total WBC count	9742	9273	9684	9583	9789

Table 7.1: Total WBC count for the scatterplots in Figure 7.6a-e.

This experiment indicates that the lysis time of 3-15 seconds does not impact the total WBC count significantly (within 5% of the mean) for "bulk" or manual lysis.

7.3.2 Quench Timing

The lysis reagent is a solution containing saponin and formic acid. Saponin is a detergent which creates holes in the membranes of cells (Francis et al., 2002). Saponin is most effective at low pH (created by the addition of formic acid), but remains active at physiological pH (pH7). In the RBC lysis protocol above, the quench solution returns the solution to pH7 (from acid conditions) which slows down, but does not eliminate, the effect of the Saponin on the cells. It was thus considered necessary to investigate the effect of quench time on the WBC subpopulations.

Whole blood ($50\mu L$) was added to an eppendorf and then mixed for 3 seconds with $600\mu L$ lysis solution (as above). The solution was left for 3 seconds before adding the quench solution, giving a total lysis time of 6 seconds. After addition of the quench solution, the solution was mixed for 5 seconds, loaded into a syringe and pumped through the

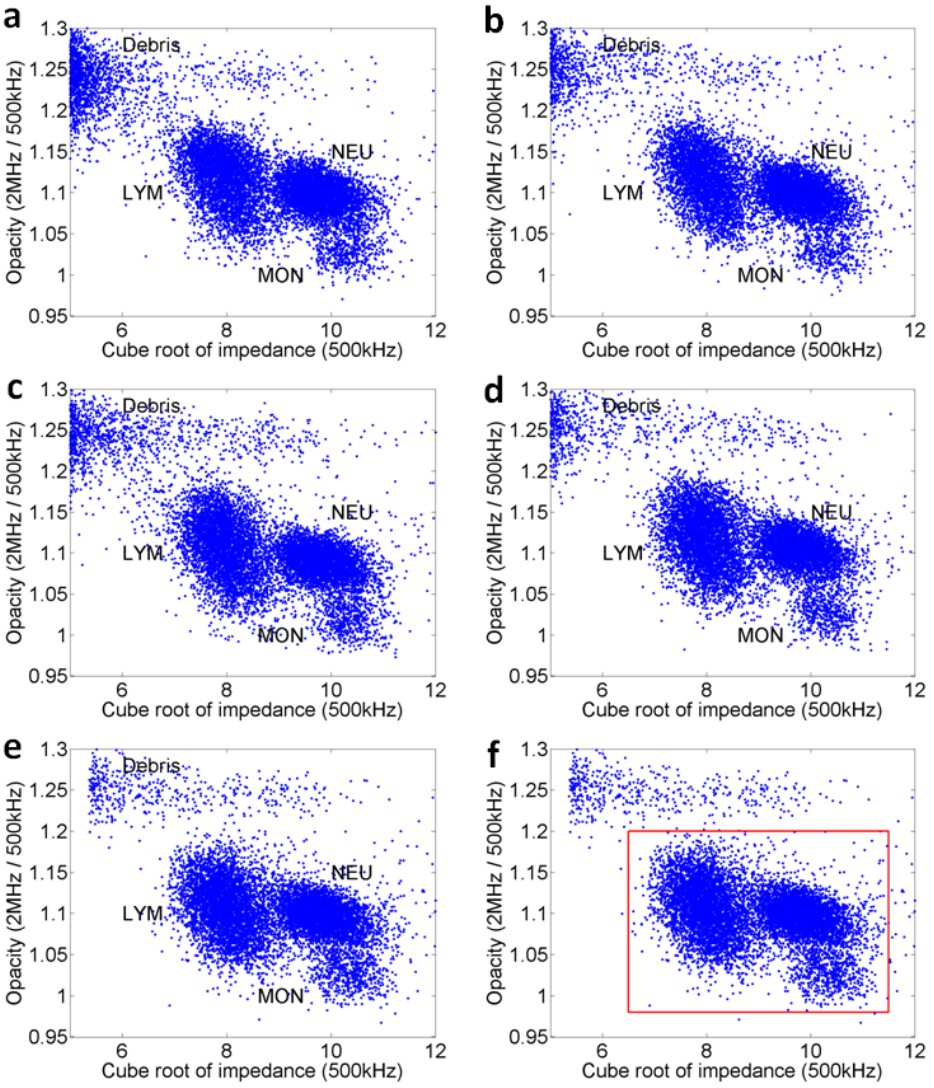

Figure 7.6: Scatter plots of the WBC subpopulations after RBC lysis time of 3, 6, 9, 12 or 15 seconds. f) Red box gate used to count the total number of WBCs for the results in a-e.

MIC chip. MIC measurement started after 1 minute which was the minimum time taken to load the sample and start recording data. The sample was measured for 14 minutes. The data was split into 1 minute segments (Figure 7.7), thus the first segment was of cells with a quench time between 1 and 2 minutes, the second segment was cells with a quench time of between 2 and 3 seconds and the final segment was cells with a quench time of between 14 and 15 minutes. By using the same sample, any differences in the sample preparation were eliminated.

Figure 7.8 shows scatterplots of the WBC subpopulation, which are similar to those in Figure 7.6. The figure show that over time the opacity of cells increases during the first 5 minutes of measurement. To determine whether this characteristic is due to the cell properties or the measurement equipment, the same experiment was repeated with

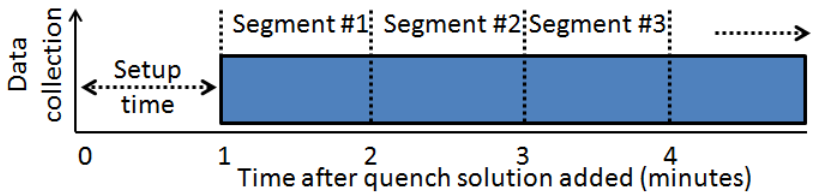

Figure 7.7: In the quench time experiments, the same is loaded into the MIC, taking the first minute after the quench solution was added. Data was recorded continuously for 15 minutes and subsequently split into 1 minute segments.

the addition of $6\mu m$ beads as a reference. The opacity of the beads was also found to increase over time, following the same trend as the cells. This indicates that the increase in opacity is due to the measurement system and not changes in the cell properties and were caused by heating in the electronic measurement circuits as the system is turned on. The greatest change in opacity occurred in the first minute so in subsequent experiments, measurements taken after leaving the equipment running for at least one minute.

The difference in electrical volume between the smaller lymphocytes and larger neutrophils and monocytes does not change for difference quench times, however the level of separation between the neutrophils and monocytes is dependent on quench time and was investigated as follows. Qualitatively, it is easier to distinguish the monocytes after 5 minutes of quench compared to 1 minute of quench. For the data in graphs 1-6 (Figure 7.8), events with a value less than 9 on the x-axis (cube root of impedance) were removed as demonstrated in Figure 7.9). This corresponds to removing the lymphocyte subpopulation which overlap the monocyte population in opacity and would prevent discrimination between neutrophils and monocytes.

The opacity was normalised (by subtracting the mean opacity) and the data is plotted as histograms in Figure 7.10. The figure demonstrates that the monocyte peak moves away from the neutrophil peak in the first few minutes of quench time, improving discrimination between each subpopulation of WBC. It is difficult to quantify this further, due to difficulty in fitting Gaussians to the histograms.

This means that the quench time should be between 5 and 15 minutes for optimum monocyte separation.

7.4 Microfluidic Lysis

In the previous section it was shown that for bulk lysis, a lysis time of up to 15 seconds does not negatively affect the WBC differential result. In addition a longer lysis time reduces the level of debris in the scatterplot. This is in contrast to Han et al. (2012), who reported a narrow window of lysis times (5-6 seconds) for a continuous flow system.

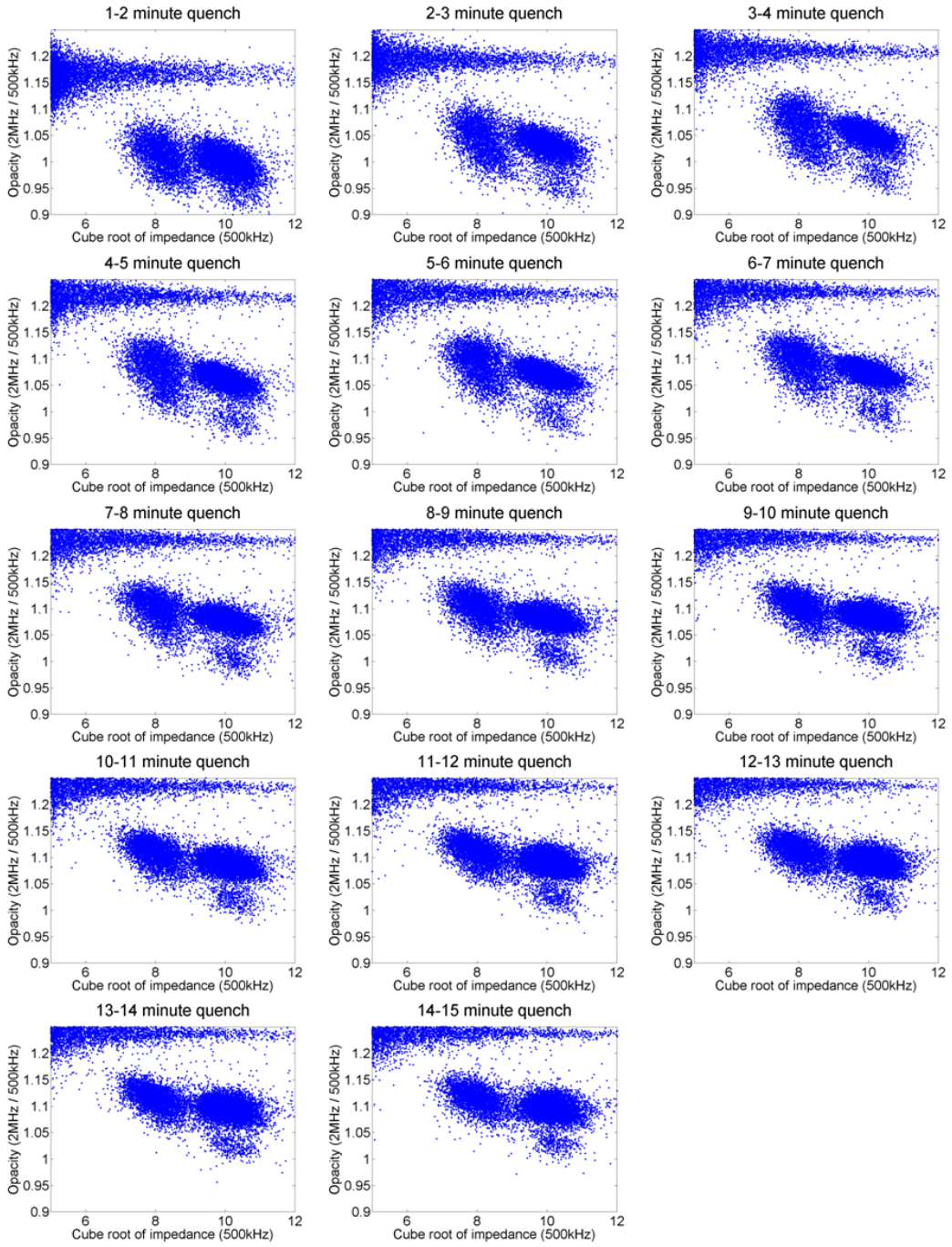

Figure 7.8: Scatter plots of the WBC subpopulations for a fixed RBC lysis time of 6 seconds and a variable quench time of between 1 and 15 minutes. Each graph is from the same sample, measured for 14 minutes and split into 1 minute segments.

However, for the fixed channel dimensions used by Han et al. (2012), increasing the lysis time was achieved by reducing the flow rates. It is challenging to pump whole blood at a stable low flow rate (less than $1.5\mu Lmin^{-1}$) due to the viscous nature of blood, and it is possible that as the flow rate was reduced, the flow became unstable which offset the gain from an increased lysis time.

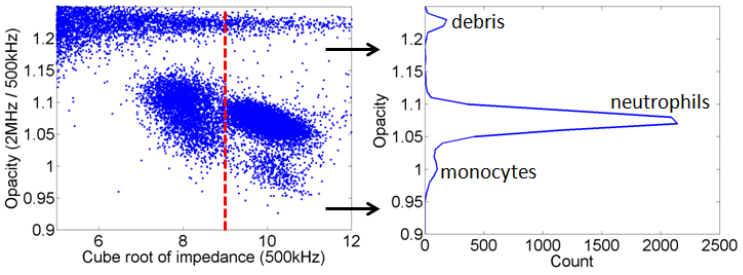

Figure 7.9: Events with an x-axis value less than 9 are removed and a histogram of the opacity of the remaining cells is created. The histogram shows a main peak in opacity at 1.03 (for the neutrophil population), a smaller peak at 1 for the less numerous monocytes and a peak at 1.23 from the debris.

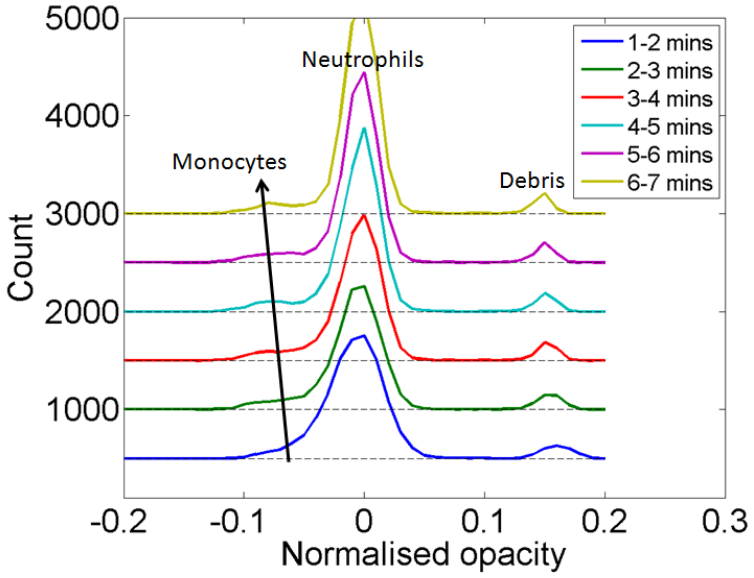

Figure 7.10: Histograms of the normalised opacity of the events greater than 9 (x-axis) from Figure 7.8. The y-axis value has been shifted by 500 between each dataset to aid visual clarity and the zero count is shown with a black horizontal line.

One of the problems with the microfluidic lysis system not reported in the paper was the high level of debris in the measurement (due to incomplete lysis before addition of the quench solution) compared to the same sample measured after bulk lysis. To address this, a microfluidic mixer was investigated that rapidly mixes the solutions.

In a fluidic network, flow is laminar and mixing only occurs due to diffusion. This means that the cells in the centre of the stream will be exposed to the lysis solution for less time compared to cells at the edge of the stream which meet the lysis solution first. There are many different methods of increasing mixing in microfluidic channels (Capretto et al., 2011), which can be classified into active or passing mixers depending on whether external energy is supplied. The chosen micro mixer was a herringbone mixer which was developed by Stroock et al. (2002). It was chosen because of its ease of

fabrication (being a passive mixer no external energy is required). A herringbone mixer uses sets of asymmetrical chevrons on the bottom of a fluidic channel to twist the flow (Figure 7.11). By twisting the flow, the area between the two fluids is increased and mixing by diffusion is therefore increased.

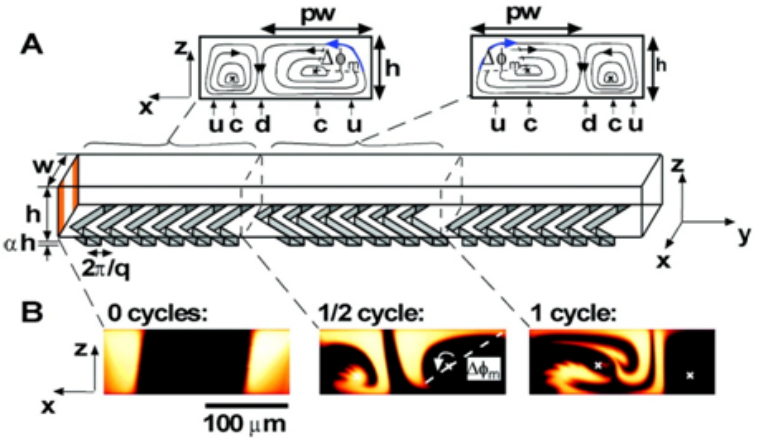

Figure 7.11: Herringbone mixer reported by Stroock et al. (2002). Sets of asymmetric chevrons etched onto the bottom of the channel twist the flow to increase the contact area (and hence diffusive mixing) between two flows.

A microfluidic lysis chip with a herringbone mixer was fabricated using standard soft lithography (replica moulding) which enabled a fast turnaround of prototypes compared to other prototyping techniques such as micro milling. Device fabrication was performed as follows:

1. A 3D design was made using Solidworks (Figure 7.12) and fabricated using a 3D printer (Objet). The channels were $1mm$ wide and $0.2mm$ deep. Chevrons were $0.35mm$ wide, $0.2mm$ deep and covered the full width of the channel.
2. The 3D printed mould was baked overnight at 80°C to fully cure, then exposed to an atmosphere of silane (Trichloro(1H,1H,2H,2H-perfluorooctyl)silane) for 10 minutes to create a non-stick surface.
3. PDMS (Sylgard 184) was mixed together as per the manufacturers instruction, degassed, poured onto the mould and cured for 1 hour at 80°C
4. The PDMS mould and a glass slide were exposed to an oxygen plasma for 30 seconds and then pressed together to form a permanent bond.
5. Fluidic inlet and outlet holes were punched using a $1mm$ diameter biopsy punch.

The mixer was designed to the footprint of a standard sized microscope slide ($76mm \times 52mm$). The extra pillars visible in the figure were added to connect to a cartridge containing syringe barrels. This is described later, but was not used in these initial experiments.

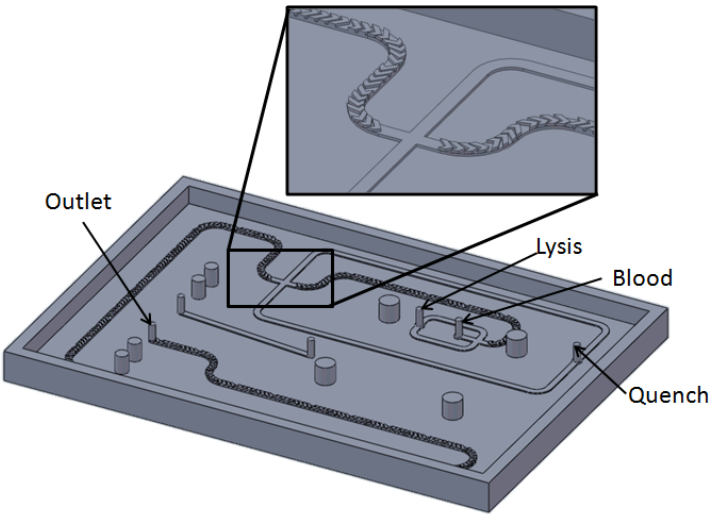

Figure 7.12: 3D design of the mould used to create the microfluidic mixer to selectively lyse RBCs from whole blood. The device is $76mm \times 52mm$.

The channel and chevron dimensions were chosen to be the smallest that could be fabricated using the 3D printer. For the RBC lysis the channel dimensions (width and height) should be as small as possible to maximise the mixing. This is because for a fixed lysis time and volumetric flow rate, the channel length is inversely proportional to the channel cross-sectional area.

The device was first tested with coloured food dye, red to represent blood, and yellow and blue to represent the lysis and quench solutions (Figure 7.13). Flow rates were 2.7, 32.8 and $14.5\mu Lmin^{-1}$ for the blood, lysis and quench solutions, the same ratios as used for the bulk lysis experiments. The total flow rate was $50\mu Lmin^{-1}$ which is double the $25\mu Lmin^{-1}$ as used by Han et al. (2012). The higher flow rate was used to reduce fluctuations caused by difficulties in pumping viscous fluids at low flow rates. Flow rates higher than $50\mu Lmin^{-1}$ could not be used due to the limited electronic sample rate (see Chapter 2 for more details). The lysis channel length was $44.5mm$ which corresponds to a lysis time of 15 seconds.

Figure 7.13 shows that the red and yellow dye mix to form an orange colour within $15mm$ which corresponds to 5 seconds residence time. Similarly when the orange colour meets the blue, a green colour is formed within $20mm$ (5 seconds).

Figure 7.13 demonstrates that the microfluidic mixer works efficiently for food dye. Next, the mixing device was tested with whole blood, using the same lysis and quench solutions as described above. The MIC measurement chip was connected to the output of the microfluidic mixer with PTFE tubing as shown in Figure 7.14. In this case the quench time is the time taken for the fluid to flow through the PDMS mixer and through the PTFE tubing to the MIC. This volume is approximately $50\mu L$ giving a quench time of 1 minute. Referring back to the quench time results (Figure 7.8) it is expected that

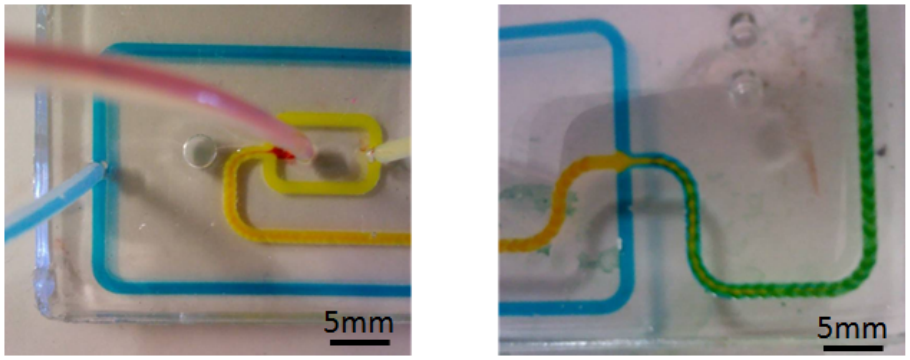

Figure 7.13: Photograph of the microfluidic mixer containing food dye for testing.

distinguishing monocytes from neutrophils will be challenging with this small quench time, however the lymphocyte and neutrophil subpopulations should be distinguishable.

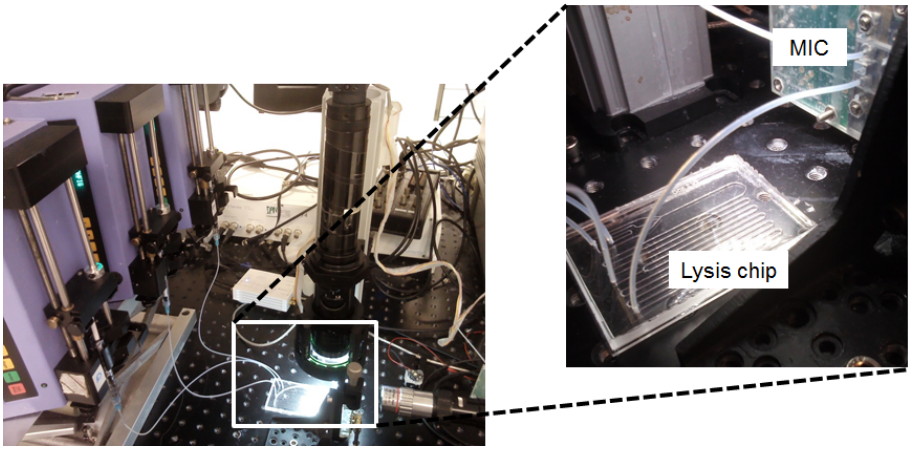

Figure 7.14: Photograph of the experimental setup. Three syringe pumps inject the blood and lysis and quench solutions into the mixer chip. The MIC is connected directly to the outlet of the mixer through a piece of tubing.

Figure 7.15 shows a series of 8 images taken from a video (30 FPS) of the junction between the blood and lysis channels. The images shows that the chevrons cause the blood to break into drops. This means that the cells are not evenly distributed along the length of the channel.

Figure 7.16a shows a section of sampled impedance signal from a typical bulk lysis experiment. The individual double Gaussian signals corresponding to single particles passing through the measurement region are clearly visible. Figure 16b shows a section of sampled impedance signal from a microfluidic lysis experiment. The data shows a section of individual WBC events, followed by a section containing overlapping events caused by unlysed RBCs. These overlapping events made analysis of the WBC impossible and thus no scatterplot is shown.

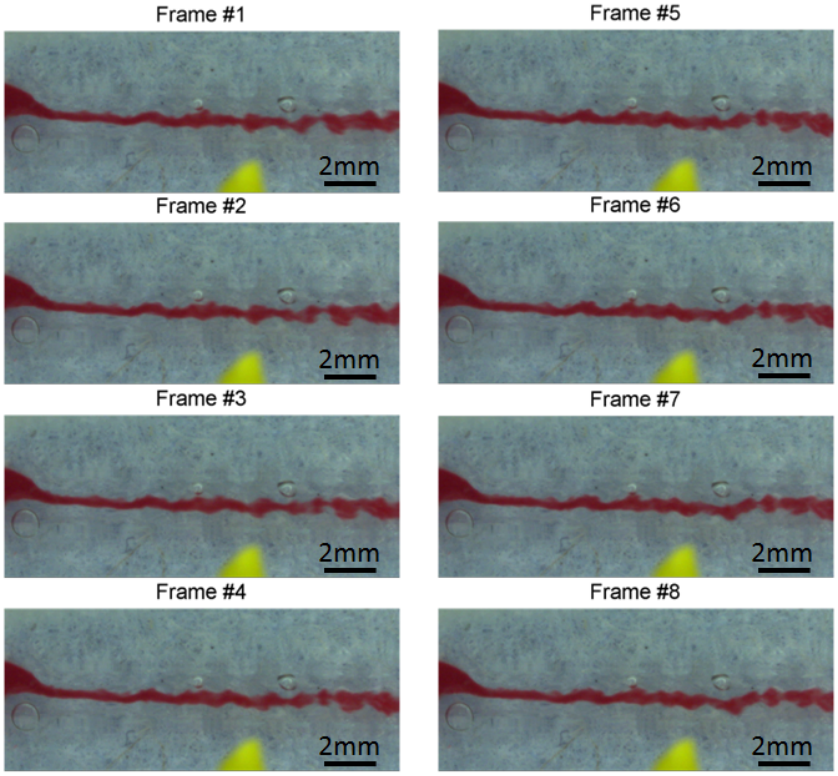

Figure 7.15: Frames of a video of the junction between the blood and lysis flow, illustrating the blood breaking into droplets.

The results reported are for one-off experiments. Many experiments were conducted, but repeatability was poor due to the following difficulties.

1. The MIC generated significant back pressure ($0.5Bar$ at $50\mu Lmin^{-1}$). This caused the flow to pulsate due to the different pumping speeds of the blood, lysis solution and quench solution. In particular, getting the system into stable steady-state flow was problematic.

2. If the blood was exposed to the lysis or quench solutions, small clots formed, which blocked the narrow region in the MIC chip.

3. Achieving stable flows often took more than 10 minutes, by which time the blood started to sediment in the syringe barrel. This increased the viscosity of the blood, reduced mixing efficiency, and consequently meant that more RBCs had to be lysed per second.

7.5 Integrated Cartridge Design

To combat problems with the pulsating flow, a cartridge with an integrated syringe barrel was designed to fit in a system which used integrated syringe pumps and was

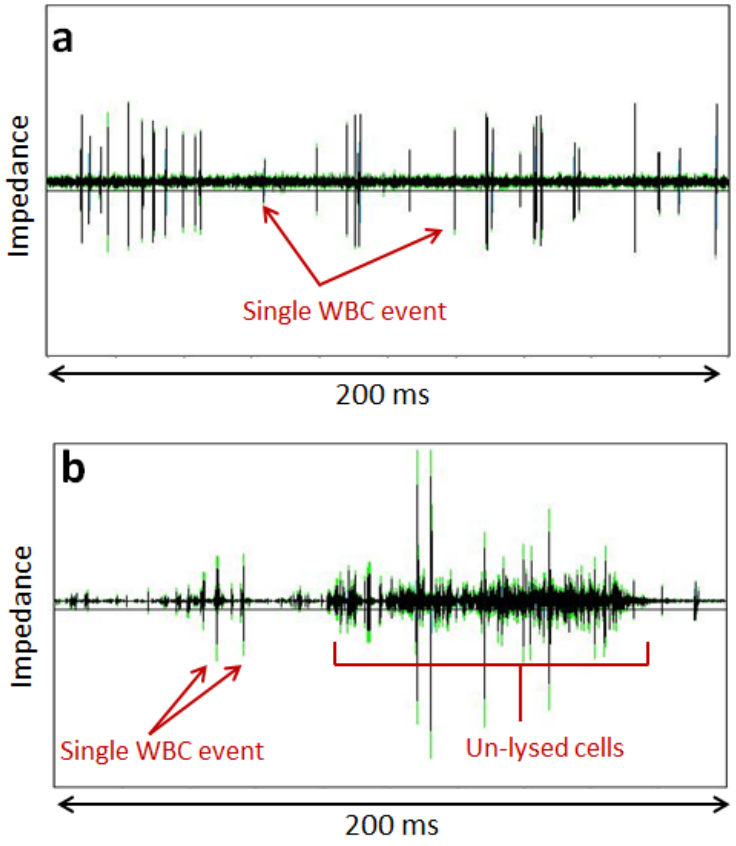

Figure 7.16: Diagram showing the impedance signal over time for a) microfluidic lysis and b) bulk lysis. In the bulk lysis the individual peak corresponding to single WBCs are clearly visible whereas in microfluidic lysis, there are sections containing many overlapping events making it impossible to count the single WBCs.

built by Philips as shown in Figure 7.17. By directly connecting the syringe barrels to the microfluidic channels, the interconnecting flexible tubing and associated dead volume was eliminated.

The cartridge uses two plungers per barrel, one of which acts in a similar way to a valve (Figure 7.18). This enables the barrels to be filled separately with the respective fluids first, and allows the flow of the blood, lysis and quench solutions to the microfluidic mixer chip to be started simultaneously, thus mitigating the start-up problems described earlier.

The cartridge was designed in two separate parts as shown in Figure 7.19. A $9mm$ thick base contains the syringe barrels and holds the MIC chip and connection circuitry. A separate $1mm$ thick lid contains the microfluidic network, which could be redesigned without the need to manufacture new bases (which was the case for the original Philips design).

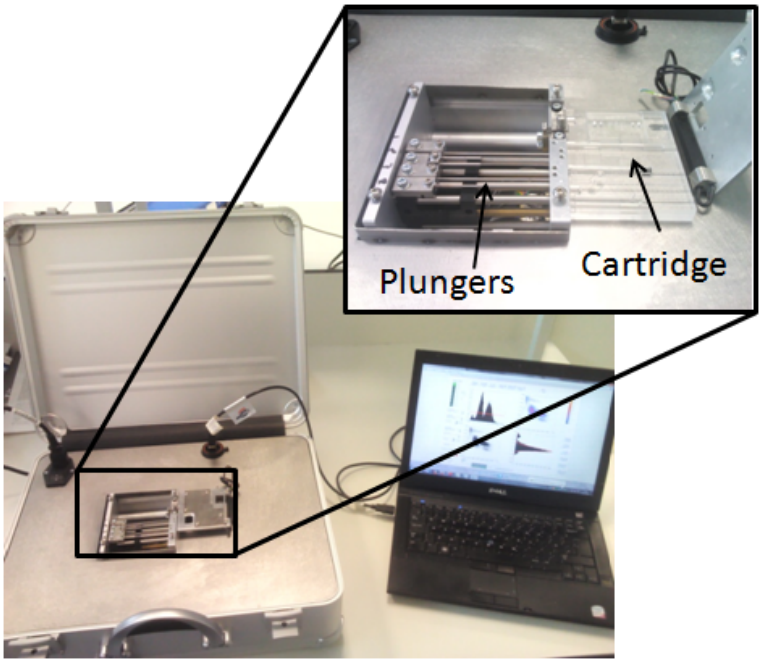

Figure 7.17: Briefcase reader built by Philips. The briefcase has plungers which connect to barrels integrated into the plastic cartridge. The cartridge is $85 \times 65 \times 10mm$.

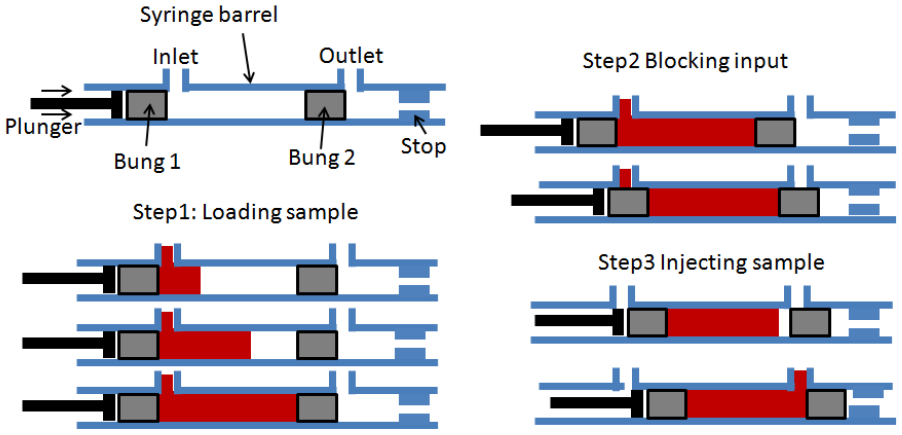

Figure 7.18: Diagram showing a single use, one-way valve created using two bungs in a syringe. This enables the syringe barrels to be loaded separately. Injection of the blood, lysis and quench solutions into the microfluidic network can start simultaneously. Designed by Philips.

One-off prototypes of the cartridge design were fabricated by Minifab in PMMA. The side walls of the barrels were rough due to poor manufacturing as shown in Figure 7.20. Rubber bungs were taken from standard syringes which should have matched the barrels in the cartridge, but these did not move freely along the barrels and as a consequence the cartridge leaked. To achieve accurate, smooth barrels, the base would have to be fabricated using injection moulding which is prohibitively expensive for prototyping.

In summary, reliable RBC lysis in a continuous flow system could not be achieved. The

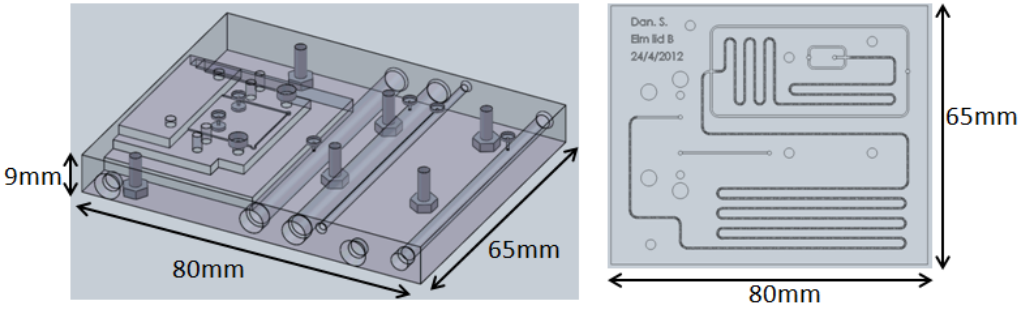

Figure 7.19: 3D design of the new cartridge. The design consists of a separate base containing syringe barrels and holder for the MIC chip and connection circuitry. A separate lid containing the microfluidic network clamps onto the base with O-rings to create a fluidic seal.

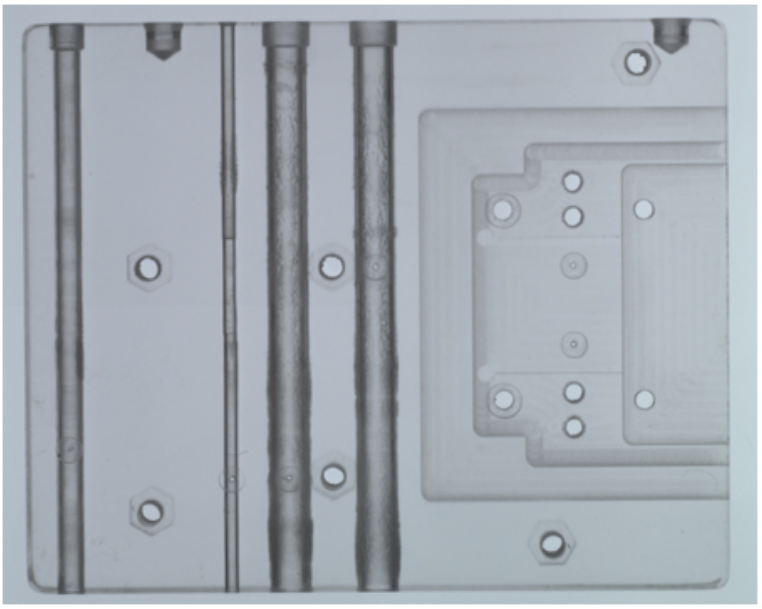

Figure 7.20: Image of the prototype cartridge base built by Minifab. The photograph shows the rough edges of the barrels.

chemical lysis was sensitive to the pulsating flow. Attempts to mitigate the pulsating flow using an integrated cartridge were also not successful due to difficulty in manufacturing. These problems perhaps could be mitigated using injection molding, but this was too expensive to test. Instead, a stirred lysis system was developed and is reported in the next section.

7.6 Stirred Lysis

An alternative to microfluidic lysis is to replicate the bulk lysis pipette technique in an automatic system. To achieve this, the blood was mixed with the lysis and quench solutions using a spinning magnetic flea in a small well.

A magnetic flea was added to a well and the magnetic stirrer was started. Whole blood ($50\mu L$) was gently pipetted into the well as shown in Figure 7.21. Next, lysis solution was gently pipetted down the side of the well and was stirred into the blood by the motion of the magnetic flea. After 6 seconds, the quench solution was gently pipetted down the side of the well. The lysis and quench solutions are transparent, but are shown as purple and green in the figure to aid viewing.

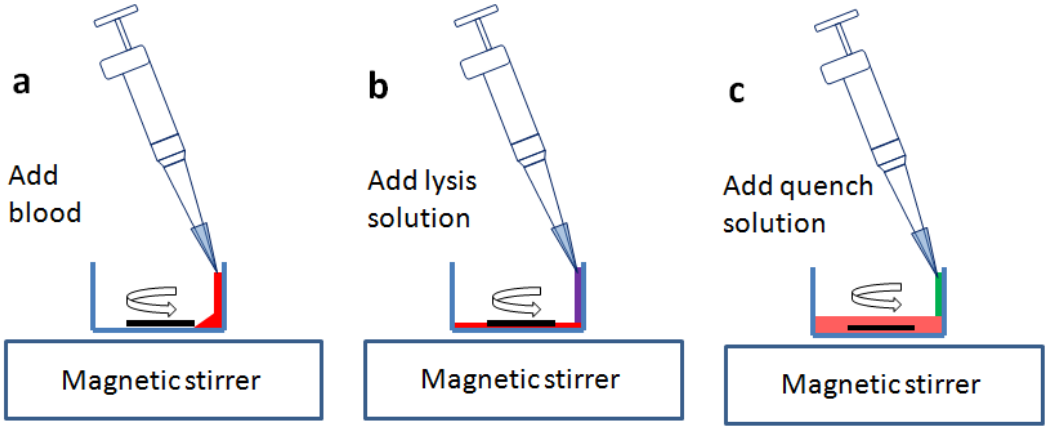

Figure 7.21: Diagram of the stirred mixing setup. The reagents are gently pipetted down the side of the well to minimise the pipette mixing.

A number of different configurations of well diameter, flea length and spin speed were tested (Table 7.2), but with identical conditions as above. The well diameter was 6.3 or $10mm$, magnetic flea size was $7\times1\times1mm$, $5\times1\times1mm$ or $2\times1\times1mm$ and the magnetic stirrer spin speed was set to the minimum or maximum speed (300 or 1400 RPM). The results of the experiments were qualitatively analysed, "good" results indicating a clear separation between the three WBC subpopulations (for example Figure 7.22a from experiment 1), "bad" result indicates that the subpopulations of WBC cannot be distinguished (Figure 7.22b from experiment 2).

Experiment #	Well diameter (mm)	Flea length (mm)	Spin speed (RPM)	Can distinguish subpopulations?
1	10	7	1400	Yes
2	10	7	300	No
3	10	5	1400	No
4	6.3	5	1400	Yes
5	6.3	2	1400	No

Table 7.2: List of configurations used to investigate a stirred lysis protocol.

All the good results are from the experiments where the spin speed was set to 1400 RPM, and the length of the magnetic flea was a large proportion of the diameter of the well. However, in all cases the mixing was qualitatively complete within the first second (the mixture was observed to be homogeneous).

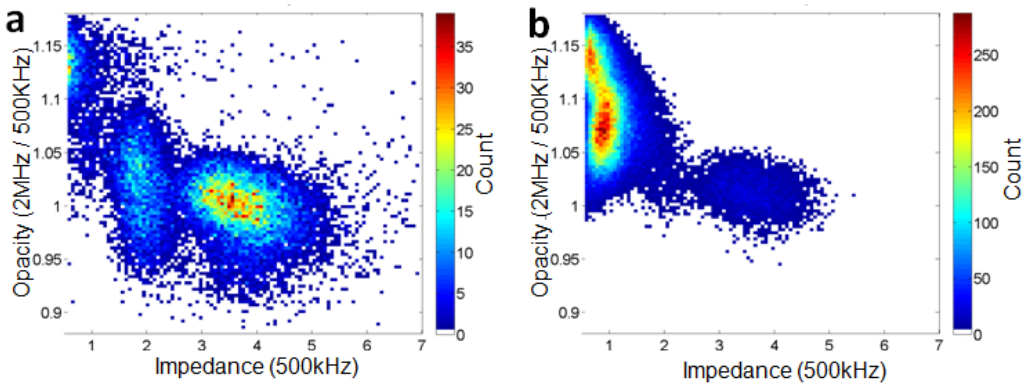

Figure 7.22: Density plot of WBC subpopulations from a) experiment 1 and b) experiment 2 (Table 7.2). Qualitatively, the three subpopulations of WBCs can be distinguished in a), but not in b).

The difference between a small and large magnetic flea for the same well diameter is that the larger flea generates a higher shear stress in the fluid. Also the higher spin speed increases the shear rate. In all cases a high number of RBCs are lysed, however if just 1% remain, then there would still be 10 times more RBCs than WBCs, which would cause a high coincidence level and prevent the WBC subpopulations from being identified.

To test the hypothesis that a small shear stress decreases the effectiveness of the RBC lysis, a bulk lysis using pipettes was repeated, but the pipette tips were shortened so that the inner diameter of the tip end was increased (from approximately 1 to $5mm$ diameter). The results (Figure 7.23) show that by reducing the shear stress on the cells, the level of debris increases significantly despite visual confirmation of successful mixing.

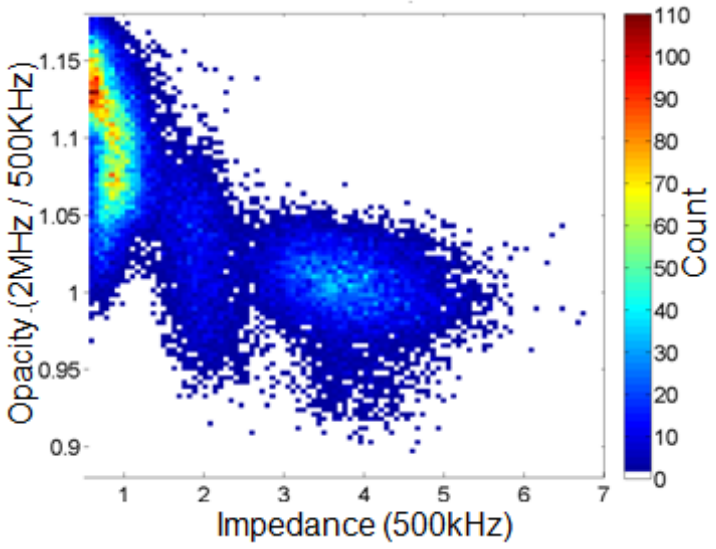

Figure 7.23: Density plot showing WBC subpopulations. RBC lysis was performed with pipettes (bulk lysis), but with the end of the pipette tip chopped off to reduce the shear stress the cells experience during mixing.

In terms of the microfluidic lysis system, shear stress is low within the channel. This explains that the higher debris level apparent in the microfluidic lysis results is due to the low shear stress in the channel. The channel dimensions were designed to prevent platelet activation and reduce the back pressure.

7.7 Discussion and Future Work

The best RBC lysis results (clearest discrimination between subpopulations) is when the quench time is greater than 5 minutes. However, this time is too long for a useful point-of-care test. To reduce this time, the concentration of the saponin and/or formic acid could be increased. The RBC lysis protocol needs to be tested on a wide range of samples, for instance patients with neutropenia (low neutrophil count) to ensure the count remains accurate.

To automate the stirred lysis system, a volume of blood around $10\mu L$ needs to be accurately metered. One example of a microfluidic metering system, reported by Puntambekar et al. (2002) is shown in Figure 7.24. A graduating reservoir is filled by capillary force from the channel on the left hand side of the figure. A capillary valve stops the fluid from exiting the channel on the right hand side. An air inlet is used to eject the metered volume of fluid from the graduating reservoir. The on-chip scale was used to measure the volume of liquid dispensed. The device could meter $50nL$ with a variation of 0.3% which is accurate enough for a WBC count. To use this system for metering a much larger volume ($10\mu L$ whole blood), channel dimensions would be greater which would make manufacturing easier.

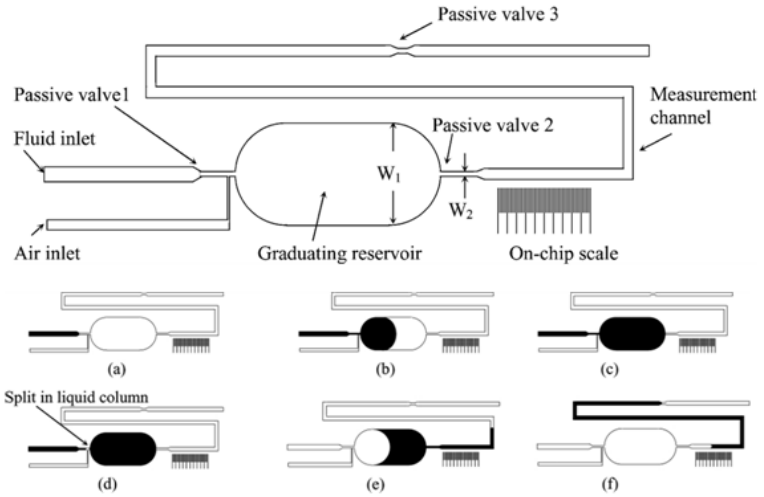

Figure 7.24: Overview of a microfluidic metering system demonstrated by Puntambekar et al. (2002). A graduating reservoir is filled by capillary force and the metered volume is ejected by flowing gas into the air inlet.

To conclude, this chapter presented results on chemical RBC lysis using a solution of saponin and formic acid. The target was a robust system which has potential to be commercialised. A continuous flow system proved to be unreliable so a stirred system was investigated. It was found that at a high shear rates, the lysis was successful, but at low shear rates the WBC subpopulations could not be distinguished. The proposed system was semi-automatic: the mixing mechanism was investigated using pipettes to meter the correct volumes of reagents. To produce a fully automatic system, a capillary fill mechanism could be used, for instance the system reported by Puntambekar et al. (2002).

Optimisation of the lysis timing was investigated in this section. The next step would be to optimise the reagent types and concentrations. For instance the common chemical RBC lysis is a solution of ammonium chloride (0.8%). Due to limited time constrains, this could not be tested. The saponin/formic acid solution was chosen because it was reported to reduce the lysis debris (Ledis et al., 1984) to enable clearer WBC subpopulation discrimination. Optimising the reagents would focus on reducing the quench time needed to distinguish the monocytes (around 5 minutes in this section).

To improve the system, an automatic delivery system would need to be investigated. A starting point could be to use an air pressure system such as electronically controlled valve to selectively inject the blood, lysis and quench solutions.

Chapter 8

Discussion and Future Direction

This chapter summarises the achievements described in the preceding chapters, and describes opportunities for further development of the MIC and integration towards complete diagnosis systems.

A complete numerical model of a Microfluidic Impedance Counter (MIC) has been developed. The numerical model was used to investigate the particle impedance signal as a function of particle position within the channel. It was found that the signal varied significantly between particles passing at the top and bottom of the channel close to the electrodes compared to those in the centre of the channel away from the electrodes. The model was further developed to incorporate the fluid flow profile within the channel which enabled direct comparison of the model with experimentally acquired data of test particles. The model showed good agreement with the experimental data in terms of the variation in particle impedance signal with position. Where the model differed from the experimental data was the number density of particles in different channel positions. This was due to inertial focusing effects which were not accounted for in the simulation due to computational limits. The model was designed using the channel dimensions of the experimental chip, but it could be adapted to model any other design of MIC. This would be useful in predicting the variation in impedance signal with particle position and to determine if the variation is below required levels, or if particle focusing would need to be implemented.

While investigating the modelling, it was found that when a particle traverses the MIC detection region, the electric field is distorted, which causes the change in impedance signal with particle position to be greater in the top half of the channel compared to the bottom half. Different electrode geometries were investigated to minimise this effect and a new design was developed which significantly reduced the variation in impedance signal with particle position. A new signal processing algorithm was also developed for the new electrode design to further reduce the particle positional dependence. This combination of improved electrode design and improved signal processing resulted in a

CV of polystyrene test particles ($3-10\mu m$) of approximately half of the manufacturer's data. Compared to similar systems described in the literature, this system produces high accuracy electrical volume measurement without complicated focusing techniques.

In the future, it may be possible to optimise the electrode geometry further (changing the widths of the electrode and spacing between the electrodes) so that the signal processing algorithm is not needed, which would reduce the computational demands for low power (or portable) applications. The electrode design uses parallel facing electrodes which must be aligned within tight tolerances ($1\mu m$). Future work would quantify the effect of misaligned electrodes on the impedance signal, and optimise the electrode design to allow the tolerances to be relaxed,simplifying manufacture.

Circulating tumour cells (CTCs) are single tumour cells which are found in blood and cause the spread of cancer by metastasis. Counting CTCs is important for diagnosis and prognosis, however CTCs are rare and enumeration is challenging. Identification is usually performed using magnetic separation and optical cytometry, however this relies on specific cell surface markers which are not expressed on all cancers. Using the new electrode geometry, MIC was investigated as a potential label-free detection method to analyse and characterise tumour cells, based on the known dielectric differences between tumour and blood cells. Cultured breast cancer cells were spiked into whole blood samples and used as a model for human CTCs. Using a frequency sweep, the dielectric properties of blood and tumour cells was investigated and found to be similar to previously reported values. Low numbers of tumour cells could be detected with the MIC system when spiked into whole blood but, due to throughput limitations, magnetic pre-separation was required to identify tumour cells at the same concentration of human CTCs. Future work would concentrate on integrating MIC with a label-free pre-processing system, for example size filtration or dielectrophoretic separation.

MIC has previously been used to enumerate white blood cells, which is an important part of the full blood count (FBC), a widely used clinical diagnostic metric. However, manual sample preparation was required, so automatic sample preparation was investigated for a miniature FBC. Microfluidic mixers were integrated into a continuous flow red blood count lysis system, however the system was not robust due to difficulties achieving stable flow and was therefore not suitable for commercialising a miniature FBC device. An alternative technique using a stirred lysis system allowing variation of the shear rate was researched. The RBC lysis efficiency for different magnetic flea and well sizes was investigated and confirmed that a high shear rate is required to achieve effective RBC lysis. This insight is useful if a continuous flow system were to be investigated further because channel dimensions should be reduced to increase the shear stress and lysis efficiency. To create a fully automatic stirred lysis system, a blood metering system would need to be developed. The obvious choice would be a capillary fill solution using a narrow channel to determine the volume of metered blood. In bulk (manual) lysis, experiments showed that a lysis time of between 5 and 15 seconds could be used without

negatively affecting the WBCs, and a quench time of 5 minutes was needed to maximise the separation between WBC subpopulations. In an automatic stirred system these timings would have to be optimised. Ideally the test should be quicker, so stronger lysis and quench solutions could be investigated. Alternate lysis solutions could be investigated, such as addition of an eosinolytic agent which was described by Li et al. (1998) to enable identification of four WBC subpopulations.

Integration of on-the-fly sample preparation into the device would extend the functionality, application of the MIC system. For example, Mach et al. (2011) produced a "centrifuge on a chip" using inertial focusing to wash cells. Cells are usually distinguished by their surface receptors (CD markers) using fluorescently labelled antibodies. Holmes and Morgan (2010) used antibody coated beads as an equivalent impedance label for MIC detection of CD4 T-cells. Manual labelling was required, but this could be automated using a microfluidic mixer for automatic detection of specific cells based on their surface markers.

High accuracy measurements of particle size (electrical volume) was achieved using a new electrode geometry, with the limit of detection determined from the noise level in the detection circuitry. To reduce the LOD of particle size without reducing channel dimensions, coded electrodes could be used as reported by Polling et al. (2010). Simultaneous fluorescence detection was used with MIC in Chapter 6, however the system was large and fragile as it utilised separate optical components. Some of these optical components such as the lenses could be miniaturised and built into the MIC chip to create a miniature system, as is performed in microfluidic optical cytometry.

The measurement frequency range is limited by the double layer capacitance (which limits low frequency measurements) and by parasitic capacitance (which limits the high frequency measurements). To improve the frequency response, the electrodes could be replaced by materials such as platinum black which have a high surface roughness which increases the surface area without making the electrodes physically larger. This would enable measurements of the surface properties of particles (alpha relaxation). By minimising the parasitic capacitances in the system (for instance in the connector boards), the frequency range could be extended to allow high frequency measurements, such as measurement of the cytoplasm conductivity of cells. This may allow for instance measurement of the DNA content of cells which varies during a cell life cycle.

It may also be possible to develop manufacturing techniques to build the cylindrical electrode geometry shown in Figure 8.1 (Caselli et al., 2010) to detect the tomography of particles, for instance to distinguish RBCs from Spherocytes which are sphere shaped red blood cells caused by an autoimmune anaemia (Hillman et al., 2011).

In summary a complete numerical model of a MIC has been developed which accurately predicts the variation in impedance signal with particle position. A new electrode geometry and signal processing algorithm have been developed which led to marked

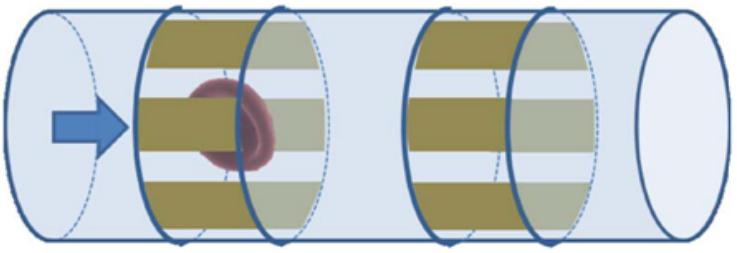

Figure 8.1: Geometry proposed by Caselli et al. (2010) to measure and distinguish different particles based on their shape.

improvements in measurement accuracy. For example, measurements of the coefficient of variation of monodisperse beads were half the manufacturer's data. The improved MIC was used to analyse a range of different cell types as part of developing diagnostic devices. MIC could successfully detect clinically relevant concentrations of individual tumour cells in a background of 10^6 times more white blood cells. Methods suitable for implementing chemical RBC lysis on-chip for a FBC were evaluated. A stirred mixing system was found to be a suitable pre-processing system that could be integrated into a miniature MIC device. Although the main aim of the research was to develop a high accuracy MIC device suitable for blood analysis, it could be used in numerous applications where counting and identification of low concentrations of particles is required.

References

Advia, 2013.
URL http://vetlabor.hu/images/laboratorium/advia120_ismerteto.ppt

Allard, W. J., Matera, J., Miller, M. C., Repollet, M., Connelly, M. C., Rao, C., Tibbe, A. G., Uhr, J. W., Terstappen, L. W., 2004. Tumor cells circulate in the peripheral blood of all major carcinomas but not in healthy subjects or patients with nonmalignant diseases. Clinical Cancer Research 10 (20), 6897–6904.

Ashworth, T., 1869. A case of cancer in which cells similar to those in the tumours were seen in the blood after death. Aust Med J 14 (3), 146–149.

Becker, F. F., Wang, X.-B., Huang, Y., Pethig, R., Vykoukal, J., Gascoyne, P., 1995. Separation of human breast cancer cells from blood by differential dielectric affinity. Proceedings of the National Academy of Sciences 92 (3), 860–864.

Benazzi, G., Holmes, D., Sun, T., Mowlem, M., Morgan, H., 2007. Discrimination and analysis of phytoplankton using a microfluidic cytometer. Iet Nanobiotechnology 1 (6), 94–101.

Berge, L. I., Jossang, T., Feder, J., 1990. Off-axis response for particles passing through long apertures in coulter-type counters. Measurement Science and Technology 1 (6), 471.

Bernabini, C., Holmes, D., Morgan, H., 2011. Micro-impedance cytometry for detection and analysis of micron-sized particles and bacteria. Lab on a Chip 11 (3), 407–412.

Bhagat, A. A. S., Kuntaegowdanahalli, S. S., Kaval, N., Seliskar, C. J., Papautsky, I., 2010. Inertial microfluidics for sheath-less high-throughput flow cytometry. Biomedical microdevices 12 (2), 187–195.

Bhagat, A. A. S., Kuntaegowdanahalli, S. S., Papautsky, I., 2008. Enhanced particle filtration in straight microchannels using shear-modulated inertial migration. Physics of Fluids 20, 101702.

Buttarello, M., Plebani, M., 2008. Automated blood cell counts state of the art. American Journal of Clinical Pathology 130 (1), 104–116.

Capretto, L., Cheng, W., Hill, M., Zhang, X., 2011. Micromixing within microfluidic devices. Top Curr Chem 304, 27–68.

Caselli, F., Bisegna, P., Maceri, F., 2010. Eit-inspired microfluidic cytometer for single-cell dielectric spectroscopy. Microelectromechanical Systems, Journal of 19 (5), 1029–1040.

Chang, C.-C., Huang, Z.-X., Yang, R.-J., 2007. Three-dimensional hydrodynamic focusing in two-layer polydimethylsiloxane (pdms) microchannels. Journal of Micromechanics and Microengineering 17 (8), 1479.

Coulter, W. H., 1956. High speed automatic blood cell counter and cell size analyzer. In: Proc Natl Electron Conf. Vol. 12. pp. 1034–1042.

Cristofanilli, M., Budd, G. T., Ellis, M. J., Stopeck, A., Matera, J., Miller, M. C., Reuben, J. M., Doyle, G. V., Allard, W. J., Terstappen, L. W., et al., 2004. Circulating tumor cells, disease progression, and survival in metastatic breast cancer. New England Journal of Medicine 351 (8), 781–791.

De Giorgi, V., Pinzani, P., Salvianti, F., Panelos, J., Paglierani, M., Janowska, A., Grazzini, M., Wechsler, J., Orlando, C., Santucci, M., et al., 2010. Application of a filtration-and isolation-by-size technique for the detection of circulating tumor cells in cutaneous melanoma. Journal of Investigative Dermatology 130 (10), 2440–2447.

Di Carlo, D., 2009. Inertial microfluidics. Lab on a Chip 9 (21), 3038–3046.

Di Carlo, D., Irimia, D., Tompkins, R. G., Toner, M., 2007. Continuous inertial focusing, ordering, and separation of particles in microchannels. Proceedings of the National Academy of Sciences 104 (48), 18892–18897.

Dupire, J., Socol, M., Viallat, A., 2012. Full dynamics of a red blood cell in shear flow. Proceedings of the National Academy of Sciences 109 (51), 20808–20813.

Francis, G., Kerem, Z., Makkar, H. P., Becker, K., et al., 2002. The biological action of saponins in animal systems: a review. British Journal of Nutrition 88 (6), 587–605.

Frankowski, M., Bock, N., Kummrow, A., Schädel-Ebner, S., Schmidt, M., Tuchscheerer, A., Neukammer, J., 2011. A microflow cytometer exploited for the immunological differentiation of leukocytes. Cytometry Part A 79 (8), 613–624.

Gascoyne, P. R., Noshari, J., Anderson, T. J., Becker, F. F., 2009. Isolation of rare cells from cell mixtures by dielectrophoresis. Electrophoresis 30 (8), 1388–1398.

Gascoyne, P. R., Shim, S., Noshari, J., Becker, F. F., Stemke-Hale, K., 2013. Correlations between the dielectric properties and exterior morphology of cells revealed by dielectrophoretic field-flow fractionation. Electrophoresis.

Gascoyne, P. R., Wang, X.-B., Huang, Y., Becker, F. F., 1997. Dielectrophoretic separation of cancer cells from blood. Industry Applications, IEEE Transactions on 33 (3), 670–678.

Gawad, S., Sun, T., Green, N. G., Morgan, H., 2007. Impedance spectroscopy using maximum length sequences: Application to single cell analysis. Review of Scientific Instruments 78 (5), 054301–054301.

Gleghorn, J. P., Pratt, E. D., Denning, D., Liu, H., Bander, N. H., Tagawa, S. T., Nanus, D. M., Giannakakou, P. A., Kirby, B. J., 2010. Capture of circulating tumor cells from whole blood of prostate cancer patients using geometrically enhanced differential immunocapture (gedi) and a prostate-specific antibody. Lab on a chip 10 (1), 27–29.

Golden, J. P., Kim, J. S., Erickson, J. S., Hilliard, L. R., Howell, P. B., Anderson, G. P., Nasir, M., Ligler, F. S., 2009. Multi-wavelength microflow cytometer using groove-generated sheath flow. Lab on a Chip 9 (13), 1942–1950.

Gupta, V., Jafferji, I., Garza, M., Melnikova, V. O., Hasegawa, D. K., Pethig, R., Davis, D. W., 2012. Apostream, a new dielectrophoretic device for antibody independent isolation and recovery of viable cancer cells from blood. Biomicrofluidics 6, 024133.

Hairer, G., Pärr, G., Svasek, P., Jachimowicz, A., Vellekoop, M., 2008. Investigations of micrometer sample stream profiles in a three-dimensional hydrodynamic focusing device. Sensors and Actuators B: Chemical 132 (2), 518–524.

Hairer, G., Vellekoop, M., 2009. An integrated flow-cell for full sample stream control. Microfluidics and nanofluidics 7 (5), 647–658.

Han, X., van Berkel, C., Gwyer, J., Capretto, L., Morgan, H., Jan 2012. Microfluidic lysis of human blood for leukocyte analysis using single cell impedance cytometry. Anal Chem 84 (2), 1070–1075.

Hillman, R. S., Ault, K. A., Rinder, H. M., et al., 2011. Hematology in clinical practice. McGraw-Hill Medical.

Holmes, D., Morgan, H., 2010. Single cell impedance cytometry for identification and counting of cd4 t-cells in human blood using impedance labels. Analytical chemistry 82 (4), 1455–1461.

Holmes, D., Morgan, H., Green, N. G., 2006. High throughput particle analysis: Combining dielectrophoretic particle focussing with confocal optical detection. Biosensors and Bioelectronics 21, 1621–1630.

Holmes, D., Pettigrew, D., Reccius, C. H., Gwyer, J. D., van Berkel, C., Holloway, J., Davies, D. E., Morgan, H., 2009. Leukocyte analysis and differentiation using high speed microfluidic single cell impedance cytometry. Lab on a Chip 9 (20), 2881–2889.

Hou, H.-H., Tsai, C.-H., Fu, L.-M., Yang, R.-J., 2009. Experimental and numerical investigation into micro-flow cytometer with 3-d hydrodynamic focusing effect and micro-weir structure. Electrophoresis 30 (14), 2507–2515.

Howell, Jr, P. B., Golden, J. P., Hilliard, L. R., Erickson, J. S., Mott, D. R., Ligler, F. S., Jul 2008. Two simple and rugged designs for creating microfluidic sheath flow. Lab Chip 8 (7), 1097–1103.

Hughes, M. P., Morgan, H., 1999. Dielectrophoretic characterization and separation of antibody-coated submicrometer latex spheres. Analytical Chemistry 71 (16), 3441–3445.

Hur, S. C., Henderson-MacLennan, N. K., McCabe, E. R., Di Carlo, D., 2011. Deformability-based cell classification and enrichment using inertial microfluidics. Lab on a Chip 11 (5), 912–920.

Jacobson, S. C., Ramsey, J. M., 1997. Electrokinetic focusing in microfabricated channel structures. Analytical Chemistry 69 (16), 3212–3217.

Kennedy, M. J., Stelick, S. J., Perkins, S. L., Cao, L., Batt, C. A., 2009. Hydrodynamic focusing with a microlithographic manifold: controlling the vertical position of a focused sample. Microfluidics and nanofluidics 7 (4), 569–578.

Kim, J. S., Anderson, G. P., Erickson, J. S., Golden, J. P., Nasir, M., Ligler, F. S., 2009. Multiplexed detection of bacteria and toxins using a microflow cytometer. Analytical chemistry 81 (13), 5426–5432.

Kim, Y. R., Ornstein, L., 1983. Isovolumetric sphering of erythrocytes for more accurate and precise cell volume measurement by flow cytometry. Cytometry 3 (6), 419–427.

Kirby, B. J., Jodari, M., Loftus, M. S., Gakhar, G., Pratt, E. D., Chanel-Vos, C., Gleghorn, J. P., Santana, S. M., Liu, H., Smith, J. P., et al., 2012. Functional characterization of circulating tumor cells with a prostate-cancer-specific microfluidic device. PLoS One 7 (4), e35976.

Kumar, P., 2009. Clark m. Kumar & Clark Clinical Medicine, 1323.

Kummrow, A., Theisen, J., Frankowski, M., Tuchscheerer, A., Yildirim, H., Brattke, K., Schmidt, M., Neukammer, J., 2009. Microfluidic structures for flow cytometric analysis of hydrodynamically focussed blood cells fabricated by ultraprecision micromachining. Lab on a Chip 9 (7), 972–981.

Kuntaegowdanahalli, S. S., Bhagat, A. A. S., Kumar, G., Papautsky, I., 2009. Inertial microfluidics for continuous particle separation in spiral microchannels. Lab on a Chip 9 (20), 2973–2980.

Ledis, S. L., Sena, T., Crews, H. R., Carter, J. H., et al., Nov. 27 1984. Method for three-volume differential determination of lymphocyte, monocyte and granulocyte populations of leukocytes. US Patent 4,485,175.

Lee, G.-B., Chang, C.-C., Huang, S.-B., Yang, R.-J., 2006. The hydrodynamic focusing effect inside rectangular microchannels. Journal of Micromechanics and Microengineering 16 (5), 1024.

Lenshof, A., Magnusson, C., Laurell, T., 2012. Acoustofluidics 8: Applications of acoustophoresis in continuous flow microsystems. Lab on a chip 12 (7), 1210–1223.

Li, Y., Young, C., Veulens, S. C., Oct. 6 1998. Reagent and method for differential determination of leukocytes in blood. US Patent 5,817,518.

Ligler, F. S., Kim, J. S., 2010. The microflow cytometer. Pan Stanford Pub.

Lin, H. K., Zheng, S., Williams, A. J., Balic, M., Groshen, S., Scher, H. I., Fleisher, M., Stadler, W., Datar, R. H., Tai, Y.-C., et al., 2010. Portable filter-based microdevice for detection and characterization of circulating tumor cells. Clinical Cancer Research 16 (20), 5011–5018.

Longmore, M., Wilkinson, I., Davidson, E., Foulkes, A., Mafi, A., 2010. Oxford handbook of clinical medicine. OUP Oxford.

Mach, A. J., Kim, J. H., Arshi, A., Hur, S. C., Di Carlo, D., 2011. Automated cellular sample preparation using a centrifuge-on-a-chip. Lab on a Chip 11 (17), 2827–2834.

Mao, X., Nawaz, A. A., Lin, S.-C. S., Lapsley, M. I., Zhao, Y., McCoy, J. P., El-Deiry, W. S., Huang, T. J., 2012. An integrated, multiparametric flow cytometry chip using microfluidic drifting based three-dimensional hydrodynamic focusing. Biomicrofluidics 6, 024113.

Mao, X., Waldeisen, J. R., Huang, T. J., 2007. microfluidic driftingimplementing three-dimensional hydrodynamic focusing with a single-layer planar microfluidic device. Lab on a Chip 7 (10), 1260–1262.

Mernier, G., Duqi, E., Renaud, P., 2012. Characterization of a novel impedance cytometer design and its integration with lateral focusing by dielectrophoresis. Lab on a Chip 12 (21), 4344–4349.

Miller, M. C., Doyle, G. V., Terstappen, L. W. M. M., 2010. Significance of circulating tumor cells detected by the cellsearch system in patients with metastatic breast colorectal and prostate cancer. J Oncol 2010, 617421.

Morgan, H., Green, N., 2003. AC electrokinetics: colloids and nanoparticles. No. 2. Research Studies Press.

Morgan, H., Holmes, D., Green, N. G., 2006. High speed simultaneous single particle impedance and fluorescence analysis on a chip. Current Applied Physics 6 (3), 367–370.

Nagrath, S., Sequist, L. V., Maheswaran, S., Bell, D. W., Irimia, D., Ulkus, L., Smith, M. R., Kwak, E. L., Digumarthy, S., Muzikansky, A., et al., 2007. Isolation of rare circulating tumour cells in cancer patients by microchip technology. Nature 450 (7173), 1235–1239.

Oakey, J., Applegate Jr, R. W., Arellano, E., Carlo, D. D., Graves, S. W., Toner, M., 2010. Particle focusing in staged inertial microfluidic devices for flow cytometry. Analytical chemistry 82 (9), 3862–3867.

Osei-Bimpong, A., McLean, R., Bhonda, E., Lewis, S., 2012. The use of the white cell count and haemoglobin in combination as an effective screen to predict the normality of the full blood count. International Journal of Laboratory Hematology 34 (1), 91–97.

Pethig, R., Schmueser, I., 2012. Marking 100 years since rudolf höbers discovery of the insulating envelope surrounding cells and of the beta-dispersion exhibited by tissue. Journal of Electrical Bioimpedance.

Pethig, R. R., 1979. Dielectric and Electronic Properties of Biological Materials. John Wiley & Sons Ltd.

Polling, D., Deane, S. C., Burcher, M. R., Glasse, C., Reccius, C. H., 2010. Coded electrodes for low signal-noise ratio single cell detection in flow-through impedance spectroscopy. In: Proceedings of MicroTAS. Vol. 1. p. 617.

Puntambekar, A., Choi, J.-W., Ahn, C. H., Kim, S., Makhijani, V., Nov 2002. Fixed-volume metering microdispenser module. Lab Chip 2 (4), 213–218.

Rao, L. V., Moiles, D., Snyder, M., 2011. Finger-stick complete blood counts: Comparison between venous and capillary blood. Point of Care 10 (3), 120–122.

Saleh, O., Sohn, L., 2002. Correcting off-axis effects in an on-chip resistive-pulse analyzer. Review of scientific instruments 73 (12), 4396–4398.

Segerink, L. I., Sprenkels, A. J., Bomer, J. G., Vermes, I., van den Berg, A., 2011. A new floating electrode structure for generating homogeneous electrical fields in microfluidic channels. Lab on a Chip 11 (12), 1995–2001.

Segré, G., 1961. Radial particle displacements in poiseuille flow of suspensions. Nature 189, 209–210.

Shapiro, H. M., 2003. Practical flow cytometry. Wiley-Liss.

Shi, J., Yazdi, S., Lin, S.-C. S., Ding, X., Chiang, I.-K., Sharp, K., Huang, T. J., 2011. Three-dimensional continuous particle focusing in a microfluidic channel via standing surface acoustic waves (ssaw). Lab on a chip 11 (14), 2319–2324.

Shim, S., Stemke-Hale, K., Noshari, J., Becker, F. F., Gascoyne, P. R., 2013. Dielectrophoresis has broad applicability to marker-free isolation of tumor cells from blood by microfluidic systems. Biomicrofluidics 7, 011808.

Simonnet, C., Groisman, A., 2006. High-throughput and high-resolution flow cytometry in molded microfluidic devices. Analytical chemistry 78 (16), 5653–5663.

Smythe, W., 1972. Off-axis particles in coulter type counters. Review of Scientific Instruments 43, 817.

Spizzo, G., Fong, D., Wurm, M., Ensinger, C., Obrist, P., Hofer, C., Mazzoleni, G., Gastl, G., Went, P., 2011. Epcam expression in primary tumour tissues and metastases: an immunohistochemical analysis. Journal of clinical pathology 64 (5), 415–420.

Stott, S. L., Hsu, C.-H., Tsukrov, D. I., Yu, M., Miyamoto, D. T., Waltman, B. A., Rothenberg, S. M., Shah, A. M., Smas, M. E., Korir, G. K., et al., 2010. Isolation of circulating tumor cells using a microvortex-generating herringbone-chip. Proceedings of the National Academy of Sciences 107 (43), 18392–18397.

Stroock, A. D., Dertinger, S. K. W., Ajdari, A., Mezic, I., Stone, H. A., Whitesides, G. M., Jan 2002. Chaotic mixer for microchannels. Science 295 (5555), 647–651.

Sun, T., Gawad, S., Bernabini, C., Green, N. G., Morgan, H., 2007a. Broadband single cell impedance spectroscopy using maximum length sequences: theoretical analysis and practical considerations. Measurement Science and Technology 18 (9), 2859.

Sun, T., Green, N. G., Gawad, S., Morgan, H., 2007b. Analytical electric field and sensitivity analysis for two microfluidic impedance cytometer designs. Iet Nanobiotechnology 1 (5), 69–79.

Sun, T., van Berkel, C., Green, N. G., Morgan, H., 2009. Digital signal processing methods for impedance microfluidic cytometry. Microfluidics and nanofluidics 6 (2), 179–187.

Sundararajan, N., Pio, M. S., Lee, L. P., Berlin, A. A., 2004. Three-dimensional hydrodynamic focusing in polydimethylsiloxane (pdms) microchannels. Microelectromechanical Systems, Journal of 13 (4), 559–567.

Thomas, R. S., Morgan, H., Green, N. G., 2009. Negative dep traps for single cell immobilisation. Lab on a Chip 9 (11), 1534–1540.

van Berkel, C., Gwyer, J. D., Deane, S., Green, N., Holloway, J., Hollis, V., Morgan, H., 2011. Integrated systems for rapid point of care (poc) blood cell analysis. Lab Chip 11 (7), 1249–1255.

Veridex, 2013.
URL http://www.veridex.com/pdf%5CMKG-1767rev3CS-TechnologyAnalyticalOverview_Customer_PresentationFINAL.pdf

Vona, G., Sabile, A., Louha, M., Sitruk, V., Romana, S., Schütze, K., Capron, F., Franco, D., Pazzagli, M., Vekemans, M., et al., 2000. Isolation by size of epithelial tumor cells: a new method for the immunomorphological and molecular characterization of circulating tumor cells. The American journal of pathology 156 (1), 57–63.

Watkins, N., Venkatesan, B. M., Toner, M., Rodriguez, W., Bashir, R., 2009. A robust electrical microcytometer with 3-dimensional hydrofocusing. Lab on a Chip 9 (22), 3177–3184.

Wirtz, D., Konstantopoulos, K., Searson, P. C., 2011. The physics of cancer: the role of physical interactions and mechanical forces in metastasis. Nature Reviews Cancer 11 (7), 512–522.

Xuan, X., Zhu, J., Church, C., 2010. Particle focusing in microfluidic devices. Microfluidics and nanofluidics 9 (1), 1–16.

Zeng, L., Balachandar, S., Fischer, P., 2005. Wall-induced forces on a rigid sphere at finite reynolds number. Journal of Fluid Mechanics 536 (1), 1–25.

Zheng, S., Lin, H. K., Lu, B., Williams, A., Datar, R., Cote, R. J., Tai, Y.-C., 2011. 3d microfilter device for viable circulating tumor cell (ctc) enrichment from blood. Biomedical microdevices 13 (1), 203–213.